



HAL
open science

Soft UV nanoimprint lithography : a versatile technique for the fabrication of plasmonic biosensors

Jing Chen

► **To cite this version:**

Jing Chen. Soft UV nanoimprint lithography : a versatile technique for the fabrication of plasmonic biosensors. Other [cond-mat.other]. Université Paris Sud - Paris XI; Northwestern Polytechnical University (Chine), 2011. English. NNT : 2011PA112024 . tel-00591992

HAL Id: tel-00591992

<https://theses.hal.science/tel-00591992>

Submitted on 10 May 2011

HAL is a multi-disciplinary open access archive for the deposit and dissemination of scientific research documents, whether they are published or not. The documents may come from teaching and research institutions in France or abroad, or from public or private research centers.

L'archive ouverte pluridisciplinaire **HAL**, est destinée au dépôt et à la diffusion de documents scientifiques de niveau recherche, publiés ou non, émanant des établissements d'enseignement et de recherche français ou étrangers, des laboratoires publics ou privés.

N° d'ordre : 9066

**UNIVERSITÉ PARIS XI
UFR SCIENTIFIQUE
D'ORSAY**

THÈSE

Présentée

Pour obtenir

**Le GRADE de DOCTEUR en PHYSIQUE
DE L'UNIVERSITÉ PARIS XI ORSAY**

PAR

Jing CHEN

**Soft UV nanoimprint lithography : a
versatile technique for the fabrication of
plasmonic biosensors**

Soutenue le 21 Mars 2011, devant la commission d'examen :

Mme Jumana Boussey	(Rapporteur)
M. Huiqing Fan	(Rapporteur)
M. Philippe Lecoeur	(Président du jury)
M. Bernard Bartenlian	(Examineur)
Mme Dongmei Zhu	(Examineur)
M. Zhengtang Liu	(Directeur de thèse)
Mme Anne-Marie Haghiri-Gosnet	(Directeur de thèse)

Résumé de la thèse

Durant la dernière décennie, la résonance de plasmons de surface (SPR) est devenue très populaire pour effectuer des analyses au cours d'un greffage chimique (ou biochimique) et étudier ainsi des réactions chimiques. Les capteurs SPR ont plusieurs mérites dont la détection en temps réel et une grande sensibilité, ce qui leur ouvrent de larges perspectives applicatives comme biocapteurs et dans l'industrie chimique. Ce champ de recherche a été récemment favorisé par une croissance rapide des outils de nanostructuration de surface parmi lesquelles les lithographies douces émergent.

Au début de ma thèse, l'approche la plus commune pour élaborer des films métalliques était la lithographie électronique (EBL) ou la lithographie par faisceau d'ions focalisés (FIB). Puisque ces deux techniques lithographiques souffrent de limitations en terme de débit (temps d'écriture trop long), nous avons choisi de développer une méthode lithographique alternative, la nanoimpression assistée UV dite "douce", qui permet de fabriquer des réseaux de nanomotifs sur de très grandes surfaces. Contrairement aux lithographies traditionnelles, cette technique repose sur la déformation mécanique de la résine. Elle permet donc d'atteindre des résolutions inégalées en deçà des limitations des techniques classiques, dues à la diffraction de la lumière ou aux effets de diffusion dans la résine. La simplicité du procédé et le faible coût du dispositif expérimental sont les principaux atouts de la nanoimpression douce (voir chapitre 1 - état de l'art).

Après l'étude de la technique de nanoimpression couplée à celle de la gravure ionique réactive, qui sont décrites dans les chapitres 2 et 3, notre étude optique a été menée tout d'abord sur des matrices de nanotrous dans des films d'or (chapitre 4). J'ai étudié le mécanisme physique du phénomène de transmission assistée par plasmons en étudiant de manière systématique les effets des paramètres structuraux sur la position du pic de transmission de la nanostructure. Une validation de principe des mesures

réalisées dans un système fluide a montré une réponse à un faible changement de l'indice de réfraction à la surface de la matrice.

Enfin, dans le dernier chapitre (chapitre 5), une nouvelle géométrie de biocapteur optique basé sur un tri-couche nanostructuré dans une géométrie de type "méta-matériau" est présentée. Les capteurs fonctionnent de façon similaire aux capteurs SPR bien établis, mais offrent une amélioration de la sensibilité de plusieurs ordres de grandeur. Les propriétés de résonance de ces méta-matériaux en grille sont discutées à l'aide d'outils de simulation numérique (en collaboration étroite avec Stéphane Collin du LPN). Enfin, nous démontrons qu'un tel capteur possède une grande sensibilité à la détection de biomolécules et serait donc adapté à l'étude d'interactions immunochimiques.

Abstract

During the last decade, surface plasmon resonance (SPR) has become widely used to characterize a biological surface and to characterize binding events in the fields of chemistry and biochemistry. Since SPR sensors exhibit many merits such as real-time detection and high sensitivity, a wide range of applications as biosensors or chemical sensors is expected. In addition, research in this field has been favored by the tremendous growth in nanofabrication methods among which soft lithographies are alternatively emerging.

At the beginning of my PhD, most commonly used lithographies were electron-beam lithography (EBL) or focused ion beam lithography (FIB). Since, both these approaches have limitations in terms of high cost and low throughput, we have studied and developed soft UV nanoimprint lithography, an emerging flexible technology allowing patterning on large area of subwavelength photonic nanostructures. Unlike traditional lithographies, this technique relies on direct mechanical deformation of the resist. Thus, beyond the limitations imposed by light diffraction or beam scattering usually observed with conventional techniques, resolution can be largely improved. The main advantages offered by soft UV nanoimprint lithography concern the simple patterning procedure and the low cost of the experimental setup. All the advantages of this technique are described and resumed in the chapter 1.

Chapters 2 and 3 present the fabrication of master stamps, the study of nanoimprinting parameters coupled with the optimization of the etching process. The physical mechanisms of the transmission phenomenon exhaled by surface plasmons were studied based on arrays of imprinted gold nanoholes (chapter 4). Extraordinary light transmission has been experimentally demonstrated. The geometrical effects on the position transmission peak were systematically analyzed. Proof-of-concept measurements performed in simple fluidic device indicate a response to small changes in

refractive index in the surface vicinity.

A novel design of optical sensor based on plasmonic nano-grating metamaterial was also studied (chapter 5). The sensor operates similarly to well-established SPR sensors, but offers large improvement in sensitivity. From numerical simulations (in collaboration with Stéphane Collin in LPN), the resonance properties of these innovative nano-grating metamaterials have been studied and discussed based on their geometrical dependence. Since this system has demonstrated higher sensitivity for detection of biomolecules, it is thus fully adapted to study immunochemical binding interactions.

Acknowledgments

In the Autumn of 2007, I was financed by China Scholarship Council to study in the Laboratoire de photonique et de nanostructures (LPN-CNRS) in Marcoussis, France. In the end of the dissertation, I'm very grateful to all the people who have offered me help and encouragement. First and foremost, I would like to express my sincere gratitude towards the director of the lab Jean-Yves Marzin.

I offer my sincerest gratitude to my advisor in France, Dr. Anne-marie Haghiri-Gosnet, for incorporating me in the group of "Nanotechnology and Microfluidic Devices" in LPN and providing me the opportunity to study in the fascinating topic. I'm greatly indebted to her constantly supported me with her extremely valuable advices, encouragements and guidances. Without her warmhearted supporting and enormous amount of patience, it's impossible for me to finish my ph.d. study so smoothly. Moreover, I would like to thank her endless help and care for my life, which greatly facilitate my life in France.

I would like to express the deepest appreciation to my advisor in China, Professor Zheng-tang Liu, who motivated and challenged me throughout this endeavor. His patience, guidance and insight were invaluable. I deeply appreciate his patient instruction and persisting guidance to the field of materials science. Besides the knowledge of my major, he also taught and encouraged me to learn more on the other research fields. I have benefited greatly from him for the guidance on reading and writing too.

Thanks are extended to my committee members: Dr. Jumana Boussey, Dr. Huiqing Fan, Dr. Philippe Lecoer, Dr. Bernard Bartenlian and Dr. Dongmei Zhu for their valuable time and suggestions.

I appreciate very much the companionship and friendship of my research colleagues during the course of my ph.d. studies. I am grateful to Dr. Jian Shi and Dr. Andrea Cattoni for sharing their experience in research and giving me kind help and useful discussion, which helped me

greatly to make a smooth progress and overcome the difficulties during the research.

I'm thankful to Dominique Decanini who helped me a lot in experimentation during these three years; Stéphane Collin and Ghenuche Petru for optical simulation and characterization; Isabelle Sagnes for FTIR analysis and the LPN clean room group for various technical support. I'm also very grateful to the members of the group: Antoine Pallandre, Qin-li Kou, Clément Nanteuil, Sébastien Méance and Guillaume Aubry for their always very cordial discussions.

I would also like to express my gratitude to my parents, my parents in law, my husband and the family of my sister for their encouragement throughout the graduate program. In addition, I'm thankful to all my friends who keep me company in both France and China: Feng Liao, Quan Dong, De-long HE, Zhuang Zhao, Xiao-yan Yang, Sheng-hong Yao, Weilong Li, Jin-yan Song, Ling-sheng Liu, Ding-yi Cong, Kohsin Li, Lin-wei Yu, Bing Wang, Ying-xin Liang, Wen-ting Liu, Feng Yan, Ting-ting Tan, Hao Tian, Qi-jun Liu, Miao Zhang, Qian Wu, Lu Liu, Xu-xu Bai for their sharing my happiness and for their support and encouragement when I met difficulties.

Contents

Résumé de la thèse	iii
Abstract	v
Acknowledgments	vii
Outline	xxiii
1 Introduction	1
1.1 Why surface plasmon resonance for bio-sensing and nanoimprint lithography?	1
1.2 Surface plasmon resonance biosensors	3
1.2.1 Brief history of SPR	3
1.2.2 Principles of SPR	4
1.2.3 SPR for biosensing	11
1.3 Soft UV nanoimprint lithography	18
1.3.1 Historical recall	18
1.3.2 Principle of UV nanoimprint lithography	19
1.3.3 UV-NIL in the roadmap	21
1.3.4 Comparison to the other lithographic techniques	26
1.3.5 Challenge of nanoimprint lithography	27
1.3.6 Advantages of soft UV-NIL	31
1.3.7 NIL for biosensing	32
1.4 Thesis objectives	34
2 Mold and stamp fabrication	45
2.1 Master mold fabrication	45

2.1.1	Commercial EBL molds	47
2.1.2	EBL process based on the PMMA resist	48
2.1.3	EBL process based on the ZEP-520 resist	50
2.2	Soft stamp fabrication	51
2.2.1	Basic soft PDMS stamp fabrication process	52
2.2.2	Improved soft stamp fabrication process	53
2.3	Anti-sticking surface treatment	54
2.3.1	State of the art	54
2.3.2	Principle of anti-sticking treatment	55
2.3.3	Anti-sticking treatment by TMCS	57
2.4	Mold pattern inversion based on NIL	57
2.4.1	Materials and fabrication	58
2.4.2	Results and discussion	60
2.5	Conclusion	64
3	Development of soft UV nanoimprint lithography	73
3.1	The nanoimprint machine	74
3.2	Soft UV nanoimprint resist	78
3.2.1	Properties of UV-NIL resist	79
3.2.2	Principles of photopolymerization	80
3.2.3	Viscosity	81
3.2.4	Commercial UV-NIL resist	82
3.3	Soft UV nanoimprint process	85
3.3.1	Theory of imprint behavior	85
3.3.2	Imprint process sequence	89
3.3.3	Imprint process optimization	93
3.4	Elimination of residual layer	97
3.4.1	Optimization initial thickness of Amonil resist	98
3.4.2	Optimization RIE conditions of Amonil resist	100
3.5	Pattern transfer	118
3.5.1	Transfer by lift-off	119
3.5.2	Transfer by RIE	122
3.5.3	Transfer by ion beam etching	126
3.6	Conclusion	126

4	Gold nanohole arrays for biochemical sensing	135
4.1	Introduction	135
4.1.1	Nanohole arrays as SPR based sensors	136
4.1.2	Patterning methods for plasmonic arrays	139
4.2	Fabrication of gold nanohole arrays	140
4.3	Experimental setup	143
4.3.1	Simple fluidic device fabrication	143
4.3.2	Chemicals	144
4.3.3	Optical measurements	145
4.4	Optical characterization	145
4.4.1	SPR of nanohole arrays with different period	145
4.4.2	SPR after chemical modification of Au nano-hole surface	146
4.5	Conclusion	149
5	Plasmonic nano-grating metamaterials for biosensing	155
5.1	Introduction	155
5.2	Localized surface plasmon resonance	158
5.2.1	Principle of LSPR sensing	158
5.2.2	Comparison with SPR sensing	162
5.3	LSPR sensing with nano-grating metamaterials	163
5.3.1	Plasmonic nano-grating metamaterials designs	164
5.3.2	Simulation results	166
5.3.3	Fabrication techniques of plasmonic metamaterials	169
5.4	Experimental procedure	171
5.4.1	Sample fabrication	171
5.4.2	Optical arrangement	174
5.4.3	Biological modification of gold surface	175
5.5	Results and discussion	178
5.5.1	Optical measurement results	178
5.5.2	Optical characterization of binding events	180
5.6	Conclusion	182
	Conclusion	187

List of Figures

1.1	SPPs on metal film interfaces	4
1.2	Dispersion of surface plasmon polaritons on a metal surface.	6
1.3	Characteristic scale of SPPs in visible and infrared bands.	7
1.4	(a) Excitation of surface plasmon-polaritons by a light beam via prism coupling and (b) Dispersion relation of SPPs and incident light.	9
1.5	(a) Excitation of surface plasmon-polaritons by light diffraction on a diffraction grating and (b) Dispersion relation of SPPs and incident light.	10
1.6	SPPs near-field optical excitation configurations: (a) excitation with a SNOM probe and (b) excitation on rough metallic surface	11
1.7	(a) Tracking absorption by most widely used prism coupler-based SPR system and (b) resonance shift in the reflected light spectrum.	12
1.8	(a) SEM image of a double-hole array with a 800 nm periodicity. The diameter of the circular hole is 200 nm and the center-to-center hole distance is 190 nm. (b) Real-time measurement of BSA on the gold surface [41].	15
1.9	(I) SEM image of the resulting structure. (II) Real-time measurement of the absorption of 10ug/ml NeutrAvidin to a free-standing gold nanotube array [42].	16
1.10	AFM images of micropatterned thin films with (a) microtriangle and (b) microhole arrays. (c) Sensogram for the detection of 10 nM IgG with different plasmonic materials [43].	16
1.11	(a) Schematic of the nanorod-based immunoassay. (b) SEM image of films of gold nanorods with about 15 nm diameter and 50 nm length for individual nanorods. (c) The LSPR peak wavelength throughout continuous immunoassay experiments. (d) Test of sensor sensitivity [44].	17

1.12	(a) Schematics of the originally proposed NIL process. (b) Scanning electron microscopy (SEM) image of a SiO ₂ mold with 10 nm minimum diameter pillars with a 40 nm period and 60 nm height. (c) SEM image of a top view of corresponding replica formed by imprinting into PMMA with 60 nm depth, demonstrated by S. Y. Chou in 1997 [46].	19
1.13	Process steps of UV nanoimprint lithography	20
1.14	Comparison of the full-wafer processing and step-and-repeat approaches in UV-NIL [52].	21
1.15	ITRS Projections for lithography technology [53]	22
1.16	(a) SEM images of a silicon oxide mold. (b) SEM images of the imprinted P-NIL resist after UV curing and mold separation. (c) SEM images of Au contacts after evaporation of metal and lift-off of the resist [54].	23
1.17	(a) AFM images of a SWNT master. (b) AFM image of a layer of PAA imprint with a mold derived from a SWNT master. (c) TEM images of Pt/C replicas formed by angled evaporation onto relief features in PAA fabricated with a similar SWNT master [55].	24
1.18	(a) Schematic illustration of the mold-assisted optical lithography. (b) SEM images of a mold structure with feature sizes ranging from 70 nm to 1 um made of a fused silica substrate and a thin film metallic cap layer and (c) SEM of replica formed by the mold-assisted near-field optical lithography [56].	24
1.19	30 nm semi-dense structure: (a) template, (b) imprinted features, (c) etched SOI fins, (d) cross-section of etched fins ready for implantation and (e) critical dimension (CD) and LWR for the 30 nm features after etch for two different wafers[57].	25
1.20	(a) SEM images of 100 nm pitch, 20 nm holes imprinted in NXR-3010 resist using P-NIL and (b) SEM images of 200 nm pitch, 65 nm pillars imprinted in NXR-2010/NXR-3010 resist over 4 inch wafer using P-NIL [58].	26
1.21	Residual thickness as a function of pattern density and mapping across the same plate [66].	30
1.22	Process flow of the soft UV-NIL nanoimprint lithography technique.	31
1.23	(Top)Process used to fabricate “nano-block molds”. (Bottom) SEM images of representative nanoblock molds derived from one-dimensional gratings by using NIL [71].	33

2.1	The basic components of a typical electron beam lithography system (excluding electronic component).	46
2.2	(a) The organization of the standard commercial stamp fabricated by NIL technology and (b) SEM images of dots array (left) and lines arrays (right) in the standard commercial stamp from NIL technology[6].	47
2.3	(a) process 1: multi-step fabrication process based on EBL PMMA resist exposure combined with lift-off and etching; (b) SEM images of nanodots (diameter = 100 nm, pitch = 100 nm) and nanolines (linewidth = 220 nm, pitch = 180 nm) structures in silicon mold patterned by e-beam lithography and reactive ion etching before the removal of Ni mask.	48
2.4	(a) process 2: a single-step fabrication process based on EBL in PMMA resist and direct etching (b) SEM images of nanoholes (diameter = 200 nm, pitch = 400 nm) and nanolines (linewidth = 200 nm, pitch = 400 nm) structures in silicon mold.	49
2.5	Schematic illustration of the basic procedure for the preparation of the soft stamp.	52
2.6	(a) Procedure for fabricating a h-PDMS/PDMS two-layer composite stamp. (b) SEM image of 200 nm nanolines arrays with a spacing of 200 nm of the silicon master and (c) Atomic force microscope (AFM) image of the replicated h-PDMS/PDMS bilayer stamp of the corresponding Si master.	53
2.7	Surface energy of the polymer, solid and interior surface.	56
2.8	Schematic diagram of the mechanism for anti-sticking treatment by using TMCS.	57
2.9	The mold inversion process based on T-NIL and ion beam etching. The daughter mold exhibits holes arrays instead of pillars on the EBL master.	59
2.10	SEM images of nanoline gratings with different linewidth: NL1: 100 nm, NL2: 70 nm, NL3: 50 nm after thermal nanoimprint lithography, reactive ion etching of the residual resist.	61
2.11	SEM images for nano square dots gratings with different diameter on the Si master, gold nanoholes arrays with different diameters after thermal nanoimprint lithography, reactive ion etching of the residual resist and ion beam etching for inversed replicating patterns of the Si master and the area distribution of the inversed replicated mold. . .	62

2.12	Images of 2 inches Si inverted replication molds (daughter molds) with (top) a 1 cm ² hole array ($d = 200/p = 400$ nm) and (bottom) a 1.5 cm ² line array ($d = 150/p = 300$ nm) fabricated based on thermal NIL and IBE.	64
2.13	(a) Schematics of the soft UV nanoimprint process and (b) SEM images of the grand-daughter mold with different diameter pillars and linewidth lines gratings based on the proceeding fabrication procedure: soft UV-NIL with the h-PDMS/PDMS bi-layer stamp obtained from the Si daughter mold patterned with 200 nm-wide nanohole arrays, tri-layer etching, lift-off and transferred into Si.	65
3.1	Photo of the NX-2500 imprinter installed in LPN clean room.	75
3.2	(a) Image of the working chamber of the NX-2500 system. (b) and (c) Photos of the drawer on which is top film ring holder and the wafer holder, the mask and wafer is put in the center of the wafer holder, sandwiched between two plastic membrane on both holder. (d) Schematic diagram shows the Air Cushion Press (ACP) offers ultra uniform pressure during imprint.	76
3.3	Substrate and mask alignment system on NX-2500: A-Wafer stage x-movement, B-Wafer stage y-movement, C-Wafer stage Θ -movement, D-Mask holder, E-Wafer chuck, F-Mask holder seating, T1-Emergency switch, T2-Power on/off, T3-Pin pressure gouge, T4-Pin pressure regulator, S1-Illumination lamp intensity, S2-Illumination lamp power on/off, S3-Illumination fiber.	77
3.4	Images of the demolding system.	78
3.5	Spin curve of NXR-2010 resist at different acceleration (3%).	83
3.6	Spin coating curves of two types Amonil resist.	84
3.7	The schematics of three imprint regimes.	88
3.8	schematic illustrations of calculated factor f in the case of periodic lines, dots and holes arrays.	89
3.9	Process scheme of soft UV nanoimprint.	90
3.10	Optical micrography of photonic crystal arrays after soft UV nanoimprint.	92
3.11	(a)-(c) The CD measurement of the mold and the imprinted Amonil in three different patterns and correspondence increase of CD upon imprint in three patterns on scales of percentages.	96
3.12	SEM images of different residual layer.	98

3.13	Schematic of four RIE process: (a) ion sputtering, (b) reactive etching, (c) radical formation and (d) radical etching.	101
3.14	Schematic diagram of an reactive ion etching system.	102
3.15	FTIR spectra of photo-polymerized Amonil resist.	103
3.16	SEM pictures of 220 nm line profiles after (a) soft UV-NIL and (b) etching by process NXR2.	105
3.17	A schematic side-wall profile after RIE (a) an ideal anisotropic etching profile with $V_{lateral} \approx 0$. (b) an anisotropic overetching profile with non-vertical sidewall (The slope of sidewall profile is described by θ).	106
3.18	SEM cross-section views of 220 nm line etched by CHF_3/O_2 plasmas with process (a) NXR5 and (b) NXR6.	107
3.19	The etch rate for 220 nm-linewidth nanoline pattern etched by CHF_3/O_2 plasmas with different gases fraction.	108
3.20	SEM cross-section views of nanoline patterns etching by O_2/CHF_3 plasmas with different gases ratio.	109
3.21	(a) The etch rate and (b) the sidewall angle for 220 nm-linewidth nanoline pattern etched by CHF_3/O_2 (6/16 sccm) with various RF power.	110
3.22	SEM cross-section views of nanoline patterns etching by 16 sccm $\text{CHF}_3/6$ sccm O_2 plasmas with different RF power.	110
3.23	SEM images of nanoline patterns etching profile by using 8 sccm $\text{CHF}_3/3$ sccm O_2 plasmas.	111
3.24	SEM cross-section views of nanoline patterns etching by SF_6/O_2 plasmas with different (a),(b) gases ratio and (b), (c) pressure.	113
3.25	SEM cross-section views of nanoline patterns etching by SF_6 plasmas with different etching parameters.	114
3.26	The etch rate for 220 nm-linewidth nanoline pattern etched by $\text{CHF}_3/\text{SF}_6/\text{O}_2$ plasmas with different CHF_3/SF_6 gases fraction.	116
3.27	SEM cross-section views of nanoline patterns etching by $\text{CHF}_3/\text{SF}_6/\text{O}_2$ plasmas with different gases fraction.	117
3.28	SEM cross-section views of nanoline patterns etching by $\text{CHF}_3/\text{SF}_6/\text{O}_2$ with 12/8/2 sccm plasmas with different power: (a) 20 W, (b) 15 W and (c) 10 W.	118
3.29	schematic diagram of general procedure of bi-layer lift-off process.	120
3.30	SEM images of a (a) 200 nm linewidth line array and (b) 200 nm pitch dot array obtained by soft UV-NIL after lift-off with Amonil/Ge/PMMA tri-layer system.	121

3.31	SEM images of nanolines arrays after RIE without and with acid treatment.	122
3.32	SEM images metallic lift off results on the patterns without and with HCl treatment.	123
3.33	Schematic representation of two ways for transferring the pattern into the substrate by RIE.	124
3.34	SEM images of nano patterns transferred into Si substrate with removal of Ni mask: (a)the hole diameter is 300nm and (b) the outer and the inner diameter of ring is 700 nm and 600 nm separately. . .	125
3.35	SEM images of PMMA pillars and lines arrays, the height is about 1 um.	125
3.36	SEM images of the lines and dot arrays transferred into silicon with different sizes. The etch depth of each pattern is about 120nm . . .	127
4.1	(a)Schematic diagram illustrating incident light scattering into SP modes and enhanced transmission at select wavelength; (b) SEM images of several nanohole arrays with various geometries and dimensions [14].	137
4.2	An overview of major routes for the development of active plasmonics.	138
4.3	Schematic depiction of nanoring fabrication by colloidal lithography method.	140
4.4	Description of the nanohole fabrication process based on soft UV nanoimprint.	141
4.5	Scanning electron micrography (SEM) recorded on the Si master for nanodot gratings, with different diameter d and period p: (a) d = 200 nm, p = 400 nm; (b) d = 300 nm, p = 600 nm. The height of the pattern is about 130 nm.	141
4.6	SEM images of arrays with sub-wavelength holes of different diameters d and periodicities p (a) d = 100 nm, p = 200 nm; (b) d = 200 nm, p = 400 nm; (c) d = 250 nm, p = 500 nm after Cr/Au lift-off.	142
4.7	Application of nanohole array sensing elements: (a) Schematic and (b) image illustrating the architecture of the simple microfluidic device with embedded nanohole arrays; (c) Schematic of the optical configuration for transmission measurements through the periodic arrays nanoholes.	143
4.8	Schematic of thiol containing alkyl chains on the surface of gold. . .	144
4.9	Chemical structural formula of sucrose molecular.	145

4.10	Transmission spectra obtained through three nanohole arrays with different diameters d and periodicities p (green) $d = 150$ nm, $p = 300$ nm; (red) $d = 200$ nm, $p = 400$ nm; (black) $d = 250$ nm, $p = 500$ nm.	146
4.11	Transmission spectra obtained through the 400 nm periodicity arrays with self-assembled monolayer (SAM) hexadecanethiol.	147
4.12	Results of sensitivity test with sucrose solutions of known refractive index. Transmission spectra were obtained through the 400 nm periodicity arrays for pure water, after sucrose solutions with increasing refractive index. (a) Schematic of sucrose flow on the gold surface. (b) Sample transmission spectra plotted together. (c) The measured value and the Lorentz fit curve for a sample with 60% sucrose solution.	148
4.13	The relative redshift in peak wavelength for four peaks exhibited by the array as a function of refractive index.	149
5.1	Schematic diagrams illustrating (a) a localized surface plasmon and (b) a surface plasmon polariton or propagating plasmon.	157
5.2	Dispersion relation of SPPs at the interface between a Drude metal with negligible collision frequency and air (gray curves) and silica (black curves) [13].	159
5.3	Schematic illustration of the oscillation of conduction band electrons of a metal nanoparticle with an electromagnetic field, resulting in a localized surface plasmon.	159
5.4	The 3D-FDTD simulation of the optical electric field distribution of a 2×2 array of Au@SiO ₂ on a single-crystal gold surface: (a) Side-view and (b) Top view of the optical electric field distribution at the gap between the particle and the surface [15].	160
5.5	Left panel: The basic element of the optical antenna array with the fundamental localized resonance is essentially confined in the dielectric layer. Right panel: scheme of the designed metamaterial structure studied in this section consisting of SiO ₂ dielectric layer between two Au films with a nanogratings on top Au layer.	165
5.6	Calculated distribution of the (a) electric field amplitude and (b) polarization whereas the green (red) arrows show the real (imaginary) part of the polarization vector for a plasmonic subwavelength rectangular nanoparticle deposited on a metal slab [28].	166

5.7	Calculated Reflectivity at 50° for a structure with gold bottom layer of 40 nm, SiO ₂ layer 40 nm, gold grating of 200 nm lines, pitch 200 nm and a thickness of (a) 40 nm (b) 30 nm and (c) 20 nm. Curve (d) has been calculated considering a SiO ₂ layer of 20 nm and gold grating thickness of 40 nm.	167
5.8	Calculated Reflectivity at 50° for a structure with gold bottom layer of 100 nm, SiO ₂ layer of (a) 40 nm and (b) 20 nm, gold grating of 200 nm lines, pitch 200 nm and a thickness of 20 nm.	168
5.9	Reflectivity spectra calculated at different angles of incidence for a structure with gold grating of 200 nm lines, pitch 200 nm and a thickness of 20 nm, a SiO ₂ layer of 20 nm and a gold bottom layer of (a) 40 nm and (b) 200 nm.	170
5.10	Scanning electron micrography (SEM) images of the Si master mold with 200 nm nanoline patterns fabricated by E-beam lithography. . .	172
5.11	Schematic of the main steps in the sample fabrication process. . . .	173
5.12	SEM image of a 400 nm period grating metamaterials after Au(20 nm)/Cr(2 nm) lift-off.	174
5.13	Schematic diagram of the setup for angle-resolved transmission and reflection optical measurements: A. FTIR spectrometer; B. achromatic optical focusing system; C. sample and detector rotation stages. The displacement sensor (symbolized by the double blue arrow) shows how to measure in transmission or reflection mode.	174
5.14	The structural formulas for EDC, S-NHS and 6-mercaptohexadecanoic acid molecules.	176
5.15	Chemical reaction of procedure adopted for immobilizing antibody on carboxylic acid end groups on SAMs.	177
5.16	Reflection spectra of the nano-grating array in the air ($n=1$) with different thickness of bottom Au/Cr layer: (a) Au/Cr=40/2 nm; (b) Au/Cr=200/5 nm.	179
5.17	Experimental absorbance spectra of nanograting spectra in an air ($n=1$) obtained via $A = 1 - T - R$	180
5.18	(a) Immobilization of anti-mouse IgG on the Au pattern surface using the SAM of 6-Mercaptohexanoic as an intermediate coupling layer. EDC/NHS was used to bind the anti-mouse IgG. Experimental tuning of the absorbance spectra by changing the dielectric environment which adjacent to the gold grating: (b) when incident at 12° and (c) plot of the the wavelength-associated maximum absorbance versus the incident angle.	181

List of Tables

1.1	Comparison of the detection limits of optical biosensors based on analyte type.	14
1.2	Comparison between nanoimprint lithography and other nanopatterning techniques.	28
2.1	Comparison of some nanorings patterns defined in ZEP-520 resist by EBL with different electron doses.	50
2.2	Summarized results of feature size (for nanohole array the dimension refers to the diameter and for nanoline array the dimension refers to the width). The first table line gives dimensions on the Si master mold and the second line gives dimensions measured on the inverted mold fabricated by T-NIL and IBE.	63
3.1	Four major master molds prepared by E-beam lithography and transferred in 2 inch Si wafer.	90
3.2	Schematic illustration of the Amonil resist flow behavior during UV-NIL process by applying different pressure and the corresponding SEM images with nanodot patterns.	95
3.3	Process parameters for UV nanoimprints with Nanonex 2500 machine.	97
3.4	The effect of imprinted thickness on the residual thickness.	99
3.5	Assignment of major peaks in Amonil.	104
3.6	The investigated etching conditions for CHF ₃ /O ₂ plasmas.	105
3.7	The measured w, d and calculated θ value of nanoline pattern etched with NXR2, NXR5 and NXR6 process.	106
3.8	The investigated etching conditions for SF ₆ and O ₂ plasma.	112
3.9	The investigated etching conditions for CHF ₃ , SF ₆ and O ₂ plasmas.	116
3.10	Comparison of different pattern transfer techniques.	128

4.1	Comparison of feature size of the Si master mold and the sample fabricated by soft UV-NIL after lift-off process.	142
5.1	Comparison between SPR and LSPR sensors [26].	163
5.2	Process parameters for RF-PECVD deposition of SiO ₂	172
5.3	The spectral positions of three peaks obtained from measurements (simulations) for 2 fabricated samples with different Au/Cr planar layer of metamaterial gratings when incident at 50°.	178

Outline

Nanotechnology as an inter-disciplinary science has developed very rapidly over the last decade and the range of applications is increasing. Metallic nanostructures exhibit unusual optical, magnetic, catalytic and mechanical properties that are inherent to their small size and not observed in bulk materials. Such nanoscopic properties have permitted the development of novel devices. One of the earliest applications concerns the development of improved chemical and biological sensors. During the last two decades remarkable progress has been made in the development of optical nanosensors for environmental monitoring, biotechnology, medical diagnostics, drug screening, food safety and security.

Amongst all sensing and characterization techniques, non-intrusive optical sensors are markedly attractive. Using light as a probe of a chemical reaction in a biological sample offers the advantage of a non-invasive detection technique. The use of an electromagnetic wave confined near the surface of the sample provides an efficient optical probe. Surface plasmons (SPs) that are defined as a collective oscillation of the free electrons at the interface between a metal and a dielectric can be used as such electromagnetic wave probe. SPs are very sensitive to any change in the near-surface dielectric constant. They are thus well-suited for detection of binding events which can be exploited in a wide variety of SPR-based sensing applications.

SPR is a suitable technique for highly sensitive affinity-based biosensing applications. Up to now, many companies have developed several commercial SPR systems. The SPR biosensor can provide real-time and kinetic information of biomolecular interactions, and it is beneficial for detecting biological analytes and analyzing biomolecular interactions. Moreover, development of SPR sensors for detection of chemical and biological species has gained considerable momentum. Lately, plasmonic nanostruc-

tures have started to be largely applied based on their intense SPR and the ability to tune this resonance by simply changing the size, the shape, the composition, and the surrounding medium of the nanostructure.

This thesis work has been conducted in the Laboratory for Photonics and Nanostructures (LPN- CNRS). As a part of the experimental research activity, we focused on the development of soft UV nanoimprint lithography technique to fabricate large-area, uniform metallic subwavelength nanostructures for SPR sensing applications. We present the flexibility of this approach by fully control the plasmonic response of nanostructure through its size. As demonstrator, the fabricated nanostructures have been used for chem/bio molecular sensing.

This dissertation is organized into 5 chapters, the contents of which are organized as follows:

Chapter 1 provides a general introduction to surface plasmon resonance and nanoimprint lithography techniques. First, the background of SPR biosensor is presented, including: a brief history of SPR, basic physics and common techniques for optical excitation and detection of SPR, applications of plasmonics in the field of sensing technology. Then, we present the history of both thermal nanoimprint lithography (T-NIL) and UV nanoimprint lithography (UV-NIL). Whereafter, the main challenges for future successful applications are discussed and recent research experiments are presented from state-of-art in literature. We also explain why soft UV-NIL appears as the most attractive method in the context of our investigation. Finally, the advantages of NIL for SPR biosensing are resumed.

Chapter 2 describes the steps of the fabrication processes of master molds based on different resists and the replication of soft mold. An introduction to various state-of-the-art anti-sticking agents for surface treatment is then given. Furthermore, a perfect copy or inversion process of a master mold is proposed by combining T-NIL and soft UV-NIL.

Chapter 3 begins with a short introduction on nanoimprinters as well as specific imprinting resists used for the experimental part of this thesis. The optimization of the parameters of the soft UV-NIL process is then discussed. Similarly the etching process for residual layer removal is given. This chapter ends with presenting different pattern transfer techniques used in combination with soft UV nanoimprint lithography for pattern replication into a substrate.

Chapter 4 reports how soft UV nanoimprint lithography can be used for the fabrication of gold nanohole arrays for surface plasmon sensor application. The SEM characterization of the imprinted patterns shows good

homogeneity over large area. Finally, a simple fluidic device that integrates gold nanohole arrays has been developed and is presented. The optical measurements indicate that such nanohole arrays can be easily integrated and used as an effective SPR detectors in a microfluidic system.

Chapter 5 presents the design of an original tri-layer geometry for the SPR sensor. Such sensor couples a planar metallic film to metallic nanogratings. To optimize the geometry of this new SPR tri-layer, numerical investigations have been done. More particularly, we show how the thicknesses of metallic film, nanograting and dielectric spacer change the reflective spectrum. Our experimental process related to the fabrication of these tri-layer SPR structures is then described and immunodetection of anti-mouse IgG process is presented. Compared with conventional label-free plasmonic devices, our approach demonstrates significant improvement in the detection of small analytes.

Chapter 1

Introduction

The goal of this thesis was to develop soft UV nanoimprint lithography (NIL) as a very powerful and flexible lithography technique for producing nanostructures on very large surfaces. The main application of soft UV nanoimprint lithography that was studied in my thesis concerns large area fabrication of uniformly oriented noble metallic nanostructures and 3-dimensional gratings. Such metallic nanostructures will have tremendous impact on biosensing due to surface plasmon resonance (SPR) effect. They can thus be integrated in microfluidic devices as highly sensitive SPR-based biosensors.

After a short general introduction, this chapter will first briefly present the properties of plasmons that are excited at an interface between a metal and a dielectric and review the state-of-the-art towards practical applications of surface plasmons in the field of SPR biosensors. In a second part, a brief history of nanoimprint lithography techniques is given followed by a comparison with the other conventional or emerging lithography techniques. We also list the advantages and potential benefits of this soft UV-NIL technique, that have attracted admiration of the research community in nanofabrication and which explains the goal of my thesis work. Finally, we conclude this chapter with a discussion of progress towards developing SPR biosensor chips based on this soft UV-NIL method.

1.1 Why surface plasmon resonance for biosensing and nanoimprint lithography?

Nowadays, nanotechnology, electronics and biology are combined in the newly emerging field of bio-nanotechnology that has very recently received

much attention due to its potential as being the next area of rapid growth for high technology. One of the earliest applications of biotechnology is the invention of new complex innovative devices. Combining fundamental studies and applied techniques in such biodevices allows creating novel biophysics methods, nanoscale biosensing and nanofluidic devices for direct manipulation and analysis of biomolecules, such as DNA and proteins [1, 2, 3, 4].

Surface plasmon resonance is an affinity-based optical detection method that measures the changes in refractive index in the vicinity of a thin metallic surface during complex formation or dissociation of chemical bonds [5]. SPR, as a surface oriented method, has shown a great potential for biosensors allowing real-time analysis of biospecific interactions without the use of labeled molecules. The other advantages of these SPR sensors concern the decrease of the sample volume and the ability of tuning the wavelength to the changing nanostructures characteristics like size, shape and material. To get such metallic SPR nanostructures with the desired size and shape, both bottom up and top down approaches can be used. Concerning one common requirement of SPR sensing, a well collimated readout beam is required which supposes hence a relatively large sensing area with a large number of identical nanostructure arrays. Based on these requirements, nanoimprint lithography (NIL) appears as the most attractive lithography method for lab-scale experiments and prototyping.

Nanoimprint lithography is now standing in the spotlight as an emerging nano-fabrication technology. Since NIL is a replication technique based on a mechanical deformation under a stamp to create a thickness contrast in a polymer, its resolution is well beyond the limitations imposed by light diffraction or beam scattering that are the well-known limits of optical and electron beam lithographies. The smallest attainable feature with NIL is mainly given by stamp resolution, without any restriction of the wavelength of the light source. Moreover, NIL provides parallel processing with high throughput and is thus suitable for large-scale patterning of nano-optical structures. Recently, NIL has attracted increased levels of attention and MIT's technology review has put NIL as one of ten alternative technologies that are likely to change the world [6]. For nanoelectronics, NIL has also been added into the International Technology Roadmap for Semiconductors (ITRS) for the next 22 nm node.

Obviously, fabrication of uniformly-oriented noble metallic nanostructures on large-area using nanoimprint lithography will have tremendous impact on a number of SPR-based sensors.

1.2 Surface plasmon resonance biosensors

1.2.1 Brief history of SPR

The first observation of surface plasmons dates back to 1902, when Wood illuminated a metallic diffraction grating with polychromatic light and noticed narrow dark bands in the spectrum of the diffracted light, which he referred as to anomalies [7]. The phenomenon was attributed to the resonant coupling of photons from the polarized light to the oscillation of metal-free electrons (Surface plasmon polaritons, SPPs), generating a strong electromagnetic evanescent wave bound to the metal surface. In 1941, theoretical work by Sommerfeld and Fano concluded that these anomalies were associated with the excitation of electromagnetic surface waves on the surface of the diffraction grating [8]. In 1958, Thurbadar observed a large drop in reflectivity when illuminating thin metal films on a substrate, but did not link this effect to surface plasmons [9]. In 1968, Otto explained Thurbadar's results and demonstrated that the drop in the reflectivity in the attenuated total reflection method is due to the excitation of surface plasmon [10]. In the same year, Kretschmann and Raether reported excitation of surface plasmons by the method of attenuated total reflection [11]. All these pioneering works of Otto, Kretschmann and Raether have established a convenient method to describe the excitation of surface plasmons, and have introduced SPR into modern optics. From this pioneer work, the application of surface plasmon resonance has been intensively studied and major properties have been assessed.

In the last two decades remarkable research and development activities were performed based on optical sensors to measure chemical and biological quantities. The first optical chemical sensors have measured changes in absorption spectrum to quantify CO₂ and O₂ concentration [12]. The potential of surface plasmon resonance for characterization of thin film and monitoring processes at metal interface was recognized in the late seventies [13, 14]. In 1983, the use of SPR for gas detection and biosensing was first demonstrated by Liedberg et al. [15]. Since then SPR has been extensively explored as one of the main optical biosensor technologies. It has gradually become a very powerful label-free tool for the the real-time determination of concentration, kinetic constants and interactions between the target and the recognized biomolecules. The principle, the development and the applications of biosensors have been well described in a lot of review papers [16, 17, 18, 19].

1.2.2 Principles of SPR

Surface plasmon polaritons

Surface plasmons are the electron plasma oscillations near a metal surface that stem from the broken translational invariance in the direction perpendicular to the surface. A combined excitation consisting of a surface plasmon and a photon is called a surface plasmon polariton.

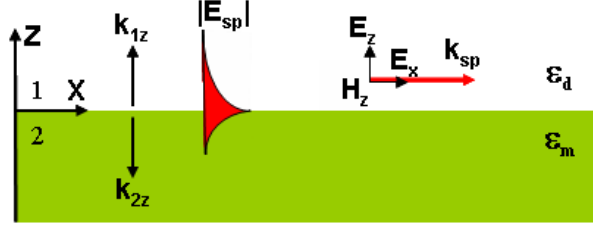


Figure 1.1: SPPs on metal film interfaces

To introduce the main parameters characterizing SPP, the simplest geometry in which a surface plasmon can exist consists of a semi-infinite metal ($z < 0$) and a semi-infinite dielectric ($z > 0$) (Fig. 1.1). The semi-infinite metal has a complex permittivity, $\epsilon_m(\omega) = \epsilon_r(\omega) + i\epsilon_i(\omega)$ in which normally the real part of the permittivity of the metal is negative and its magnitude is much larger than the imaginary part $|\epsilon_r(\omega)| \gg \epsilon_i(\omega)$. The semi-infinite dielectric ($z > 0$) has a real permittivity ϵ_d . Assuming that two kinds of medium are non-magnetic materials, which commonly constitute an optical waveguide, the magnetic permeability μ_i (i is m or d) is equal to the free-space permeability μ_0 . Surface plasmon polariton is a transverse-magnetic (TM) wave. Therefore its vector of magnetic field intensity lies in the plane of metal-dielectric interface and is perpendicular to the direction of propagation. In a Cartesian system of coordinates the distribution of magnetic intensity vectors of a surface plasmon can thus be expressed as:

$$H_{1y}(x, z) = A \exp(ik_{sp}x - k_{1z}z), \quad z > 0 \quad (1.1)$$

$$H_{2y}(x, z) = B \exp(ik_{sp}x + k_{2z}z), \quad z < 0 \quad (1.2)$$

where A and B denote the modal field amplitude, $k_{1z} = \sqrt{k_{sp}^2 - \epsilon_d k_0^2}$, $k_{2z} = \sqrt{k_{sp}^2 - \epsilon_m(\omega) k_0^2}$, k_{1z} and k_{2z} are all positive, $k_0 = \omega/c$ is the free-space wavenumber, c is the speed of light in vacuum. According to Maxwell's

curl equations:

$$\nabla \times E = -\mu_0 \partial H / \partial t \quad (1.3)$$

$$\nabla \times H = \epsilon_0 \epsilon(\omega) \partial E / \partial t \quad (1.4)$$

The distribution of electric field can be expressed by:

$$E_1(x, z) = -\frac{ik_{1z}}{\omega \epsilon_0 \epsilon_d} A \exp(ik_{sp}x - k_{1z}z), \quad z > 0 \quad (1.5)$$

$$E_2(x, z) = \frac{ik_{2z}}{\omega \epsilon_0 \epsilon_m(\omega)} A \exp(ik_{sp}x + k_{2z}z), \quad z < 0 \quad (1.6)$$

According to the boundary conditions of Maxwell's equations, the components of the electric and magnetic field intensity vectors parallel to the boundaries of the waveguiding layer ($z = 0$) are continuous at the boundaries, from Eqs.(1.1), (1.2), (1.5) and (1.6). This yields for:

$$A = B, \quad A \frac{k_{1z}}{\epsilon_d} + B \frac{k_{2z}}{\epsilon_m(\omega)} = 0 \quad (1.7)$$

from Eqs.(1.7)

$$\frac{\epsilon_d}{\epsilon_m(\omega)} = -\frac{k_{1z}}{k_{2z}} \quad (1.8)$$

Since k_{1z} and k_{2z} are all real numbers, it can be concluded that the interface surface waves exist providing that ϵ_d and $\epsilon_m(\omega)$ are of opposite signs on both sides of the dielectric interface. In nature, for most of the media, the real part of dielectric constant is positive, while real part of metal dielectric constant in the visible and near-infrared bands is negative, so the TM polarized surface waves only exist in the metal and dielectric interface, which refer to SPPs. The dispersion relation of SPPs on metal - dielectric interface can be estimated from Eq.(1.8):

$$k_{sp} = \frac{\omega}{c} \sqrt{\frac{\epsilon_d \epsilon_m(\omega)}{\epsilon_d + \epsilon_m(\omega)}} \quad (1.9)$$

The real and imaginary parts of SPPs wavevector can be expressed as:

$$k_{sp}' = \frac{\omega}{c} \sqrt{\frac{\epsilon_r \epsilon_d}{\epsilon_r + \epsilon_d}} \quad (1.10)$$

$$k_{sp}'' = \frac{\omega}{c} \frac{\epsilon_i}{2\epsilon_r^2} \left(\frac{\epsilon_r \epsilon_d}{\epsilon_r + \epsilon_d} \right)^{3/2} \quad (1.11)$$

The respective dispersion relation of surface plasmon polaritons on metal surface are shown in Figure 1.2 together with the photon dispersion in the dielectric. Since $k'_{sp} > \sqrt{\epsilon_d}\omega/c$, it can be seen from Figure 1.2 that the SPPs dispersion curve lies on the larger - wavevector side of the light dispersion in the adjacent dielectric, SPPs cannot radiate in light, and cannot be excited with conventional illumination from the adjacent medium. The concrete methods of excitation of SPPs will be explained in next section.

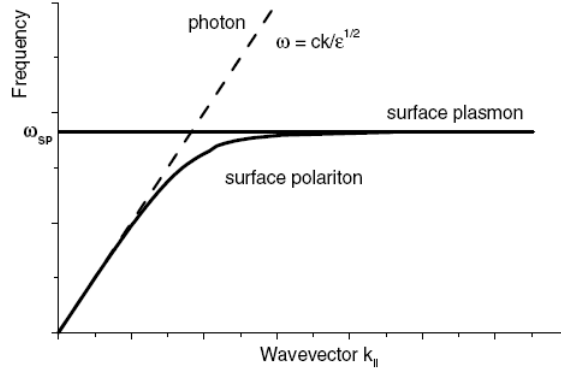


Figure 1.2: Dispersion of surface plasmon polaritons on a metal surface.

This analysis explain the basic characteristics in case of transversally magnetic mold (TM), if the surface electromagnetic field of transverse electric mode (TE) is considered. The electric field can be similarly expressed by simply exchanging the components of magnetic field towards the ones of the electrical field in Eq.(1.1) and Eq.(1.2). According to Maxwell's curl equations Eq.(1.4), the two vectors of magnetic field can be obtained. The boundary conditions of Maxwell's equations are introduced and there is no non-zero solution of eigenvalue equation for TE modes. This indicated that the surface electromagnetic field of TE mode on the surface of metal can not exist. Thus SPPs can only support TM mode. Therefore, SPPs can only be TM polarization.

The electric field of the surface plasmon polaritons propagating on a metal surface ($z = 0$) in the x-direction can be expressed as [20]:

$$\begin{aligned} E_{sp}(x, z) &= E_0 \exp(ik_{sp}x - k_z|z|) \\ &= E_0 \exp(ik'_{sp}x - k''_{sp}x - k_z|z|) \end{aligned} \quad (1.12)$$

This field configuration corresponds to a surface mode propagating along the surface with wavevector $k_{||} = k_{sp}$ and exponentially decaying from

the surface with the decay constant k_z . With the dispersion relation of SPPs, each length scale can be discussed, since which is key index for sub-wavelength photonic devices designing. These length scales are the SPPs propagation length δ_{sp} , the SPPs wavelength λ_{sp} , the penetration depth of the electromagnetic field associated with SPPs mode into the dielectric medium δ_d and the penetration depth of the field into the metal δ_m . These four length scales for surface plasmon polaritons in the visible and near-infrared are schematically shown in Figure 1.3. The SPPs wavelength, λ_{sp} , the oscillation period of electrons on the metal surface, can be obtained from the real part of the surface plasmon wavevector (equation 1.10):

$$\lambda_{sp} = \frac{2\pi}{k'_{sp}} = \lambda_0 \sqrt{\frac{\epsilon_r + \epsilon_d}{\epsilon_d \epsilon_r}} \quad (1.13)$$

We can see from equation (1.13) that the SPPs wavelength λ_{sp} is always slightly less than the free space wavelength λ_0 . Therefore to use surface structures as a means to manipulate SPPs, e.g. through the use of periodic structures that act as Bragg scatters, the length scale of such structure should be of the order of the wavelength involved. In practice, for SPPs in the visible and near-IR, the size of the structures should be in the range $\sim 400\text{-}1000$ nm.

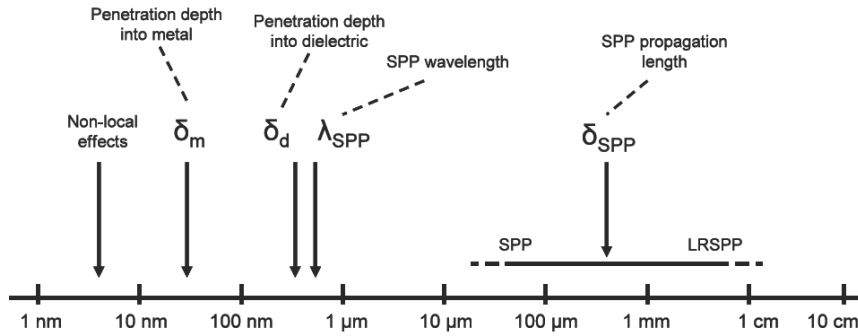


Figure 1.3: Characteristic scale of SPPs in visible and infrared bands.

To guaranty that the wavelength scale structure noted above can be effective in manipulating SPPs, the SPPs should have a propagation length that correspond to several times of their wavelength. The SPPs propagation length δ_{sp} , which is determined by the imaginary part of the surface plasmon polariton wavevector, is defined as the distance in the direction of propagation at which the energy of the surface plasmon decreases by a

factor of $1/e$. According to Eq.(1.11) and (1.12), the propagation length can be written as:

$$\delta_{sp} = \frac{1}{2k'_{sp}} = \lambda_0 \frac{\epsilon_r^2}{2\pi\epsilon_i} \left(\frac{\epsilon_r + \epsilon_d}{\epsilon_r\epsilon_d} \right)^{3/2} \quad (1.14)$$

Provided low losses inside the metal and the condition $|\epsilon_r| \gg |\epsilon_d|$ satisfied, this propagation length can be approximated as:

$$\delta_{sp} \approx \lambda_0 \frac{\epsilon_r^2}{2\pi\epsilon_i} \quad (1.15)$$

From equation(1.15), we can see that for a long propagation length, low losses in the metal are needed, which means that the relative permittivity of the metal needs to have a large real part ϵ_r and small imaginary part ϵ_i . Propagation length δ_{sp} represents an upper limit of the size of the structures one can use in case of photonic devices based on SPPs. So one effective method to increase the scale of SPP modes is to utilize the coupled SPPs modes supported by symmetrically clad thin metal films [21]. Moreover, owing to the fact that the SPPs propagation length is obviously greater than the SPPs wavelength, $\delta_{sp} \gg \lambda_{sp}$, wavelength scale gratings and other periodic surface structures can be used to manipulate SPPs since the modes are able to interact over many periods of such structure.

The field decay in the direction perpendicular to the metal-dielectric interface is characterized by the penetration depth that is defined as the distance from the interface at which the amplitude of the field decreases by a factor of $1/e$. From the dispersion relation equation(1.9), the penetration depth into dielectric δ_d and metal δ_m can be expressed separately as follows (here we have assumed again that $|\epsilon_r| \gg |\epsilon_i|$):

$$\delta_d = \frac{1}{k_0} \left| \frac{\epsilon_r + \epsilon_d}{\epsilon_d^2} \right|^{\frac{1}{2}} \quad (1.16)$$

$$\delta_m = \frac{1}{k_0} \left| \frac{\epsilon_r + \epsilon_d}{\epsilon_r^2} \right|^{\frac{1}{2}} \quad (1.17)$$

The penetration depth of the field into the dielectric δ_d is of the light wave order. It gives us a measurement of the length scale over which the SPPs mode is sensitive to the presence of refractive index changes, such as a air gap in the Otto configuration for coupling light to SPPs, or the binding of specific bio-molecules in biosensors. The penetration depth into the metal gives us a measurement of the required thickness of metal films which can excite SPPs (typically 50 nm in the visible spectrum), the thickness of metal films for super lens [22] and the thickness of metal films where the SPPs modes on the two metal surface interact [23] and so on.

Excitation of surface plasmon polaritons

Exciting surface plasmon polaritons with large efficiency is a primary task in SPPs control. Surface plasmon polaritons on metal-dielectric interface can be excited only if the energy and the momentum of the TM polarized incident light match the ones of surface plasmon polaritons. This first condition is easily satisfied, since the frequency of the incident light has to equal the frequency of the SPPs. The main difficulty is to implement the momentum matching, which means that the component of the wavevector of the incident light parallel to the surface has to equal the wavevector of the SPPs. Nevertheless, as it can be seen from the SPPs dispersion relation (Fig. 1.2), the SPPs wavevector is larger than the photon wavevector of the light in the adjacent dielectric medium. Thus, light illumination of a smooth metal surface cannot be directly coupled to surface plasmon polaritons and the momentum of the incident optical wave has to be enhanced to match the momentum of the SPPs.

The most common approach to achieve this momentum change is to use a prism coupler and the attenuated total reflection method. In this Kretschmann configuration (Fig. 1.4(a)), a thin metal film layer with permittivity ϵ_m is evaporated on the surface of dielectric plate, that is connected to a high refractive index prism by the index matching liquid. These three materials are of the same refractive index n . When a light wave propagates in the prism at a certain incident angle θ , the wavevector along the surface of dielectric layer can be expressed as:

$$k_x = nk_0 \sin \theta = n \frac{\omega}{c} \sin \theta \quad (1.18)$$

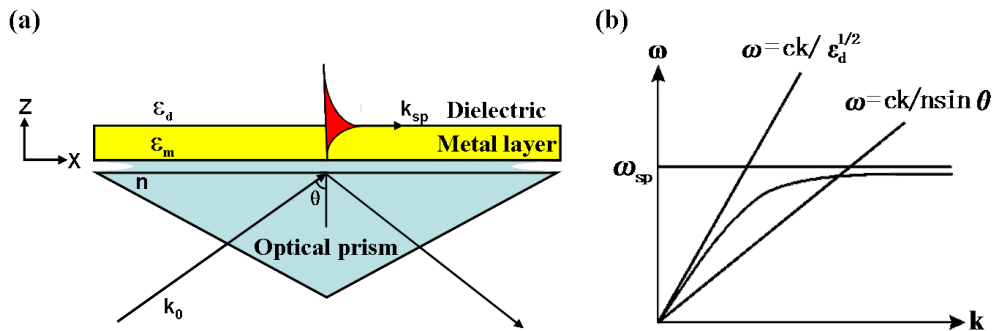


Figure 1.4: (a) Excitation of surface plasmon-polaritons by a light beam via prism coupling and (b) Dispersion relation of SPPs and incident light.

If the metal film is sufficiently thin (less than 100 nm for light in visible and near infrared part of the spectrum), tunneling of incident photons through the metal film occurs and light is coupled to surface polaritons:

$$k_{sp} = n \frac{\omega}{c} \sin \theta = \frac{\omega}{c} \sqrt{\frac{\epsilon_d \epsilon_m}{\epsilon_d + \epsilon_m}} \quad (1.19)$$

where ϵ_d is the permittivity of a semi-infinite dielectric. The solvability condition of this equation is $n > \sqrt{\epsilon_d}$, namely the wavevector of light is increased in the optically more dense medium while the incident angle is greater than the critical angle for total internal reflection [24]. Figure 1.4(b) illustrates the dispersion relation of SPPs in this prism coupling configuration. An intersection point in the dispersion curve of the excitation wave with the dielectric wave on the metal surface can be obtained, as shown in Figure 1.4(b). Therefore, SPPs with the same frequency than the incident light can be only excited by varying the angle of incidence at the dielectric/metal interface.

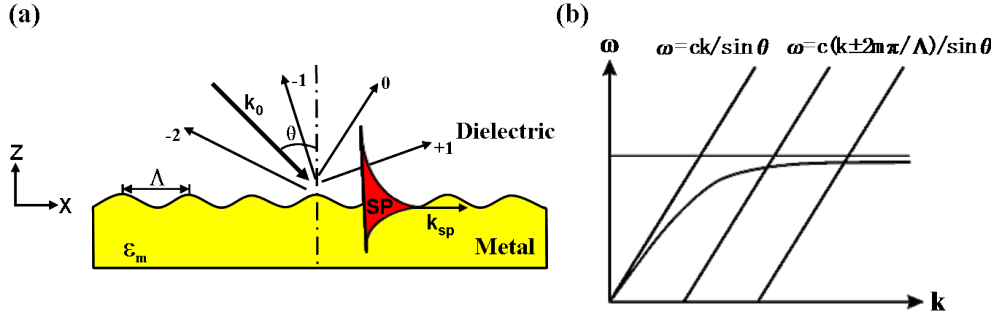


Figure 1.5: (a) Excitation of surface plasmon-polaritons by light diffraction on a diffraction grating and (b) Dispersion relation of SPPs and incident light.

Another approach for optical excitation of surface plasmons is based on the diffraction of the light in a grating coupler (Fig. 1.5(a)). In this method, a light wave is incident from the dielectric medium on the surface of the metallic grating. The component of the wavevector in the plane of the grating k_x is:

$$k_x = k_0 \sin \theta \pm m \frac{2\pi}{\Lambda} \quad (1.20)$$

where m is an integer and denotes the diffraction order and Λ is the pitch of the grating. Figure 1.5(b) presents the dispersion relation of SPPs and incident light produced by a diffraction of light on a diffraction grating.

The in-plane component of the wavevector intersects with the dispersion curve of SPPs after periodic translation, and SPPs wavevector is equal:

$$k_{sp} = k_0 \frac{\omega}{c} \sin \theta \pm m \frac{2\pi}{\Lambda} \quad (1.21)$$

SPPs can be also excited by near-field optical methods [25]. The optical probe of a scanning near-field optical microscope (SNOM) is shown to act as a point source for surface plasmon polaritons (see Figure 1.6(a)). In this set-up configuration, a probe tip has to be very close to the metallic surface in the near field region of the probe. The near-field diffraction field includes all the component of the wavevectors. Among them some components can match with SPPs wavevectors and thus produce energy transfer. This is one way to excite SPPs on metal surfaces in near-field techniques. Likewise, the SPPs excitation can also be achieved by scattering on a rough surface (Fig. 1.6(b)). Due to a strong presence of the evanescent field of the scattering light over the metal, SPPs can also be excited if the matching condition for vectors is satisfied. Unfortunately, scattering caused by both SNOM probe and random roughness on the metal surface are all non-resonant excitation. Only a small part of the energy can thus be coupled into SPPs, resulting in a low efficiency of light-to-SPPs coupling.

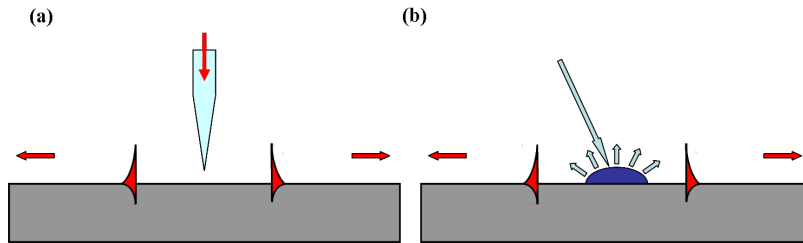


Figure 1.6: SPPs near-field optical excitation configurations: (a) excitation with a SNOM probe and (b) excitation on rough metallic surface

1.2.3 SPR for biosensing

Surface plasmon resonance (SPR) biosensors are optical sensors that use the excitation of the surface plasmons to probe interactions between an analyte in solution and a biomolecular recognition element immobilized on the SPR sensor surface. Major application areas include the detection of biological analytes and analysis of biomolecular interactions, where SPR biosensors are capable of characterizing binding reactions in real-time without labeling requirements.

In SPR biosensing, the adsorption of a target analyte molecules by a surface functionalized bioreceptor is measured by tracking the change in the conditions of the resonance coupling of incident light to the propagating surface plasmon wave (SPW). The existence of this surface plasmon wave is dictated by the electromagnetic (EM) properties of a noble metal (typically gold or silver) and a dielectric (sample medium) interface. Thanks to the fact that majority of the SPW field is concentrated in the dielectric, the propagation constant of the SPW is extremely sensitive to any change in the dielectric refractive index. A change in the refractive index shifts the plasmon resonance condition, which can be detected as intensity, wavelength or angle shift to provide quantitative information about the binding event (Fig. 1.7).

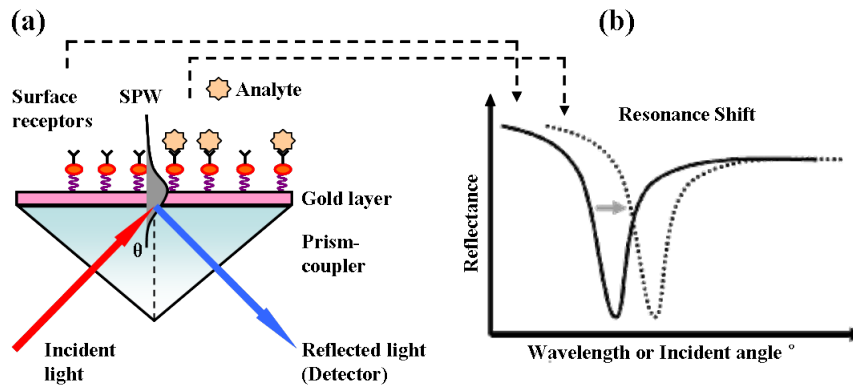


Figure 1.7: (a) Tracking absorption by most widely used prism coupler-based SPR system and (b) resonance shift in the reflected light spectrum.

Main performance characteristics of SPR sensors

The main performance characteristics of SPR biosensors include sensitivity, resolution and limit of detection.

- **Sensitivity:** The sensitivity of SPR sensors is an important parameter to evaluate the sensor performance which is defined as the derivative of the monitored SPR parameter (resonant angle or wavelength) with respect to the parameter to be determined (refractive index, thickness of the overlayer and concentration, etc.). The sensitivity of a SPR sensor can be decomposed into two components : (1) sensitivity to the refractive index change produced by the analyte binding to the biospecific coating on the sensor's surface S_{RI} and (2) the efficiency

E which depends on the properties of the target analyte and the ability of the biospecific coating to capture analyte molecules :

$$S = \frac{\partial P}{\partial n} \frac{\partial n}{\partial c} = S_{RI} E \quad (1.22)$$

where n is the refractive index change caused by the binding of the analyte with the concentration c .

- Resolution: Resolution is the key performance characteristic of a SPR sensor which is defined as the minimum change in the bulk refractive index producing a detectable change in the sensor output. The resolution of a SPR sensor, r_{RI} , is typically expressed in the terms of the standard deviation of the noise of the sensor output, σ_{so} , translated to the refractive index of bulk medium, $r_{RI} = \sigma_{so}/S_{RI}$.
- Limit of detection: The limit of detection (LOD) is another important characteristic describing the ability of a SPR sensor to detect an analyte. LOD corresponds to the concentration of the analyte derived from the smallest measure which can be detected with reasonable certainty. Typically, there are three ways to specify the LOD: first, LOD can be expressed in units of refractive index units (RIU), which enables a rough comparison of the sensing capability among different sensing technique and structures; second, LOD can be expressed using surface mass density (or total mass) in units of pgmm^{-2} , which corresponds to the true mass change really measured by the biosensor that can be used to evaluate the sensor performance; third, LOD can be expressed using sample concentration (in units of ngml^{-1} or molarity). These three methods are correlated and the relationship between them can be studied for each biosensor.

Table 1.1 provides a summary of different architectures of the optical biosensing techniques as well as some of the best reported results for these techniques in terms of LOD/sensitivity. Note that surface plasmon biosensors appear among the most sensitive sensors available. This large sensitivity is related to the fact that the majority of the optical field is located in the dielectric and the field is concentrated close to the surface producing a quite sharp resonance (although not as sharp as a typical dielectric resonance).

Sensing technique	Optical structures	Analyte	Detection limit	Ref.
SPR	SPR	Bulk solution	10^{-5} - 10^{-8} RIU	[26]
	SPR imagine	Bulk solution	10^{-5} - 10^{-7} RIU	[27]
	SPR	Protein(CA19-9)	$66.7 \text{ unit ml}^{-1}$	[28]
Interferometer	Interferometer	Bulk solution	10^{-7} RIU	[29]
		Protein	20 pg mm^{-2}	[30]
	Microchannel	Bulk solution	7×10^{-9} RIU	[31]
Waveguide	Resonant mirror	Protein	$\sim 0.1 \text{ pg mm}^{-2}$	[32]
	Metal-clad waveguide	Bacterial spore	$\sim 10^5$ spores ml^{-1}	[33]
Ring resonator	Ring on a chip	Bulk solution	10^{-4} - 10^{-7} RIU	[34]
		DNA	$\sim 100 \text{ nM}$	[35]
		Bacteria	10^5 cfu ml^{-1}	[35]
	Dielectric microsphere	Bulk solution	10^{-7} RIU	[36]
Optical fiber	Nanofiber	Bulk solution	10^{-7} RIU	[37]
	Fiber coupler	Bulk solution	4×10^{-6} RIU	[38]
		Protein	0.5 ug ml^{-1}	[38]
Photonic crystals	2-D PC	Bulk solution	10^{-5} RIU	[39]
		Protein	0.4 pg mm^{-2}	[39]
	1-D microcavity array	Bulk solution	7×10^{-5} RIU	[40]

Table 1.1: Comparison of the detection limits of optical biosensors based on analyte type.

Applications of SPR biosensors

The major advantage of SPR over a majority of other transduction technologies is that it allows real-time monitoring of interactions between the ligand and the analyte. This is why SPR biosensors has been used in a number of applications involving the interactions of any biological system from cell, phage, oligonucleotide, oligosaccharides, to small molecules, such as proteins and viral particles. Some examples of applications which are relevant to the present study are given below.

a. Detection of biomolecular binding

Recently, Lesuffleur et al. [41] have demonstrated that combining the enhanced transmission effect and the shape resonance of nanohole arrays

in a gold film allows real-time and label-free measurements of molecular binding. In this work, they used arrays of apertures consisting of two overlapping circular holes to produce sharp apertures (Figure 1.8(a)) and demonstrated a 50% improvement in sensitivity. A real-time measurement of bovine serum albumin (BSA) adsorption on the gold surface was also presented as it is shown in Figure 1.8(b).

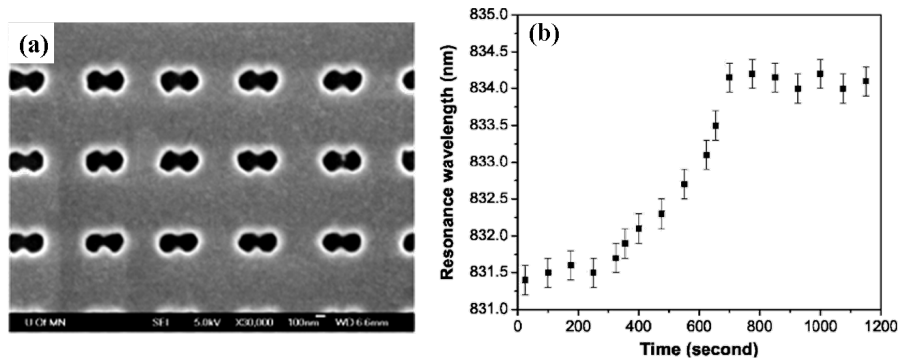


Figure 1.8: (a) SEM image of a double-hole array with a 800 nm periodicity. The diameter of the circular hole is 200 nm and the center-to-center hole distance is 190 nm. (b) Real-time measurement of BSA on the gold surface [41].

While the refractive index biosensing capability of many plasmonic nanostructures has been reported, more recently, vertically aligned gold nanotube arrays was also proposed for label-free bioanalytical sensing [42]. Figure 1.9(I) shows a sample gold nanotube arrays fabricated on glass substrates by bottom-up self-assembling technique. Free-standing nanotubes were also investigated as label-free biosensors through the binding of NeutrAvidin protein (Fig. 1.9(II)). This work also demonstrate the ability to probe single cell.

To improve the sensing performance of SPR based sensors, triangles and microhole arrays (Fig. 1.10(a) and (b)) prepared by modified nanosphere lithography have been studied [43]. To demonstrate the biosensing potential of such materials and geometries, an IgG biosensor was constructed on triangle and microhole arrays. The SPR response for a 10 nM IgG solution was improved significantly with triangular geometry as it can be observed in the Figure 1.10(c) that compares the response obtained with triangles, nanoholes and continuous thin films. All those results prove that such novel plasmonic structure are of large interest for SPR biosensing comparatively to the standard approach based on continuous Au film .

b. Detection of antibody-antigen interactions

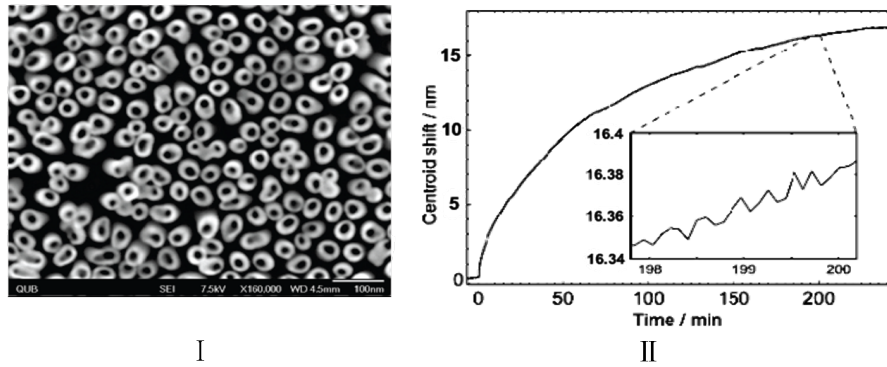


Figure 1.9: (I) SEM image of the resulting structure. (II) Real-time measurement of the absorption of 10ug/ml NeutrAvidin to a free-standing gold nanotube array [42].

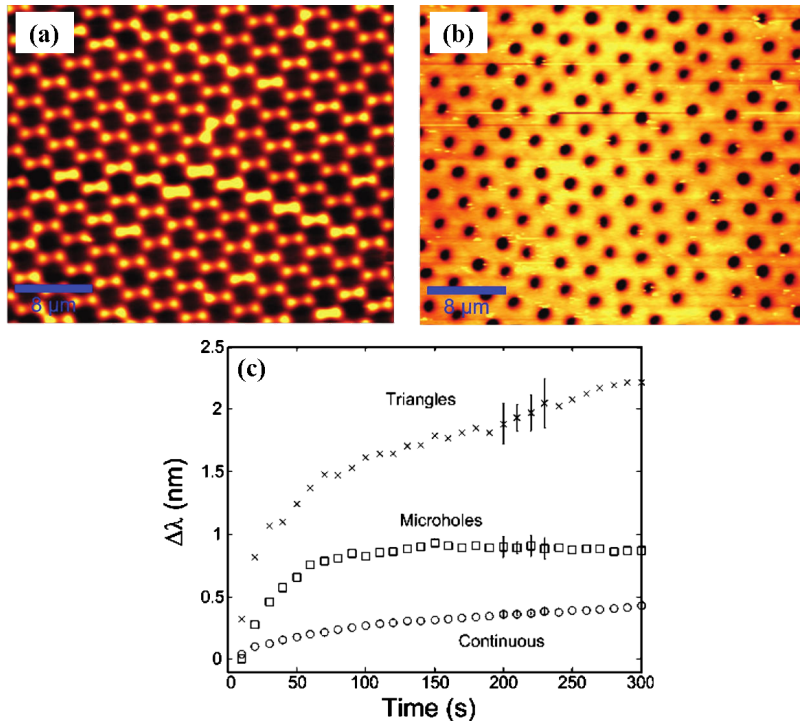


Figure 1.10: AFM images of micropatterned thin films with (a) microtriangle and (b) microhole arrays. (c) Sensogram for the detection of 10 nM IgG with different plasmonic materials [43].

Localized surface plasmon resonance (LSPR) sensing monitors the resonance condition similarly to SPPs in thin gold film, but it greatly broadens their scientific and technological applications since LSPR sensing is not temperature sensitive. LSPR sensing studies have been thus mainly fo-

cused on antigen/antibody interactions. Real-time LSPR analysis of antibody/antigen interactions with gold nanorod has been systematically studied as presented in the Figure 1.11 [44]. The gold nanorods with highly homogeneity were produced by seed-mediated, surfactant directed synthesis. The LSPR peak wavelength spectra has been measured through a continuous experiments: conjugating with capture antibodies by carbodiimide cross-linking and interacting with a specific secondary antibody. The results shows successful measurement of binding kinetics, thus demonstrating that the nanorod LSPR sensor can monitor real-time dynamic interactions.

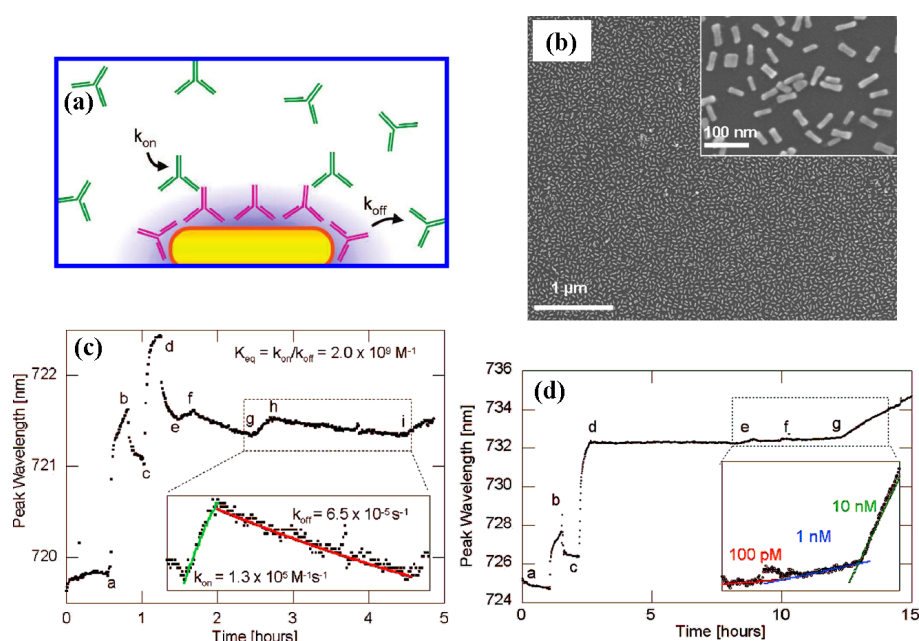


Figure 1.11: (a) Schematic of the nanorod-based immunoassay. (b) SEM image of films of gold nanorods with about 15 nm diameter and 50 nm length for individual nanorods. (c) The LSPR peak wavelength throughout continuous immunoassay experiments. (d) Test of sensor sensitivity [44].

Surface plasmon resonance, as one of the main surface sensitive optical technique, is a suitable technique for highly sensitive affinity-based biosensing applications. SPR devices are capable of performing real-time high-throughput biomolecular interaction analysis and have the major advantage that prior labeling of the analytes is not required. Nowadays, SPR biosensors have become a central tool for characterizing biomolecular interactions. Moreover, development of SPR sensors for the detection of a variety of chemical or biological species has gained considerable momen-

tum, which will further extend the potential of SPR sensing technology to be used more widely.

1.3 Soft UV nanoimprint lithography

1.3.1 Historical recall

The original nanoimprint lithography, i.e. thermal nanoimprint lithography (T-NIL), was first developed by S. Y. Chou's group in 1995 [45]. In this method, the hard mold that contains nanoscale surface-relief features is brought into a physical contact with a thin polymeric material spin coated on the substrate and highly pressed with a pressure in the range of 50-100 bar. The polymer is held some 90-100 °C above its glass-transition temperature (T_g), in a few minutes, during which the polymer can flow to fill in the volume delimited by the mold topology. After cooling down both the stamp and the substrate and relieving the pressure, the mold can be retrieved without damage. Finally, the thin residual layer of polymer remaining in the pressed areas is removed via reactive ion etching. The Figure 1.12(a) gives the schematic of such T-NIL process. At this stage, the process is complete and one can either etch the substrate, or evaporate the metal on the substrate to perform a lift-off.

This imprinting-based lithography that has attracted numerous attention presents the ability of replicating patterns with ultrahigh resolution. After its inception, Chou et al. has demonstrated replication with unprecedented precision of 10 nm diameter and 40 nm periodic holes arrays in polymethylmethacrylate (PMMA) on silicon, as shown in the Figure 1.12(b) and (c) that present the SEM images of the mold pattern and its replica of hole arrays.

In contrast to conventional methods based on exposure and development, nanoimprint lithography have several advantages. First, it offers high resolution [46]. Also NIL performs pattern transfer simply by inducing a local displacement of the resist under mechanical deformation instead of any photo-/electro-induced chemical or physical modification of the resist that is the basis of classical lithography. Limitations imposed by light diffraction or beam scattering in these classical techniques can be overcome. As a second advantage, NIL provides parallel processing with high throughput, that is thus suitable for large-scale patterning with high resolution. Finally, a huge benefit of NIL concerns the cheap equipment involved compared to classical nano lithographies such as electron beam

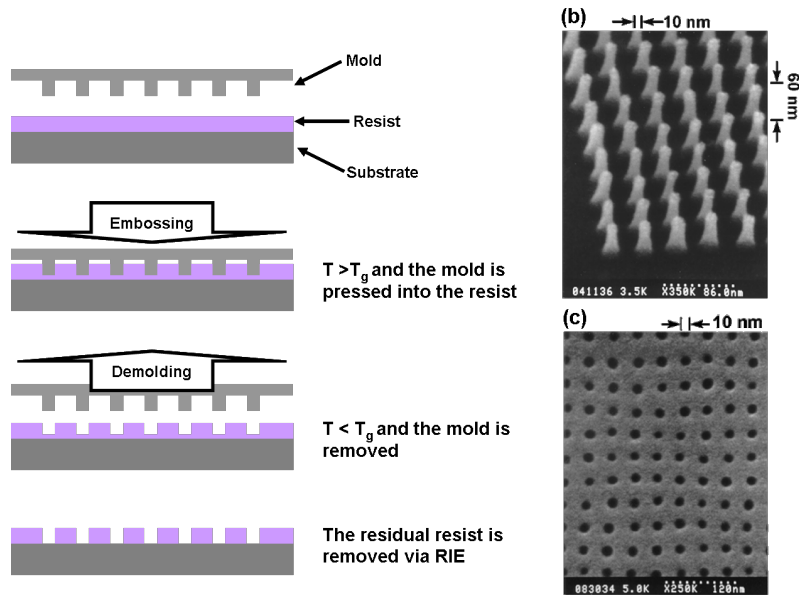


Figure 1.12: (a) Schematics of the originally proposed NIL process. (b) Scanning electron microscopy (SEM) image of a SiO₂ mold with 10 nm minimum diameter pillars with a 40 nm period and 60 nm height. (c) SEM image of a top view of corresponding replica formed by imprinting into PMMA with 60 nm depth, demonstrated by S. Y. Chou in 1997 [46].

lithography. Nowadays, NIL can provide high resolution wafer-scale patterning using standard clean room process offering simplicity and low cost [47, 48].

1.3.2 Principle of UV nanoimprint lithography

Thermal nanoimprint lithography techniques allows for a very simple setup, which results in very short setup times (from seconds to minutes). While on the other hand, the simple setup technology is connect with relatively long cycle times which are mainly caused by the fact of each temperature cycling. In addition, because thermal NIL requires high pressure conditions, it's difficult to attain overlay accuracy because of the distortion of the multilayer.

In order to enhance the capability of the standard NIL process, in 1996 Haisma et al. have proposed another approach based on a low-viscosity UV curable prepolymer instead of a thermoplastic resist [49]. They called this technique “UV light-assisted NIL (UV-NIL)”. In the following years, since it offers several advantages compared to T-NIL, this variant technique has

been widely studied and developed by many research groups and centers, such as the institute of semiconductor electronics (IHT) of RWTH, AMO GmbH and “University of Texas” at Austin [50, 51]. Since the UV resist can be photopolymerized under UV exposure through the transparent mold at room temperature and under low pressure, UV-based approaches gain several decisive advantages concerning both speed and overlay.

The principle of UV-NIL is schematically illustrated in Fig. 1.13. In UV-NIL, a UV sensitive resin (monomer) that is liquid at room temperature is spin coated on the substrate. The transparent template is brought into contact with the substrate under a moderate pressure (0-5 bar). The template is then illuminated through its backside producing at room temperature crosslinking and hardening of the resin. After the separation of the template, the residual layer of resist can be finally etched using reactive ion etching (RIE) to form a high resolution feature.

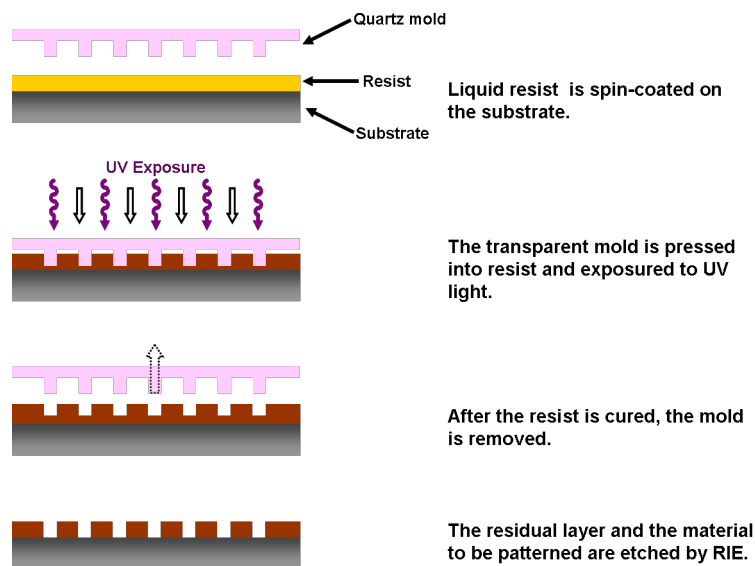


Figure 1.13: Process steps of UV nanoimprint lithography

UV nanoimprint lithography offers several decisive technical advantages concerning overlay alignment accuracy, patterning of various patterns over a wide range scale simultaneously, tool design due to the absence of high imprint pressure and temperature cycles. Currently, UV-NIL offers two ways for patterning based either on rigid optically transparent molds (Hard UV-NIL) or soft stamps. Materials for hard molds are quartz or glass, whereas for soft stamp they are mainly based on flexible elastomer such as PDMS material (see chapters 2 and 3). Since UV-NIL is a room

temperature process, it has been adopted in industry very rapidly. Step and stamp procedures have been proposed to replicate nanostructures on several fields [51]. Here, step-and-flash imprint lithography (SFIL) is an industrial approach that consists of dispensing a drop of low viscosity, photopolymerizable organosilicon solution onto the substrate surface prior to imprint (Fig. 1.14). Since the unit process is conducted at room temperature and at low pressure, the template can be stepped to pattern the whole wafer area as in a stepper lithography tool. Some examples of both UV-NIL and SFIL will be given in the following part of this chapter.

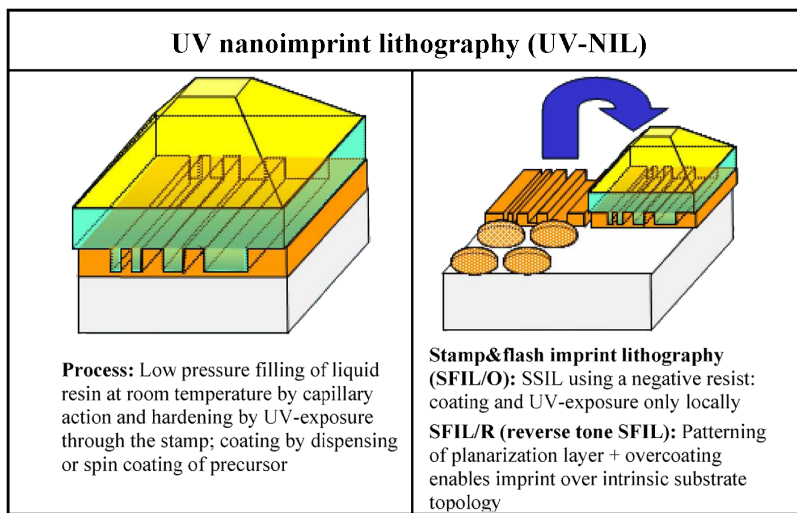


Figure 1.14: Comparison of the full-wafer processing and step-and-repeat approaches in UV-NIL [52].

1.3.3 UV-NIL in the roadmap

The International Technology Roadmap for Semiconductors (ITRS) lays out a quite challenging path for the further development of these NIL patterning techniques. The main objective is to create the smallest feature size in the limits of resolution. Since standard lithographies such as electron beam lithography (EBL) need expensive tools, this simple NIL technique appears competitive and has thus entered the ITRS Roadmap as “next generation lithography” (NGL) technique. As it can be seen from Figure 1.15, it’s generally believed that extension of the Roadmap for semiconductor industry beyond 32 nm will probably require the development of NGL technologies such as ultraviolet lithography (EUVL), maskless (ML2) and imprint lithography (NIL). Among them, it’s obvious that NIL, which thus

been included in ITRS roadmap for 22 nm and 16 nm nodes, can achieve much better resolution.

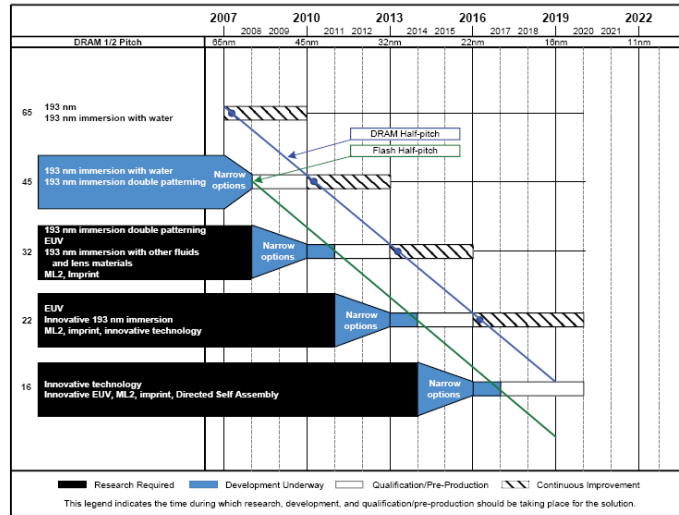


Figure 1.15: ITRS Projections for lithography technology [53]

Research in the lab

Significant efforts from both academic and industry have been put in NIL research and development. The current state-of-the-art resolution in UV-NIL is about 5 nm, that was pursued by Chou et al. in 2004. [54]. In their work, these authors have demonstrated pattern replication of 5 nm-wide lines spaced by 14 nm. UV-NIL was performed at room temperature with a pressure less than 15 psi and a backside UV illumination through the glass substrate. For the application of single macromolecule devices, they also fabricated gold contact gaps as narrow as 5 nm by NIL as it can be seen in Figure 1.16. Finally, they demonstrate excellent uniformity pattern replication over 4 inch wafer in a single step. One should note that this research demonstration was possible since these authors used a very high resolution mold that was obtained by EBL in the 5 nm scale.

We note that mold fabrication is thus one key point for ultra high resolution imprinting. However, it is quite to fabricate mold of this type by using conventional means, such as electron beam lithography, due to limits in resolution and patterning nonuniformities at sub-5 nm length scale. For this reason mold formed by cleaved and etched edges of substrates

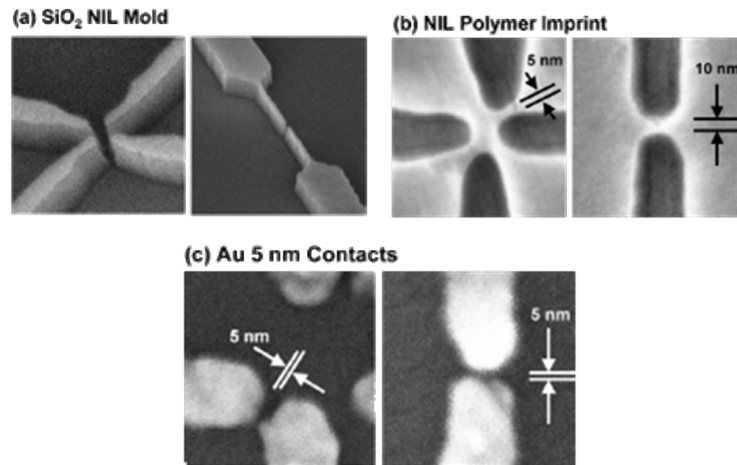


Figure 1.16: (a) SEM images of a silicon oxide mold. (b) SEM images of the imprinted P-NIL resist after UV curing and mold separation. (c) SEM images of Au contacts after evaporation of metal and lift-off of the resist [54].

with multilayer stacks deposited by molecular beam epitaxy have also been proposed. However such cleaved mold suffers from certain limitations in geometry. Figure 1.17 presents another approach based on single-walled carbon nanotubes (SWNT) as templates. Such SWNT template allows performing soft imprinting lithographic process with feature sizes as small as 2 nm that are comparable to the size of an individual molecule [55]. The imprinting results obtained in this recent work demonstrates the ability for reliable replication features with horizontal and vertical dimensions greater than 2 nm, thus providing a new and simple method for evaluating the resolution limits of imprinting lithography.

Since UV-NIL uses a UV-curable resist to define a pattern contrast, one other key point concerns the removal of the residual layer of the polymerized resist (see step 4 of process in Fig. 1.13). Other approaches have been thus proposed to try to avoid any residual resist in the imprinted nanocavities. During the 24th international conference of Micro & Nano Engineering (MNE) (1998), Chen et al. has reported a new approach of mold-assisted lithography based on photopolymerization under near-field regime. In this experiments, polymerization occurs only in the transparent region of the mold so that the residual layer can be removed after in the solvent (Fig. 1.18(a)). Pattern with feature sizes ranging from 70 nm to 1 μ m have been formed by such technique (see Figure 1.18(c)). In parallel, the group of Kurz [50] and the group of Willson of Texas University [51] have provided two similar approaches based on this same idea of localized

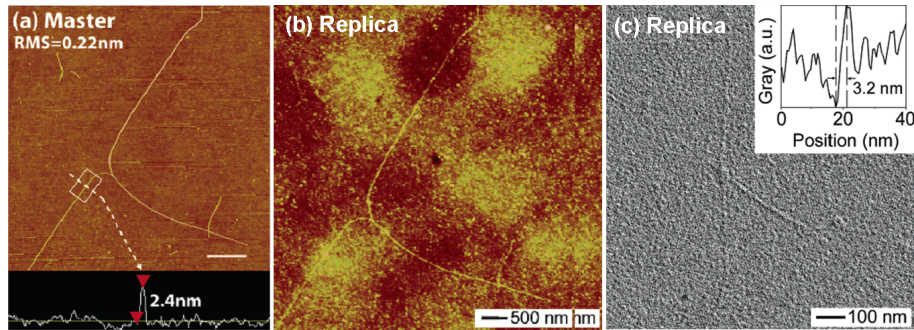


Figure 1.17: (a) AFM images of a SWNT master. (b) AFM image of a layer of PAA imprint with a mold derived from a SWNT master. (c) TEM images of Pt/C replicas formed by angled evaporation onto relief features in PAA fabricated with a similar SWNT master [55].

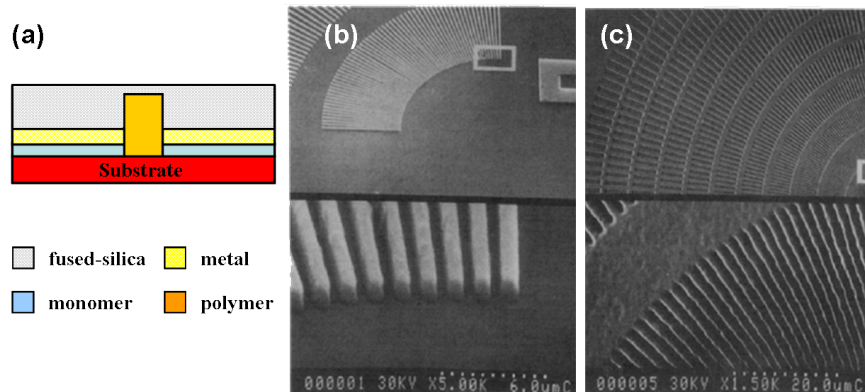


Figure 1.18: (a) Schematic illustration of the mold-assisted optical lithography. (b) SEM images of a mold structure with feature sizes ranging from 70 nm to 1 um made of a fused silica substrate and a thin film metallic cap layer and (c) SEM of replica formed by the mold-assisted near-field optical lithography [56].

UV light photopolymerization with specific resist materials and masks.

Research from the industry

Now, several companies are also working to optimize UV nanoimprint lithography. Molecular Imprints, Nanonex, Obducat and EV Group are the most famous companies that are not developing conventional photolithography scanners, but rather machines that utilize UV and liquid emersion technologies to imprint patterns on a wafer. Nanoimprint technology also seems to have the backing of large corporations, such as KLA-Tencor, MII, DARPA and Motorola, that was the first large semiconductor manu-

facturer to test a nanoimprint tool in 2002.

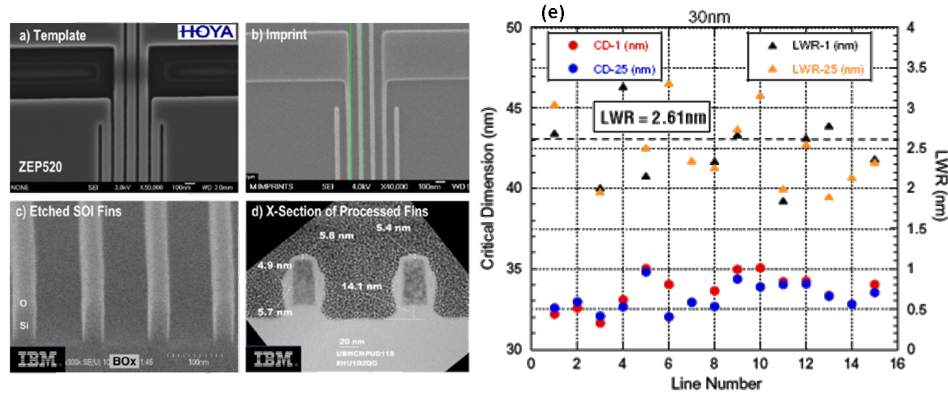


Figure 1.19: 30 nm semi-dense structure: (a) template, (b) imprinted features, (c) etched SOI fins, (d) cross-section of etched fins ready for implantation and (e) critical dimension (CD) and LWR for the 30 nm features after etch for two different wafers[57].

Figure 1.19 shows the SEM images of a 30 nm-wide typical test structure on the master mold (Fig. 1.19(a)) and its corresponding imprint (Fig. 1.19(b)). This experiment has been performed by Molecular Imprint. A Drop-On-DemandTM method was employed to deposit the photopolymerizable acrylate based solution in each field across a large 200 nm wafer. After imprinting, the Silicon on Insulator (SOI) wafers were etched (Fig.1.19(c) and (d)). It demonstrates that a resolution of 30 nm can be achieved on very large surface. The evolution of the linewidth roughness (LWR) is also of great interest as shown in Figure 1.19(e): LWR of etched pattern is shown to fit with LWR of master pattern. NIL is thus able to replicate faithfully the master pattern, which imposes the use of a perfect master mold. Such SFIL experiments meet the requirement of ITRS at 32 nm node. Nanonex has successfully demonstrated excellent duplication over 4 inch wafer scale of 20 nm holes with a pitch of 100 nm (Fig 1.20(a)) and 65 nm pillars with a pitch of 200 nm (Fig 1.20(b)) in their Nanonex photo-curable resist. Besides imprinting gratings with high uniform pattern density, they also shown imprinting with good CD control of isolated feature, such as the gate level of MESFET (metal semiconductor field effect transistor) circuit. Numerous work has convinced the ability of NIL for fine patterning in all kinds of applications, including data storage, life science, MEMS, biochip, sensor and optics with low cost.

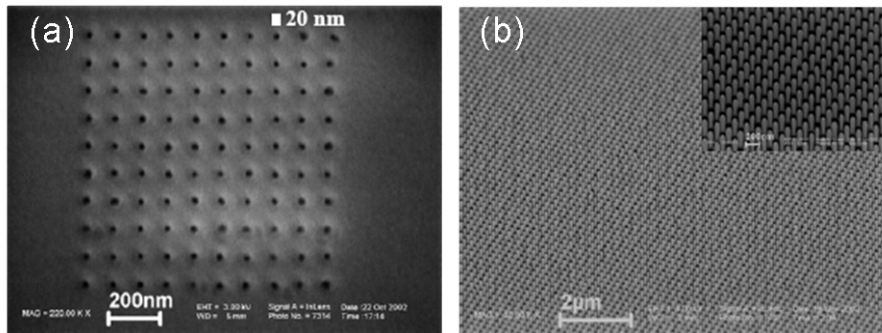


Figure 1.20: (a) SEM images of 100 nm pitch, 20 nm holes imprinted in NXR-3010 resist using P-NIL and (b) SEM images of 200 nm pitch, 65 nm pillars imprinted in NXR-2010/NXR-3010 resist over 4 inch wafer using P-NIL [58].

1.3.4 Comparison to the other lithographic techniques

To appreciate the potential of nanoimprint lithography, an overview of different current lithographic patterning techniques is also briefly given here for comparison.

Photolithography, in other words the standard lithography working with a UV light source, is a process that has been extensively employed throughout the semiconductor industry to create a pattern by projection from a photomask. The limiting factor to reach high resolution is the wavelength of the light that governs the diffraction across the mask. In addition, the replication systems and the complex phase-shift masks for high resolution are very expensive. Today deep UV light (DUV) working with a wavelength of 250 nm and 190 nm allows feature sizes down to 50 nm. To go further to higher resolution in the sub-50 nm scale, extreme ultraviolet lithography (EUV) that works at $\lambda = 13.5$ nm can be used as alternative method. However, EUV suffers from several disadvantages such as the cost of its source and the optical elements (X-Ray reflecting mirrors) to be inserted, which limit the light power and thus enhance the exposure time.

X-ray lithography (XRL) is similar to photolithography in terms of exposure configuration. As X-rays have wavelengths that are much shorter than UV light ($\lambda \cong 1$ nm), high resolution in the sub-20 nm scale can be reached with extreme precision. The main drawbacks of this method include: (1) the systems require a powerful and reliable X-rays source which can only be practically achieved using synchrotron radiation; (2) 1:1 mask

and a small gap (10-20 μm) between mask and substrate is required [59].

Electron beam lithography (EBL) is one of the most powerful methods for forming nano-patterns. In this technique, a beam of electrons is utilized to generate patterns on the substrate. It uses high voltage electrons in the range of 1-100 KV to nano-pattern the resist on the substrate by directly writing onto it. The short wavelength associated with high-energy electron beams gives EBL as the best method to pattern with extremely high resolution of several nanometers. The resolution limit is determined by forward scattering in the photoresist and secondary electron travel in the photoresist. Despite the high resolution, the commercial value of EBL is also limited because of the very slow pattern generation of the serial point-by-point e-beam writing. This is a cost limitation compared with techniques as photolithography in which the entire surface is patterned once. The throughput of e-beam systems has been increased through the development of the “shaped beam” concept due to its high current density. Based on this concept, projection PREVAIL (projection reduction exposure with variable axis immersion lenses) which combines e-beam projection with e-beam scanning through the use of curvilinear variable axis lenses has been explored. PREVAIL - electron projection lithography (EPL) offers high resolution and large process margins with reasonable throughput and multigeneration tool characteristics holds promise for the next-generation lithography.

FIB systems generally employ a highly focused beam of ions, such as Ga^+ that is raster scanned over the sample surface in a similar manner to an electron beam in a scanning electron microscope [60]. However, it differs in that gallium atoms from the ion beam are implanted into the top few nanometers of the sample surface which is destructive to the specimen. Although ultrafine structures (several nm) can be fabricated with FIB, the low throughput and the limitation of ion beam current limit its application for lithographic purposes.

In table 1.2, comparison between nanoimprint lithography and other nanopatterning techniques has been given. Clearly, nanoimprint lithography is a fast rather cheap nanolithography tool that is ideal for replicating features with a resolution in the order of a few tens of nanometers.

1.3.5 Challenge of nanoimprint lithography

Nanoimprint can currently achieve high resolution and reasonable high throughput at low cost, but there are still some challenges to overcome

Technique	Resolution	Patterning time	Cost
Contact optical lithography	500 nm	Short	Low
Projection optical lithography	45 nm	Short	Very high
Extreme UV lithography	50 nm	Short	Extremely high
Electron beam lithography	5 nm	Long	High
X-ray lithography	20 nm	Short	Very high
Ion beam lithography	8 nm	Very long	High
Nanoimprint lithography	5 nm	Moderate	Low

Table 1.2: Comparison between nanoimprint lithography and other nanopatterning techniques.

that will require further developments.

- Template fabrication

One of the most important components for the realization of the nano-scale feature replication by NIL is the minimum feature size on the mold. Two important challenges in NIL mold production are (1) the faithful duplication of existing NIL molds and (2) the production of NIL molds with features beyond traditional nanopatterning capabilities. For comparison, a UV photomask can support feature sizes 4x larger than those desired on the wafer, since pattern magnification is possible (based on lens insertion between mask and wafer). The templates for NIL should exhibit the same pattern size 1x as the wafer pattern size. This means that the master pattern cannot be magnified. The pattern mask resolution has to be always four times better than an optical lithography mask. Mask resolution and mask inspection are thus very challenging for NIL. This renders the NIL template fabrication significantly more difficult and expensive than the standard photomask process. Thus, in order to reduce total cost and to increase the overall throughput, a process combining NIL and reactive ion etching for template fabrication has been studied (see chapter 2). However, the anisotropy etching, the random motion of etchant ions and the resist chemistry can produce severe pattern distortion and increased line edge roughness (LER) which can limit the high quality NIL mold production. We will see along this thesis that those RIE steps are critical and have to be studied similarly, as the NIL process itself, if one wants to optimize both resolution, pattern profile and LWR [62, 63].

Another challenge for NIL templates is how to make them defect-free. Concerning quality inspection, approaches for defect analysis will need

to be carried out with SEM, AFM and more pioneering method based on optical microscopy of fluorescent dye loaded in printable polymers [64]. The effect of the smaller defect size on imprint template cost (cost for both defect inspection and repair of template defects) should also be considered in the overall cost of nanoimprint lithography.

- Multilevel issue

One of the crucial problem lies in NIL is the multilevel capability. To get over this problem, the first step is to find solutions for in-plane alignment to control overlayer better than 10 nm. Normally, the functionality of template for nanoimprint is equivalent to the photo projection mask for conventional optical projection lithography. The overlayer accuracy depends on the alignment techniques. With a three step alignment procedure based on diffractive gratings overlay accuracies in the sub-50 nm regime have been achieved recently [65].

- Throughput

In contrast to UV photolithography that simply requires exposure for each field, imprint requires not only exposure, but also material dispense, template fill and field by field alignment. Normally, NIL throughput can be roughly estimated from the time of actual printing, loading alignment and separation, which corresponds more often to a current time of 10-15 minutes. Other factors also contribute to throughput among which the stamp size, the high density of features, the sticking, the polymer curing time, the temperature and the pressure during imprint and the stamp life time. Some factors leading to influence the throughput are listed below:

(1) *The mold feature density.* The mold feature complexity and feature size all play an important role. Combining large and small feature sizes into a single mold will causes several problems, among which the most important is the non uniformity in thickness of the residual resist layer across the imprinted area. With such differences in thickness: first, it's challenging to remove the right amount of residual polymers to complete the pattern definition; secondly, extra cleaning time will be needed to remove completely the excess resist left in the valleys. Such increase in RIE time will increase the overall time of NIL process, and thus decrease the final throughput. Figure 1.21 presents a work of the residual thickness obtained on the same plate with nanoline pattern of varying density realized by C. Courgon and coworkers [51]. It's showed that the imprinting uniformity is strongly dependent on the pattern density across the wafer.

In the case where the linewidth (L) of printed line is narrower than the adjacent space (S), the residual thickness is inhomogeneous at the scale of all the wafer.

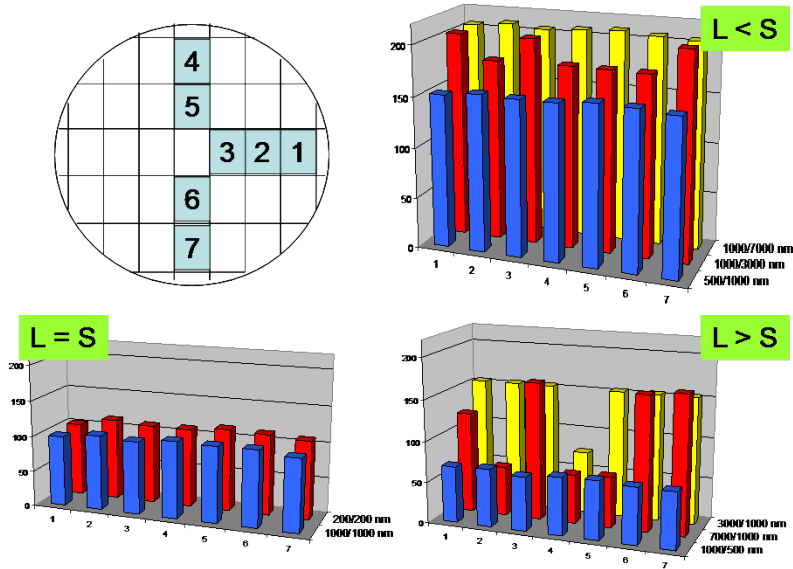


Figure 1.21: Residual thickness as a function of pattern density and mapping across the same plate [66].

(2) *Stamp size.* Ideally the stamp size will have a size compatible with standard production equipment. As the stamp size determines the field area to be printed, the stamp area should be as large as possible. For SFIL allowing step-and-repeat process, the stamp size can be largely reduced.

(3) *Imprint temperature and pressure.* Reducing the imprint pressure required for reliable pattern definition by lowering the environmental pressure and also decreasing the temperature as low as possible will increase the throughput by decreasing time of pressure and temperature cycling.

In summary, challenges concerning throughput, defect tolerance and multi layer overlay still need supreme efforts by tool makers, resist developers and template manufacturers. NIL is still not yet established as a mass fabrication technique and in competition with other established and emerging lithographies. Whether imprint lithography is suitable for high-volume semiconductor production is still an open question. Regarding the current activities, nanoimprint lithography seems best suited for single imprinting of complex patterns or in multiple imprints in which alignment is not critical. One of the examples would be in the biosensor fabrica-

tion, where NIL proves its ability in simple, high resolution, wafer-scale fabrication of reproducible, large-scale plasmonic structures.

1.3.6 Advantages of soft UV-NIL

Soft UV-NIL process merges the two main techniques that are outstanding in research and development: Soft Lithography [67, 68] and UV Nanoimprint Lithography (UV-NIL) [51]. Due to the use of flexible stamp, soft lithography techniques can generate 3D structures and patterns on non-planar surfaces. These soft methods can be also used to transfer chemical molecules and thus pattern specific chemical functionalities on surface (microcontact-printing method). Meanwhile, UV-NIL uses hard rigid (quartz or glass) stamps combined with a low viscosity monomer enabling patterning high contrast three-dimensional nanostructures. Nevertheless, full wafer patterning in Hard UV-NIL can only be performed by SFIL, in which the imprint cycle is performed over a small area corresponding to one field. Hard UV-NIL is thus limited in practice in terms of patternable area.

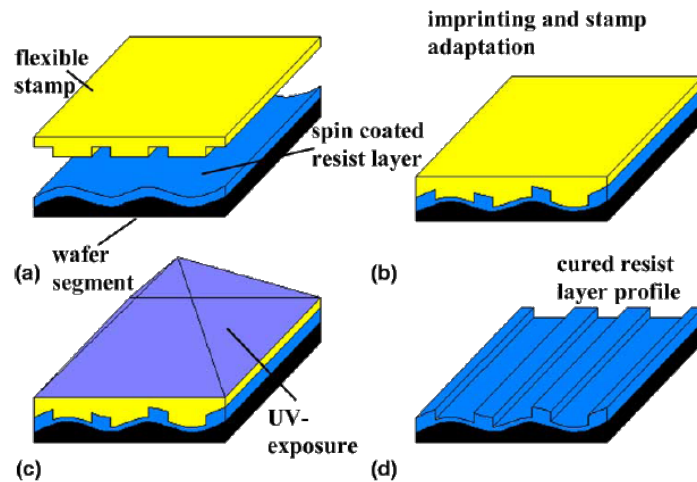


Figure 1.22: Process flow of the soft UV-NIL nanoimprint lithography technique.

Soft UV-NIL that combines the advantages of both techniques is a soft lithographic process for nanopatterning on wafer scale in only one imprint step. Patterning is performed at room temperature with low imprint pressures below 1 bar and even on non-flat surface. The main advantages of this process are based on the two following properties: the transparent

flexible stamp and a low viscosity UV-curable resist. In soft UV-NIL, the elastomeric stamps are basically replicated by molding and curing a liquid prepolymer from a three dimensional template. The most commonly used materials for flexible stamp fabrication is poly(dimethylsiloxane) PDMS that exhibits attractive properties like low interfacial free energy (~ 21.6 dyn/cm), good chemical stability and high optical transparency.

The standard fabrication process of soft UV-NIL is shown in Figure 1.22. In soft UV-NIL process, (1) the substrate is first coated with a photocurable resist layer; (2) then the soft PDMS stamp is lowered into the resist and adjusts to the topography of the substrate until fully contact is achieved; (3) followed by the UV-light irradiation directly through the transparent stamp, which cures the monomer to make it solidified; (4) finally, the soft stamp is released.

Obliviously, permeability of soft stamp inhibits problems caused by trapped air bubbles in the resist layer when imprinting at ambient pressure. In the other hand, the usage of low viscosity UV-curable resists allows 3D patterning at low pressure without any heating cycles, thus minimizing the risk of deformation of the soft stamp.

1.3.7 NIL for biosensing

Nanofabrication technology has enabled methods to manipulate and probe individual molecules in a biosensor system. This type of application often requires to fabricate a large number of identical biosensors which imposes the fabrication of multisensor arrays. Each sensor should be sensitive for one chemical/biological component. Therefore, it's possible to determine the composition of the unknown substance by using such sensing system. The development of biosensing has been largely applied for different applications including food industry, detection of pollution, drug discovery, proteomics etc.

More recently, numerous biosensor research has been devoted to the evaluation of the relative merits of various signal transduction methods including optical, radioactive, electrochemical, magnetic and mass spectrometric. Among these methods, in particular those base on evanescent electromagnetic fields such as SPP (surface plasmon polaritons) at the noble metallic surface has been rapidly exploited in a wide variety of SPR based biosensors [69, 70].

Various nanofabrication techniques have been employed to fabricate the desired nanopatterns utilized in SPR based biosensing studies. UV

photolithography is a widely used method, but its feature sizes are limited by its diffraction limit of $\lambda/2$. The leading nanotechnologies for suboptical domain fabrication are electron-beam lithography and x-ray lithography. Although EBL has outstanding resolution yielding features of 1-2 nm, its serial processing speed is limited in terms of commercially acceptable throughput. XRL resolution is limited by photoelectrons range and diffraction effect to 20 nm, but its capability to produce simultaneously large number of nanostructures is really encouraging. Nanosphere lithography is another fabrication method to produce periodic particle arrays with a precise control, which makes it a promising fabrication candidate for commercialized SPR applications. However, surface coverage and geometric constraints reduce the type of SPR biosensors that can be obtained with this nanosphere lithography.

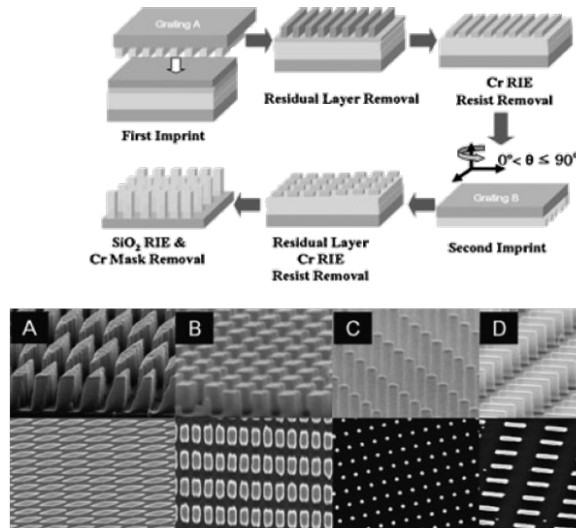


Figure 1.23: (Top) Process used to fabricate “nano-block molds”. (Bottom) SEM images of representative nanoblock molds derived from one-dimensional gratings by using NIL [71].

Consequently there is substantial interest in developing nanofabrication techniques that can integrate both the resolution of EBL and the throughput of XRL. In this context, nanoimprint lithography appears as an ideal fabrication method since it allows parallel replication of identical nanoarrays.

More recently, several works have been done to study the behavior of surface plasmon resonance biosensor. Guo et al. have proposed an approach based on NIL and one-dimensional gratings (Fig 1.23 (Top)) to

produce a two-dimensional array of “nano-block molds” (Fig 1.23 (Bottom)). Such nanoblock molds have been used to fabricate large area metallic nano-particles arrays (NPAs) through conventional NIL process. They have successfully demonstrated the flexibility of this approach by complete control of the plasmonic response of NPAs through their composition, size and shape. In our work, the purpose of the biosensing application is mainly focused on how to optimize the process latitude in order to get homogeneous nanostructures on large area. We hope that such study will open in the future the way to fabricate parallel multi-channel fluidic biodevices integrating SPR biosensors for detection. The related work will be present in chapter 5 and chapter 6.

1.4 Thesis objectives

Surface plasmon resonance biosensors have become increasingly popular for the qualitative and quantitative characterization of the specific binding of mobile reactants to a binding partner immobilized on the sensor surface. Today, the development of SPR biosensors is geared towards the ability to produce compact, low cost and sensitive nanostructure arrays. Hence, the ability to fabricate nanoscale plasmonic structures with high precision, high throughput at low fabrication cost is of crucial importance to real-life applications. Being a next generation lithography candidate, NIL provides high resolution wafer-scale processing using standard clean room procedures offering simplicity and low cost.

Meanwhile, in order to perform many optical measurements in SPR biosensor, it's necessary to bring the sample solution in the vicinity of the sensing surface of the device. For this purpose, microfluidics are proposed to be implemented in various sensing platforms. Such platform offers as advantages faster response, manipulation of smaller sample volume and easiness to miniaturize the entire analytical sensing system. which results in a compact biosensing device [72, 73]. NIL-based technology platform allows integration of plasmonic components into more complex devices, e.g. microfluidic channel devices for biosensing.

Therefore, we have focused on the development of such innovative biodevices that can be used in different biosensing application fields. The first objective of this thesis work is to design and develop SPR nanoarray sensors based on both nanohole arrays and nanograting metamaterials. The second main objective is to apply and develop UV nanoimprint lithography technique for producing high resolution plasmonic nanostruc-

tures on large area. We have also investigated such process reproducibility allowing to reliably measure the biomolecular interactions in our device.

Bibliography

- [1] H. C. Hoch, L. W. Jelinski and H. C. Craighead. Nanofabrication and biosystems: integrating materials science, engineering, and biology. Cambridge Univ. Press, (1996).
- [2] O. Kohls and T. Scheper. Setup of a fiber optical oxygen multisensor-system and its applications in biotechnology. *Sens. Actuators B Chem.*, **70**:121, (2000).
- [3] L. J. Guo, X. Cheng and C. -F. Chou. Fabrication of size-controllable nanofluidic channels by nanoimprinting and its application for DNA strenching. *Nano Lett.*, **4**:69, (2004).
- [4] J. O. Tegenfeldt, C. Prinz, H. Cao, R. L. Huang, R. H. Austin, S. Y. Chou, E. C. Cox and J. C. Sturm. Micro- and nanofluidics for DNA analysis. *Anal. Bioanal. Chem.*, **378**:1678, (2004).
- [5] F. Markey. What is SPR anyway?. *Bia Journal*, **1**:14, (1999).
- [6] *Special Report Technol. Rev.* **106**:36, (2003).
- [7] R. W. Wood. On a remarkable case of uneven distribution of light in a diffraction grating spectrum. *Philos. Mag.*, **4**:96, (1902).
- [8] U. Fano. The theory of anomalous diffraction gratings and of quasi-stationary waves on metallic surfaces (Sommerfeld's waves). *J. Opt. Soc. Am.*, **31**:213, (1941).
- [9] T. Turbadar. Complete absorption of light by thin metal films. *Proc. Phys. Soc.*, **73**:40, (1959).
- [10] L. M. Zhang and D. Uttamchandani. Optical chemical sensing employing surface plasmon resonance. *Electron. Lett.*, **24**:1469, (1988).
- [11] C. Nylander, B. Liedberga and T. Linda. Gas detection by means of surface plasmon resonance. *Sens. Actuators*, **3**:79, (1982).

- [12] D. W. Lubbers and N. Optiz. Eine neue pCO₂-bzw: pO₂-messsonde zur messung des pCO₂ oder pO₂ von gasen und flüssigkeiten. *Zeitschrift Für Naturforschung C*, **30**:532, (1975).
- [13] I. Pockrand, J. D. Swalen, J. G. Gordon and M. R. Philpott. Surface plasmon spectroscopy of organic monolayer assemblies. *Surf. Sci.*, **74**:237, (1978).
- [14] J.G. Gordon and S. Ernsta. Surface plasmons as a probe of the electrochemical interface. *Surf. Sci.*, **101**:499, (1980).
- [15] B. Liedberg, C. Nylander and I. Lundstrom. Surface plasmon resonance for gas detection and biosensing. *Sens. Actuators*, **4**:299, (1983).
- [16] J. Homola, S. S. Yee and G. Gauglitz. Surface plasmon resonance sensors: review. *Sens. Actuators B Chem.*, **54**:3, (1999).
- [17] J. Homola. Present and future of surface plasmon resonance biosensors. *Anal. Bioanal. Chem.*, **377**:528, (2003).
- [18] X. D. Hoa, A. G. Kirk and M. Tabrizian. Towards integrated and sensitive surface plasmon resonance biosensors: a review of recent progress. *Biosens. Bioelectron.*, **23**:151, (2007).
- [19] J. Homola. Surface plasmon resonance sensors for detection of chemical and biological species. *Chem. Rev.*, **462**:108, (2008).
- [20] H. Raether. Surface plasmons on smooth and rough surfaces and on gratings. Berlin: Springer-Verlag, 62, (1988).
- [21] D. Sarid. Long-range surface plasma waves on very thin metal films. *Phys. Rev. Lett.*, **47**:1927, (1981).
- [22] J. B. Pendry. Negative refraction makes a perfect lens. *Phys. Rev. Lett.*, **85**: 3966, (2000).
- [23] P. Berini. Plasmon-polariton waves guided by thin lossy metal films of finite width: Bound modes of symmetric structures. *Phys. Rev. B*, **61**:10484, (2000).
- [24] E. Kretschmann and H. Raether. Radiative decay of non-radiative surface plasmons excited by light. *Z. Naturforsch.*, **23A**:2135, (1968).

- [25] B. Hecht, H. Bielefeldt, L. Novotny, Y. Inouye and D. W. Pohl. Local excitation, scattering, and interference of surface plasmons. *Phys. Rev. Lett.*, **77**:1889, (1996).
- [26] D. Monzón-Hernández and J. Villatoro. High-resolution refractive index sensing by means of a multiple-peak surface plasmon resonance optical fiber sensor. *Sens. Actuators B Chem.*, **115**:227, (2006).
- [27] T. M. Chinowsky, M. S. Growa, K. S. Johnston, K. Nelson, T. Edwards, E. Fua and P. Yager. Compact, high performance surface plasmon resonance imaging system. *Biosens. Bioelectron.*, **22**:2208, (2007).
- [28] J. W. Chunga, R. Bernhardt and J. C. Pyun. Additive assay of cancer marker CA 19-9 by SPR biosensor. *Sens. Actuators B Chem.*, **118**:28, (2006).
- [29] R. G. Heideman and P. V. Lambeck. Remote opto-chemical sensing with extreme sensitivity: design, fabrication and performance of a pigtailed integrated optical phase-modulated Mach-Zehnder interferometer system. *Sens. Actuators B Chem.*, **61**:100, (1999).
- [30] M. Weisser, G. Tovar, S. Mittler-Neher, W. Knoll, F. Brosinger, H. Freimuth, M. Lacher and W. Ehrfeld. Specific bio-recognition reactions observed with an integrated Mach-Zehnder interferometer. *Biosens. Bioelectron.*, **14**:405, (1999).
- [31] Z. L. Wang and D. J. Bornhop. Dual-capillary backscatter interferometry for high-sensitivity nanoliter-volume refractive index detection with density gradient compensation. *Anal. Chem.*, **77**:7872, (2005).
- [32] <http://www.neosensors.com>.
- [33] M. Zourob, S. Mohr, B. J. T. Brown, P. R. Fielden, M. B. McDonnell and N.J. Goddard. An integrated metal clad leaky waveguide sensor for detection of bacteria. *Anal. Chem.*, **77**:232, (2005).
- [34] K. De Vos, I. Bartolozzi, E. Schacht, P. Bienstman and R. Baets. Silicon-on-Insulator microring resonator for sensitive and label-free biosensing. *Opt. Express*, **15**:7610, (2007).
- [35] A. Ramachandran, S. Wang, J. Clarke, S. J. Ja, D. Goad, L. Wald, E. M. Flood, E. Knobbe, J. V. Hryniewicz, S. T. Chu, D. Gill, W. Chen,

- O. King and B. E. Little. A universal biosensing platform based on optical micro-ring resonators. *Biosens. Bioelectron.*, **23**:939, (2008).
- [36] N. M. Hanumegowda, C. J. Stica, B. C. Patel, I. M. White and X. Fan. Refractometric sensors based on microsphere resonators. *Appl. Phys. Lett.*, **87**:201107, (2005).
- [37] F. Xu, P. Horak and G. Brambilla: Optical microfiber coil resonator refractometric sensor: erratum. *Opt. Express*, **15**:9385, (2007).
- [38] H. Tazawa, T. Kanie and M. Katayama. Fiber-optic coupler based refractive index sensor and its application to biosensing. *Appl. Phys. Lett.*, **91**:113901, (2007).
- [39] B. Cunningham, P. Li, B. Lin and J. Pepper. Colorimetric resonant reflection as a direct biochemical assay technique. *Sens. Actuators B Chem.*, **81**:316, (2002).
- [40] S. Mandal and D. Erickson. Nanoscale optofluidic sensor arrays. *Opt. Express*, **16**:1623, (2008).
- [41] A. Lesuffleur, H. Im, N. C. Lindquist and S. -H. Oh. Periodic nanohole arrays with shape-enhanced plasmon resonance as real-time biosensors. *Appl. Phys. Lett.*, **90**:243110, (2007).
- [42] J. McPhillips, A. Murphy, M. P. Jonsson, W. R. Hendren, R. Atkinson, F. Höök, A. V. Zayats and R. J. Pollard. High-performance biosensing using arrays of plasmonic nanotubes. *ACS Nano*, **4**:2210, (2010).
- [43] L. S. Live, O. B. Bolduc and J. -F. Masson. Propagating surface plasmon resonance on microhole arrays. *Anal. Chem.*, **82**:3780, (2010).
- [44] K. M. Mayer, S. Lee, H. W. Liao, B. C. Rostro, A. Fuentes, P. T. Scully, C. L. Nehl and J. H. Hafner. A label-free immunoassay based upon localized surface plasmon resonance of gold nanorods. *ACS Nano*, **4**:687, (2008).
- [45] S. Y. Chou, P. R. Krauss and P. J. Renstrom. Imprint of sub-25 nm vias and trenches in polymers. *Appl. Phys. Lett.*, **67**:3114, (1995).
- [46] S. Y. Chou, P. R. Krauss, W. Zhang, L. J. Guo and L. Zhuang. Sub-10 nm imprint lithography and applications. *J. Vac. Sci. Technol. B*, **15**:2897, (1997).

- [47] S. Y. Chou, P. R. Krauss and P. J. Renstrom. Nanoimprint lithography. *J. Vac. Sci. Technol. B*, **14**:4129, (1996).
- [48] L. J. Heyderman, H. Schiff, C. David, J. Gobrecht and T. Schweizer. Flow behavior of thin polymer films used for hot embossing lithography. *Microelectron. Eng.*, **54**:229, (2000).
- [49] J. Haisma, M. Verheijen, K. V. D. Heuvel and J. V. D. Berg. Mold-assisted nanolithography: A process for reliable pattern replication. *J. Vac. Sci. Technol. B*, **14**:4124, (1996).
- [50] M. Bender, M. Otto, B. Hadam, B. Vratzov, B. Spangenberg and H. Kurz. Fabrication of nanostructures using a UV-based imprint technique. *Microelectron. Eng.*, **53**:233, (2000).
- [51] M. Colburn, S. Johnson, M. Stewart, S. Damle, T. Bailey, B. Choi, M. Wedlake, T. Michaelson, S. V. Sreenivasan, J. Ekerdt and C. G. Willson. Step and flash imprint lithography: A new approach to high-resolution patterning. *Proc. SPIE*, **3676**:379, (1999).
- [52] H. Schiff. Nanoimprint lithography: An old story in modern times? A review. *J. Vac. Sci. Technol. B*, **26**:458, (2008).
- [53] The international technology roadmap for semiconductors, 2007 edition lithography. www.itrs.net/Links/2007ITRS/Home2007.htm.
- [54] M. D. Austin, H. X. Ge, W. Wu, M. T. Li, Z. N. Yu, D. Wasserman, S. A. Lyon and S. Y. Chou. Fabrication of 5 nm linewidth and 14 nm pitch features by nanoimprint lithography. *Appl. Phys. Lett.*, **84**:5299, (2004).
- [55] F. Hua, Y. G. Sun, A. Gaur, M. A. Meitl, L. Bilhaut, L. Rotkina, J. F. Wang, P. Geil, M. Shim and J. A. Rogers. Polymer imprint lithography with molecular-scale resolution. *Nano Lett.*, **4**:2467, (2004).
- [56] Y. Chen, F. Carcenac, C. Ecoffet, D. J. Lougnot and H. Launois. Mold-assisted near-field optical lithography. *Microelectron. Eng.*, **46**:69, (1999).
- [57] N. Khusnatdinov, G. M. Schmid, C. B. Brooks, D. L. Brake, D. J. Resnick, M. W. Hart, K. Gopalakrishnan, R. Shenoy, R. Jih, Y. Zhang, E. Sikorski, M. B. Rothwell, J. Owens and A. Ford. Minimizing linewidth roughness in step and flash imprint lithography. *Microelectron. Eng.*, **85**:856, (2008).

- [58] M. T. Li, H. Tan, L. S. Kong and L. Koecher. Four-inch photo-curable nanoimprint lithography using NX-2000 nanoimprinter. *Proc. SPIE*, **5374**:209, (2004).
- [59] Y. Chen and A. Pépin. Nanofabrication: Conventional and nonconventional methods. *Electrophoresis*, **22**:187, (2001).
- [60] S. Reyntjies and R. Puer. A review of ion beam applications in microsystem technology. *J. Micromech. Microeng.*, **11**:287, (2001).
- [61] B. Bhushan. Nanoimprint lithography. *Springer Handbook of Nanotechnology*, Springer, (2007).
- [62] H. Namatsu, M. Nagase, T. Yamaguchi, K. Yamazaki and K. Kurihara. Influence of edge roughness in resist patterns on etched patterns. *J. Vac. Sci. Technol. B*, **16**:3315, (1998).
- [63] Y. S. Ma, G. Tsvid and F. Cerrina. Line edge roughness of sub-100 nm dense and isolated features: experimental study. *J. Vac. Sci. Technol. B*, **21**:3124, (2003).
- [64] C. Finder, M. Beck, J. Seekamp, K. Pfeiffer, P. Carlberg, I. Maximov, F. Reuther, E. -L. Sarwe, S. Zankovich, J. Ahopelto, L. Montelius, C. Mayer and C. M. Sotomayor Torres. Fluorescence microscopy for quality control in nanoimprint lithography. *Microelectron. Eng.*, **67-68**:623, (2003).
- [65] A. Fuchs, B. Vratzov, T. Wahlbrink, Y. Georgiev and H. Kurz. Interferometric in situ alignment for UV-based nanoimprint. *J. Vac. Sci. Technol. B*, **22**:3242, (2004).
- [66] C. Gourgon. Etude et développement de la technique de nanolithographie par nanoimpression. *Mémoire d'habilitation à diriger des recherches*, Joseph Fourier University, (2007).
- [67] Y. N. Xia and G. M. Whitesides. Soft lithography. *Annu. Rev. Mater. Sci.*, **28**:153, (1998).
- [68] L. Libioulle, A. Bietsch, H. Schmid, B. Michel and E. Delamarche. Contact-inking stamps for microcontact printing of alkanethiols on gold. *Langmuir*, **15**:300, (1999).
- [69] A. G. Brolo, R. Gordon, B. Leathem and K. L. Kavanagh. Surface plasmon sensor based on the enhanced light transmission through arrays of nanoholes in gold films. *Langmuir*, **20**:4813, (2004).

-
- [70] K. A. Tetz, L. Pang and Y. Fainman. High-resolution surface plasmon resonance sensor based on linewidth-optimized nanohole array transmittance. *Opt. Lett.*, **31**:1528, (2006).
- [71] B. D. Lucas, J. -S. Kim, C. Chin and L. J. Guo. Nanoimprint lithography based approach for the fabrication of large-area, uniformly oriented plasmonic arrays. *Adv. Mater.*, **20**:1129, (2008).
- [72] A. Lesuffleur, H. Im, N. C. Lindquist, K. S. Lim and S. -H. Oh. Laser-illuminated nanohole arrays for multiplex plasmonic microarray sensing. *Opt. Express*, **16**:219, (2008).
- [73] A. De Leebeeck, L. K. Swaroop Kumar, V. De Lange, D. Sinton, R. Gordon and A. G. Brolo. On-chip surface-based detection with nanohole arrays. *Anal. Chem.*, **79**:4094, (2007).

Chapter 2

Mold and stamp fabrication

As previously described in chapter 1, the quality of the master mold (high resolution, defect-free) is of fundamental importance to nanoimprint lithography (NIL). The fabrication process of such master mold is more often based on the electron beam lithography (EBL) since this technique is very flexible and can produce high resolution features in the sub-10nm range. This first EBL step used to get the master mold is thus very important. This chapter will present the different EBL processes that have been used during my thesis. After the preparation of the hard master mold, soft stamps (PDMS, h-PDMS/PDMS) can then be obtained by replication from the master mold. This last duplication step for producing flexible NIL stamps will also be described.

2.1 Master mold fabrication

Electron beam lithography (EBL) is one of the most powerful methods for creating high resolution nanoscale structures. The main advantages of EBL over the conventional photolithography techniques include very high resolution, greater accuracy and the ability to write a variety of pattern geometries.

In EBL, a beam of electrons is utilized to generate patterns on a substrate surface. The principle of this technique is to use a high voltage electrons in the range of 1 kV - 100 kV to nanopattern the electrosensitive resist deposited on the substrate by directly writing onto it. A very high resolution of several nanometers can be obtained with this method. A typical electron beam lithography system is shown schematically in figure 2.1, it consists of an electron gun, electron optical column, and a vacuum

chamber containing a laser controlled x/y stage for accurately positioning the substrate under the beam. The electron optical column is used to form and direct a focused beam of electrons onto the surface of the substrate. The electrons are produced in the electron gun. After the electron beam emerges from the gun, it passes through several additional stages in the electron optical column that perform specific beam modification processes to produce a beam having the required current and the spot size correctly located onto the substrate.

The short wavelength associated with high-energy electron beam gives to EBL an ultra high resolution capability. However, the resolution limit is determined not by the beam size, but by the scattering effects occurring in the resist after interaction with the electrons of high energy. Different scattering effects exist among which the more important are the forward scattering of the primary electron beam, the secondary electron travel and the electron backscattering. Working with a higher energy electron beam (above 50KeV) or in a very thin resist layer allows to largely reduce the forward scattering in order to reach very high resolution with dimension in the range of the beam size. However, the secondary backscattering effect (also called the proximity effect) is a bothering over exposure that occurs at the resist-substrate interface due to backscattered electrons. This proximity effect that is dependent of the substrate material has to be largely minimized in case of high resolution experiments.

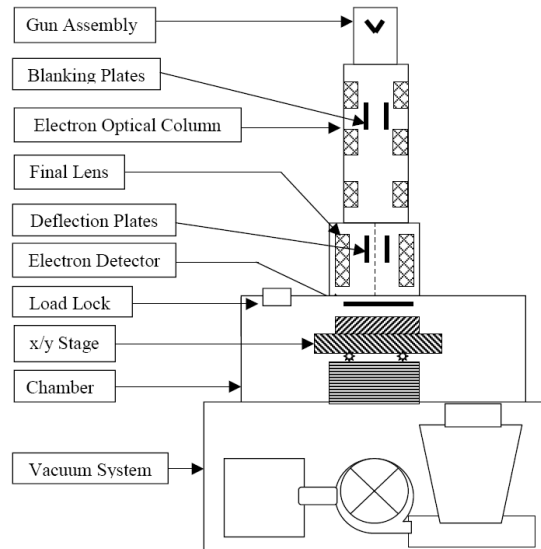


Figure 2.1: The basic components of a typical electron beam lithography system (excluding electronic component).

2.1.1 Commercial EBL molds

The standard commercial stamp with multi-patterns manufactured by NIL Technology (Denmark) has been used first for the initial testing of the nanoimprint process and test of NIL equipment [6]. This mold is fabricated by E-beam lithography and transferred in nickel plate by electroplating. Figure 2.2(a) and (b) show the details of the mold. There are nine patterned areas with the size of $200\ \mu\text{m} \times 200\ \mu\text{m}$ occupied the center of the 2 inch wafer. Each of the area contains four different type patterns included lines, pillars, cross-bars and checker-board, with four different line widths/periods ($250/500\ \text{nm}$, $200/400\ \text{nm}$, $150/300\ \text{nm}$ and $100/200\ \text{nm}$) and $200\ \mu\text{m}$ spacing. The protrusion height is $105\ \text{nm}$ (with $x=100\ \text{nm}$ the protrusion height is $65\ \text{nm}$).

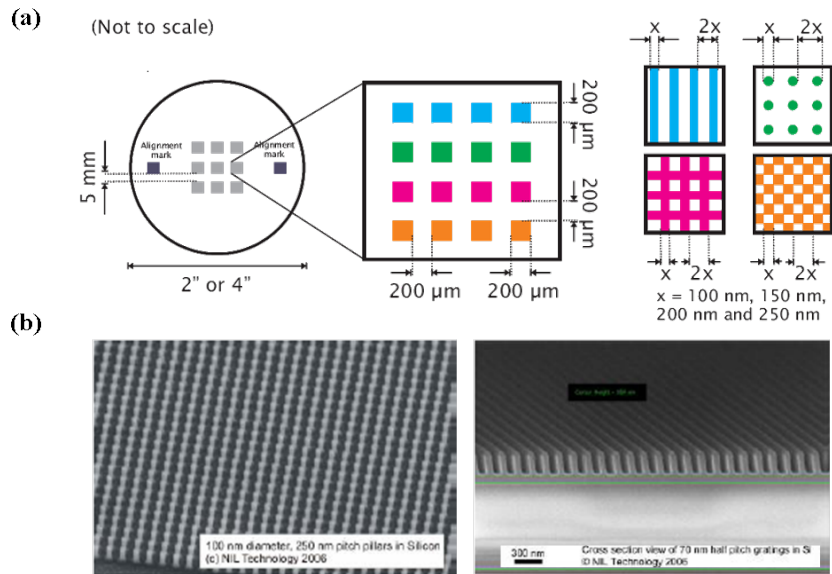


Figure 2.2: (a) The organization of the standard commercial stamp fabricated by NIL technology and (b) SEM images of dots array (left) and lines arrays (right) in the standard commercial stamp from NIL technology[6].

In our work, the studied sub-wavelength photonic nanostructures were obtained by EBL with the LPN LEICA EBPG 5000+ e-beam system. Three different e-beam resists have been tested for high resolution e-beam direct writing. I will now report on those three different EBL processes and their performance for both resolution and pattern profile.

2.1.2 EBL process based on the PMMA resist

PMMA (polymethyl methacrylate) that has been firstly discovered and studied as EBL polymeric material is a positive e-beam resist for directly EBL writing and can be used as well in deep UV and X ray microlithography processes [1]. The most prominent features of this PMMA resist are its high resolution, its high contrast associated with its low sensitivity and its wide process latitude. The master molds have been fabricated by EBL based on PMMA resist in two different approaches: (1) a conventional multi-process with PMMA resist exposure combined with lift-off and Si reactive ion etching (Fig. 2.3(a)) and (2) single-step process with PMMA resist exposure and Si direct etching (Fig. 2.4(a)).

In the first multi-process, nanodots and nanolines are defined by EBL at 100 KeV in the PMMA resist that has been previously pre-backed at 180 °C for 30 minutes. After development and Ni lift-off, the final patterns are transferred into the silicon wafer by reactive ion etching (RIE) with $\text{CHF}_3\text{-SF}_6$ gases. Figure 2.3(b) shows the SEM images of nanopattern transferred on silicon wafer after reactive ion etching with Ni metal layer as a mask. Before replication, the Ni layer has to be removed by chemical wet etching in a HNO_3 acid solution.

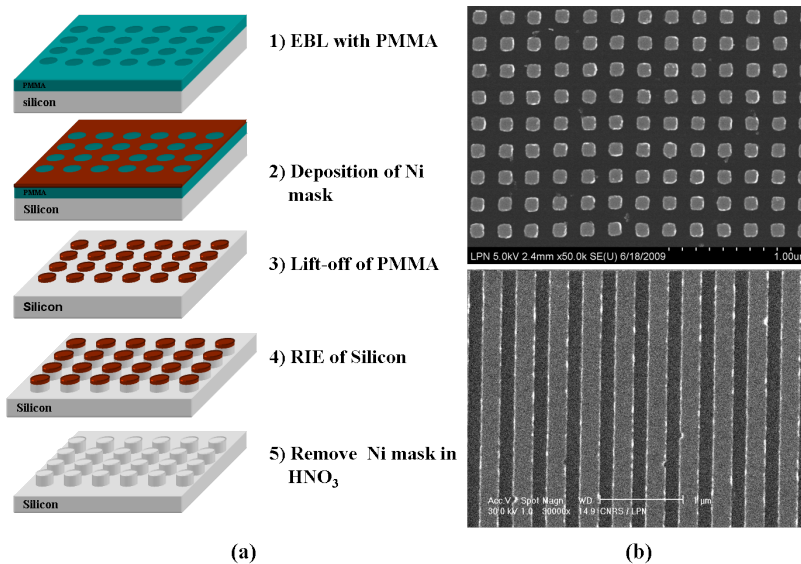


Figure 2.3: (a) process 1: multi-step fabrication process based on EBL PMMA resist exposure combined with lift-off and etching; (b) SEM images of nanodots (diameter = 100 nm, pitch = 100 nm) and nanolines (linewidth = 220 nm, pitch = 180 nm) structures in silicon mold patterned by e-beam lithography and reactive ion etching before the removal of Ni mask.

Since this first process is complicated and involves multiple intermediate steps that are difficult to optimize, a faster and more reliable approach (process 2) has been developed. After the standard EBL exposure at 100 KeV in a 430 nm thick layer of PMMA (950PMMA A5, MicroChem Corp.), the samples are developed in a methylisobutylketone (MIBK)/isopropanol (IPA) solution at 20 °C for 35 s, rinsed in IPA for 10 s and then dried with nitrogen gun. The direct etching step of Si is then performed. A highly anisotropic RIE process based on $\text{CHF}_3/\text{SF}_6/\text{O}_2$ allows to transfer nanopatterns in Si. PMMA resist is finally removed in acetone. Fig. 2.4(b) shows a SEM images of nanohole arrays and nanoline arrays recorded in Si master. These images show clearly a better edge profile of the patterns combined with a better homogeneity in dimension (hole diameter and line width) compared to the multi-step fabrication process 1 (compare Fig. 2.4(b) and Fig. 2.3(b)). However, this master mold has a negative polarity (holes in silicon for example) compared to the process 1 master mold (pillars in silicon). The polarity of the soft NIL stamp will also be different and produce different imprinting results. These important points will be discussed in chapter 3.

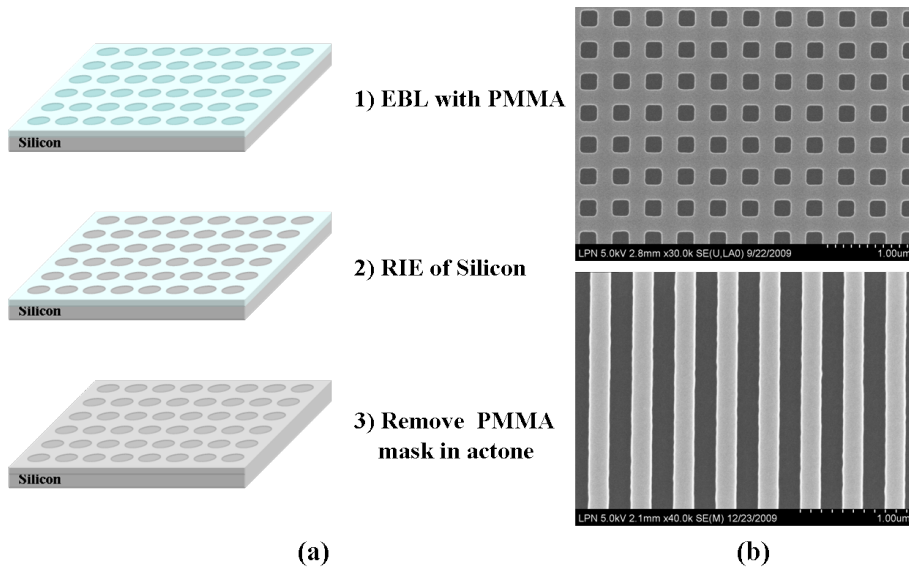


Figure 2.4: (a) process 2: a single-step fabrication process based on EBL in PMMA resist and direct etching (b) SEM images of nanoholes (diameter = 200 nm, pitch = 400 nm) and nanolines (linewidth = 200 nm, pitch = 400 nm) structures in silicon mold.

2.1.3 EBL process based on the ZEP-520 resist

In contrast to PMMA, ZEP-520 is an excellent positive e-beam resist with a higher sensitivity in which improvements in the minimum feature size have been shown. ZEP-520 is a chain scission resist consisting of copolymers of α -chloromethacrylate and α -methylstyrene [2]. This resist has also a better dry etch resistance than PMMA, but is still not adequate for some plasma chemistries and large etching times [3]. It presents also poor adhesion (requires HMDS prime layer) and normal exposure doses result more often in reentrant pattern profiles. Nanorings have been patterned based on

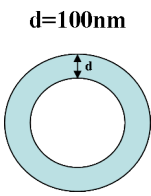
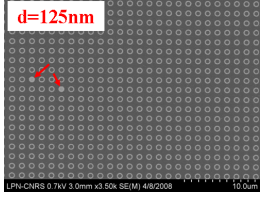
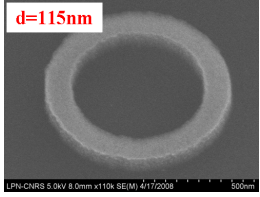
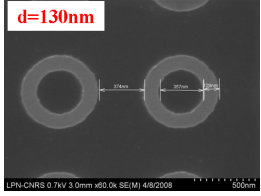
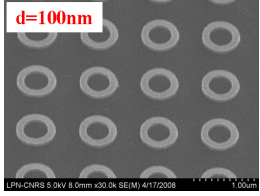
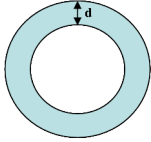
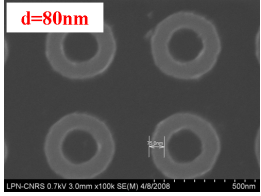
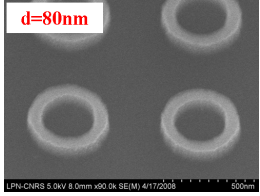
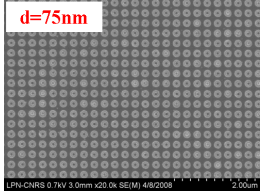
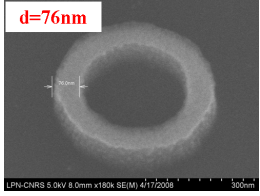
Designed feature size	Dose (nC/cm ²)	After Ni lift-off	After Si etching and remove of Ni
 d=100nm	500	 d=125nm	 d=115nm
	550	 d=130nm	 d=100nm
 d=60nm	550	 d=80nm	 d=80nm
	600	 d=75nm	 d=76nm

Table 2.1: Comparison of some nanorings patterns defined in ZEP-520 resist by EBL with different electron doses.

EBL in a ZEP-520 resist layer that was pre-baked at 170 °C. After Ni lift-off, RIE with CHF₃-SF₆ gas is used to transfer patterns in the silicon

substrate. Some selected results obtained after Ni lift-off and anisotropic etching are shown in table 2.1.

As it can be seen from table 2.1, the resulting structures show a good performance of EBL in resolution despite the sizes slightly differ from the designed ones. However, some inaccuracies are also encountered. For example, for the nanoring ($d = 125$ nm) arrays after Ni lift-off, some central part of nanoring isn't fully lifted, thus the finally pattern appears as nanodot (see the red arrows on the image). Such defect and dimension control can be adjusted by optimizing both the electron dose and RIE etching time.

2.2 Soft stamp fabrication

The molds used in nanoimprint lithography take up the same important role as the photomask in photolithography. Both thermal NIL (T-NIL) and step-and-flash imprint lithography (S-FIL) utilize the hard molds which distinguish from soft lithographic methods that use soft electromagnetic stamps as patterning elements. Considering the hardness, compatibility with traditional microfabrication processing and the thermal expansion coefficient of the material, normally materials include silicon, dielectric materials (e.g: silicon dioxide, silicon carbide or silicon nitride), metals (e.g: Nickel) or polymeric materials with sufficient Young's modulus have been chosen for T-NIL molds fabrication [7]. Hard features of the different templates are that they have a high mechanical strength and durability. The properties of these hard molds can allow imprinting of features in polymer materials with resolutions below 10 nm, and also are crucial for producing nanoscale features because the protrusion patterns on the template should not deform, buckle, or collapse during imprint, even at elevated temperatures, which isn't possible to be achieved by soft lithography using an elastomeric stamp.

Compared with T-NIL and SFIL, soft imprint technique uses an elastomeric stamp with patterned relief structures on its surface. Several types of materials, including polycarbonate resins [8], cross-linked novolak based epoxy resin [9], fluoropolymer materials and tetrafluoroethylene (TFE) [10], etc. have been used in soft lithography. It turned out that poly (dimethylsiloxanes) (PDMS) offers numerous attractive properties for use as stamp elastomer because: (1) its flexible backbone enables accurate replication of relief shapes in the fabrication of the patterning elements [11], (2) its low Young's modulus (~ 750 KPa) [12] and low surface energy enable con-

formal contact with surface without applied pressure and nondestructive release from patterned structures [13], (3) its good optical transparency down to a light wavelength of approximately 256 nm [14], (4) its commercial availability in bulk quantities at low cost. PDMS can be used as a backplane or imprint layer for soft UV nanoimprint lithography. Several procedure for preparing the stamp are summarized below.

2.2.1 Basic soft PDMS stamp fabrication process

Stamps are typically replicated by firstly mixing two commercial PDMS components: 10:1 PDMS RTV 615 (part A) siloxane oligomer and RTV 615 (part B) cross-linking oligomers (General Electric) thoroughly and degassing, then casting a mixture onto the anti-sticking treated surface of nickel or silicon nanostructured master molds. After curing at 60 °C for 24h, the stamps have been left to cool to room temperature and then carefully peeled off from the print master. A schematic illustration of the protocol used for the preparation of soft stamps is given in Figure 2.5.



Figure 2.5: Schematic illustration of the basic procedure for the preparation of the soft stamp.

PDMS normally includes a base polymer (part A) containing polydimethylsiloxane bearing vinyl groups and a platinum and a curing agent (part B) which contains a cross-linker containing silicon hydride (Si-H) groups for forming covalent bonds with vinyl groups. Controlling the mixing ratio of PDMS's two components (part A and part B), different mechanical properties of PDMS can be achieved. Young's modulus can be tuned by changing the mixing ratio from 1:10 to 1:5 (part A : part B): the smaller the ratio, the lower the resulting Young's modulus (the softer the nature) [15].

While PDMS offers some advantages, there are a number of properties inherent to PDMS which severely limit its capabilities in soft UV-NIL. First, its low Young's modulus limits the fabrication of features with high aspect ratios due to collapse, merging and buckling of the relief structures;

second, its surface energy ($\approx 22\text{-}25 \text{ mNm}^{-1}$) isn't low enough to replicate profiles with high fidelity; third, its high elasticity and thermal expansion can lead to deformation and distortions during the fabrication; finally, it shrinks by $\sim 1\%$ curing and the cured PDMS can be readily swelled by most organic liquids [16, 17].

2.2.2 Improved soft stamp fabrication process

To improve the resolution and fidelity in soft UV-NIL, we have developed one composite stamp composed of two layers: a stiff layer supported by a flexible PDMS layer, which presents enhanced mechanical characteristics compared with PMDS soft mold.

The most widely used material for this stiff layer is the so-called “h-PDMS” (“hard” PDMS) which was prepared from a commercially available trimet - hylsiloxy terminated vinylmethylsiloxane (VDT-731, Gelest) and meth-ylhydrosiloxane-dimethylsiloxane (HMS-301, Gelest) copoly-mers. h-PDMS has cross-linkers with relatively short lengths as compared to those in the normal PDMS. Also it possesses a relatively high modulus ($\sim 9 \text{ N/mm}^2$), but its elongation at break is much lower than that of normal PDMS[18, 19].

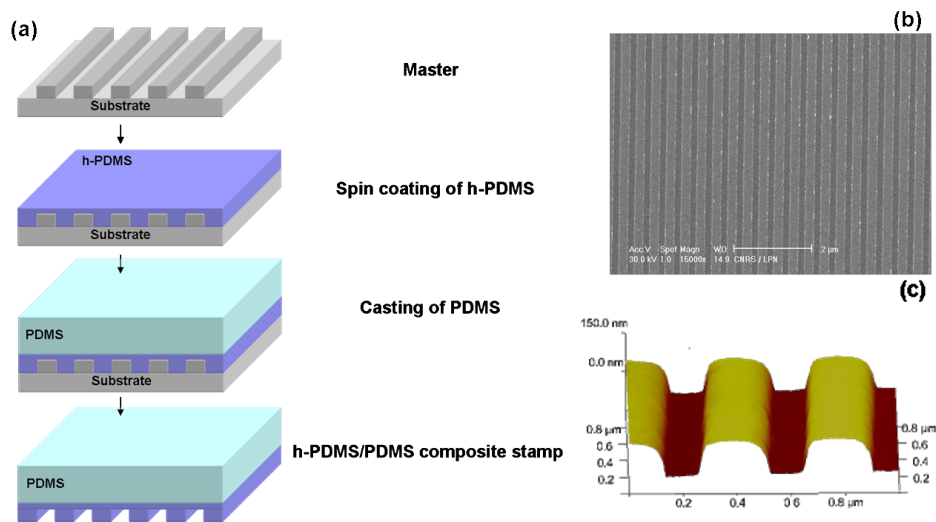


Figure 2.6: (a) Procedure for fabricating a h-PDMS/PDMS two-layer composite stamp. (b) SEM image of 200 nm nanolines arrays with a spacing of 200 nm of the silicon master and (c) Atomic force microscope (AFM) image of the replicated h-PDMS/PDMS bilayer stamp of the corresponding Si master.

Figure 2.6(a) summarized the procedure for preparing a bi-layer stamp from h-PDMS and normal PDMS. The h-PDMS solution is first spin coated onto a master at 5000 rpm for 30 s and then degassed in vacuum for 10 mins to make sure the h-PDMS can flow into the recessed nanoareas of the master. Note that, below a certain critical lateral dimension, the PDMS cannot completely fill up the recessed nanoareas due to its high viscosity, and the height of the soft stamp nanostructures will be thus lower than the height of the master patterns. A mixture of commercial available (RTV615 from GE) two component solution (1:10) of conventional PDMS is then directly poured on top of the cured thin h-PDMS layer. After degassing and solidifying at 60 °C for 24 hours, the bi-layer stamp can be peeled off from the master. In figure 2.6(b) SEM images of an array with 200 nm nanolines on the surface of the silicon master are shown. The 3D AFM picture of the replicated h-PDMS/PDMS stamp (figure 2.6(c)) shows the replicated pattern uniformity along the vertical dimension. This composite stamp combines some attractive advantages of both a more rigid layer (to achieve high-resolution pattern transfer) and a more flexible support (to enable conformal contact with a surface without external pressure).

2.3 Anti-sticking surface treatment

2.3.1 State of the art

A mold used for nanoimprint lithography typically has a high density of nanoscale protrusion features on its surface, which increases the total surface contact areas with the polymer layer in nanoimprinting and stamping process and leads to a strong tendency of adhesion of the polymer to the mold. Thus, adhesion is a major issue in the creation of reliable and high-yield techniques for the replications of more complex and smaller structures. The solutions to this problem are (1) incorporating an internal release agent into the resist formulation, (2) applying a low surface tension coating to the mold to reduce its surface energy (or a combination of both approaches) and (3) choosing a mold material with an intrinsically low surface surface energy [7]. Among these solutions, most research is in progress to investigate the use of anti-sticking layer providing a low energy surface to enhance mold release and thereby minimizing distortions in the pattern during mold removal from the solidified polymeric material.

N. Roos, M. Wissen and H. -C Scheer have proposed two methods of tailoring adhesion properties of thermosets in hot embossing lithogra-

phy. The first method was based on a plasma-deposition of a fluorinated film followed by a self-assembled monolayer (SAM) coating of fluoroalkyl-trichlorosilane. The second one used C_4F_8 as a feed gas to deposit Teflon-like anti-sticking layers by plasma deposition and formed the SAM layer from the gas phase [23, 24].

Byeon et al. studied the anti-sticking treatment of Nickel nanoimprint template. In their study, a thin layer of SiO_2 film was deposited on nickel surface and silane based hydrophobic SAM layer could be stable formed on SiO_2 film. As a result, the imprint defects generated by using nickel template which has a poor anti-sticking property can be avoided by such proper releasing layer [26].

Recently, researches from the “University of the Texas System” present an invention for getting diamond-like carbon films (commonly referred to as “DLC” films) that act as a release layer on a template. Such DLC film has generally similar properties as polycrystalline diamond coatings, such as low energy friction, high hardness and low surface energy and thus exhibits excellent release characteristics of the cross-linked polymer material from the template [25]. Whereafter F. A. Houle and L. Tao et al. also indicated that DLC coatings is a useful alternative for fluorosilane layers [27, 28].

Among these reported methods, many researches used a commercially available F_{13} -OCTS (Tridecafluoro - 1,1,2,2 - tetrahydrooctyl) - trichlorosilane [29, 30] or OTMS (octadecyltrimethoxysilane) [31] to deposit anti-adhesive coating on the surface of SiO_2 or Si stamp. It was also shown that solution-based procedures for forming the SAM releasing layer on the mold does not work well for high resolution molds with sub-100nm pitch and high aspect ratio, while vapor-phase processes allow superior coating of the releasing agent, mainly because the vapor can penetrate more easily into the nanoscale patterns of the mold than a solution [32].

2.3.2 Principle of anti-sticking treatment

Since UV-NIL is based on squeeze flow of a viscous resist between a stamp and a substrate, the interface between the two materials has to be considered throughout the entire process. Several effects contribute to the adhesion between the interface. Mechanical adhesion from a large area contact, surface roughness, dovetail stamp structures and friction interlocking. Chemical adhesion originates from chemical bonds across the interface. Physical adhesion is the interaction between the surface from

Van der Waals force and hydrogen bridges.

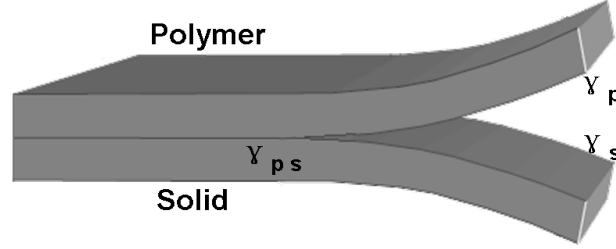


Figure 2.7: Surface energy of the polymer, solid and interior surface.

It's known that the adhesion energy, W_{ad} is the energy that should be applied to separate two surfaces that are adhering one to each other. Taking the surface energy of a polymer γ_p , the surface energy of a solid γ_s and the interfacial energy between the polymer and solid γ_{ps} (Figure 2.7), the adhesive energy is given by

$$W_{ad} = \gamma_s + \gamma_p - \gamma_{ps} \quad (2.1)$$

The interior surface energy between polymer and solid is calculated from the given formula by [33]

$$\gamma_{ps} = \gamma_p + \gamma_s - 2C\sqrt{\gamma_p\gamma_s} \quad (2.2)$$

where C is a constant and in the reference [33], $C=1$. Now the expression for the adhesive energy γ_{ps} can be expressed as

$$W_{ad} = 2C\sqrt{\gamma_p\gamma_s} \quad (2.3)$$

From this simple expression, one can explain intuitively that good adhesion is obtained for a surface with a large surface energy and poor adhesion for a surface with a small surface energy. Concerning the adhesion during NIL, it's observed from equation (2.3) that the stamp should have a lower surface energy than the one of the polymer, and the substrate should have a large surface energy to adhere well to the polymer.

2.3.3 Anti-sticking treatment by TMCS

In our experiment, functionalization of all the mold surface, including both the master mold and the PDMS stamp, are accomplished by simply evaporated Trichloromethylsilane (TMCS, chlortrimethylsilane redistilled, 99%, Sigma Aldrich), the usability with which has been proved in our group before. The surface treatment procedure used in our soft UV-NIL process is based on this treatment. Silicon templates should be first cleaned with a piranha solution (1 part H_2O_2 to 5 parts H_2SO_4) for 1 hour to remove any surface organic contaminants. Then the mold was immersed successively in HF and H_2O_2 for 2 min and finally the mold was dried with nitrogen gun. The mold was then placed inside a closed box with a small quantity of TMCS inside for 10 min. When the gaseous molecules come into contact with the mold surface they react immediately to form a covalent link as described in Figure 2.8.

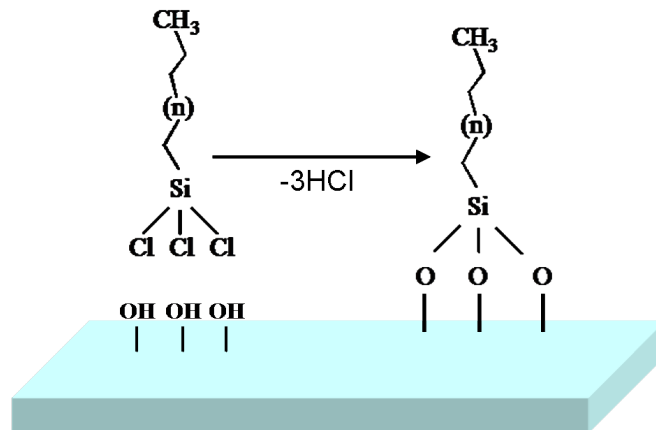


Figure 2.8: Schematic diagram of the mechanism for anti-sticking treatment by using TMCS.

2.4 Mold pattern inversion based on NIL

Traditionally, the most common nanolithographies used for sub-100nm scale patterning are electron beam lithography [34] and focused ion beam lithography [35], but they are not suitable for mass production because of their long writing time and expensive equipments as described in chapter 1. In this context, nanoimprint lithography has been demonstrated to be one of the most promising alternative techniques for producing dense periodic

nanostructures on large areas at reasonable cost [36]. With intensive developments from materials (i.e. resists, mold) to imprinting tools, NIL has now passed the barrier from laboratory scale to industrial preproduction [37].

However, one NIL key parameter for both resolution and pattern smoothness concerns the fabrication of the master mold. Since NIL allows faithful pattern duplication even of nanometer variations on a pattern sidewall, it is important to fabricate NIL master molds of high resolution and with minimal sidewall roughness. These molds are generally patterned using EBL at high energy. To reduce both writing time and fabrication time, developing other strategies for master replication or inversion at the whole wafer scale is thus important. In this part, we propose a two steps process that allows pattern inversion at each step. The first step combines thermal nanoimprint lithography, ion beam etching (IBE) and reactive ion etching for pattern transfer, whereas the second step is based on soft UV nanoimprint lithography associated only with reactive ion etching. We have here studied how each pattern transfer process will affect feature size, pattern shape and homogeneity. Sub-200nm nanostructures have been inverted with good reproducibility and homogeneity on field as large as 1 cm². Two successive inversions were finally performed in order to quantify changes in both linewidth and pattern shape between the original EBL Si master mold and the grand-daughter Si mold (step 2) replicated from the daughter mold (step 1) by soft UV-NIL.

2.4.1 Materials and fabrication

T-NIL and soft UV-NIL were performed on our commercial Nanonex NXR-2500 imprint tool. The fabrication process can be divided in two parts: (Fig. 2.9) T-NIL combined with IBE and RIE is first used to invert an EBL master mold (step 1). Then soft h-PDMS/PDMS transparent stamps are casted on the daughter Si to perform UV-NIL (step 2 - Fig. 2.13(a)). Finally, after RIE pattern transfer, the grand-daughter Si mold exhibits the same pattern polarity as the original EBL master.

Master mold fabrication

Each pattern field on the silicon masters (mother molds) used in this work contains either nanopillars arrays or nanolines arrays. The master patterns are defined by electron beam lithography at 100 KeV in a resist layer (ZEP 520 or PMMA depending of the pattern size) and transferred into a silicon

wafer by anisotropic reactive ion etching (RIE) with $\text{CHF}_3\text{-SF}_6$ gas [38, 39], resulting in sub-100nm features with a depth of 100 nm. Finally, the surface of the patterned silicon mold was treated with trichloromethylsilane (TMCS) as release agent.

Thermal nanoimprint lithography (T-NIL) inversion process

First, T-NIL is used to invert the Si master mold, for example to get holes arrays starting from pillars arrays (Figure 2.9). A thin gold layer (20 nm) that will act as mask during IBE pattern transfer is first deposited on the silicon wafer. The NXR-1020 resist (Nanonex) is then spin coated to get a thickness of 180 nm on Au/Si wafers and is finally annealed on hotplate at 120°C during 10 min to remove the solvent. The Si master mold is gently placed in contact with the NXR-1020/Au/Si sample and sandwiched between the two membranes of the NXR-2500 Nanonex, which provides optimal uniformity over the whole imprinted field [38]. Imprint is performed at 130°C in two successive pressuring steps: 10 s at 120 psi (8 bars) followed by 30 s at 200 psi (14 bars). The imprint tool is cooled down below the estimated glass transition temperature of the resist, before careful demolding of the master.

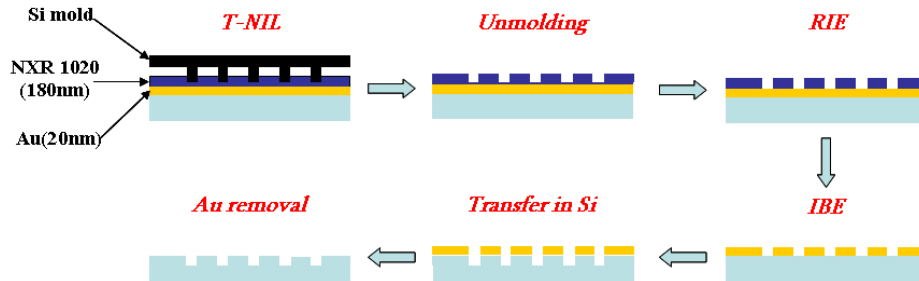


Figure 2.9: The mold inversion process based on T-NIL and ion beam etching. The daughter mold exhibits holes arrays instead of pillars on the EBL master.

After T-NIL step, the residual NXR1020 resist layer is removed under O_2 plasma at a rate of 30nm/min, and the thin Au mask layer is etched by Ar ion beam etching (IBE) at high energy (350 V). This IBE step is crucial for pattern dimension control as it will be discussed later. The resist layer is then simply removed in acetone. Finally, the patterns are transferred into silicon wafer with standard Si RIE process [38, 39] and the Au mask is removed in a $\text{KI}+\text{I}_2$ solution. At the end of this step 1, inverted patterns are obtained in the daughter Si mold (for example holes as shown in Fig.

2.11).

UV nanoimprint lithography (UV-NIL) replication process

In soft UV-NIL [40], patterns are replicated in a low viscosity UV-curable polymer from a flexible transparent mold that offers many advantages. This polydimethylsiloxane (PDMS) soft stamp can be easily cast more than twenty times on the same master mold. Moreover this cheap stamp is sufficiently flexible to be in perfect conformal contact during printing. Here we used our specific h-PDMS/PDMS bi-layer transparent stamps [38] to perform replications in the sub-100nm range (see Figure 2.6).

These arrays (for example pillars) are replicated by soft UV-NIL in an Amonil/Ge/PMMA tri-layer system that allows pattern transfer with high aspect ratio [39]. PMMA bottom layer is first spin-coated with a thickness between 150-300 nm and pre-baked at 180 °C for 10 min. A 10 nm-thin intermediate germanium (Ge) is then deposited by electron-beam evaporation. Finally a 180 nm thick Amonil resist (AMO-MMS4) layer is spin coated on the top of the Ge layer. UV-NIL is realized at room temperature using the optimized pressure of 8 psi (0.55 bars).

UV imprinted patterns (for example holes arrays) in Amonil resist are then transferred using three successive RIE steps with O₂/CHF₃, SF₆ and O₂ plasma. A 20 nm-thin Ni layer is deposited by electron-beam evaporation and lifted in acetone. The final patterns (pillars in the case-see Figure 2.13) are etched in Si with our standard CHF₃/ SF₆ gas mixture. The Ni mask is then removed with nitric acid (HNO₃). After this whole process, the grand-daughter Si mold exhibit pillar arrays similarly to the original EBL master mold. The detail of the fabrication process of soft UV-NIL (include optimizing parameters for both UV-NIL and reactive ion etching) will be explain in chapter 4.

2.4.2 Results and discussion

Unlike other conventional lithography, nanoimprint lithography replicates patterns by producing a 3D topography in a thin resist film. Such pattern contrast can be obtained either by embossing a thermoplastic resist at an elevated temperature (T-NIL) or by curing with UV a resist precursor at room temperature (UV-NIL). In order to achieve high resolution pattern over wafer-scale area, applying a uniform pressure is a key parameter. After imprinting to maintain both feature size and pattern shape, pattern transfer by etching is a key step that has to be optimized. The ability

of each etching step to properly transfer patterns (IBE or RIE) will be discussed below.

Master inversion by using T-NIL

Pillars and lines arrays of different sizes and periods ranging from 70 nm to 1 μm have been selected as test structures to investigate the replication performances of T-NIL.

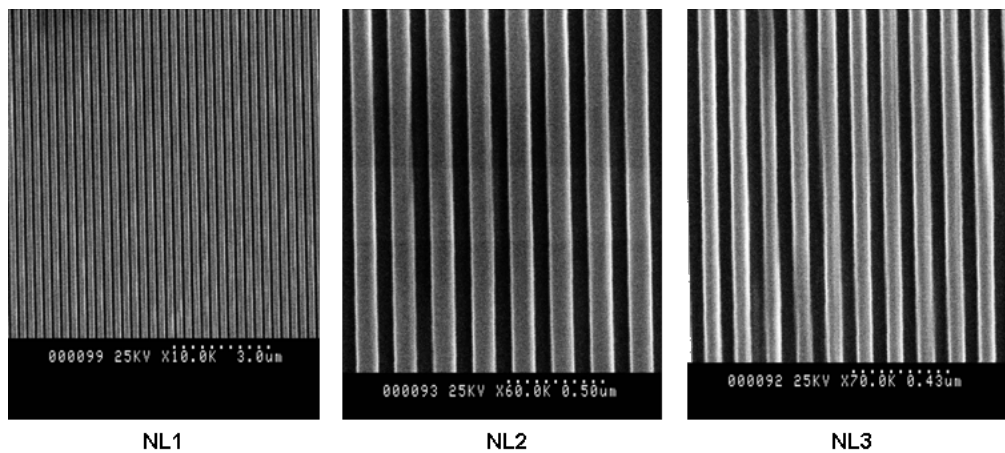


Figure 2.10: SEM images of nanoline gratings with different linewidth: NL1: 100 nm, NL2: 70 nm, NL3: 50 nm after thermal nanoimprint lithography, reactive ion etching of the residual resist.

Typical results after T-NIL and both RIE and IBE are presented in Fig. 2.11 and Fig. 2.10. SEM images of Fig. 2.11 show respectively nanohole arrays of 100 nm, 80 nm and 50 nm and corresponding Si master for direct comparison. Figure 2.10 presents the line gratings with a linewidth of 100 nm, 70 nm and 50 nm. These results show clearly the ability of the process to reach resolution to 100 nm. However, for feature size smaller than 100 nm, even if the general shape is maintained, the pattern size can be affected. As shown in 2.11 and 2.10, the shape of the 100 nm wide structures is similar as the master one, even if a small broadening is observed. Lines even at small width don't exhibit significant lateral defects. However, for the smaller nanoholes with diameter of 70 nm and below, defects appear and the general squared shape of the hole is not well preserved as it can be seen in Fig. 2.10. To analyze more precisely changes in pattern width (or diameter), these SEM images have been analyzed using the "Image J" software that extracts contrast and pattern outline.

The feature size distribution can thus be calculated from the listed area distribution. Table 2.2 gives the different mean feature size values recorded on both Si master fabricated by EBL and the daughter inverted Si mold. An average broadening of 20 nm is observed for patterns (nanoline and nanohole) with feature size above 70 nm; while for smaller feature (50 nm), the broadening becomes bigger (~ 30 nm).

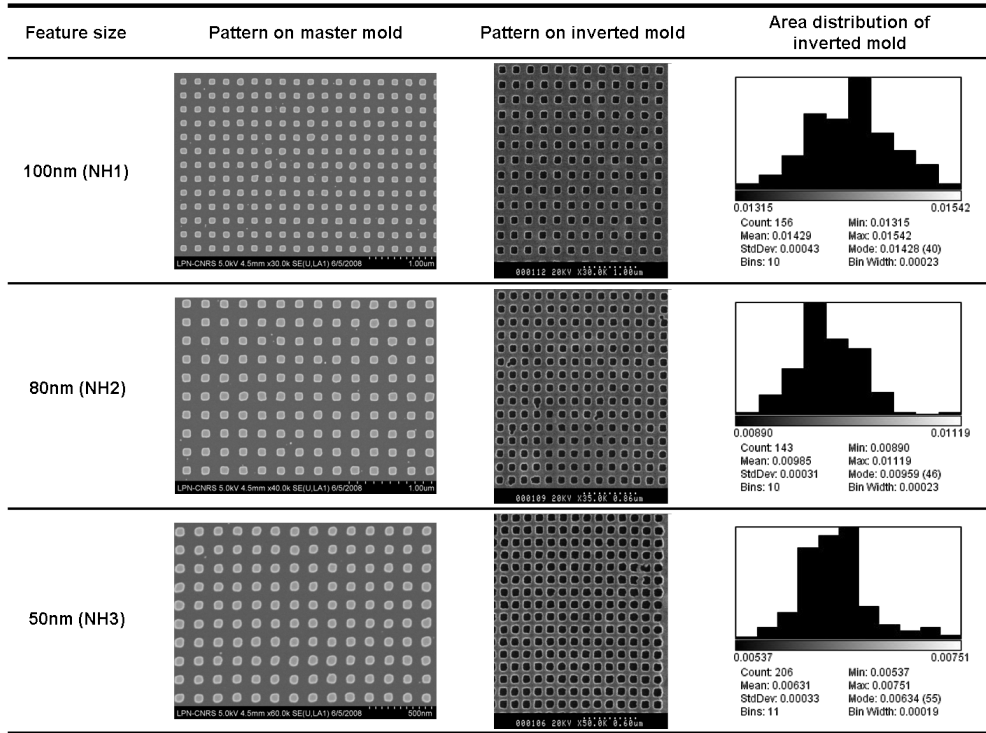


Figure 2.11: SEM images for nano square dots gratings with different diameter on the Si master, gold nanoholes arrays with different diameters after thermal nanoimprint lithography, reactive ion etching of the residual resist and ion beam etching for inversed replicating patterns of the Si master and the area distribution of the inversed replicated mold.

This broadening originates from a loss of etch resistance of the NXR-1020 mask resist during Ar IBE at high energy. If the first oxygen RIE step for residual layer removal of NXR1020 doesn't affect feature size, the IBE transfer of the resist pattern inside the intermediate Au layer is more critical. Thus, in order to minimize the loss of etch resistance of NXR-1020, it would have be possible to both decrease NXR-1020 and Au thicknesses to reduce more IBE etching time. Finally, for this step 1, the IBE etching resistance of the NXR-1020 resist has thus to be improved in the future to avoid any size broadening.

Nanopatterns	NH1	NH2	NH3	NL1	NL2	NL3
Pattern size on the master (nm)	100	80	50	100	70	50
Pattern size on the inverted mold (nm)	120±4	102±5	80±6	120±2	90±5	80±5

Table 2.2: Summarized results of feature size (for nanohole array the dimension refers to the diameter and for nanoline array the dimension refers to the width). The first table line gives dimensions on the Si master mold and the second line gives dimensions measured on the inverted mold fabricated by T-NIL and IBE.

We have also applied this T-NIL inversion process to field as large as 1.5 cm² for 200nm-wide pillar arrays and for 150nm-wide line arrays. For these dimensions higher than 100 nm, the inverted replication worked more successfully in faithfully keeping the profile and dimension. Figure 2.12 shows images of 2 inches silicon inverted replication molds (daughter molds). The first one has been patterned on 1 cm² field with 200nm-wide holes arrays (top) and the second one exhibit a 1.5 cm² patterned area with 150 nm - wide line arrays (down). A good homogeneity and uniformity can be observed over the whole imprint field up to 1.5 cm². SEM images also show that a good uniformity can be obtained on the whole large field without noticeable variation in critical dimension, sidewall roughness. This turns out that larger than 100 nm patterns can be replicated with a well controlled process and then be transferred into the substrate by direct etching.

Soft UV-NIL imprint and transfer

In order to test pattern shape and feature dimension control of the inverted daughter silicon molds, bi-layer hard PDMS/PDMS flexible stamps have been used. Fig. 2.13(a) shows the fabrication sequence with the soft h-PDMS/PDMS stamp replicated from the daughter mold by using soft UV-NIL. Soft UV-NIL has been performed in the Amonil/Ge/PMMA tri-layer stack. Note that the hard bi-layer h-PDMS/PDMS stamps used in this study can guaranty a good contact between mold and the substrate, thus producing a homogeneous replication on the whole large area. After the three RIE steps and the metallic lift-off, we obtain similar nanostructures than those on the initial EBL master mold. Figure 2.13(b) shows the tilted SEM images of both nanopillars and nanolines gratings with different feature size. We observed a small widening of both the pillars and lines,

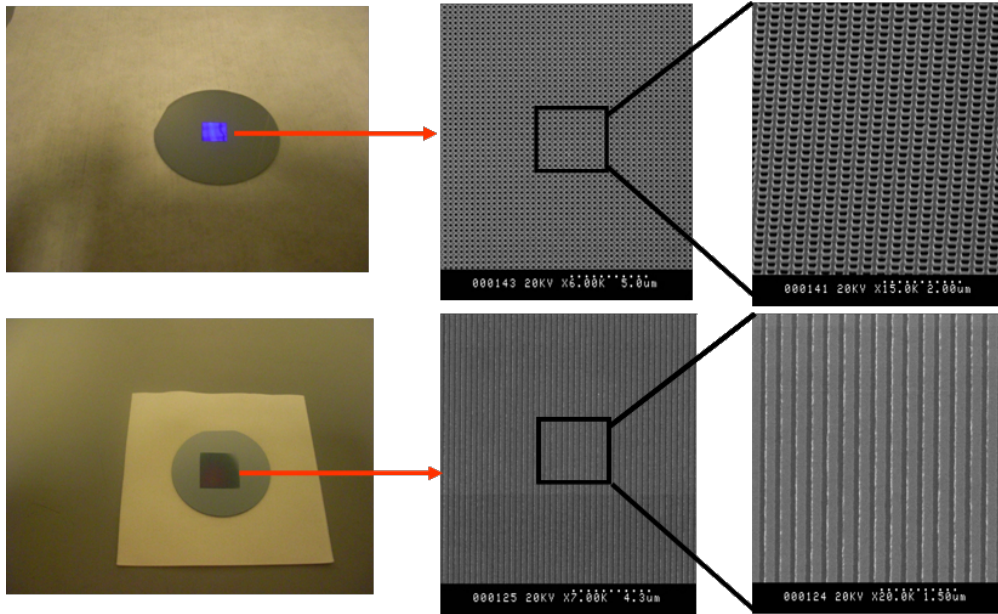


Figure 2.12: Images of 2 inches Si inverted replication molds (daughter molds) with (top) a 1 cm^2 hole array ($d = 200/p = 400 \text{ nm}$) and (bottom) a 1.5 cm^2 line array ($d = 150/p = 300 \text{ nm}$) fabricated based on thermal NIL and IBE.

which can be minimized to 10nm by optimizing the parameters of three continuous etching steps as follows: (1) removal of the Amonil residual layer inside the nanopatterns with O_2 and CHF_3 mixture at a 40 nm/min etching speed, (2) etching of the thin Ge layer using SF_6 plasma and finally (3) O_2 plasma etching of the thick PMMA underlayer. If the first Amonil etching step (1) has to be well optimized to get faithful pattern profile compared with the original pattern, the last PMMA etching step (3) allows perfect control of the feature size.

Finally, the verticality of the pattern profiles observed on the SEM images of the grand-daughter Si mold (Figure 2.13) proves that this inversion process based on several etching steps is sufficiently controlled in terms of anisotropy.

2.5 Conclusion

Both rigid master mold and soft stamp are the key elements in soft UV nanoimprint lithography since they carry the pattern on their surface, thus playing a fundamental role for high resolution patterning. We started

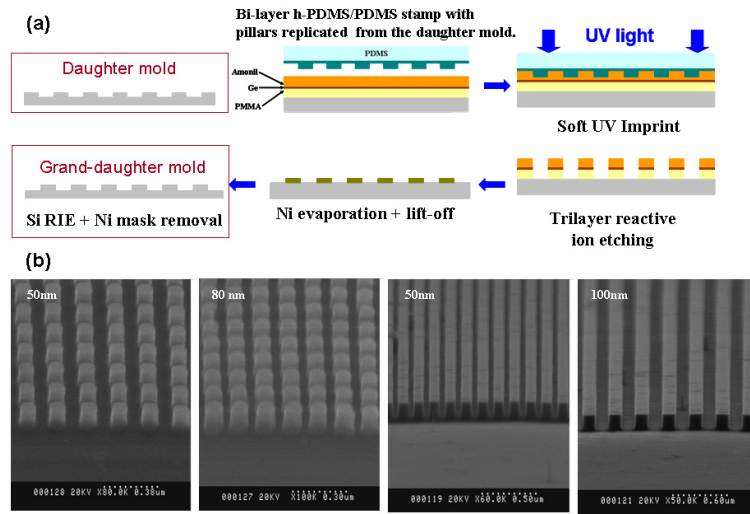


Figure 2.13: (a) Schematics of the soft UV nanoimprint process and (b) SEM images of the grand-daughter mold with different diameter pillars and linewidth line gratings based on the proceeding fabrication procedure: soft UV-NIL with the h-PDMS/PDMS bi-layer stamp obtained from the Si daughter mold patterned with 200 nm-wide nanohole arrays, tri-layer etching, lift-off and transferred into Si.

from the fabrication of master mold and two different positive electron beam resists have been presented. For the replication of the patterned relief structures from the master, two configurations based on soft PDMS elastomeric stamp have been studied (basic PDMS stamps and improved bi-layer stamp). If resolution down to 100-200 nm can be achieved with the basic PDMS stamp, when the feature size is smaller than 100 nm, other strategy based on h-PDMS/PDMS bi-layer flexible stamp have been successfully proposed. All the NIL experiments performed in the following chapter are mainly based on h-PDMS/PDMS stamps.

Finally, a mold pattern inversion method based on thermal nanoimprint lithography (T-NIL) associated with lift-off and direct etching has been proposed for the fabrication of sub-100nm nanostructures. Two successive mold inversions have been realized at the whole wafer scale. The good shape homogeneity and size uniformity of the replicated nanostructures over field as large as 1.5cm^2 proves that this low cost whole fabrication process appears as a reliable technique for replicating and inverting expensive EBL master molds.

Bibliography

- [1] I. Haller, M. Hatzakis, R. Srinivasan. High-resolution positive resists for electron-beam exposure. *IBM Journal of Research and Development.*, **12**:251, (1968).
- [2] D. J. Resnick, T. C. Bailey, W. J. Dauksher, D. Mancini, K. J. Nordquist, E. Ainley, K. Gehoski, J. H. Baker, S. Johnson, M. Meissl, S. V. Sreenivasan, J. G. Ekerdt and C. G. Willson. High resolution templates for step and flash imprint lithography. *Proc. SPIE.*, **4688**:205, (2002).
- [3] D. A. Czaplewski, D. R. Tallant, G. A. Patrizi, J.R. Wendt and Bertha Montoya. Improved etch resistance of ZEP 520A in reactive ion etching through heat and ultraviolet light treatment. *J. Vac. Sci. Technol. B*, **27**:581, (2009).
- [4] N. Gadegaard and D. McCloy. Direct stamp fabrication for NIL and hot embossing using HSQ. *Microelectronic Engineering*, **84**:2785, (2007).
- [5] C. -C. Yang and W. -C. Chen. The structures and properties of hydrogen silsesquioxane (HSQ) films produced by thermal curing. *J. Mater. Chem*, **12**:1138, (2002).
- [6] NIL Technology: <http://www.nilt.com>.
- [7] L. J. Guo. Nanoimprint lithography: methods and requirements. *Adv. Mater.*, **19**:495, (2007).
- [8] D. Posognano, S. D'Amone, G. Gigli and R. Cingolani. Rigid organic molds for nanoimprint lithography by replica of high glass transition temperature polymers. *J. Vac. Sci. Technol. B*, **22**:1759, (2004).
- [9] K. Pfeiffera, M. Finka, G. Ahrensa, G. Gruetznera, F. Reuthera, J. Seekampb, S. Zankovych, C.M. Sotomayor Torres, I. Maximov, M.

- Beck, M. Graczyk, L. Montelius, H. Schulz, H. C. Scheer and F. Steingrueber. Polymer stamps for nanoimprinting. *Microelectron. Eng.*, **61-62**:393, (2002).
- [10] D. Y. Khang, H. Kang, T. I. Kim and H. H. Lee. Low-pressure nanoimprint lithography. *Nano Lett.*, **4**:633 (2004).
- [11] Y. N. Xia, N. Venkateswaran, D. Qin, J. Tien and G. M. Whitesides. Use of electroless silver as the substrate in microcontact printing of alkanethiols and Its application in microfabrication. *Langmuir*, **14**:363, (1998).
- [12] M. A. Unger, H. P. Chou, T. Thorsen, A. Scherer and S. R. Quake. Monolithic microfabricated valves and pumps by multilayer soft lithography. *Science*, **288**:113, (2000).
- [13] K. J. Hsia, Y. Huang, E. Menard, J.-U. Park, W. Zhou, J. Rogers and J. M. Fulton. Nanoimprint lithography: methods and materials requirements. *Appl. Phys. Lett.*, **86**:154106, (2005).
- [14] H. Schmid, H. Biebuyck and B. Michel. Light-coupling masks for lensless, sub-wavelength optical lithography. *Appl. Phys. Lett.*, **72**:2379, (1998).
- [15] M. Liu and Q. F. Chen. Characterization study of bonded and unbonded polydimethylsiloxane aimed for bio-microelectromechanical systems-related applications. *J. Micro/Nanolith. MEMS MOEMS*, **6**:023008, (2007).
- [16] Y. N. Xia and G. M. Whitesides. Soft lithography. *Annu. Rev. Mater. Sci.*, **28**:153, (1998).
- [17] T. T. Truong, R. Lin, S. Jeon, H. H. Lee, J. Maria, A. Gaur, F. Hua, I. Meinel and J. A. Rogers. Soft lithography using acryloxy perfluoropolyether composite stamps. *Langmuir*, **23**:2898, (2007).
- [18] H. Schmid and B. Michel. Siloxane polymers for high-resolution, high-accuracy soft lithography. *Macromolecules*, **33**:3042, (2000).
- [19] K. M. Choi and J. A. Rogers. A photocurable poly(dimethylsiloxane) chemistry designed for soft lithographic molding and printing in the nanometer regime. *J. Am. Chem. Soc.*, **125**:4060, (2003).

- [20] J. Scheirs. *Modern Fluoropolymers*. Jhon Wiley & Sons, Ltd: New York, 435, (1997).
- [21] J. P. Rolland, E. C. Hagberg, G. M. Denison, K. R. Carter and J. M. De Simone. High-resolution soft lithography: enabling materials for nanotechnologies. *Angew. Chem. Int. Ed.*, **43**:5796, (2004).
- [22] SOLVAY SOLEXIS: Functional PFPEs for soft lithography, *SOLVAY S.A*, (2007).
- [23] N. Roos, H. Schulz, M. Fink, K. Pfeiffer, F. Osenberg and H. -C. Scheer. Performance of 4-in. wafer-scale thermoset working stamps in hot embossing lithography. *Proceedings of SPIE-Emerging Lithographic Technologies*, **4688**:232, (2002).
- [24] M. Wissen, N. Bogdanski, R. Jerzy, Z. E. Berrada, M. Fink, F. Reuther, T. Glinsner and H. -C. Scheer. Silanised polymeric working stamps for hot embossing lithography. *Proceedings of SPIE-Emerging Lithographic Technologies VIII*, **5374**:998, (2004).
- [25] T. C. BAILEY, N. A. STACEY, E. R. Engbrecht and J. G. Ekerdt. Release layer comprising diamond-like carbon (DLC) or doped DLC with tunable composition for imprint lithography templates and contact masks. *United States Patent Application Publication*, **No. US 2006/0145398 A1**, (2006).
- [26] K. -J. Byeon, K. -Y. Yang and H. Lee. Thermal imprint lithography using sub-micron sized nickel template with thin SiO₂ layer. *Microelectron. Eng.*, **84**:1003, (2007).
- [27] F. A. Houle, C. T. Rettner, D. C. Miller and R. Sooriyakumaran. Antiadhesion considerations for UV nanoimprint lithography. *Appl. Phys. Lett.*, **90**:213103, (2007).
- [28] L. Tao, S. Ramachandran, C. T. Nelson, M. Lin, L. J. Overzet, M. Goeckner, C. Lee, C. G. Willson, W. Wu and W. Hu. Durable diamond-like carbon templates for UV nanoimprint lithography. *Nanotechnology*, **19**:15302, (2008).
- [29] H. Schiff, S. Saxer, S. Park, C. Padeste, U. Pieves and J. Gobrecht. Controlled co-evaporation of silanes for nanoimprint stamps. *Nanotechnology*, **16**:S171, (2005).

- [30] M. Beck, M. Graczyk, I. Maximov, E. -L. Sarwe, T. G. I. Ling, M. Keil and L. Montelius. Improving stamps for 10 nm level wafer scale nanoimprint lithography. *Microelectron. Eng.*, **61-62**:441, (2002).
- [31] L. Ressler, C. Martin, B. Viallet, J. Grisolia B. Viallet, J. Grisolia and J. -P. Peyrade. Control of micro- an nanopatterns of octadecyltrimethoxysilane monolayers using nanoimprint lithography and atmospheric chemical vapor deposition. *J. Vac. Sci. Technol. B*, **25**:17, (2007).
- [32] G.-Y. Jung, Z. Y. Li, W. Wu, Y. Chen, D. L. Olynick, S. -Y. Wang, W. M. Tong and R. S. Williams. Vapor-phase self-assembled monolayer for improved mold release in nanoimprint lithography. *Langmuir*, **21**:1158, (2005).
- [33] H. S. Nalwa. Nanomaterials and magnetic thin films. *Handbook of thin film materials*, **5**, Academic Press (2002).
- [34] C. Vieu, F. Carcenac, A. Pépin, Y. Chen, M. Mejias, A. Lebib, L. Manin-Ferlazzo, L. Couraud and H. Launois. Electron beam lithography: resolutions limits and applications. *Appl. Surf. Sci.*, **164**:111, (2000)
- [35] X. M. Jiang, Q. Ji, L. L. Ji, A. Chang and K. -N. Leung. Resolution improvement for a maskless microion beam reduction lithography system. *J. Vac. Sci. Technol. B*, **21**:2724, (2003).
- [36] S. Y. Chou, P. R. Krauss and P. J. Renstrom. Imprint lithography with 25-nanometer resolution. *Science*, **272**:85, (1996).
- [37] N. Khusnatdinov, G. M. Schmid, C. B. Brooks, D. LaBrake, D. J. Resnick, M. W. Hart, K. Gopalakrishnan, R. Shenoy, R. Jih, Y. Zhang, E. Sikorski, M. Beth Rothwell, J. Owens, A. Ford. Minimizing linewidth roughness in Step and Flash Imprint Lithography. *Microelectron. Eng.*, **85**:856, (2008).
- [38] J. Chen, J. Shi, D. Decanini, E. Cambril, Y. Chen, A. M. Haghiri-Gosnet. Gold nanohole arrays for biochemical sensing fabricated by soft UV nanoimprint lithography. *Microelectron. Eng.*, **86**:632, (2009).
- [39] J. Shi, J. Chen, D. Decanini, Y. Chen, A. M. Haghiri-Gosnet. Fabrication of metallic nanocavities by soft UV nanoimprint lithography. *Microelectron. Eng.* **86**:596, (2009).

- [40] Y. Chen and A. Pépin. Nanofabrication: Conventional and nonconventional methods. *Electrophoresis*, **22**:187, (2001).

Chapter 3

Development of soft UV nanoimprint lithography

Soft UV nanoimprint lithography technique is a very promising low-cost nanomanufacturing process that involves two steps. The first step is “imprinting” which relies on deforming a thin UV sensitive polymer layer using a flexible stamp that contains nanostructures and leaving a characteristic pattern in the polymer layer. In order to achieve a reasonable process time and yield in this step, polymer materials with relatively low viscosities have been proposed. In the second “pattern transfer” step, a thin residual layer of the resist left underneath the mold protrusions is removed by an etching process such as reactive ion etching (RIE). This removal of the residual resist layer is important to complete the pattern definition. This process is a UV light irradiation process as opposed to thermal nanoimprint lithography that is based on mechanically deforming the viscous molding material.

The purpose of this chapter is the study of soft UV nanoimprint lithography. First we will give a brief introduction to both the UV imprinting tools and the resists that have been used in this thesis. Then, we will discuss the imprinting process and show the optimization of the different parameters for our commercial imprinter for soft UV-NIL. Finally, we will conclude this chapter by presenting different pattern transfer processes used in combination with soft UV nanoimprint lithography for pattern replication into a substrate.

3.1 The nanoimprint machine

The contact-based nanoimprint lithography, such as thermal nanoimprint and UV-nanoimprint, is a highly dynamic process where the vertical sinking movement of a stamp is transformed into a 3D flow with large lateral flow components. To achieve nanoimprinting process, nanoimprint lithography equipment needs a precise pressing mechanism with specific requirements on mechanical stiffness, uniformity and homogeneity over large areas [1, 2, 3]. Meanwhile, it should also adapt to local variations of pressure and temperature because of the imperfections and tolerances in stamps and substrates. Concerning those demands, an imprint machine must have required some multi-functional parts including imprinting head, self-alignment wafer stage, overlay and alignment system for multi-layer process, and anti-vibration parts, etc.

According to increase in demand for nanoimprint lithography techniques, a number of imprint tool manufacturers such as Molecular Imprints, EVG, Nanonex, Suss MicroTec and Obducat, have been making steady progress in order to fully achieve such requirement [4]. Being the first company to commercialize nanoimprint lithography, Obducat offers both thermal NIL, hot embossing, UV-NIL as well as Obducat's proprietary Simultaneous Thermal and UV imprint process. Molecular Imprint Inc. is developing nanoimprint lithography systems for high resolution 3D pattern replication. They have commercialized a proprietary imprint lithography technology (S-FILTM), which is a room temperature, low pressure and non-contact imprint that has demonstrated sub-20nm resolution. EV Group provides both high volume embossing systems and a complete product line for UV-based nanoimprint lithography including single step UV-imprinting systems and step and repeat large area UV-nanoimprint systems. Suss MicroTec's equipment supports nanoimprinting with thermal and UV, single imprint and step and repeat imprint technologies. With their currently developed "Substrate Conformal Imprint Lithography" technology, Suss MicroTec has very recently demonstrated excellent performances for substrate conformity and pattern fidelity over large areas. Similarly Nanonex showed a tool for sub-10nm resolution replication that integrates a layer-to-layer alignment system. The Nanonex NIL machine is based on a patented technology that is opposed to the traditional solid-plate mechanism with rigid master and wafer holders. This new technology gives many unique advantages over any tool on the market. Their single machine allows performing all forms of nanoimprint processes, including thermal, photocurable and embossing imprinting.

Based on the comparative evaluation of different nanoimprint systems coupled with our specific applications, the LPN laboratory has chosen the NX-2500 imprint machine from Nanonex company. The Nanonex NX-2500 is a multi-level nanoimprinter with imprint capabilities in thermoplastic, photo-curable and embossing. It offers excellent uniformity regardless of backside roughness of substrate and template and can correct waving and bowing of surface. All the tools are computer controlled with user friendly graphic interface (GUI), while the loading and unloading of samples are manual. This machine also eliminates relative lateral shifting between substrate and mold which affects mold lifetime. For thermal nanoimprint, a very small thermal mass ensure rapid heating and cooling, resulting in fast process cycles. For UV nanoimprint, with a high sensitive photocurable resist (NXR2030, Nanonex), sub-10 nm nanostructures could be obtained. This system is also extremely convenient for whole wafer (up to 8") replication. Figure 3.1 shows the imprinter installed in LPN clean room.

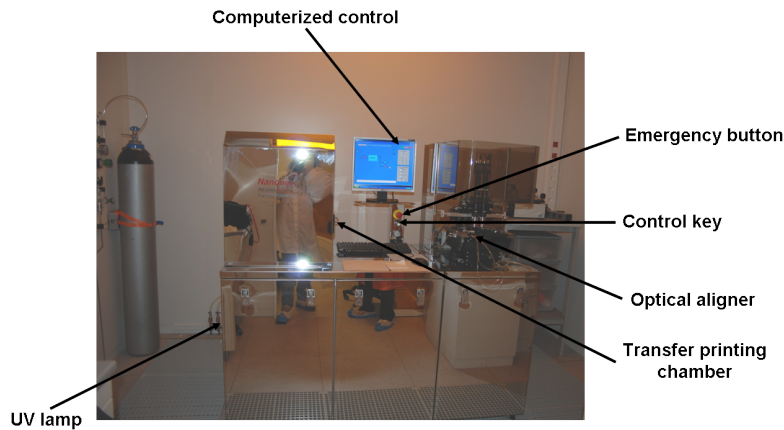


Figure 3.1: Photo of the NX-2500 imprinter installed in LPN clean room.

The description of NX-2500 is listed below:

1. UV source: A narrow band UV lamp (320-390 nm) with a power of 200 W.
2. Pressure and temperature: The system supports the pressure range from 0 to 4 Mpa and the temperature range from 0 to 300°C for thermoplastic imprint module. Both the heating and cooling rate $> 300\text{ }^{\circ}\text{C}/\text{min}$, the imprinting cycle time on the machines is less than 60 seconds.

3. Air Cushion Press (ACP): A novel developed pressing method named ACP of the Nanonex imprinter, which applied air pressure for conformal contact and imprint through the two flexible plastic membrane on both top film ring holder and the wafer holder, Figure 3.2(a)-(c) shows the working chamber and the configuration of mold, sample, membrane. Figure 3.2(d) schematically explains the principle of ACP technology achieving uniform pressure during imprint. Unlike the traditional imprint tools which utilize solid parallel plate press has the inherent problem of relative shift between the mold and the substrate and non uniform pressure distribution, this ACP technology enables conformal contact between mold and substrate and also reduces the influence of dust particles [5, 6].

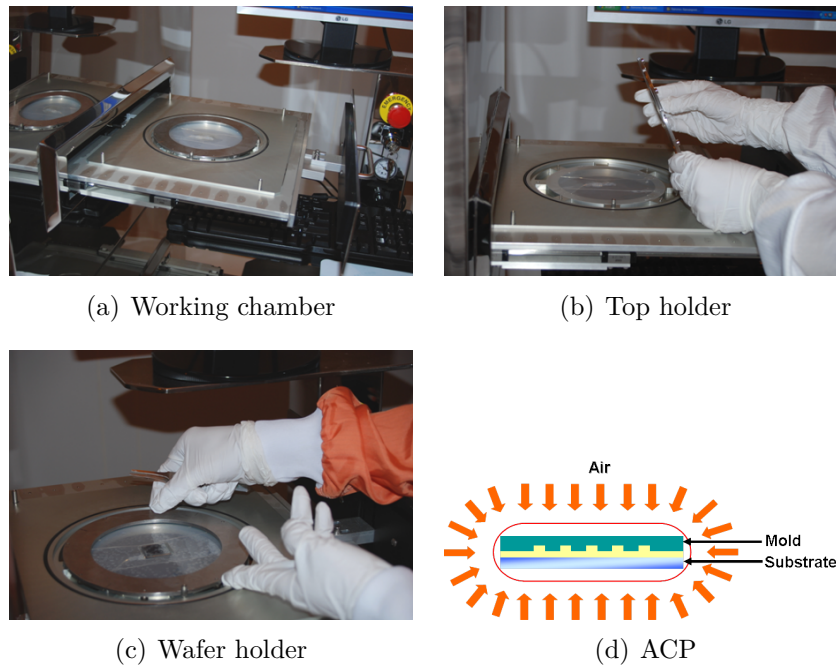


Figure 3.2: (a) Image of the working chamber of the NX-2500 system. (b) and (c) Photos of the drawer on which is top film ring holder and the wafer holder, the mask and wafer is put in the center of the wafer holder, sandwiched between two plastic membrane on both holder. (d) Schematic diagram shows the Air Cushion Press (ACP) offers ultra uniform pressure during imprint.

4. Optical aligner: Figure 3.3 shows both front and side view and features of the optical aligner of the NX-2500 system. Sub 1 um over-layer alignment accuracy was specified with an imprint mold size of up to 4 inch. Instead of applying the imprint pressure mechanically,

this alignment module use gas pressure on the back side of the wafer (or the mold). Spacers with certain value keep to the template enable the template to slide across the wafer during alignment. When two layers are aligned, gas pressure is applied to distort the wafer (or the mold) very gently, just sufficient to press the mold into the resist on the wafer. Such system provides several advantage, for example, there is no mechanical movement after alignment until the end of the imprint process and using gas ensures that the imprint pressure is uniform on the whole imprint area.

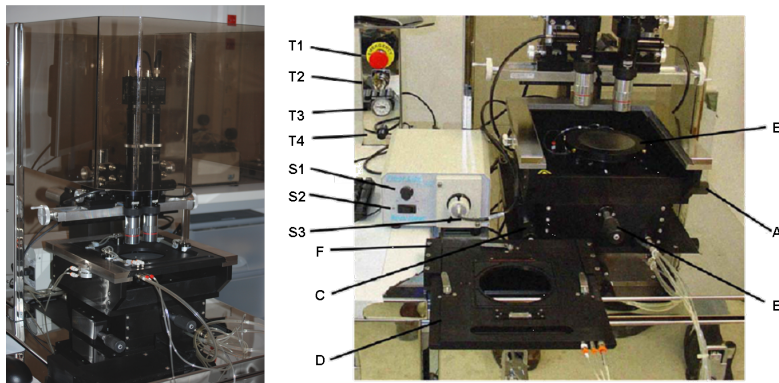


Figure 3.3: Substrate and mask alignment system on NX-2500: A-Wafer stage x-movement, B-Wafer stage y-movement, C-Wafer stage Θ -movement, D-Mask holder, E-Wafer chuck, F-Mask holder seating, T1-Emergency switch, T2-Power on/off, T3-Pin pressure gouge, T4-Pin pressure regulator, S1-Illumination lamp intensity, S2-Illumination lamp power on/off, S3-Illumination fiber.

5. Demolding system: Mold-wafer separation, or so-called demolding after NIL, is one of the unique nature of the nanoimprint lithography process that different from conventional DUV photolithography. The separation process is crucial for any commercial high-volume manufacturing using nanoimprint. For a full-wafer NIL, most demolding processes were done manually and separately from the nanoimprint process because the demolding force could be significantly larger than the vacuuming force between the mold and the substrate and the vacuum chuck holding them. Figure 3.4 presents the accessory parts for mold detachment from nanonex, a needle and razor blade is used for the injecting nitrogen and separating mold/substrate separately inside the system during demolding process. Here the demolding system is specialized for the separation of 4 inch circular molds and substrates.



Figure 3.4: Images of the demolding system.

All the nanopatterns showed in this thesis work were fabricated on the Nanonex NX-2500 imprinter. We are able to precisely control the applied pressure, temperature and UV exposure time, the unique ACP system help us to obtain good imprint homogeneity on the surface, which show great advantage for mold duplication. Besides of the main studying of soft UV nanoimprint, we have also tested with this machine thermal nanoimprint, for which we obtained high resolution patterns with low processing time.

3.2 Soft UV nanoimprint resist

Soft UV nanoimprint lithography is attracting more and more interests as a technique to transfer nanosized patterns without using expensive optical exposure tools. Nevertheless its progress is closely linked to the availability of the suitable resists and polymers which meet all the requirements of this technology. The implementation of NIL will largely depend on the availability of tailor-made polymers and resists. They are a key element on the way to an industrial production in the semiconductor industry.

Resists used for NIL are either used as an intermediate masking layer for the substrate or as a functional layer for a specific application. Typically an imprint resist is a mixture of various polymerizable components, each adding desired characteristics to the final polymeric material. There are four basic components to any UV curable resist systems: monomer, photoinitiator, oligomer and additive.

- Monomers are added to the polymer system for various reasons. The viscosity of the system can be lowered or adjusted by adding monomer. Addition of more low molecular weight monomer can increase the volatility and odor. Monomer addition will slow the cure speed and can increase shelf life. While reducing the amount

of monomer can reduce volume shrinkage and surface stresses. A monomer with a high Si or siloxane content can provide the oxygen-etch resistance needed to transfer the pattern onto the underlying substrate.

- The photoinitiator is the key component linking the UV light source to the polymerization reaction. Anionic photoinitiators generate reactive free radicals which are sensitive to oxygen. Oxygen free atmospheres can help in the depth and degree of cure of this kind of polymer, while oxygen rich atmospheres can increase their shelf life. Cationic photoinitiators generate acids which act as a catalyst and are not sensitive to oxygen. In addition, the cationic polymer can undergo a post-thermal cure, so this type of systems have a much greater depth of cure.
- Oligomers typically exhibit the opposite properties of what was mentioned for the monomers. The backbone of the oligomer may be made up of a variety of polymer types and can control the final properties of the cured polymer.
- Additives can mainly control the final properties of the UV curable systems. They can vary to up to 50% of the system. Additive include pigments, surfactants, dispersants and stabilizers.

3.2.1 Properties of UV-NIL resist

The resolution of UV nanoimprint lithography is limited by the availability of patterns that can be resolved on a mold and the availability of an appropriate UV curing material. This material has to fulfill several requirements such as low viscosity, low adhesion to the mold, good adhesion to the substrate, fast curing times, and high etch resistance to allow pattern transfer into the substrate. To achieve these properties, UV curing resist formulations are usually acrylic based, but vinyl-ether-based or fluorinated-based materials have shown appropriate imprint properties [9, 10].

The selection of the polymer material is the critical part of the imprinting process. Thus resists for soft UV-NIL have to meet several requirements before it can be successfully used as an imprint resist:

- Low viscosity resists was desired during the imprint process for easy flow through the empty channels between the mold and the substrate to yield a uniform film over the entire imprint area and also

significantly influences the necessary imprint force and compression time. Therefore the viscosity of the resist formulation must have low enough viscosity after spin coating at least for a period required to step through the whole wafer and its composition must not change significantly due to evaporation. Currently, both pure organic materials and a mixtures of organic and inorganic components with viscosities in the range between 50 and 200 mPa.s are utilized for UV-NIL [7, 8].

- The resist can be photo-polymerized rapidly to maintain high throughput, and the shrinkage due to polymerization must be minimal.
- Since the major issue in soft UV-NIL approaches is the reproducibility of the printed results, an important prerequisite for reproducibility is to avoid sticking of the resist to the surface of the mold after detachment. So the resist used in soft UV-NIL must adhere to the substrate as strong as possible, be able to release from the imprint template the easier the better, and also have sufficient mechanical properties and integrity in order to avoid feature collapse.
- The composition of the imprint resist has a strong impact on etch rates, selectivity and transferred feature quality. Hence the resists must be thermally stable to common temperatures associated with reactive ion etching, and must possess the high etch selectivity that required to produce high aspect ratio device features.

Often trades-off are needed in order to achieve a good balance between good physiochemical properties and the suitability for the nanoimprint process. There are also some contradictory requirements that are difficult to satisfy simultaneously.

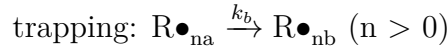
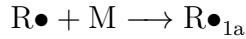
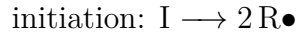
3.2.2 Principles of photopolymerization

Compared with thermal nanoimprint obtaining nanopatterns by embossing a thermoplastic resist with high temperatures and high pressures, UV radiation curing technologies applied in soft UV nanoimprint provide a number of advantages, such as high curing speed that reduces the cycle time, low energy requirements as polymerization proceeds at room temperature, no pattern shift due to the absence of mismatch of the coefficients of thermal expansion of mold and substrate, non-polluting and solvent-free formulations and low cost. They use UV light beams to start photochemical and

chemical reactions in organic materials (monomers, oligomers, polymers), in order to form a new polymeric material.

The photopolymerization reaction proceeds through several well established steps. Radical, cationic and anionic polymerizations can be first initiated by the excitation of suitable photoinitiating systems under the UV light. It then process through initiation of polymerization by charge, energy transfer, or radical reaction; propagation and the termination of the chain.

The functional-group reaction scheme for polymerizations of multifunctional monomers with the formation of trapped radicals is shown below [11, 12]:



In this scheme, I is an initiator, $R\bullet$ is a primary radical, $R\bullet_{1a}$ is a chain initiating radical, $R\bullet_{na}$ and $R\bullet_{nb}$ are active and trapped (buried) radicals with n functional groups reacted, M is a functional group, P_{n+m} is a dead polymer with $(n+m)$ functional groups reacted, k_p is the rate constant for propagation, k_b is the rate constant for radical trapping (burying), and k_t is the rate constant for the termination [11, 12].

In the initiation step, the initiator splits into two primary radicals $R\bullet$, each of which reacts with a functional group to form a chain initiating radical $R\bullet_{1a}$. Propagation consists of the growth of active radicals by the successive addition of functional groups. Finally, the termination reaction can be by combination or by disproportionation, depending upon the monomer used [13].

3.2.3 Viscosity

Specific for soft UV-NIL is the use of low viscosity resists which strongly affects the filling behavior of the liquid resist during the imprint process and significantly influences the necessary imprint force and compression time.

Viscosity (η) which is the most important property used to describe the flow of the resists represents the resistance to flow, and is defined as

$$\eta = \frac{\text{shear stress}}{\text{shear rate}} = \frac{\tau}{\dot{\gamma}} \quad (3.1)$$

and the viscosity of the resists used for soft UV-NIL are typically measured in a rotation rheometer setup.

The most important factor determining the viscosity is the temperature. The temperature dependence of the zero shear viscosity, η_0 , is described by the Vogel-Fulcher law, which has the form [14]

$$\eta_0(T) = B e^{-T_A/(T-T_V)} \quad (3.2)$$

where B is constant, T_A is the activation temperature, and T_V is the Vogel-temperature. From this it can be seen that the zero shear viscosity is strongly dependent on the temperature. Increasing the temperature makes the polymer chain motion easier, since the chains more easily overcome the energy barrier for rotation of the bonds and for breaking the entanglements.

The viscosity not only has a temperature dependence but also depends strongly on the resist's molecular weight [15]:

$$\eta_0 = \begin{cases} M, & M < M_c \\ M^{3.4 \pm 0.2}, & M > M_c \end{cases} \quad (3.3)$$

where M_c is a critical molecular weight of a given polymer. Specifically, a lower molecular weight polymer having lower shear viscosity will tend to fill the mold more readily under given imprinting conditions.

In practice, low molecular weight polymers can be imprinted at lower temperatures, lower pressures or within shorter times. However, the absence of a network of entangled may lead to more brittle behavior and could result in the fracture of the imprinted polymer features during the mold separation step. Hence, choice of both temperature and critical molecular weight is important in keeping pattern structural stability.

3.2.4 Commercial UV-NIL resist

Different enterprises and institutes have made UV-curable materials, such as Nanonex, MII, AMO and Obducat offer their materials adapted to their proprietary process and tool. Nevertheless, there are few publications dealing with UV polymer system for soft UV-NIL, and their properties and characteristics are not known accurately.

In this thesis, two types of UV curable resists have been used: NXR-2010 (Nanonex, America) and Amonil (AMO GmbH, German). Both the technical information and the comparison of each resist is discussed below.

a. NXR 2010 Resist

The NXR-2010 photo-curable resist (Nanonex) which is designed for both sub-10 nm nanostructure engineering and micro- and nano- patterning. NXR-2010 nanoimprint resist offers super low viscosity (0.63 Pa.s) and low curing dosage of 40 mJ/cm² in an oxygen-free environment. NXR-2010 resist can be spin-coated using a standard spinner in an environment with ultraviolet light filtered out. A filter (0.2 μ m) is recommended to use when applying the resist to wafers. The resist film can be prepared up to several hundreds of nanometers in thickness, depending on resist concentration and spin-coating conditions. The spin coating curve of NXR-2010 (3%) is shown in Figure 3.5. The resist solution must be kept in a cool and dark place when not in use. NXR-2010 photo-curable resist is typically

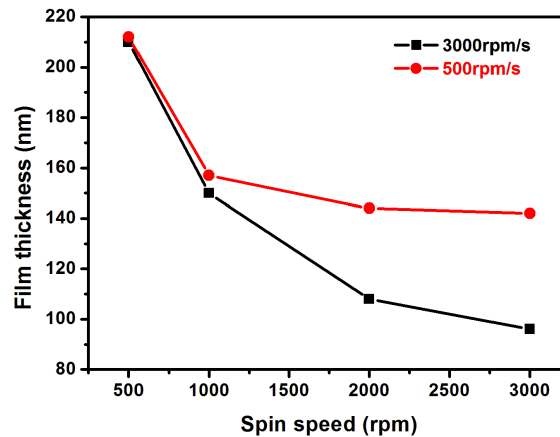


Figure 3.5: Spin curve of NXR-2010 resist at different acceleration (3%).

used with NXR-3010 and NXR-3020 resist, serving as an imaging layer on top. After NXR-2010 resist is deformed by a mold with patterns, the resist is cross-linked using UV light (200-400 nm wavelength), transferring patterns on the mold to the resist with high resolution and in excellent fidelity. NXR-2010 resist can be etched with CHF₃ and O₂ with a speed of 16 nm/min under the condition: 30 w RF power, 30 mtorr pressure and 2 sccm O₂ and 20 sccm CHF₃, and possesses a selectivity of larger than 10

to NXR-3020 resist in oxygen plasma.

b. Amonil resist

Amonil UV curable resist is a commercial resist developed by AMO GmbH (Germany). The composite materials of Amonil are nearly the same as Laromer based photo curable resist which is composed by monomer LR-8765 and photo curable agent Irgacure 369, diluted in 2-Isopropoxyethanol solvent [16]. They include the monomer and photo curable agent designed for UV-curing at 365 nm wavelength. The exposure dose is 2 J/cm^2 . The available thickness could reach at 100 nm by spin coating. The capability for step-repeat cycles more than 1000 imprints have also been demonstrated [17].

For our experiments, two commercially available resists (MMS4 and MSS 10) proposed by AMO GmbH have been tested. The spin curves of the two resist are presented in Fig. 3.6. Compared with MMS4, Amonil MMS 10 has lower viscosity, thus thinner resist layer can be obtained.

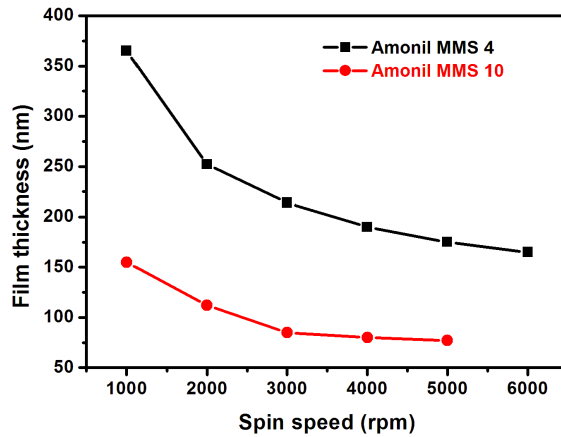


Figure 3.6: Spin coating curves of two types Amonil resist.

In summary, Amonil resist is a methacrylate based imprint material. It offers resist interface for good anti-sticking performance due to included anti-sticking compounds. Nevertheless, as the soft PDMS mold was treated with TMCS before the first imprint, no mold surface treatment was performed every time before imprint. The NXR 2010 resist is expensive but it offers excellent flow properties, high photo-sensitivity, excellent thermal stability and high etch resistance in plasma, which makes it ideal for

UV-NIL applications. Both Amonil resist and NXR resist exhibit good performance for resolution and etching resistance. In our experiments, Amonil resist has been mostly adopted, since NXR 2010 resist can only be preserved for one month.

3.3 Soft UV nanoimprint process

To become a reliable and controllable process, one should find the optimal processing parameters for soft UV-NIL, such as imprint time, protrusion height, initial polymer film thickness, temperature and pressure. Therefore it's essential to understand the physical phenomena involved in the NIL process.

3.3.1 Theory of imprint behavior

Within this part two approaches to understand the rheologic aspects of the mold-filling process will be presented: (1) fluid mechanics and (2) stamp geometry.

a. Fluid mechanics during imprint

Navier-Stokes equation

Fluid mechanics is describe by Navier-Stokes equations which arise from applying Newton's second law to fluid motion. Newton's second law is expressed as:

$$m\dot{v} = \sum_i F_i \quad (3.4)$$

Considering a unit volume, the above Newton's second law equations is rewritten as:

$$\rho\dot{v} = \frac{1}{V} \sum_i F_i = \sum_i f_i \quad (3.5)$$

where f_i is an effective density of force from the force F_i acting on the volume V . Through the application of the chain rule to acceleration, the time derivative of the velocity vector is given by:

$$\dot{v} = \frac{\partial v}{\partial t} + (v \cdot \nabla)v \quad (3.6)$$

where the rightmost term enclosed in parentheses originates from the time dependence of the position vector to a fluid particle. Term $\frac{\partial v}{\partial t}$ represents

changes at a point with respect to time, whereas the second term gives the changes of a quantity with respect to position. By examining the force acting on a volume element dV , there are three types of forces that can act on this fluid element: body forces, pressure gradient forces and viscous forces due to velocity gradients in the fluid. From the definition of the stress tensor, $\sigma = -p + \tau$, then the sum of all the forces per unit volume is given by

$$\begin{aligned}\sum_i f_i &= f_{body} + \nabla \cdot \sigma \\ &= f_{body} + \sum_j \nabla_j \sigma_{ij}\end{aligned}\quad (3.7)$$

The elements in the stress tensor, σ_{ij} is given by

$$\sigma_{ij} = -p\delta_{ij} + \eta(\nabla_i v_j + \nabla_j v_i - \frac{2}{3}\nabla \cdot v\delta_{ij}) \quad (3.8)$$

where the first term is the pressure contribution along the coordinate axis, the second and the third term are the viscous contribution due to velocity gradient, and the last term are tensile stress from compressible fluid.

The Navier-Stokes equation is obtained by combining Eqs. (3.5), (3.6), (3.7) and (3.8):

$$\rho\left(\frac{\partial v}{\partial t} + (v \cdot \nabla)v\right) = -\nabla p + \eta\nabla^2 + \frac{1}{3}\eta\nabla(v \cdot \nabla) + f_{body} \quad (3.9)$$

where ∇ is the flow velocity, ρ is the fluid density, p is the pressure and f_{body} represents body force acting on the fluid.

As can be seen the Navier-Stokes equations are too complicated to be solved in a closed form. Thus, based on some assumptions the equation can be simplified to linear equation:

- Incompressible fluid $\nabla \cdot v = 0$.
- All body force can be neglected.
- Steady flow which means set all changes of fluid properties with time to zero.

$$\nabla p = \eta\nabla^2 v \quad (3.10)$$

Therefore, the viscous force balance the force from the pressure gradient.

Imprint regimes

The molding stage of soft UV nanoimprint lithography moves polymer around from one place to another, which can be characterized on the

basis of the residual resist thickness. Here considering the polymer flow during imprint of a circular shaped protrusion into a polymer film, a few assumptions are made to simplify the situation on how polymer flow during imprint: (1) the mold is round with a radius R much larger than the circular structures with radius r ($R \gg r$); (2) the contact between the surface of the mold and the substrate is parallel; (3) no surface waviness of both the mold and substrate (4) surface tensions and capillary forces are neglected and (5) the polymer during imprint as a non-compressible Newtonian liquid is regarded.

The equation of resist residual thickness (h_r) can be derived based on the above Navier-Stocks equations under these assumptions:

$$h_r = \begin{cases} \sqrt[3]{n \cdot \frac{3\pi\eta\mu r^4}{4F}}, & \text{if } F \leq F_1 \\ h_i - \frac{1}{1 + A_e/A_r} \cdot h_m, & \text{if } F_1 \leq F \leq F_2 \\ \sqrt[3]{\frac{3\pi\eta\mu R^4}{4F}}, & \text{if } F \geq F_2 \end{cases} \quad (3.11)$$

where

$$F_1 = n \cdot \frac{3\pi\eta\mu r^4}{4\left(h_i - \frac{1}{1 + A_c/A_r} \cdot h_m\right)^3} \quad (3.12)$$

and

$$F_2 = \frac{3\pi\eta\mu R^4}{4\left(h_i - \frac{1}{1 + A_c/A_r} \cdot h_m\right)^3} \quad (3.13)$$

where h_i is the initial polymer film thickness, h_m is the depth of features etched into the mold, A_e/A_r is the ratio of the mold covered with protrusions, $\mu = \frac{dh}{dt}$ is the initial imprint speed and η is the viscosity of the polymer liquid.

From Eqs.(3.11) it can be considered that three imprint regimes can be divided during molding process of soft UV nanoimprint lithography (An illustration of this is seen in Fig. 3.7):

- When $F \leq F_1$, the recessed areas on the mold have not yet been completely filled up (incomplete molding regime), so the imprint speed is high in this regime. In this case, h_r depends strongly on the imprint force F and the size of the protrusions on the mold.

- When $F_1 \leq F \leq F_2$, the cavities are completely filled but no polymer is pushed out of the sides of the mold, thus the imprint speed decrease and when all the mold cavities are filled, the imprint will essentially stop. In this regime (Optimal molding regime), the residual resist thickness depends only on the initial film thickness and the geometry of the mold. On condition that neglect the change in volume of the polymer, the conservation of matter can be expressed by a relationship $h_i = h_r + fh_m$, where $f = \frac{A_r}{A}$, A_r and A being the etched total cavity area and total mold area separately. This equation represents the condition for an optimal imprint.
- When $F \geq F_2$, the force is great enough to depress the mold further, consequently, the polymer under the mold is forced to flow outside of the mold. The minimum force required for this further depression of the mold is given by F_2 , and the residual polymer thickness depends strongly on the mold radius R and the force F .

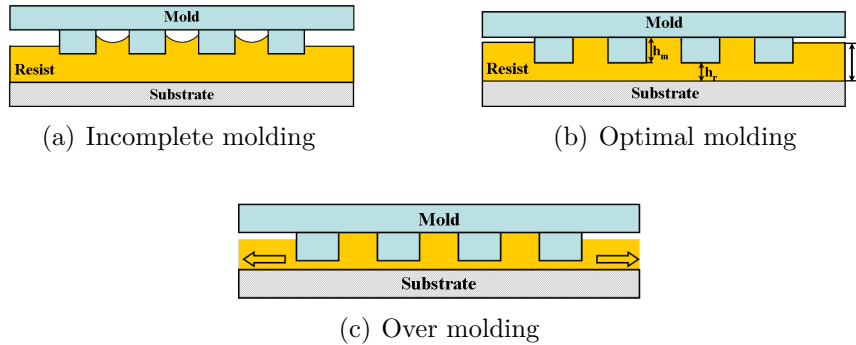
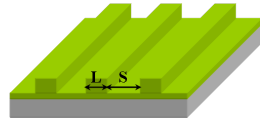


Figure 3.7: The schematics of three imprint regimes.

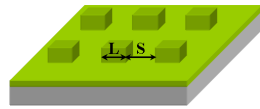
b. Stamp geometry

Besides the polymer flow, the influence of the stamp geometry on the imprinted pattern is also important to soft UV-NIL. In order to work in the optimal molding regime for totally filling of mold cavities, the right relationship must be found between the depth of the mold features h_m , the initial thickness of the polymer h_i and the residual thickness of those features that have been cleared out h_r . In the case of periodic structures, $h_i = h_r + fh_m$ can be used to calculate the thickness of residual thickness, therefore to optimize the initial polymer.

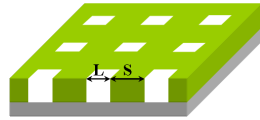
The factor f can be thus calculated in the case of lines, dots and holes arrays in the polymer, as shown in Fig. 3.8:



$$f = \frac{1}{1 + S/L}$$



$$f = \frac{L^2}{(L + S)^2}$$



$$f = 1 - \frac{L^2}{(L + S)^2}$$

Figure 3.8: schematic illustrations of calculated factor f in the case of periodic lines, dots and holes arrays.

It's clear that the initial thickness of polymer depends sensitively on the type of pattern to be imprinted. Hence, for arrays with different dimensions or different geometries, we must choose the greatest value of f for a perfect imprint. Moreover, it's preferred to distribute the protrusions homogeneously over the whole surface to keep the spacing large enough to facilitate the polymer local motion.

Table 3.1 listed the designed patterns and dimension together with the etch depth for four major master molds fabricated by EBL in this thesis work, among which mold 1 and mold 2 is for SPR application in chapter 4 and chapter 5 respectively and mold 3 and mold 4 is mainly applied for imprint test.

3.3.2 Imprint process sequence

The basic soft UV-NIL process are shown in Fig.3.9 which includes two steps: first, patterns are imprinted by pressing a mold on the resist layer; second, the resist relief pattern imprinted into the resist is treated by reactive ion etching until its recessed areas are fully removed (removal of the residual resist layer).

To realize soft UV-NIL, we need first a master mold and its replicated soft PDMS stamp. Once the master mold is ready and has been anti-sticking treated, the basic or improved PDMS stamp is then fabricated

Mold number	Mold pattern	Dimension (L/S)	Height (h_m)
Mold 1	Nanodots arrays	100/100 nm	130 nm
		200/200 nm	
		250/250 nm	
		300/300 nm	
Mold 2	1cm ² Nanolines arrays	150 nm (Note)	130 nm
		100 nm (Note)	
		50 nm (Note)	
Mold 3	Nanodots and nanolines	80/80 nm	100 nm
		100/100 nm	
		200/200 nm	
		300/300 nm	
		500/500 nm	
		750/750 nm	
Mold 4	1cm ² Nanodots arrays	100/100 nm	100 nm
		1000/1000 nm	

Note: The dimension is the value of difference between outer and inner radius.

Table 3.1: Four major master molds prepared by E-beam lithography and transferred in 2 inch Si wafer.

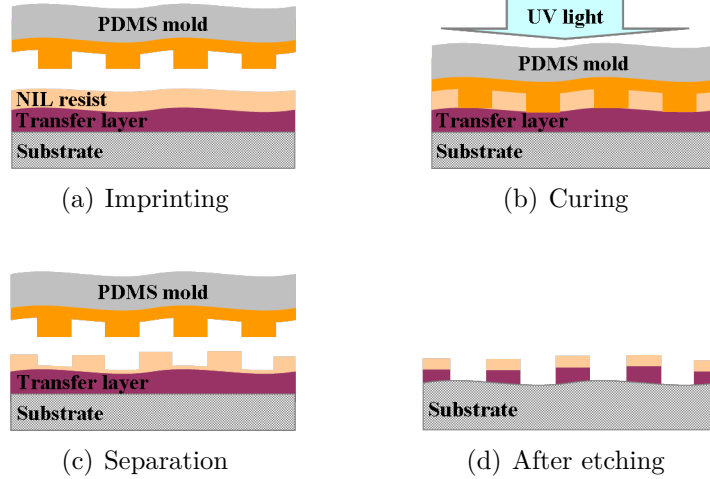


Figure 3.9: Process scheme of soft UV nanoimprint.

according to the feature size. After TMCS anti-sticking treatment, the soft replicated stamp should be kept inside a clean box to avoid dust pollution. Meanwhile, the substrate chosen to use should also be carefully cleaned, since any dust on both surface of substrate and soft stamp will introduce defects into the final pattern.

The cleaning of stamp is either washing in isopropanol or using scotch tape before every imprint. It was chosen to use silicon or thin glass slide as substrate in our experiment, so the process sequence for substrate preparation is given below:

- For silicon substrates: First, pre-wash it in acetone solvent within ultrasonic bath for 5 mins; thereafter immerse it into trichloroethylene at 80 °C for 5 mins on a hotplate; followed by isopropanol, blown dry in high purity nitrogen gas and baked on the hot plate at 180 °C for 10 min to make sure that the solvent has been fully dried out. This treatment was found to improve the wet ability of the polymer films on the wafers.
- For glass substrates: First, pre-wash it in acetone solvent within ultrasonic bath for 5 min to clean big dust particles; second, rinse it in deionized (DI) water for at least 5 min to ensure fully removal of acetone; third, put the samples in the beaker, and use piranha ($\text{H}_2\text{SO}_4:\text{H}_2\text{O}_2=5:1$) cleaning for 30 mins to remove all organics; when the piranha clean is completed, rinse the sample in DI for 5 mins; finally blow them dry with the N_2 gun, after getting most of the water off, dry the samples more on a hotplate at 180 °C for 10 min.

Afterward, a bottom layer of thermoplastic resist (PMMA or NXR-3020) is first spin coated on the substrate and pre-baked at 180 °C for 1 min (for NXR-3020 resist, pre-bake at 100 °C for 30 min in a vacuum oven) to completely evaporate solvent. This layer is used as the transfer layer for obtaining resist patterns with high aspect ratio and consequently to facilitate the metal lift off used for the pattern transfer into substrate. The UV-curable photosensitive resist with low viscosity is then spin coated over the bottom layer (Figure 3.9(a)). Subsequently, the soft stamp is put slowly into contact with the resist and then both stamp and substrate are placed between the printing membranes inside the NX-2500 machine. Note that contact could be not perfect if some gas bubbles appear between stamp and substrate, but it's forbidden to remove the stamp, before the end of the process and UV resist reticulation. The soft UV-NIL process was carried out at low imprint pressure (≤ 10 psi) that is controlled by the N_2 flow inside the pressure chamber. After applying pressure, a first important waiting time is imposed before starting UV (referred as t_1). The resist is cured by photopolymerization due to UV radiation through the transparent stamp at room temperature (Figure 3.9(b)). The time specified for curing (referred as t_2) depends on the sensitivity of the resist. For Amonil resist,

this time is about 10 min. After curing, stamp is separated from the substrate and a image stays behind (Figure 3.9(c)). Finally, the imprinted patterns and the residual layer and the underlying layer were etched down to substrate to produce the final structure (Figure 3.9(d)).

Nevertheless, before pattern transfer, the imprinted patterns should be inspected by the optical microscope to ascertain if the patterns are well transfer inside the resist layer. Some bad cases can be sometimes observed : (1) if some parts of the pattern is missing, its cause maybe the sticking of resist to the stamp; (2) if no pattern has been imprinted in the resist, the reason maybe that the stamp has been reversely placed (flat surface instead of pattern top surface). To avoid such mistake we made big corner marks on the top surface of the stamp; (3) if there are some distortions of the imprinted features, it means that the imprint process should be adjusted to optimize the resist disturbance.

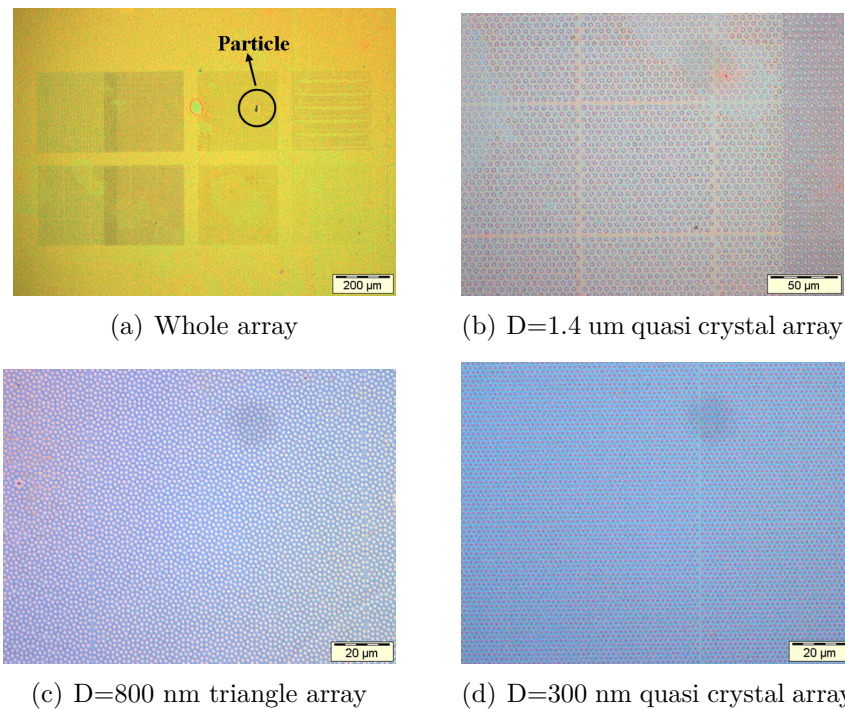


Figure 3.10: Optical micrography of photonic crystal arrays after soft UV nanoimprint.

Figure 3.10(a) shows an optical micrography of two types of photonic crystal (PC) structures with four feature sizes (1.4 μm, 800 nm, 300 nm and 200 nm). In this figure, one array is missing while the other arrays have been well replicated and also a defect caused by a particle on the

mold or substrate surface can be seen on the image. Figure 3.10(b)-(d) show zoomed images of 1.4 μm quasi crystal array, 800 nm triangle array and 200 nm quasi crystal array respectively, it's seen that the transferred patterns are completely replicated from the stamp, but some defects near the border of cavities were found.

3.3.3 Imprint process optimization

The process conditions during the imprint step will directly influence flow behavior, which determines the accuracy of the final geometry of imprinted nanoscale structures. The imprint specific process parameters like UV curing time and pressure have thus to be optimized for each geometry. To introduce soft UV-NIL as a high-resolution and high throughput patterning technique for low cost fabrication of a wide range of functional application, it appears very important to determine these specific imprint parameters. This optimization is the subject of this section.

In our work, a series of test imprints with various pressing time and pressure were performed.

- **Time:** One parameter in soft UV-NIL, the exposure does, may change the shape of the replicated patterns and the value of the demolding force. Generally, the control of the exposure dose can be done by selecting either the light intensity or the exposure time. In our experiments the time duration of UV light exposure is used to control the dose. The experiments are performed at room temperature and the UV time was varied alternatively from 5 min to 15 min. Through the evaluation of the resulted resist pattern, we found that un-precise curing time may induce the resist structure collapse, because changing the curing time will change the modulus or the strength of the resist and the interface. If the curing time is so short that the modulus of the resultant resist is too low, the filled patterns in the resist will be much more adhesive and it is easy to be blurred after being demolded from the mold. Whereas too long a curing time will make the resist obtains excessive modulus, which will damage the mold due to excessive demolding force. So it is necessary to keep the modulus of the exposed resist at a moderate level. According to the adjustment of UV curing time, the converting process from liquid to solid state of resist can be controlled, which is helpful to refill the cavity between nanostructures of mold and resist film caused by press release, and reduce the trend of island like polymerization in

resist surface layer. To summarize our experimental analysis, the optimal times determined for Amonil resist are as follows: prepumping time: 1 min 30 s, processing time t_1 : 2-4 mins, UV time t_2 : 10 mins (here longer processing time could be helpful in case of non perfect contact).

- **Pressure:** The viscosity of the resist primarily determines the choice of the imprint pressure. Due to the low viscosity of the UV resists we used, only low pressure is needed to press the mold into the resist. Table 3.2 shows imprint patterns on Si substrate with increasing pressure of 0 psi, 5 psi, 10 psi, 15 psi, 30 psi and 50 psi (with the optimal UV imprint time as previously mentioned).

1. 0-5 psi: As shown in the second row of table, it's very clear that the pressing force (0-5 psi) didn't satisfy the requirement of resist filling. The result is only partial filling of the recessed areas due to an insufficient amount of material being displaced. Thus the top of the structure isn't flat and the pattern sidewall are not perfect. This is because the loading force is deficient and the thickness of resist film inside the recessed area is not sufficiently reduced. For this low pressure, it is impossible to perfectly transfer resist pattern into the substrate during subsequent etching.

2. 10-15 psi: When the pressing force is increased up to 10-15 psi, as shown in the third row of the table, the top surface of the pattern becomes very flat and the sidewall's collapse is avoided. Replication is perfectly done without any distortion of the patterns from the elastomeric PDMS stamp. For this optimal pressure, the depth of imprint is sufficiently high to ensure a minimized residual resist layer in the recessed areas.

3. 30 psi and 50 psi: At higher pressure between 15 psi to 30 psi, an increase of deformation has been observed, as shown in the fourth row. The width of the feature size becomes enlarged and all the pattern structure is destroyed. Additionally, pattern sidewall is not regular and the thickness of Amonil residual is random. When the pressure reaches 50 psi, the nanostructures are totally distorted because of the low stiffness (2-5 orders of magnitude lower than quartz) the structural integrity of the soft mold is jeopardized. Local as well as global deformation may occur, which limit the resolution of soft UV-NIL. To conclude soft UV-NIL has to be often carried out at moderate pressure, around 10-15 psi.


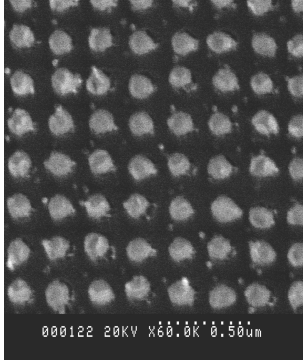

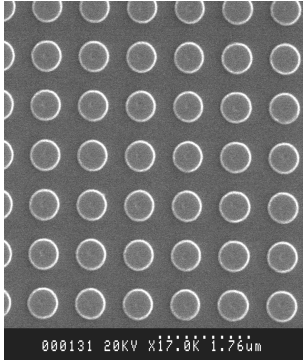

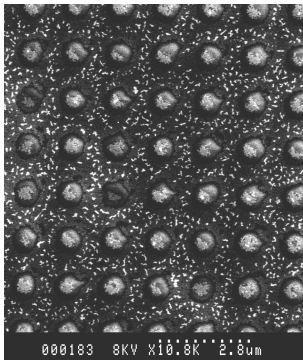

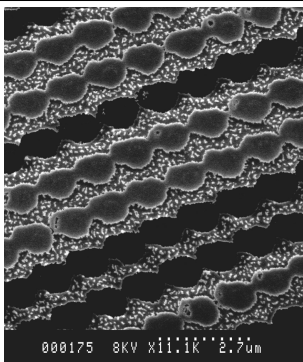
Schematic of stamp deformation	Imprint pressure	SEM image after UV-NIL
 <p data-bbox="373 663 655 696"><i>Incomplete molding</i></p>	0-5 psi	 <p data-bbox="1011 725 1238 741">000122 20KV x60.0K 0.50um</p>
 <p data-bbox="395 1043 635 1077"><i>Optimal molding</i></p>	10-15 psi	 <p data-bbox="1011 1122 1238 1137">000131 20KV x17.0K 1.70um</p>
 <p data-bbox="416 1536 612 1570"><i>Over molding</i></p>	30 psi	 <p data-bbox="1011 1503 1238 1518">000183 8KV x10.0K 2.0um</p>
	50 psi	 <p data-bbox="1011 1883 1238 1899">000175 8KV x11.1K 2.7um</p>

Table 3.2: Schematic illustration of the Amonil resist flow behavior during UV-NIL process by applying different pressure and the corresponding SEM images with nanodot patterns.

Through the analysis of our experimental results, accurately control of pressure is very important to ensure perfect replication of the patterns with fidelity. High pressure can generate distortions of resist patterns during process which is very harmful since the errors will be transferred into final functional structures. When the pressing force is about 10 psi, the patterns look nicely replicated and large aspect ratio can also be guaranteed.

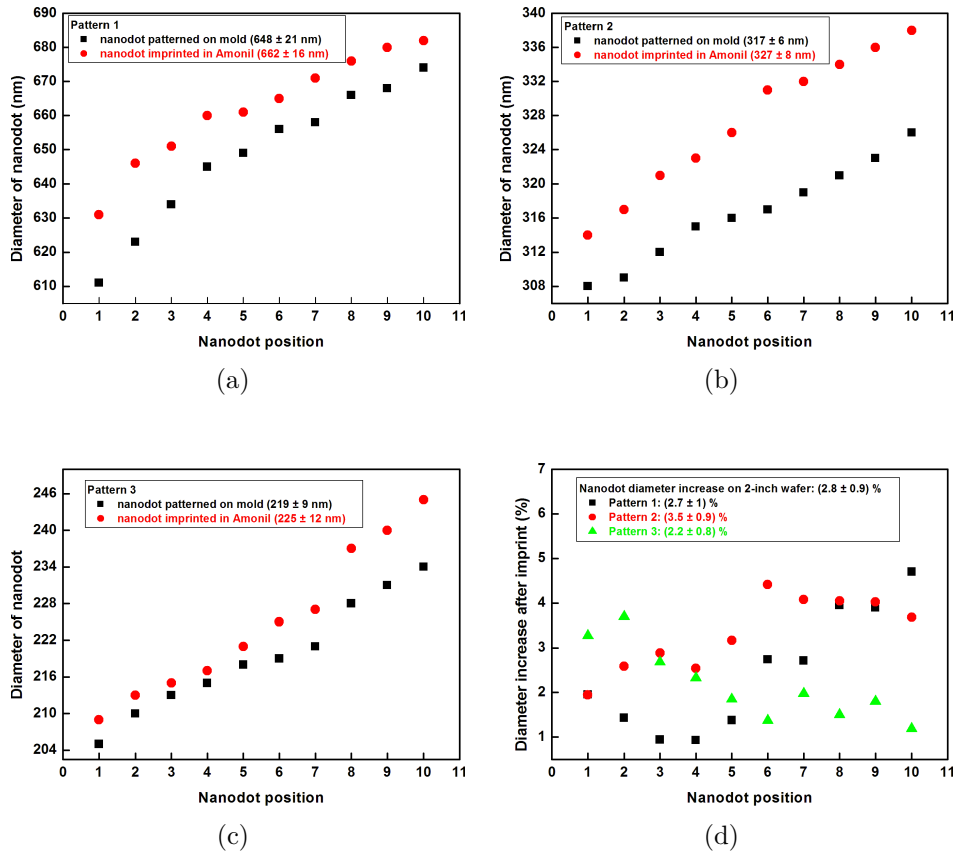


Figure 3.11: (a)-(c) The CD measurement of the mold and the imprinted Amonil in three different patterns and correspondence increase of CD upon imprint in three patterns on scales of percentages.

Here, we also investigated the pattern transfer fidelity of soft UV-NIL on a two-inch wafer scale under this optimum pressure (10 psi). Nanodot patterns with three different dimensions have been chosen for this study. Each pattern is $200 \mu\text{m} \times 200 \mu\text{m}$ in footprint on the wafer. The critical dimension (CD) of the nanodot patterns on the mold and imprinted in resist were measured using an ultrahigh-resolution scanning electron microscopy (Figure 3.11(a)-(c)). Comparison of the measurement (Fig. 3.11(d)) re-

veals that the as-imprinted nanodots in Amonil resist are 2.8% on average larger than those on the mold with a standard deviation of 0.9%. Among the three pattern arrays, the smallest CD increase after imprint occurs in pattern 3 and largest in pattern 2, with an intermediate increase in pattern 1. Compared with photolithography, soft UV-NIL shows a better CD controls. Thus, we choose a pressure of 10 psi for all our replication on both Si substrate and glass substrate (on glass substrate we can increase the pressure up to 30 psi without any problem of distortion).

Finally, we used the parameters that are summarized in table 3.3. This table can be used as a guideline for the reported investigation in this dissertation, even if sometimes parameters are finely adapted to the specific circumstances, such as for example different stamp design.

Imprint pressure	10 psi
Imprint temperature	20 °C
Pumping time	1 min 30 s
Processing time	2-4 min
UV time	10 min in Amonil resist

Table 3.3: Process parameters for UV nanoimprints with Nanonex 2500 machine.

Soft UV-NIL is an excellent method for pattern definition in a polymer, as long as these patterns are periodic, which is the case for a number of advanced high density applications in optics and electronics. When large differences in pattern size or pattern group size have to be imprinted, the material transport inherent to this technique will limit the imprint quality as long as imprint pressure cannot be increased accordingly. Thus, soft UV-NIL will not be the optimal solution for any patterning problem regardless of the specific design. It was found that small and periodic patterns are replicated most easily into the resist.

3.4 Elimination of residual layer

Soft UV-NIL utilizes a multi-layer scheme to pattern the underlying films after the imprinting process. Because of the presence of a thin residual layer over the thick transfer underlayer, it is essential to minimize the thickness of this residual layer in order to perform subsequent pattern transfer with fidelity in both size and profile. Thin residual layers can thus help to transfer the pattern into a substrate with a high-dimensional accuracy.

3.4.1 Optimization initial thickness of Amonil resist

The initial thickness of the resist is related to the residual resist thickness (equation 3.11). Since the minimum initial thickness of resist depends on its viscosity, we estimate that the residual layer thickness can be reduced to a feasible value by using a lower viscosity resist such as Amonil MSS10.

The thickness of the resist coating was carefully calibrated with the spin coating speed. By varying this spin coating speed, we have thus produce resist films with different thicknesses. It becomes possible to determine which thickness will ensure a complete filling of the relief without leaving an excessively thick residual layer.

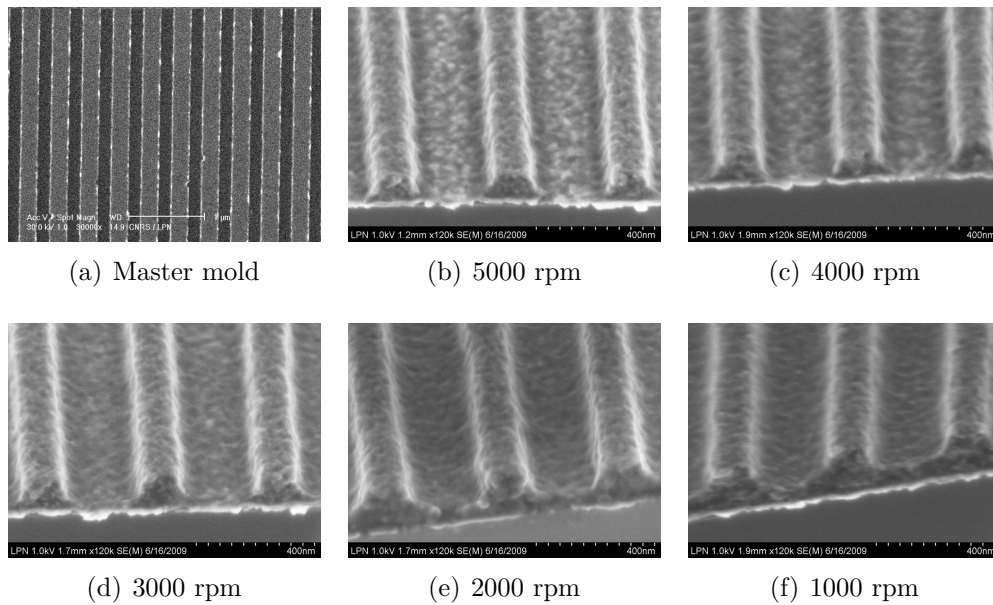


Figure 3.12: SEM images of different residual layer.

Imprints were done into Amonil MSS10 resist with five different film thicknesses corresponding roughly to the five spin speed of 5000 rpm, 4000 rpm, 3000 rpm, 2000 rpm and 1000 rpm, respectively. The imprinting parameters are the same as we described in the previous part: 10 psi pressure, UV imprint 10 mins. A silicon master mold with 220 linewidth/180 nm pitch and 120 nm etch depth grating structure was employed. In the tests, a thin layer of 20 nm Al was first deposited on the Si substrate by e-beam evaporation, followed by Amonil MMS 10 resist spin coated on top (here the adoption of Al layer is for later RIE condition optimization study). After imprint, the samples are observed with electron scanning microscope

(HITACHI S4800).

Fig. 3.12 shows SEM pictures of the mold patterns and the corresponding features printed in the Amonil resist layer with different initial thickness. We find that the residual layer is uniform when the spin speed at 1000 rpm, 2000 rpm and 3000 rpm, while the residual layer start to be discontinuous when the spin speed is higher than 4000 rpm.

Spin speed (rpm)	ACCN (rpm/s)	Time (s)	Total hight (nm)	Hight of residual layer (nm)
5000	2000	30	113	discontinuous
4000	2000	30	108	discontinuous
3000	1000	30	149	28
2000	1000	30	163	70
1000	500	30	202	78

Table 3.4: The effect of imprinted thickness on the residual thickness.

By studying the cross-sectional profile of the periodic nanoline arrays in each SEM image shown in Fig. 3.12, both the total thickness of deformed polymer and residual thickness have been measured after imprint for various initial thickness conditions. Because Amonil is a liquid photoresist and its initial thickness can't be measured directly. Consequently, we have measured and reported here the thickness of the Amonil resist (h_i^*) after UV curing process (performed on a test sample). The initial thickness of Amonil can be caculated by considering the factor of resist shrinkage due to the curing step. Here, we estimated that the shrinkage ratio of Amonil resist after UV exposure is around 10% [18]. The resulted measurements of h_i^* and relevant thickness of residual layer are shown in table 3.4. As the initial thickness of Amonil resist increases, the residual thickness also increases.

These experimental results show that the residual layer thickness could be largely decreased by simply optimizing the initial polymer thickness, which can be achieved by adjusting the spin coating speed. The minimum residual layer thickness achieved for the Amonil MSS10 resist was about 28 nm for a spin coating speed of 3000 rpm (note that these optimal parameters are highlighting with green color in table 3.4). This minimized residual thickness which is close to calculated value (20 nm) is sufficient to perform pattern transfer of nanosized patterns into a substrate.

3.4.2 Optimization RIE conditions of Amonil resist

After the reduction in thickness of the residual layer, its reactive ion etching process has also to be optimized. Obtaining a good critical dimension (CD) control on the substrate requires a very good residual thickness uniformity. Ideally the uniformity of the residual thickness has to be independent of the shape, size, and pattern density. Indeed, the final CD of the patterns is closely related to the residual polymer thickness removal during its etching process.

Moreover, there are other important etch characteristics that also need to be controlled. These include sidewall profile, selectivity, uniformity, and surface damage. In particular, for optical structures like nano gratings, the most critical properties are the smoothness of the sidewalls and the vertical profile. Any irregularities in the surface such as sidewall roughness will enhance optical scattering which leads to optical losses. Sidewall roughness is mainly induced during reactive ion etching (RIE), the most commonly used technique for patterning polymers in plasma. Hence, it is important to understand the effects of etching parameters on both profile and sidewall roughness since both will have an important role on optical properties of the nanostructures. In our work, the residual Amonil resist thickness that remains in the recessed areas is removed as a first step of the subsequent pattern transfer. The optimization of this first etching step plays the most important role for successful pattern transfer, mainly because all the defects resulted in this step will influence the subsequent etching process. In order to define the optimal process conditions, the aim of the present work in this subsection was to get nanostructures with vertical sidewall profile and minimum roughness.

I. Reactive ion etching

The etching process used for pattern transfer generally fall into two categories: wet and dry etching. During wet etching process the material is removed when immersed in a chemical solution. Wet chemical etching is generally isotropic. It's a very simple process with good etch rates. However, due to undercut effects, this technique remains limited for nanometric patterns etching. By contrast, the dry etching method allows perfect control of the selective etching anisotropy.

Reactive ion etching (RIE) is a plasma-based dry etching technique characterized by a combination of physical sputtering with the chemical activity of reactive species, which is most common used dry etching method

to transfer nanometric patterns nowadays. In this approach, materials is removed from a sample surface through bombardment with energetic ions that carve out the surface.

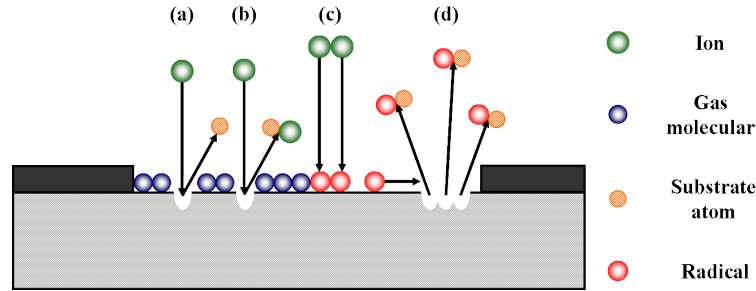


Figure 3.13: Schematic of four RIE process: (a) ion sputtering, (b) reactive etching, (c) radical formation and (d) radical etching.

The RIE process, as schematically shown in Fig. 3.13, is four main processes taken place simultaneously:

1. Ion sputtering: The high energy ion (several tens of eV to several keV) sputter the sample surface in a vacuum environment. At low energy, it helps to remove initially any hydrocarbon contaminants and native oxide layer and thus create a fresh material surface, promoting absorption of gas molecules onto the material surface. Ion sputtering is a purely physical sputtering etching that can also remove material atoms.
2. Reactive etching: If the ions are reactive species, they can directly react with material atoms to form volatile compounds which escape from the sample surface. This process is known as the chemical part of reactive ion etching which is isotropic and similar to the wet chemical etching.
3. Radical formation: The ions can dissociate the absorbed gas molecules to produce radicals on the sample surface which is a combination of both physical and chemical process.
4. Radical etching: The radicals can move around at the sample surface and react with the material surface atoms to form volatile compounds leaving the surface. All the volatile compounds are pumped away, so that no redeposition occurs in the vicinity of etched patterns during the etching process.

In our work, the capacitively coupled plasma reactive ion etching (CCP-RIE) is used for both Amonil residual layer etching and subsequent transferring imprinted pattern into Si or SiO₂ substrate.

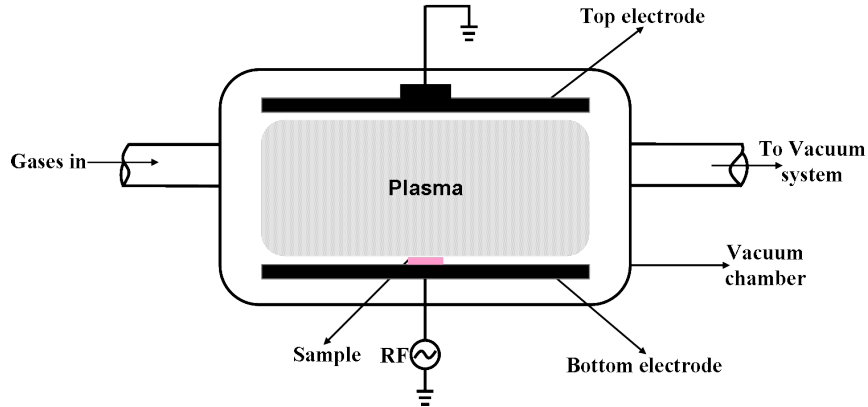


Figure 3.14: Schematic diagram of an reactive ion etching system.

In a CCP-RIE system, plasma is created between two parallel plates by an RF power supply working at 13.56 MHz and applied to the bottom electrode while the top electrode is grounded as is shown exemplarily in Figure 3.14. A glow discharge is used to generate, from a suitable feed gas by dissociation or ionization, the gas phase etching environment that contains radicals, positive and negative ions, electrons and neutrals. Accumulating electrons on the DC-isolated bottom plate create a negative self bias. The self bias exerts an acceleration voltage towards the bottom plate which is directly proportional to the ion density and thus cannot be controlled separately.

In this dissertation, the influence of several RIE process parameters on Amonil resist etching conditions was studied by utilizing Nextral NE100 (GCEMarket, America) parallel plates reactor system.

II. Chemical analysis of Amonil before RIE

FTIR is a non-destructive technique that produces a fingerprint of a sample with absorption peaks corresponding to the frequencies of vibrations between the bonds of the atoms making up the materials. Infrared spectroscopy can give a qualitative analysis of every different kind of material, because of each different material being a unique combination of atoms. Thus, two different compounds never produce the exact same infrared spectrum. Therefore, commercial Fourier transform spectrom-

eter (FTIR, Bruker Equinox 55) was used to characterize the photo-polymerized Amonil resist layer before its exposure to different RIE plasmas. This will give us a basic reference to understand the chemical changes inside Amonil induced by different plasmas. The IR spectrum for Amonil resist after UV curing is given in Fig. 3.15.

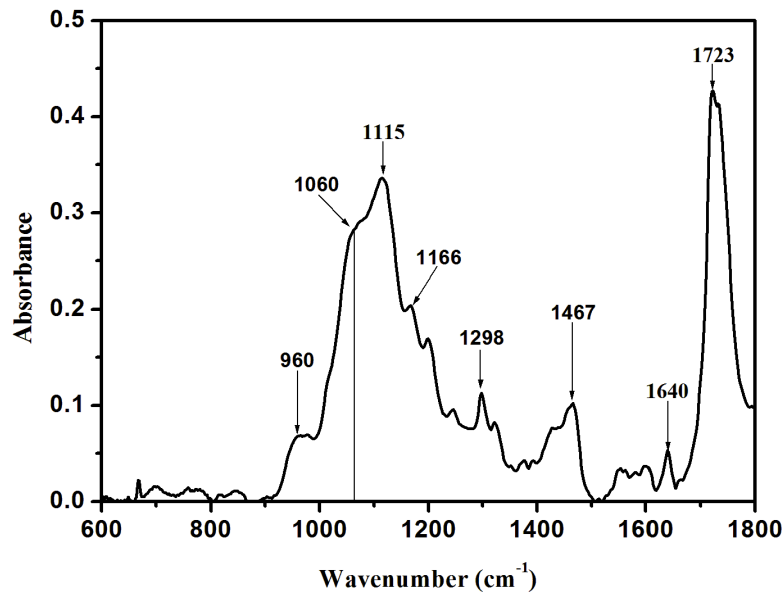


Figure 3.15: FTIR spectra of photo-polymerized Amonil resist.

The functional groups corresponding to the particular frequencies are given in table 3.5. Distinct from conventional optical resist, the Amonil resist used for soft UV-NIL has a different material formulation. We find different chemical functional groups that are: alcohol, ester, ether, methylene and silicone. A certain percentage of Si content renders Amonil interesting in our experiment since the higher the silicon content the higher the selectivity that can be achieved during its etching [19]. The broad band in the region 960 cm^{-1} is due to overlap of Si-O-Si stretching and is associated to aliphatic ether and secondary alcohol stretching.

Although FTIR is a perfect tool for organic analysis, it's difficult for us to obtain quantitative informations of different chemical functional groups here, since the area of the peaks depends strongly on the processing of rough spectra.

Peak location (cm^{-1})	Chemical structures	Motion
960	C=CH	Rocking
1060	Si-O-Si C-O-C and C-O	Stretching
1115	C-O-C and C-O	Associated aliphatic ether and secondary alcohol stretching
1166	C-O-C	Ester asymmetric stretching
1298	O-H	Secondary alcohol deformation
1467	C-H	Deformation
1640	C=C	Stretching
1723	C=O	Ester stretching

Table 3.5: Assignment of major peaks in Amonil.

III. Study of CHF_3/O_2 etching for Amonil

From the chemical analysis mentioned above, Amonil is a mixture of organic and inorganic compounds, the permanent presence of Amonil residual in the ground of nano patterns needs a specific RIE process before the etch of PMMA bottom underlayer. Therefore, based on the previous study [16] in our group and the other empirical results [20], the NXR2 process has been chosen as the first process to get vertical sidewall (parameters of this NXR2 process are listed in table 3.6). In order to define the optimal process conditions, series of experiments were then performed by changing some of our controlled RIE parameters, such as gas flow, RF power (P), chamber pressure (p) and the type of reactant gas used. The different process variables used in these series of CHF_3/O_2 plasma etchings are tabulated in table 3.6.

One master test structure with 220/400 nm (linewidth/period) periodic nanoline arrays has been fabricated in 2 inch silicon wafer using the optimal conditions described in subsection 3.3.3. Before spin coating of Amonil resist, a 20 nm Al film was introduced as a barrier underlayer, so that the influence of each etching process on the Si substrate could be eliminated. Fig 3.16(a) shows a cross-section SEM view of the nanoline test structure obtained just after imprinting in the Amonil resist. Note that the profile of the resist nanolines is vertical. After imprinting, the Amonil residual layer is removed using NXR2 process for 3 mins. The result is shown in Fig. 3.16(b), where the nonvertical rough sidewall is observed (note that the sidewall angle is about 42°).

Process number	Power(W)	Pressure(mTorr)	Gas/flux(sccm)	
			CHF ₃	O ₂
NXR2	25	7	20	2
NXR5	12	7	20	2
NXR6	25	5	20	2
NXR8	25	7	18	4
NXR7	25	7	16	6
NXR17	20	7	16	6
NXR13	12	7	16	6
NXR16	30	7	16	6
NXR10	25	7	8	3
NXR14	25	7	14	8
NXR15	25	7	12	10

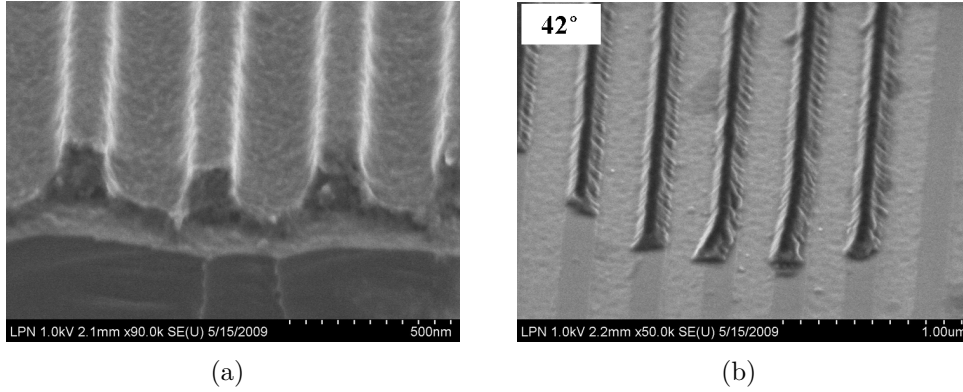
Table 3.6: The investigated etching conditions for CHF₃/O₂ plasmas.

Figure 3.16: SEM pictures of 220 nm line profiles after (a) soft UV-NIL and (b) etching by process NXR2.

This sidewall angle will be used to describe the inclination of the pattern profile. The sidewall angle θ (see Fig. 3.17(a)), defined as the angle between the slope and horizontal direction of nanoline structure, can be calculated by:

$$\theta = \arctan\left(\frac{2h}{d-w}\right) \quad (3.14)$$

where w is the top surface width of nanoline pattern, d is the underside width and h is the height of nanoline. The desired etched side-wall profile can be achieved by adjusting the sidewall angle.

In order to achieve vertical sidewall profile ($\theta = 90^\circ$), the ratio between

the lateral etching width and vertical etching depth has to be minimized. Figure 3.17(b) shows a schematic of perfect anisotropic etching with vertical sidewall profile. For this perfect anisotropic etch, the vertical etch rate is much larger than the lateral etch rate, which means that the lateral etch rate can be approximated to zero ($V_{lateral} \approx 0$) when compared to the vertical etch rate.

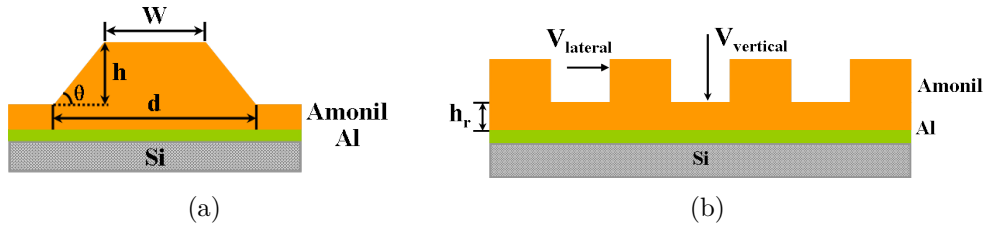


Figure 3.17: A schematic side-wall profile after RIE (a) an ideal anisotropic etching profile with $V_{lateral} \approx 0$. (b) an anisotropic overetching profile with non-vertical sidewall (The slope of sidewall profile is described by θ).

A. Variation of the power and pressure

From our experimental results mentioned above, the etching conditions optimization can be initiated based on our process NXR2. We have varied the controlled parameters such as the RF power and the chamber pressure. As shown in figure 3.18(a) when the power was decreased to 12 W (process NXR5) while other parameters were kept invariable, the sidewall angle of nanoline pattern changes from 42° to 58° and the surface roughness along the side of the line decreases. Figure 3.18(b) (process NXR6) shows the role of the chamber pressure on the sidewall angle when RF power was maintained at 25 W. We see that the sidewall angle reaches 63° with the pressure reduced to 5 mtorr.

process number	w(nm)	d(nm)	h(nm)	θ
NXR2	67.5	217	67.3	42°
NXR5	72	184	89.6	58°
NXR6	59.3	150.4	91	63°

Table 3.7: The measured w, d and calculated θ value of nanoline pattern etched with NXR2, NXR5 and NXR6 process.

The results obtained for the preliminary tests based on optimization of process NXR2 are summarized in table 3.7. When pressure increases, the mean free path between the reacting species decreases and the number

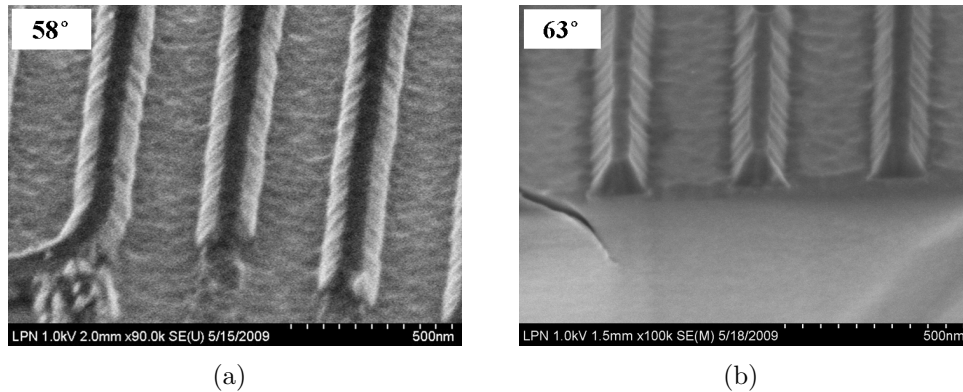


Figure 3.18: SEM cross-section views of 220 nm line etched by CHF_3/O_2 plasmas with process (a) NXR5 and (b) NXR6.

of chemically active ions is enhanced promoting an isotropic etching. At the same time, with the increase of pressure, the reacting species such as atoms, molecules, electrons and ions become nondirectional. Since the angle of incidence of the reacting species is larger, significant etching occurs at the sidewalls of the line which enhances sidewall roughness and reduces linewidth. Compared with the effect of low power (NXR5), a low pressure (NXR6) results in a more vertical sidewall profile. Despite this, both these two processes are still not optimized since minimized sidewall roughness and perfectly vertical profile haven't been obtained.

B. Variation of gas composition and RF power

We have also investigated how the gas composition can affect the pattern profile. The fraction of CHF_3 and O_2 has been changed while the total gas flow was maintained at 22 sccm. The variation of Amonil resist etch rates in CHF_3/O_2 is shown in Fig. 3.19 as a function of O_2/CHF_3 flux ratio. The etching rate increased almost linearly with increasing the O_2 addition by changing O_2/CHF_3 flow rate ratio from 1/10 to 10/12. This observation explains the role of CHF_3 in the plasma [21]. A similar effect of O_2/CHF_3 ratio on etch speed while etching submicron-wide trenches patterns in commercial PMMA was reported by Zhang et. al [22]. They observed that the etch rate of PMMA gradually decreased with increasing amount of CHF_3 due to the formation of the passivation layer. CHF_3 is known as a polymerizing gas that may produce fluorocarbon deposition on the surface. The species generated from CHF_3 in the plasma are H^+ and CF_3^- , and the CF_3^- species can quench the activity of CF_3^+ in the plasma. The introduction of oxygen plasma increases the dissociation of C-F bonds through reaction with oxygen atoms. The concentration of fluorine atoms

which are responsible for the etching are thus enhanced. Hence, the etching rate of Amonil resist decreases upon the increasing of CHF_3 amount, and increases with the increasing of O_2 amount.

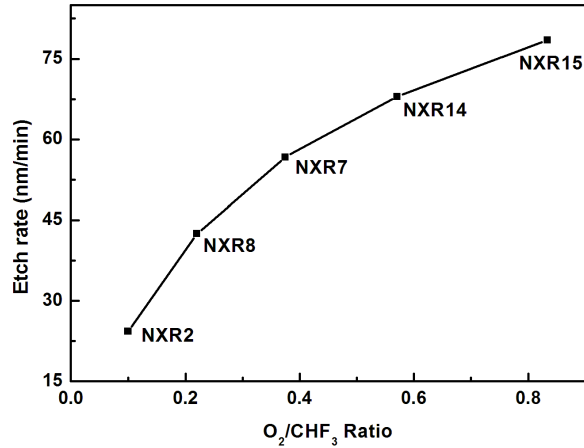


Figure 3.19: The etch rate for 220 nm-linewidth nanoline pattern etched by CHF_3/O_2 plasmas with different gases fraction.

Besides affecting the etch rate of Amonil, it was also found that the sidewall profile becomes more vertical when the O_2/CHF_3 ratio approached 10:12 (Fig. 3.20 d), all other parameters like pressure, power and etching time being fixed at 7 mtorr, 25 W and 1 min 30 s, respectively. This reveals that a reduction of CHF_3 could be beneficial for vertical sidewalls. Meanwhile, O_2 is also found to affect the surface roughness. As it can be seen from Fig. 3.16(b) and Fig. 3.20, increasing O_2/CHF_3 ratio from 1/10 to 10/12, enhances the surface roughness.

There are two possible reasons that can explain these results: first, an increase in the O_2/CHF_3 ratio results in a dilution of the concentration of F atoms that are mainly responsible of the chemical reactions occurring in the RIE process, thus reducing the chemical etching rate and contributing to a rougher surface; second, an increase in the O_2/CHF_3 ratio produces more oxygen ions, which will lead to enhanced physical ion bombardment and thus the surface roughness.

Here, supplementary explanations are needed to understand the excessive surface roughness of the sample etched by process NXR15 (shown in Fig. 3.20(d)). Before NXR15 experiment one change has been done in the reactor: the quartz insulator ring around electrodes was replaced by an alumina ring. In RIE batch reactors using fluorine chemistries, the choice of this kind of materials results in surface roughening since the in-

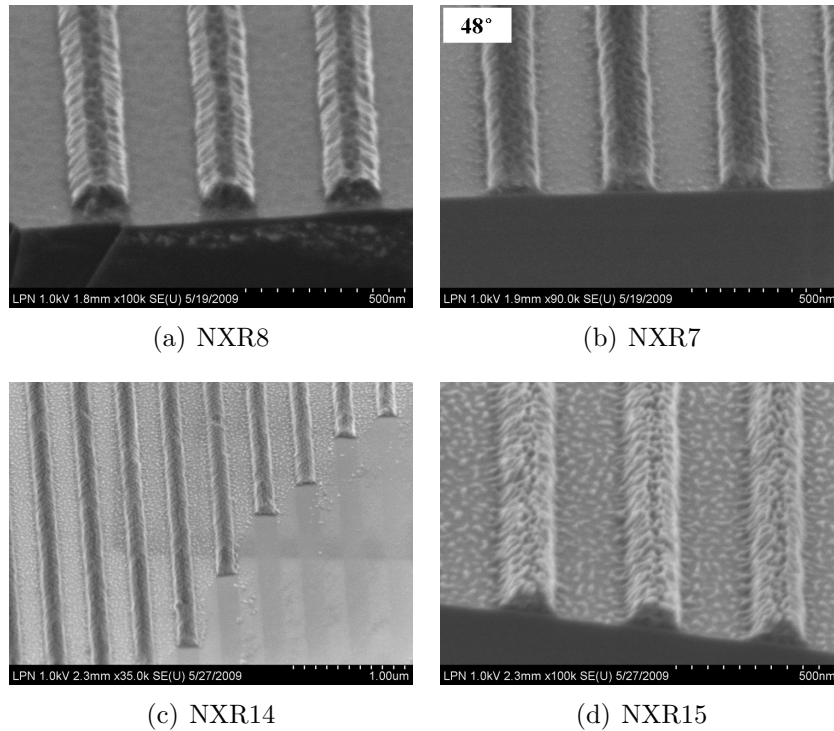


Figure 3.20: SEM cross-section views of nanoline patterns etching by O_2/CHF_3 plasmas with different gases ratio.

volatile AlF_3 is deposited onto the sample surface during processing. An other explanation could be that the etching process itself leads to chamber contamination [23].

In this experiment, there is a trade off relationship between the addition of O_2 to CHF_3 . It was observed that keeping the O_2/CHF_3 ratio at 6/16 (NXR7), a relatively good compromise is obtained for both sidewall profile and roughness control. As mentioned previously, the RF power in RIE is also an important parameter for controlling the etching anisotropy. We have thus applied three different powers base on the process NXR 7. Our goal was still to optimize this process for better etch results.

The variation of Amonil etch rate as a function of rf power for CHF_3/O_2 is shown in Fig. 3.21(a). Gas flows were fixed at 16 sccm for CHF_3 and 6 sccm for O_2 . The chamber pressure was kept at 7 mTorr. The etching rate is observed to increase linearly with the RF power. In general, the increase of RF power will increase electron energy. High energy electron can both generate more ions and build up a self-bias field, which accelerates ions toward cathode. Accelerated ions bombarding cathode where the

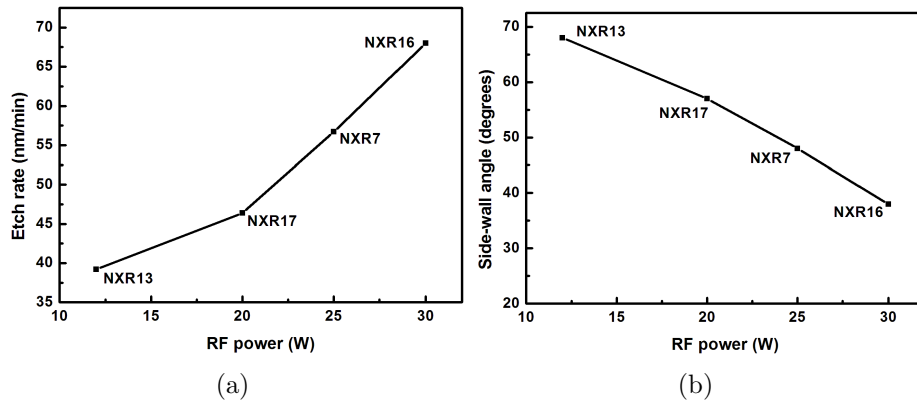


Figure 3.21: (a) The etch rate and (b) the sidewall angle for 220 nm-nanoline pattern etched by CHF_3/O_2 (6/16 sccm) with various RF power.

sample is placed can thus enhance the etching rate. The evolution of the nanoline sidewall angle is plotted in Fig. 3.21(b) as a function of the RF power. Amonil resist shows a decrease in this sidewall angle when power is increased.

When RF power is increased, atomic oxygens etch the planar polymeric film faster than sidewall. Also the angle of incidence of the reacting species is more vertical, which results in a minimized roughness at highest power (30 W), as shown in fig 3.22.

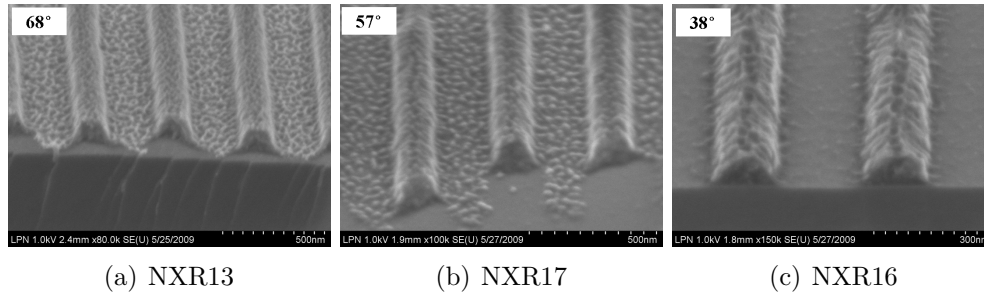


Figure 3.22: SEM cross-section views of nanoline patterns etching by 16 sccm $\text{CHF}_3/6$ sccm O_2 plasmas with different RF power.

C. Variation of total gas flow

In a third set of experiments, we explored the role of the total flow. A mixture of CHF_3 and O_2 with a constant ratio O_2/CHF_3 (equal to 3/8) was used to etch at 7 mtorr and 25 W. Figure 3.23 shows the SEM images of the etching profile of Amonil nanolines. Compared with Fig. 3.20(b), it can be noted that the etching side-wall angle increases when total gas

flow increases.

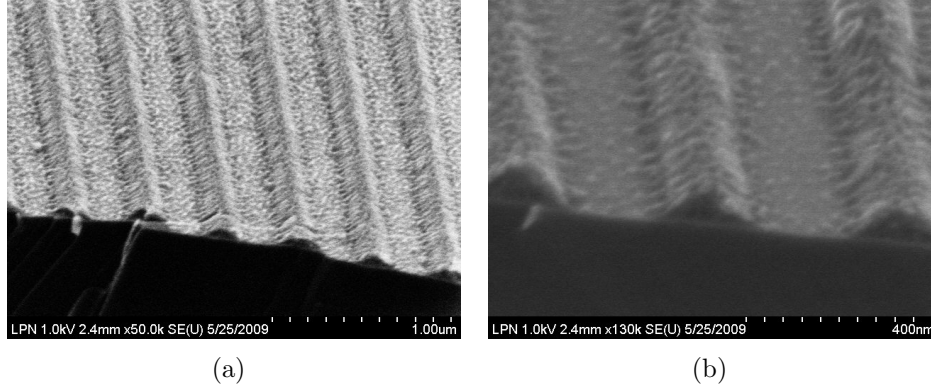


Figure 3.23: SEM images of nanoline patterns etching profile by using 8 sccm $\text{CHF}_3/3$ sccm O_2 plasmas.

In this part, we have studied $\text{CHF}_3\text{-O}_2$ based RIE process for Amonil resist etching. Some technological criterions to obtain vertical sidewall profile and smooth surface can be summarized as follows:

- Anisotropy increases as pressure of CHF_3/O_2 gases increases.
- O_2 plays a significant role in affecting the etch rate through a modulation of the concentration of F atoms that are the main etching species. It has also a more direct influence on the etched surface roughness. Increasing O_2 fraction leads to an enhancement of both the etch rate and the surface roughness. The relative better etching conditions were found to occur at 6 sccm O_2 .
- By carefully adjust the RF power from our process NXR7, we found that large power provides highest etching speed and least surface roughness, but meanwhile, it results in smallest side-wall angle.
- The etching side-wall angle increases when total gas flow increases.

In this part, the relative optimum etching conditions were found to occur at 6 sccm $\text{O}_2/16$ sccm CHF_3 , 25 W power at 7 mtorr pressure.

IV. Study of SF₆/O₂ etching for Amonil

The aim of this part is to continue to explore an etching process that will produce smooth roughness and high anisotropy. SF₆ will replace CHF₃ to etch Amonil resist. The etching parameters with SF₆/O₂ plasmas in this test are resumed in the table 3.8. Compared to a CHF₃ plasma, a SF₆ plasma contains more active F-containing species but has a weaker sputtering component. Therefore, a faster etch rate in the SF₆-rich plasmas is expected from the abundance of active fluorine species in the SF₆-rich plasma.

Process number	Power(W)	Pressure(mTorr)	Gas/flux (sccm)	
			SF ₆	O ₂
NXR9	25	7	20	2
NXR11	25	7	16	6
NXR12	25	5	16	6
NXR18	25	7	20	0
Gej10	10	30	10	0

Table 3.8: The investigated etching conditions for SF₆ and O₂ plasma.

A. Variation of gas ratio

The effect of gas ratio on etch rate, sidewall profile and roughness has been tested. Keeping the power and the pressure constant at 25 W and 7 mtorr, individually, the gas ratio of O₂/SF₆ was maintained at 2/20 (9.1% O₂ content, NXR9) or 6/16 (27.3% O₂ content, NXR11). The etch speed increases from 255 nm/min to 340 nm/min when the O₂ concentration increases. In the simulation study of Si and SiO₂ etching in O₂/SF₆ plasma reported by R. Knizikevičius [24], it's found that as O₂ content increases, the concentration of F atoms also increases due to the reaction of O atoms with SF₅ radicals. At the maximum concentration of F atoms (when O₂ content approaches 27%), almost all SF₅ radicals in O₂+SF₆ have reacted. Therefore, the Si etching rate is enhanced with the O₂/SF₆ increases, with a maximum value corresponding to an O₂ content being around 27% [24]. In our test with low oxygen concentration, oxygen increase helps the conversion of SF₆ to F* radicals, thereby hindering oxygen reaction with F* radicals and the subsequent reformation of SF₆. The result is a net increase in the concentration of fluoride radicals, thus leading to an increase in Amonil etch rate [28].

The effect of oxygen concentration on etch profile and roughness is

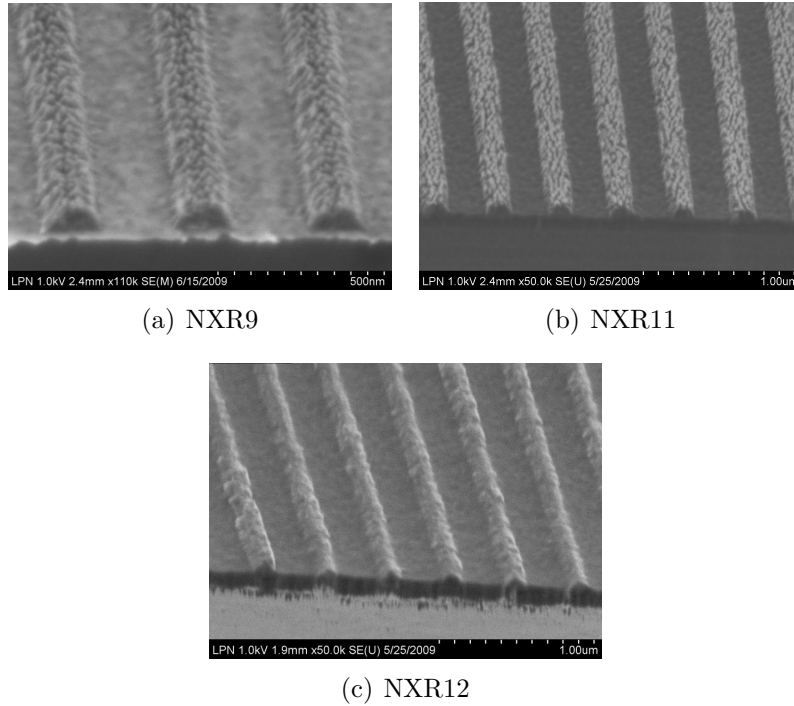


Figure 3.24: SEM cross-section views of nanoline patterns etching by SF_6/O_2 plasmas with different (a),(b) gases ratio and (b), (c) pressure.

shown in Fig. 3.24(a) and 3.24(b). Since the sidewall angle was impossible to determine precisely from these two images, we concluded that oxygen increase produces a relatively steeper sidewall profile associated with an enhanced roughness.

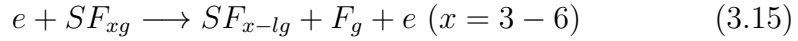
B. Variation of pressure

RIE pressure was varied from 7 (NXR11) to 5 (NXR12) mtorr, keeping fixed all other parameters (RF power at 25 W, O_2 flow rate at 6 sccm and SF_6 flow rate at 16 sccm as shown in table 3.8). The etch rate increases from 283 nm/min to 340 nm/min when pressure increase from 5 to 7 mtorr, which is consistent with above mentioned results in CHF_3/O_2 plasmas etching. SEM images of nanolines patterns fabricated at pressures ranging from 5 to 7 mtorr are shown in Fig. 3.24(b) and 3.24(c). As shown in the SEM images, the sidewall roughness increases with pressure. The roughness produced depends on the angle of incidence of the etchant species with respect to the surface. At low pressure, the reactant flux is normal to the surface. Thus, the vertical incident reactants do not affect the sidewalls, which will result in a low edge roughness. While at higher pressure, species are obliquely incident towards the surface. These reac-

tants affect the sidewalls, which enhances edge roughness. On the contrary, the side-wall angle decreases from 60° to 50° .

C. Pure SF_6 plasmas

Amonil resist etching tests in pure SF_6 plasma have also been performed with different flow rate, pressure and power. The detail of process parameters are listed in previously presented table 3.8. The nanolines etched under two different conditions (NXR18 and Gej10) are shown in figure 3.25. The slope of the side wall profile of the sample etched with pure SF_6 is a few low compared with that of the sample etched with O_2/SF_6 gases mixture. This can be explained based on the etch mechanism of SF_6 plasma. SF_6 plasma etching of Amonil with fluorinated compounds is primarily due to free fluorine [25]. The dissociation reactions of the form



The etching of Amonil occurs by a reaction with F atoms. The overall stoichiometry of etching by atomic F is [26]



Due to the intensive exothermic reaction in Eq. 3.16 taking place at the sidewalls, the sidewall angle decrease compared with previous results by O_2/SF_6 plasmas etching. On the other hand, a dense needle like nanostructure was found under high pressure SF_6 etching (Figure 3.25). Therefore, the addition of O_2 to SF_6 in an optimized ratio will improve both the sidewall smoothness and the sidewall profile of Amonil nanolines.

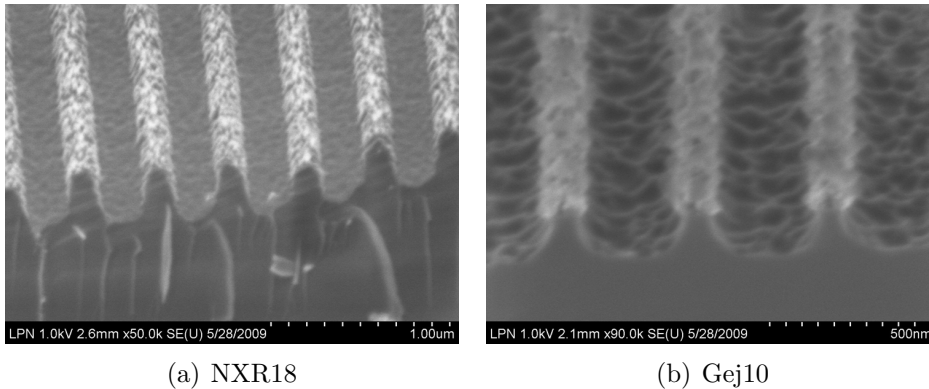


Figure 3.25: SEM cross-section views of nanoline patterns etching by SF_6 plasmas with different etching parameters.

The anisotropic etching of Amonil nanolines using SF₆ and O₂ gas mixtures or pure SF₆ gas process has been studied.

- Our results suggest O₂ concentration to be the principal factor to monitor both etch profile and roughness.
- The etching anisotropic can be enhanced by lowering the total pressure or by enhancing the oxygen fraction in the working gas.

V. Study of CHF₃/SF₆/O₂ etching for Amonil

RIE using CHF₃, SF₆ and O₂ gas mixtures for the anisotropic etching of Amonil resist has been studied in this last section. Each gas of the complex mixture a CHF₃/SF₆/O₂ has a known specific function and influence. O₂ is a special etching agent with complicated effects. It is known that when O₂ gas is added to a SF₆ plasma, the O* radicals will first increase the F-atom density by preventing the recombination reaction of SF₆. However, the O* radicals will also help to form a thin film passivation layer on the sidewall. This protecting layer will be removed by CHF₃ or SF₆ through the formation of volatile product CO_xF_y or SO_xF_y allowing Amonil etching to proceed further [27]. With these competing effects, the etching anisotropy and the sidewall profiles can be subtly controlled by monitoring the flow rates of SF₆, CHF₃ and O₂ gases. In this part, various gas ratio of CHF₃/SF₆ were examined to provide different etch rate and sidewall profile, the detail of different process is shown in table 3.9.

In Fig. 3.26, the effect of SF₆/CHF₃ ratio on the etch rate of Amonil resist are shown. The Amonil resist etch rate always increases as the SF₆/CHF₃ ratio is increased (the other parameters are fixed : flow rate of O₂ at 2 sccm, pressure at 7 mtorr and power at 25 W), since higher SF₆ flows will increase the fluorine concentration in the gas mixture. In other words, the increase of CHF₃ concentration reduces the etch rate. In CHF₃ plasma, polymer-forming radicals can deposit on the substrate to form a barrier layer consisting of various bonds of carbon and fluorine (i.e., CF_i, i=1, 2, 3). This protective layer acts as a diffusion barrier for both F radicals to reach the surface of the material to be etched and also for volatile compounds.

After etching, samples were characterized with SEM. When there is no CHF₃ added, as it is shown in Fig. 3.24), the etch surface roughness is high, resulting in grassing surface. On the opposite, it's observed that the

Process number	Power(W)	Pressure(mTorr)	Gas/flow rate(sccm)		
			CHF ₃	SF ₆	O ₂
NXR21	25	7	5	15	2
NXR20	25	7	8	10	2
NXR19	25	7	10	10	2
NXR22	25	7	12	8	2
NXR27	20	7	12	8	2
NXR28	15	7	12	8	2
NXR29	10	7	12	8	2
NXR23	25	7	15	5	2
NXR26	25	7	16	4	2
NXR25	25	7	17	3	2
NXR24	25	7	18	2	2

Table 3.9: The investigated etching conditions for CHF₃, SF₆ and O₂ plasmas.

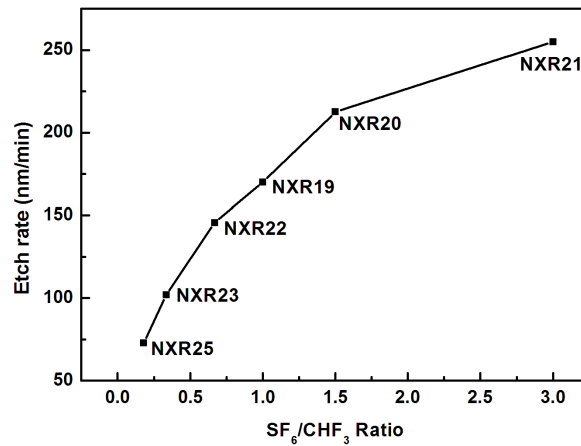


Figure 3.26: The etch rate for 220 nm-linewidth nanoline pattern etched by CHF₃/SF₆/O₂ plasmas with different CHF₃/SF₆ gases fraction.

addition of CHF₃ to an SF₆/O₂ gas mixture can significantly improve the etch surface quality, as shown in both Fig. 3.27(a)-(d). This is because the addition of CHF₃ into SF₆/O₂ gases suppresses the formation of passivation on the top surface, which favors smoothing of the etched surface. However, this doesn't mean the lower the SF₆/CHF₃ ratio, the smoother the sample surface. In fact, we observed that the surface will be rough (Fig. 3.27(e)-(h)) when sample is etched at high rate under high SF₆/CHF₃ ratio (> 12/8).

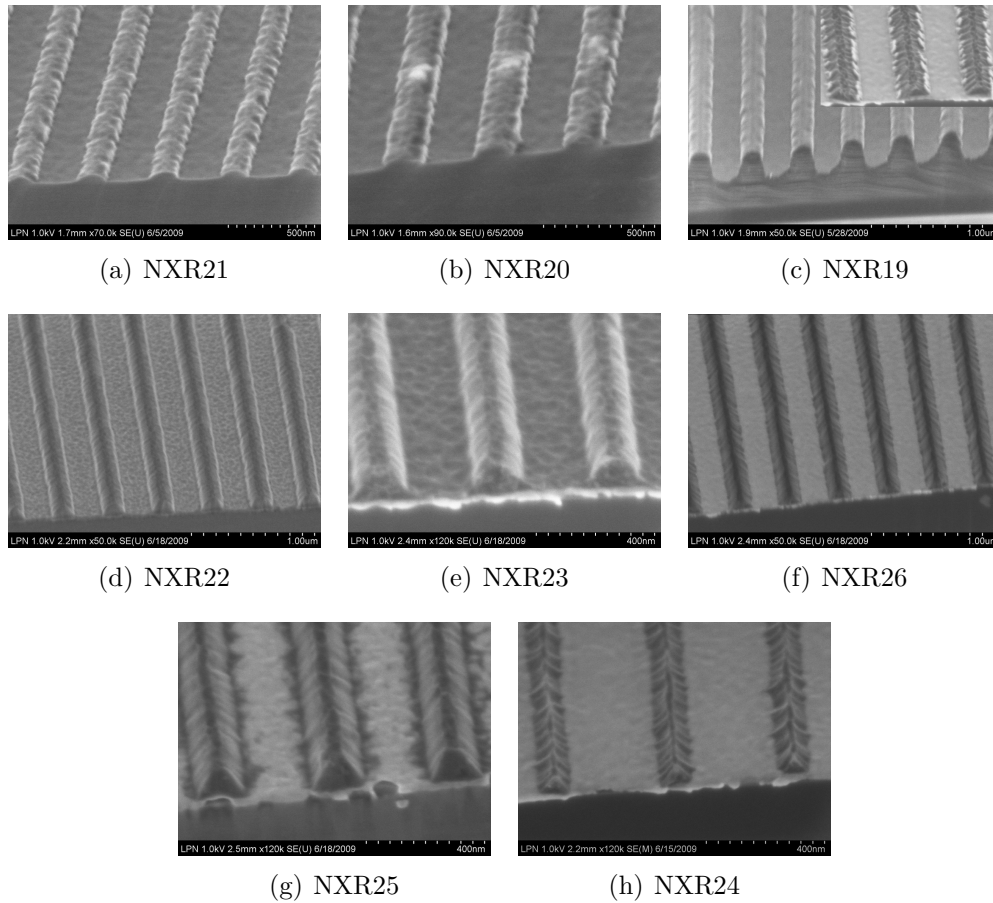


Figure 3.27: SEM cross-section views of nanoline patterns etching by $\text{CHF}_3/\text{SF}_6/\text{O}_2$ plasmas with different gases fraction.

The addition of CHF_3 not only results in relatively smooth surfaces, but also slightly affects the sidewall profile. The effect of CHF_3 concentration on Amonil etch profile is shown in Fig. 3.27. At high CHF_3 flow, the reduced O atom concentration associated with a reduced formation of the passivation layer [28] produces a more isotropic etching profile. At an CHF_3/SF_6 flow of 10/10 sccm (Fig. 3.27(c), process NXR19) and 12/8 sccm (Fig. 3.27(d), process NXR22), the Amonil etch profile is largely anisotropic and the surface roughness is greatly improved. However, process NXR 19 was observed to be not easily reproduced, as it is observed in the inset SEM image in Fig. 3.27(c). Therefore, optimized etching conditions able to produce a smooth etched surface were found to occur at 12/8/2 sccm $\text{CHF}_3/\text{SF}_6/\text{O}_2$ flow rate, at pressure of 7 mtorr, at which the etch rate attained its value of 145.7 nm/min.

Finally, we have tested the influence of RF power on the optimized etching process previously mentioned. The variation of RF power was carried out from 20 to 10 W, keeping other parameters fixed to values of process NXR22. As shown in Fig. 3.28 that has to be compared with Fig. 3.27(d), no obvious variations can be observed in both profile and roughness.

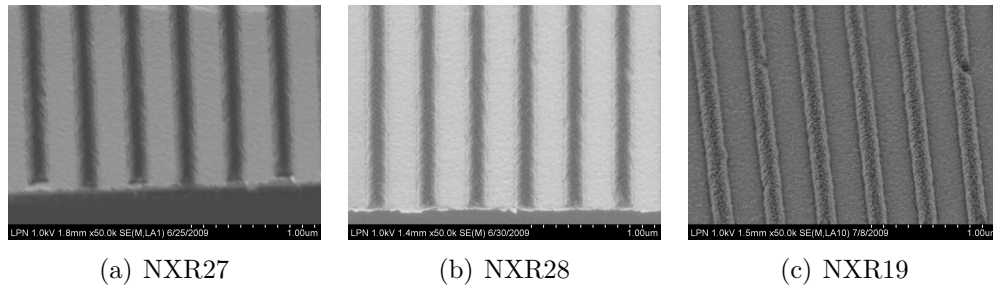


Figure 3.28: SEM cross-section views of nanoline patterns etching by $\text{CHF}_3/\text{SF}_6/\text{O}_2$ with 12/8/2 sccm plasmas with different power: (a) 20 W, (b) 15 W and (c) 10 W.

The Amonil nanolines etched using the $\text{CHF}_3/\text{SF}_6/\text{O}_2$ plasmas present quite optimized results for both sidewall profile and surface roughness. However, careful cleaning program has to be executed before each etching to ensure reproducible and stable etch process.

3.5 Pattern transfer

Although nanoimprint process is a key stage of nanofabrication, it's far from sufficient to satisfy all the needs. Indeed, the resist isn't the material in which nanostructures are to be created, instead, it's only constitutes a sensitive sacrificial layer. Then the imprinted resist patterns must be transferred into more relevant materials. This transfer should preserve size and shape of resist nanopatterns. It is an important nanofabrication step. There are two common ways for transferring nanostructures into the active layer: one is the so-called subtractive transfer technique which employs wet or dry etching techniques; the other is related to the additive transfer methods including electroplating and lift-off.

3.5.1 Transfer by lift-off

One key element to establish NIL as a viable research technology and production tool is the development of a stable and well-controlled method for lift-off. In the lift-off process, a sacrificial photoresist layer is imprinted using a mask that contains inverse patterns (compared with the final pattern obtained after lift-off). The metallic or oxide pattern is created by blanket coating the photoresist pattern with metal or oxide, these materials can be deposited by vacuum vapor deposition or sputtering. Finally, the sacrificial layer is simply washed away in a suitable solvent. Any material which was deposited on the sacrificial layer is removed, while any material which was in direct contact with the substrate remains. The result is that the material (metal or oxide) is only deposited within the patterns originally imprinted in the resist. The opening in the resist are thus transformed into a deposited pattern of the chosen material localized on the nanometer scale.

The lift-off process is very simple and efficient. However to implement it successful one should pay attention to some issues:

- First, the film deposited on the resist must be clearly discontinuous across resist patterns. If not, the retention problems can occur. This usually happens when the photoresist is completely covered by metal or oxide, leaving no opening in the metal/oxide coating for the solvent to penetrate and dissolve the photoresist. Thus, the unwanted metal pattern remains on the wafer and can't be lifted-off. To solve this problem, the lithography parameters must be carefully adjusted to yield highly vertical sidewall in the resist.
- Second, the thickness of the deposited layer must be less than the thickness of the resist layer, otherwise the patterns maybe completely blocked up with deposited material. Normally, a ratio of 3:1 between the thickness of resist and the material to be deposited is enough for successful lift-off.

While lift-off processes have been proposed which use from one to three layers of resist [29, 30, 31]. In this subsection, we present bi-layer and tri-layer two different systems for lift-off tests.

a. Bi-layer system

Two layers materials are required for this process. The process is illustrated in Fig. 3.29. A thin film of thermal PMMA resist is deposited on the

substrate. Then a layer of UV-curable photopolymer Amonil is spin-coated over the PMMA layer. After soft UV-NIL, the residual resist layer is removed by CHF_3 , SF_6 and O_2 plasmas or only CHF_3 and O_2 plasmas. The Amonil patterned layer was used as a mask to transfer the pattern into the PMMA layer down to the substrate by O_2 RIE (flux of O_2 is 10 sccm, pressure is 10 mtorr and power is 30 W). A thin Ni layer is then deposited on the substrate via e-beam evaporation. Finally a thin Ni layer is lifted-off, giving the structures on the substrate.

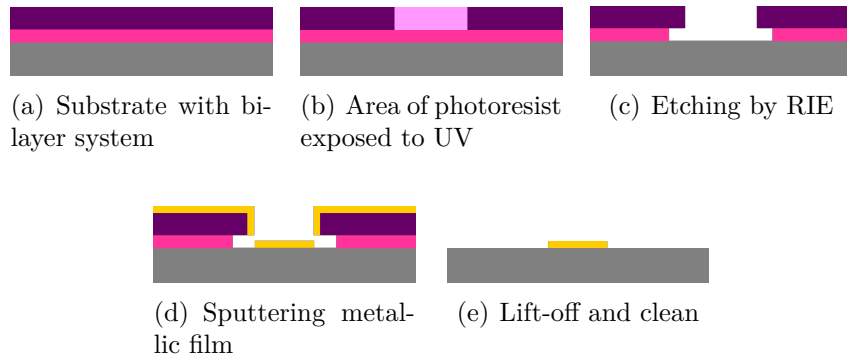


Figure 3.29: schematic diagram of general procedure of bi-layer lift-off process.

The length of time for lift-off will depend on the film quality. Generally, the higher the film quality, the more impermeable it is and the longer it will take to lift-off. Depending on how robust the film and substrate are, PMMA and the on top metal layer can be removed by two ways: (1) directly put the sample into the solvent bench ultrasonic bath or (2) using a clean paper to scrape gently on the surface. The second way is more destructive thus the first method is more often used. However, one should pay attention to the fact that the ultrasonic intensity should not be too high and ultrasonic time should not be too long, otherwise, the patterns will be ragged.

Bi-layer lift-off metalization techniques offer significant advantages in resolution, removal, process simplicity and undercut control. Nevertheless because high resolution patterning require very thin layer polymers, the so called tri-layer technique has to be considered to obtain high aspect ratio features.

b. Tri-layer system

On the basis of previous mentioned bi-layer lift-off process, we have developed a tri-layer system. Between PMMA bottom layer and Amonil top

layer, an intermediate 10 nm thin layer of germanium (Ge) was deposited by e-beam evaporation. After UV-imprinting, the residual layer of Amonil is firstly etched. Afterward, the patterned top layer is used as mask for a second RIE to etch Ge with SF_6 at a gas flow rate of 10 sccm, a pressure of 30 mTorr and a power of 30 W. Finally, Ge is used as mask for a third RIE to etch the PMMA bottom layer with O_2 . A thin 20 nm Ni film is then deposited by e-beam evaporation and lift-off is performed in an acetone bath.

Compared to the traditional bi-layer transfer system, here, the adding of intermediate Ge layer shows several advantages [31]: first, the Ge layer allows increasing the etching selectivity, so that high aspect ratio and high resolution pattern can be obtained; second, because of the good conductivity of the intermediate Ge layer, the etched sample can be easily analyzed by scanning electronic microscopy; lastly, with this tri-layer transfer system, the whole process latitude is largely enhanced and a better pattern homogeneity can be achieved. To illustrate these points, we report in Figure 3.30 SEM pictures of a (a) dot array of 200 nm diameter and (b) line array with 200 nm linewidth after lift-off.

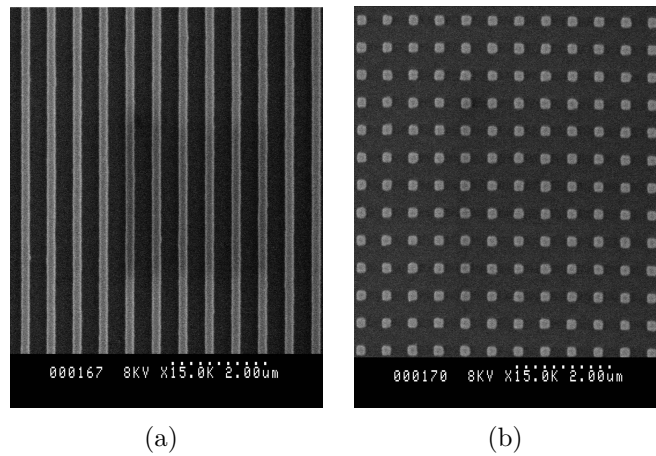


Figure 3.30: SEM images of a (a) 200 nm linewidth line array and (b) 200 nm pitch dot array obtained by soft UV-NIL after lift-off with Amonil/Ge/PMMA tri-layer system.

If our tri-layer processing combined with soft UV-NIL method allows pattern replication of various geometries with a high resolution ($> 100\text{nm}$), high aspect ratio and good homogeneity over a large area, RIE is shown to produce more often some small residual particles on the sample surface. To solve this problem, we treated all our etched samples in diluted HCL after the last RIE step. Figure 3.31 shows the SEM images of nanolines arrays

after reactive ion etch, without and with acid treatment. The particles formed after RIE will form large cores after metalizations and finally lead to dirty surface after lift-off as shown in Fig. 3.32(a). We do not know if this problem is intrinsic to our etching processes. It could be related to the chemistry of discharge such as the fluorocarbon film, or to the formation of nonvolatile compounds with film impurities. The removed material during etching could thus redeposit somewhere else in the vicinity of the etched pattern. The redeposition of nonvolatile materials problem could be severe since unwanted defects will be created on top of each etched sample, thus resulting in defective patterns. To solve this problem, chemical treatment can be used to clean the surface of the sample after RIE. However, chemically cleaning can degrade the feature resolution. With our HCl treatment we do not observe any lateral change, but one should take care of eventual excessive erosion of the resist, leaving non-vertical sidewalls and rounded corners.

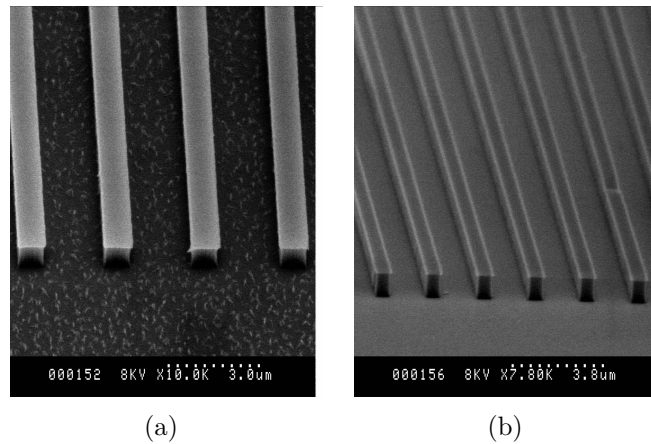


Figure 3.31: SEM images of nanolines arrays after RIE without and with acid treatment.

In our experiment, these small particles were removed by 37% HCl acid solution for 15 s. After resolving these cleanliness problems, different sizes and forms structures have been easily transferred by RIE and we obtain good results after lift-off. Figure 3.32(b) shows typical SEM images of nanoholes arrays after HCl treatment.

3.5.2 Transfer by RIE

One goal of producing high-resolution and high fidelity patterns by lift-off is to use the lifted patterns as mask to fabricate nanostructures in solid

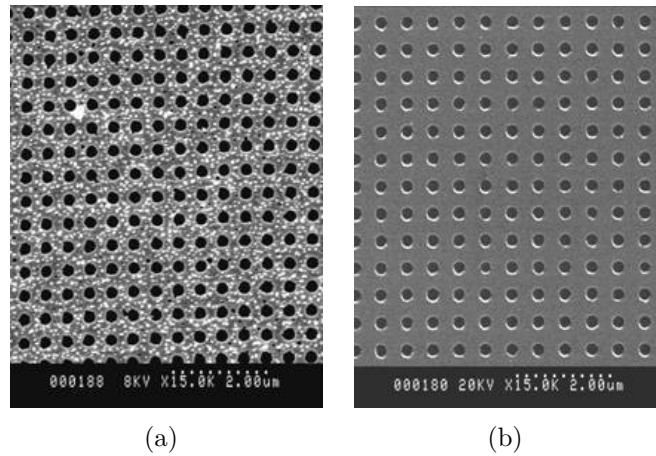


Figure 3.32: SEM images metallic lift off results on the patterns without and with HCl treatment.

substrate. For the final pattern transfer into the substrate or the active layer, several approaches can be used. One of them involves: removing the residual resist from the recessed parts (windows) of the pattern by RIE; followed by depositing a hard mask metal layer over the patterned resist substrate and applying a lift-off technique that removes the resist template and the material on top, leaving a patterned mask layer on the Si substrate; finally, an anisotropic RIE process is used to selectively etch away the Si material in the unmasked region (see Fig. 3.33(a)). Another approach is the use of a multilayer, typically a bilayer of one polymer on another polymer layer. In the bilayer approach, the penetration of the master pattern by imprinting is through the upper layer into the underlying polymer layer. The idea of this method is to create a relief by molding the resist and then to convert the thickness contrast into a suitable substrate profile by direct reactive ion etching (see Fig. 3.33(b)).

a. Transfer after metallic lift-off

The fabrication of optical structures in silicon has emerged as an excellent opportunity to leverage the capabilities of silicon processing for the definition of optical nanostructures over the past several years. In particular, silicon diffractive optical elements with feature sizes below one quarter of the wavelength of light are widely used as polarization sensitive beam splitters, grating couplers, dispersive filters, graded index diffractive optical lenses and Bragg reflectors. In all of these optical applications, dense nanostructures need to be defined and transferred several hundreds

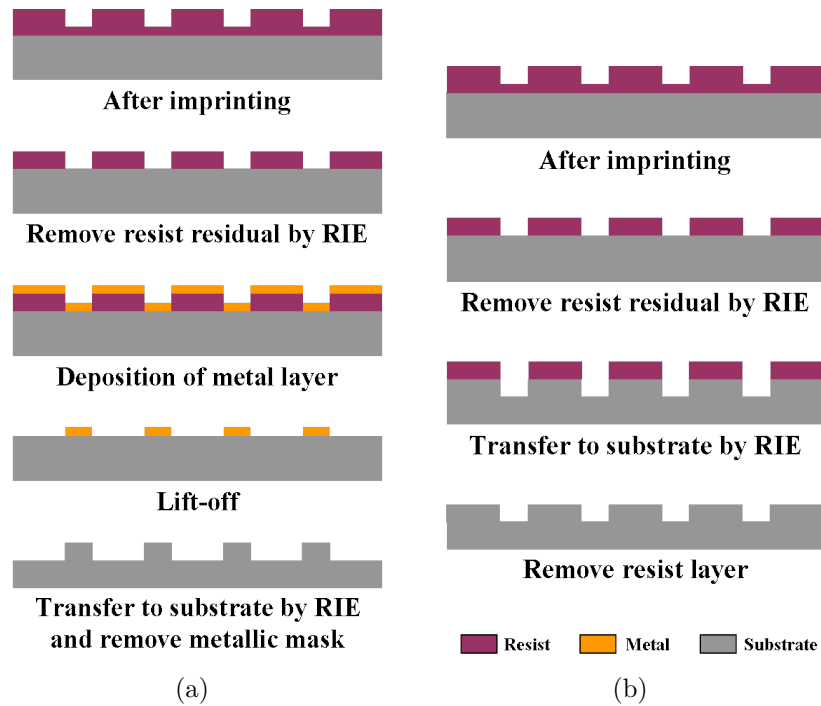


Figure 3.33: Schematic representation of two ways for transferring the pattern into the substrate by RIE.

of nanometers deep into the silicon.

After transfer nano patterns on the silicon substrate by lift-off, the patterned Ni film can be used as mask for dry etching, thereby define the patterns on the substrate. Finally, Ni is removed by HNO_3 solution. Patterns can be transferred into Si by a highly anisotropic RIE process based on CHF_3/SF_6 plasmas. The optimized parameters used for Si etching are: CHF_3 gas with a gas flow rate of 10 sccm, SF_6 gas with a gas flow rate of 4 sccm, working pressure 8 mtorr and a power of 5 W, the etching speed is 36 nm/min. Fig. 3.34 shows the nanostructures etched in Silicon with the RIE process described above.

b. Direct pattern transfer by RIE

Compared with lift-off process, a direct etch process offers advantages over lift-off methodology since this method etches the features as they are imprinted. In our experiment, because of the high resistance of Amonil resist, the printed Amonil by UV-NIL can be used as mask to directly transfer the patterns into PMMA, which can be finally transfer to Si. On Si sub-

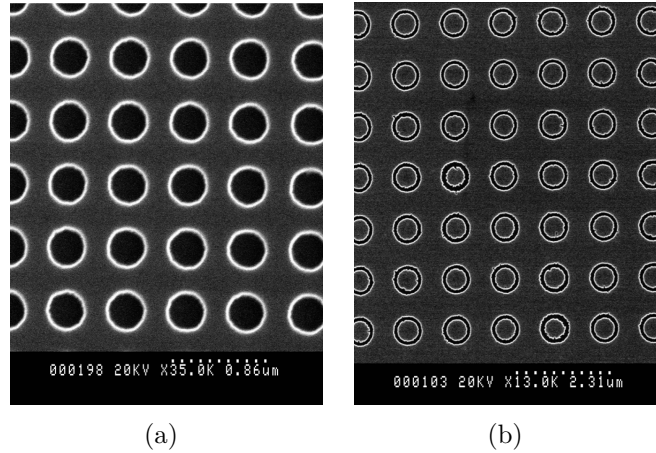


Figure 3.34: SEM images of nano patterns transferred into Si substrate with removal of Ni mask: (a) the hole diameter is 300 nm and (b) the outer and the inner diameter of ring is 700 nm and 600 nm separately.

strate, 50 g/l PMMA bottom layer was spin coated with a thickness about 1 μm . Amonil resist was then spin coated as a top layer as previously described. After UV imprint, the residual layer of Amonil is firstly etched, then, oxygen plasma is used to transfer the patterns into PMMA by using Amonil as mask. During RIE, we noted that the pattern size will decrease because of the horizontal etching at the same time. Figure 3.35 shows the pillars and lines etched in PMMA.

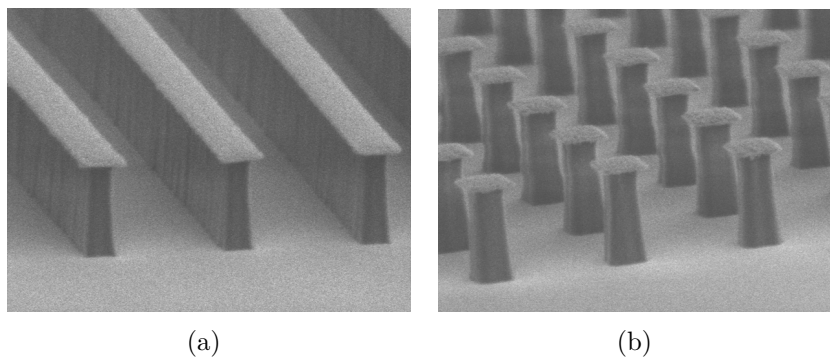


Figure 3.35: SEM images of PMMA pillars and lines arrays, the height is about 1 μm .

In soft UV imprint parts, we have studied both lift-off process to obtain the nanostructures in metal or use direct etching way to transfer the patterns in PMMA to obtain high aspect ratio plastic nanostructures. However, there are limitations associated with these processes. For example,

in the lift-off process the undercut dimension would constraint the size of features that could be created. Also, pattern transfer of dense vias pattern using lift-off would not be possible. In our work, it's quite difficult to obtain the holes via lift-off since the edges of the holes are easily destroyed during ultrasonic when feature size is below 100 nm. Therefore to obtain this kinds of nanostructures, we propose to use ion beam etching for better quality control of pattern transfer.

3.5.3 Transfer by ion beam etching

Ion beam etching (IBE) is the simplest dry etching method. In this approach, an ion beam which can be electrostatically neutralized to avoid charge effects in the target material is directed with normal incidence at the sample surface. Ions are typically noble gas ions such as argon, which exhibit no chemical activity with respect to the target atoms. Etching is therefore purely collisional. This type of etch can produce almost vertical sides on etched features, due to the normal incidence of the ions on the sample surface and their large kinetic energy in the perpendicular direction.

Ion beam etching was performed to transfer test structures obtained by thermal nanoimprint lithography process. On the Si substrate, 20nm gold was first deposited on top, then, NXR1020 resist was spin coated on the gold surface. Thermal nanoimprint has been performed with the conditions described in Chapter 2. After imprinting and RIE removal of residual resist layer, we used the NXR1020 resist as mask to etch the gold film by ion beam etching (Roth&Rau, German) under Ar gas. The bias was about 350 V, the angle was 0 degree, and etching time was fixed to 30s. After IBE the resist layer was removed by acetone. Gold can be then used as mask to transfer the patterns into Si. Figure 3.36 shows the SEM images of different nanostructures after silicon etch with the depth of around 120 nm. Compared to lift-off, this method is more easy to obtain high resolution holes patterns and better for mold inversion.

The comparison between these three different pattern transfer techniques have been summarized in table 3.10.

3.6 Conclusion

The aim of this chapter was to perform a systematic study of soft UV nanoimprint lithography process and all the associated etching processes.

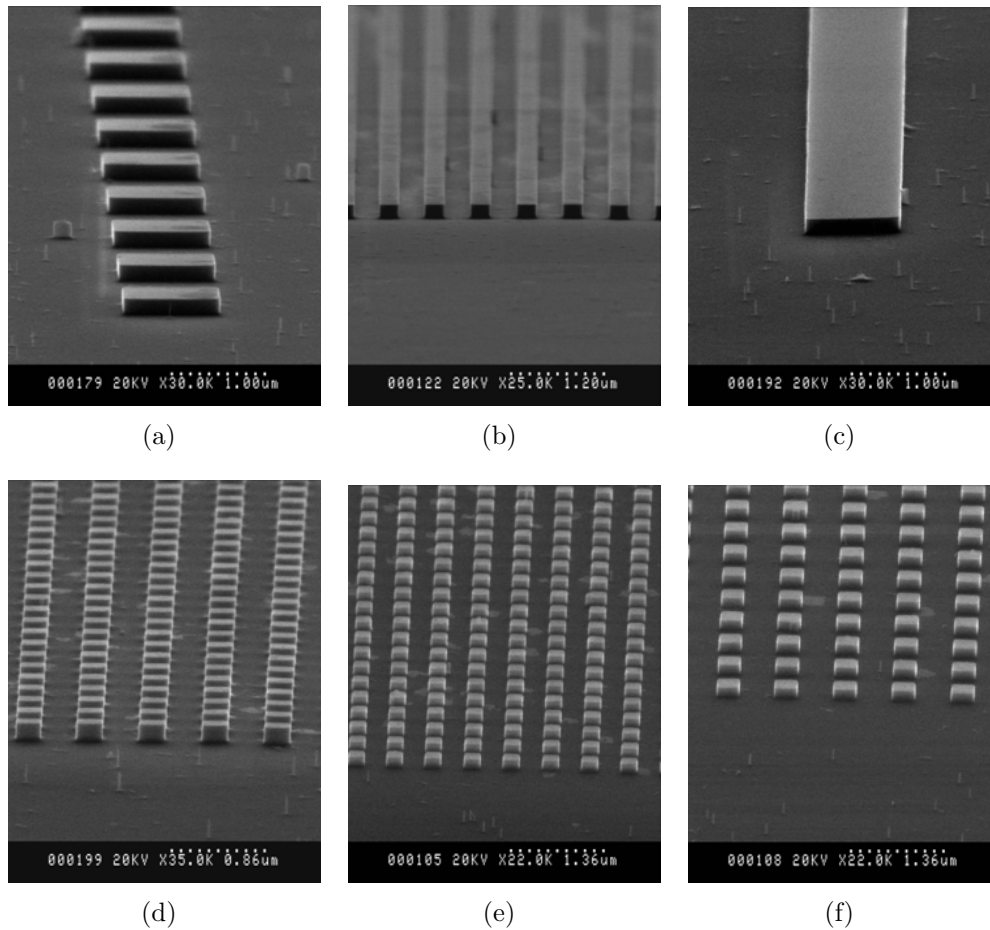


Figure 3.36: SEM images of the lines and dot arrays transferred into silicon with different sizes. The etch depth of each pattern is about 120nm

To develop soft UV nanoimprint lithography and also thermal nanoimprint lithography, we have introduced this chapter by presenting the new imprinter - Nanonex 2500 system, with which the pressure can be precisely applied. Meanwhile, both UV-NIL and T-NIL utilized a ACP system equipped on this Nanonex imprinter that shows advantage of ultra-uniformity, low lateral stress, less damage to both the mold and substrate. This point mainly embodies in mold duplication. After brief introduction of imprint tools, two types of photocurable resists were analyzed (Amonil and NXR). Both of these two resists offer high photo-sensitivity and high plasma etch resistance, but NXR resist is more expensive as well as the storage time is very short. The soft UV nanoimprint lithography process has been studied both theoretically and experimentally. Two primary im-

Pattern transfer technique	Advantages	Disadvantages
RIE	<ol style="list-style-type: none"> 1. High resolution and cleanliness 2. Anisotropic etch profiles 3. Faithfully transfer patterns into under layer 4. Better process control 	<ol style="list-style-type: none"> 1. Re-deposition of non-volatile compounds 2. Need expensive equipment 3. Some gases are quite toxic and corrosive
Lift-off	<ol style="list-style-type: none"> 1. High resolution 2. Versatile 3. Multi-layer 4. Limited damage 5. Low temperature 	<ol style="list-style-type: none"> 1. Limited thickness 2. Rounded feature profile 200/200 nm
IBE	<ol style="list-style-type: none"> 1. Versatile 2. Good homogeneous 	<ol style="list-style-type: none"> 1. Limited depth 2. Surface damage 3. Re-deposition in the walls

Table 3.10: Comparison of different pattern transfer techniques.

printing parameters: pressure and UV exposure time have been optimized: 10 psi pressure and 10 min UV exposure time can be applied for successful fabrication nanopatterns by soft UV-NIL.

After imprint, we have shown that the elimination of residual layer could have an essential effect on successful pattern transfer. Thus a detailed discussion of RIE etching Amonil process with CHF_3/O_2 , SF_6/O_2 , $\text{CHF}_3/\text{SF}_6/\text{O}_2$ plasmas has been presented: (1) in a CHF_3/O_2 plasma, O_2 plays very important role in affecting both the etch rate and the surface roughness. It's concluded from the above experiments that a relatively large sidewall angle of nanoline structures is obtained when the O_2/CHF_3 flow rate at 6/16 sccm, the power at 25 W and the pressure at 7 mtorr. (2) In a SF_6/O_2 plasma, SF_6 is used to instead of CHF_3 to enhance the etching speed. It's found that the O_2 concentration is of vital importance to monitor etch profile and surface roughness. (3) In a $\text{CHF}_3/\text{SF}_6/\text{O}_2$ plasmas, CHF_3 is added into SF_6/O_2 gas mixture and is shown to lower the surface roughness. A smooth and vertical line profile is obtained with $\text{CHF}_3/\text{SF}_6/\text{O}_2$ gas flow at 12/8/2 sccm, the pressure at 7 mtorr and the RF power can be varied from 10 W to 25 W.

For transfer, both bi-layer and tri-layer system have been described. Whereas, a tri-layer system is mostly employed due to the enhanced process latitude. But with the feature size down to 100 nm, we found that it's difficult to transfer the nanostructures. To solve this problem, we proposed to use IBE system transfer the patterns by direct etching. Finally, high

resolution pattern can be transferred to Si substrate by traditional RIE.

In a word, although soft UV-NIL is an emerging lithographic technology that promises high-throughput patterning of nanostructures with high resolution, challenges concerning throughput, defect tolerance and multi layer overlay still need supreme efforts.

Bibliography

- [1] N. Roos, T. Luxbacher, T. Glinsner, K. Pfeiffer, H. Schulz and H. -C. Scheer. Nanoimprint lithography with a commercial 4-in. bond system for hot embossing. *Proc. SPIE*, **4343**:427, (2001).
- [2] L. Bendfeldt, H. Schulz, N. Roos and H. -C. Scheer. Groove design of vacuum chucks for hot embossing lithography. *Microelectron. Eng.*, **61-62**:455, (2002).
- [3] T. Haatainen, J. Ahopelto, G. Gruetzner, F. Marion and K. Pfeiffer. Step & stamp imprint lithography using a commercial flip chip bonder. *Proc. SPIE*, **3997**:4874, (2000).
- [4] Molecular Imprints: <http://www.molecularimprints.com>; EVG: <http://www.evg.com>; Nanonex: <http://www.nanonex.com>; Suss MicroTec: <http://www.suss.com>; Obducat: <http://www.obducat.com>.
- [5] H. Tan, L. S. Kong, M. Li, C. Steere and L. Koecher. Current status of nanonex nanoimprint solutions. *Proc. SPIE*, **5374**:213, (2004).
- [6] M. T. Li, H. Tan, L. S. Kong and L. Koecher. Four-inch photocurable nanoimprint lithography using NX-2000 nanoimprinter. *Proc. SPIE*, **5374**:209, (2004).
- [7] M. Bender, M. Otto, B. Hadam, B. Spangenberg and H. Kurz. Multiple imprinting in UV-based nanoimprint lithography: related material issues. *Microelectron. Eng.*, **61-62**:407, (2002).
- [8] M. Bender, A. Fuchs, U. Plachetka and H. Kurz. Status and prospects of UV-nanoimprint technology. *Microelectron. Eng.*, **83**:827, (2006).
- [9] E. K. Kim, N. A. Stacey, B. J. Smith, M. D. Dickey, S. C. Johnson, B. C. Trinke and C. G. Willson. Vinyl ethers in ultraviolet curable formulations for step and flash imprint lithography. *J. Vac. Sci. Technol. B*, **22**:131, (2004).

- [10] E. K. Kim, M. D. Stewart, K. Wu, F. L. Palmieri, M. D. Dickey, J. G. Ekerdt and C. G. Willson. Vinyl ether formulations for step and flash imprint lithography. *J. Vac. Sci. Technol. B*, **23**:2967, (2005).
- [11] M. Wen and A. V. McCormick. A kinetic model for radical trapping in photopolymerization of multifunctional monomers. *Macromolecules*, **33**:9247, (2000).
- [12] M. Wen, L. E. Scriven and A. V. McCormick. Kinetic Gelation Modeling: Kinetics of Cross-Linking Polymerization. *Macromolecules*, **36**:4151, (2003).
- [13] A. Ravve. Principles of Polymer Chemistry. 1st and 2nd editions, Springer, New York, (1995 and 2000).
- [14] G. Strobl. The Physics of Polymers. Springer, (1996).
- [15] H. S. Nalwa. Nanomaterials and magnetic thin films. *Handbook of thin film materials*, **5**, Academic Press, (2002).
- [16] J. Shi. Développement et exploration de la lithographie par nanoimpression molle assistée par UV pour les application biologiques. *PhD thesis*, Paris 6 University, (2007).
- [17] AMO GmbH: <http://www.amo.de/>.
- [18] P. Voisin, M. Zelsmann, R. Cluzel, E. Pargon, C. Gourgon and J. Boussey. Characterisation of ultraviolet nanoimprint dedicated resists. *Microelectron. Eng.*, **84**:967, (2007).
- [19] Y. Namba and H. Takahashi. Chemically amplified Si-containing resist bilayer resist process. *J. Photopolym. Sci. Technol.*, **11**:663, (1998).
- [20] F. Hamouda, G. Barbillon, S. Held, G. Agnus, P. Gogol, T. Maroutian, S. Scheuring, B. Bartenlian. Nanoholes by soft UV nanoimprint lithography applied to study of membrane proteins. *Microelectron. Eng.*, **86**:583, (2009).
- [21] C. Gatzert, A. W. Blakers and P. N. K. Deenapanray. Investigation of reactive ion etching of dielectrics and Si in CHF_3/O_2 or CHF_3/Ar for photovoltaic applications. *J. Vac. Sci. Technol. A*, **24**:1857, (2006).
- [22] C. C. Zhang, C. S. Yang and D. F. Ding. Deep reactive ion etching of commercial PMMA in O_2/CHF_3 , and O_2/Ar -based discharges. *J. Micromech. Microeng.*, **14**:663, (2004).

- [23] S. M. Rosnagel, J. J. Cuomo and W. D. Westwood. Fundamentals, etching, deposition and surface interactions. *Handbook of plasma processing technology*, Noyes publications, (1989).
- [24] R. Knizikevičius. Simulations of Si and SiO₂ etching in SF₆+O₂ plasma. *Acta Phys. Pol. A*, **117**:478, (2010).
- [25] Y. -J. Lii and J. Jorné. Plasma etching of silicon in SF₆. *J. Electrochem. Soc.*, **137**:3633, (1990).
- [26] W. W. Brandt and T. Honda. Mass spectrometric transient study of dc plasma etching of Si in SF₆/O₂ mixtures. *J. Appl. Phys.*, **49**:3796, (1978).
- [27] A. K. Paul, A. K. Dimri and R. P. Bajpai. Plasma etch models based on different plasma chemistry for micro-electro-mechanical-systems application. *Vacuum*, **68**:191, (2003).
- [28] R. Legtenberg, H. Jansen, M. D. Boer and M. Elwenspoek. Anisotropic reactive ion etching of silicon using SF₆/CHF₃/O₂ gas mixtures. *J. Electrochem. Soc.*, **142**:2020, (1995).
- [29] J. Minter, M. Ross, W. Livesay, S. Wong, M. Nancy and T. Marlowe. Advanced metal lift-off process using electron beam flood exposure of single layer photoresist. *Proc. of SPIE*, **3678**:1074, (1999).
- [30] J. X. Liang, F. Kohsaka, T. Matsuo, X. F. Li and T. ueda. Improved bi-layer lift-off process for MEMS applications. *Microelectron. Eng.*, **85**:1000, (2008).
- [31] A. Lebib, Y. Chen, F. Carcenac, E. Cambriil, L. Manin, L. Couraud and H. Launois. Tri-layer systems for nanoimprint lithography with an improved process latitude. *Microelectron. Eng.*, **53**:175, (2000).

Chapter 4

Gold nanohole arrays for biochemical sensing

In this chapter, we present a method to fabricate high quality periodic gold nanohole arrays. These arrays exhibit transmission enhanced surface plasmon resonance (SPR) and can thus be used for biochemical sensing applications. After a short introduction on the recent development of nanohole arrays for SPR based sensors and the conventional patterning methods, we describe the details of our fabrication process based on soft UV nanoimprint lithography combined with both reactive ion etching and Cr/Au lift-off. Then, we present our results including the SEM characterization and the measured optical spectra. Finally, we provide a theoretical analysis to show that such array could detect the absorption of chemical or biological molecules with high sensitivity.

4.1 Introduction

Recent progress in nano-optics has paved the route toward the development of highly sensitive and label-free optical transducers using the surface plasmon resonance of metal nanostructures. Metal nanostructures have attracted considerable attention both fundamentally and technologically because of their unique physical and chemical properties compared to their bulk counterparts. One of the most fascinating aspects is their optical properties, including extraordinary light transmission [1], collimation of light through a subwavelength aperture [2], giant field enhancement [3] and surface plasmon waveguiding [3, 4].

Although initially only spherical nanoparticles were investigated, aniso-

tropy effects were very rapidly observed to be more important than those derived from size and even composition. Therefore, research on metal nanorods [5], nanowires [6], nanocubes [7], nanorings [8], nanoshells [9], nanoprisms [10, 11], or even nanostars [12] has demonstrated that small variations in the morphology of the particles could strongly influence the optical response. Among the various metal nanostructures, nanohole array has attracted considerable interest in optical phenomena and applications due to the discovery of its extraordinary transmission [1, 13]. It's generally agreed that surface plasmon resonances play a key role in enhancing the transmission of light through apertures in noble metal films, although diffraction effects, especially in the presence of long-range order, also need to be considered.

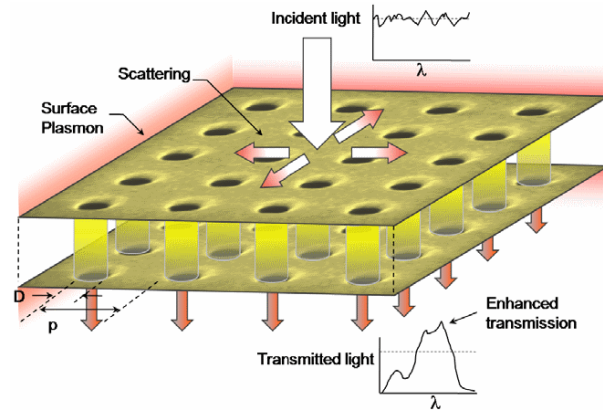
4.1.1 Nanohole arrays as SPR based sensors

In 1998, Ebbesen and co-workers reported enhanced transmission of light through arrays of subwavelength holes in optically thick metallic films, at normal incidence [1]. Peaks in the transmission spectra were observed, and the transmission efficiency was found to exceed unity when normalized to the hole-area. Figure 4.1(a) shows a schematic illustrating enhanced transmission through nanohole arrays, and a sample of many hole geometries and configurations that have been investigated by different groups (including Brolo et al. [15], Gordon et al. [16], Tetz et al. [17], Dintinger et al. [18]). As shown in this figure, the maxima can be seen in the transmission spectra which result from a resonant interaction of the incident light with surface plasmons, whereas the minima associated with Wood's anomaly occurs when diffracted light becomes tangent to the metal surface.

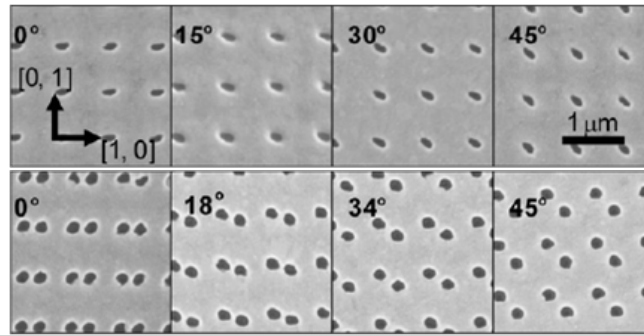
The properties of enhanced transmission is attributed to initial scattering of the incident light into surface plasmons (SPs) that penetrate the nanoholes and are again scattered on the other side of the film. The coupling of light with a surface plasmon (SP) on a periodically corrugated metal surface follows the law of momentum conservation:

$$k_{sp} = k_x + iG_x + jG_y \quad (4.1)$$

where k_{sp} is the SP wave vector, $k_x = \hat{x}(2\pi/\lambda)\sin\theta$ is the \hat{x} component of the incident light's wave vector ($\theta = 0^\circ$ corresponds to normal incidence) that lies in the plane of the sample, G_x and G_y are the reciprocal lattice vectors for a square-lattice with $G_x = G_y = 2\pi/p$ (i and j are integers).



(a)



(b)

Figure 4.1: (a) Schematic diagram illustrating incident light scattering into SP modes and enhanced transmission at select wavelength; (b) SEM images of several nanohole arrays with various geometries and dimensions [14].

The SP dispersion is given by:

$$k_{sp} = \frac{\omega}{c} \left(\frac{\epsilon_d \epsilon_m}{\epsilon_d + \epsilon_m} \right)^{1/2} \quad (4.2)$$

Meanwhile, the conditions for the occurrence of Wood's anomaly can be gained by exchanging the wave vector of the grazing light that has a magnitude $k_{diff} = 2\pi n_d / \lambda$ (where $n_d = \sqrt{\epsilon_d}$) for k_{sp} . The minima always occurring at slightly shorter wavelengths than the maxima. With normal incident light ($\theta = 0$), the transmission maxima occurs at the wavelength λ_{sp} that satisfies the two-dimensional grating SPR coupling conditions given by reduce Eqs. 4.1 and 4.2 to:

$$\lambda^{SP}(i, j) = p(i^2 + j^2)^{-1/2} \left(\frac{\epsilon_d \epsilon_m}{\epsilon_d + \epsilon_m} \right)^{1/2} \quad (4.3)$$

where p is the periodicity of the array, ϵ_d is the effective dielectric constant of the medium in contact with the metal and ϵ_m is the dielectric constant of the metal. The enhanced transmission was observed for typical metals that support SPPs in the visible range, such as gold, silver and copper films. On the other hand, the phenomenon was not observed from nanostructures in materials that do not support SPPs, such as Germanium films.

The extent of SPs generation depends on the combination of incident light wavelength, hole geometry/periodicity and material/medium dielectric constants. Figure 4.2 gives an overview of major routes for active plasmonics: active tuning of dielectric constant of surrounding media; active tuning of the size/shape of metal nanostructures; charge/discharge of metal nanostructures; active tuning of interparticle distance and spinplasmonics.

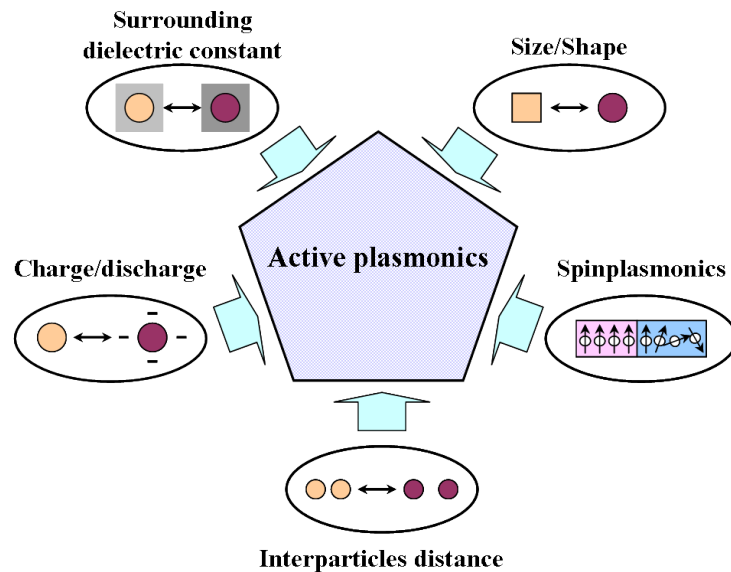


Figure 4.2: An overview of major routes for the development of active plasmonics.

Recent works have shown that the shape of the nanoholes has an important influence on the polarization of the transmitted light, as well as on the resonance peak wavelength. Changing the basis shape from circular holes to elliptical [16] and rectangular holes [19] has a strong influence on the polarization and resonance properties.

4.1.2 Patterning methods for plasmonic arrays

Although much progress has recently been made in SPR field, there are still many challenges in the fundamental understanding and devising applications of plasmonic phenomena. The first and one of the most significant challenges is nanofabrication, especially the low cost and high throughput production of metal nanostructures with tailorable plasmonic properties. Therefore, there is a growing interest in developing cost-effective and high-efficient fabrication techniques and effective nanoengineering approaches for metal nanostructure arrays of various shapes and sizes. Several methods such as near field optical lithography, electron beam lithography, imprint lithography, scanning probe lithography and dip pen lithography have been developed in order to achieve nanometer-scale features.

Nanosphere lithography(NSL) is an inexpensive and versatile hybrid bottom-up fabrication method introduced by Van Duyne for fabricating periodic arrays of metallic nanostructures on surfaces [20]. This technique begins with the self-assembly of size-monodispersed nanospheres to form a two-dimensional colloidal crystal deposition mask. As the solvent evaporates, capillary forces draw the nanospheres together, and the nanospheres crystallize into a hexagonally close-packed pattern on the substrate. Following self-assembly of the nanosphere mask, a metal or other material is then deposited. After metal deposition, the nanosphere mask is removed, leaving behind surface-confined nanoparticles. NSL has been implemented in both a single layer and double layer approach with extensive characterization and utilization of triangular nanoparticles resulting from the single layer method. Limitations of NSL technique includes surface coverage and the geometric constraints.

Colloidal lithography is the other versatile technique that can be used to form random arrays of nanoholes, nanorings and nanodisks [21]. This unconventional nanofabrication technique involves absorbing polystyrene particles onto substrate by electrostatic self-assembly. Then the randomly adsorbed particles are used as a mask for subsequent evaporation or etching process wherein the size of the sphere dictates the size of the resulting nanostructures (Fig. 4.3). Although the preparation of a colloidal mask is facile, compared to other lithographic techniques, this colloidal lithography appears less controllable since the shape of the pattern cannot be precisely defined.

In order to compensate limitations encountered by a number of current metal nanostructures fabrication methods, we propose here to use nanoimprint lithography to pattern on large area nanohole arrays. These nanohole

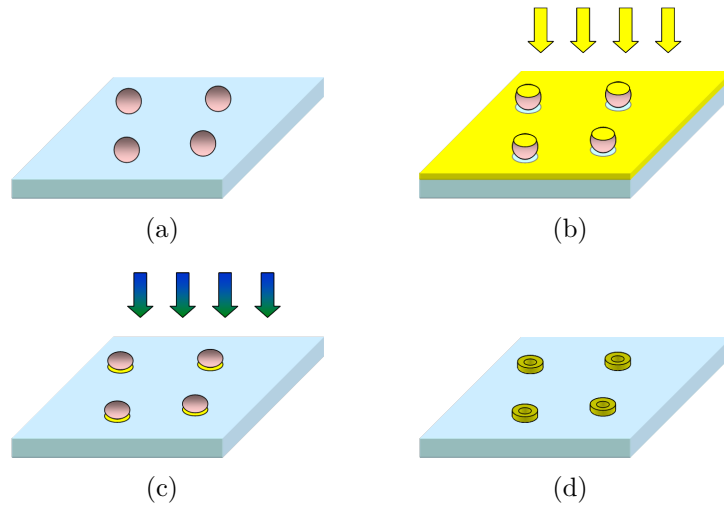


Figure 4.3: Schematic depiction of nanoring fabrication by colloidal lithography method.

arrays can then be integrated into a microfluidic device for further sensing even with parallel multichannels.

4.2 Fabrication of gold nanohole arrays

Soft UV nanoimprint lithography combined with both reactive ion etching and Cr/Au lift-off processes has been used to replicate metal nanohole arrays on large surfaces. The tri-layer soft UV nanoimprint previously presented in Chapter 3 was used to fabricate these gold nanohole arrays on standard glass slides. The nanoimprint patterning process is schematically described in Fig. 4.4.

Si master mold was obtained by E-beam lithography and RIE etch which consists of nanodots with various diameter/period (e.g., 100/200 nm, 200/400 nm, 250/500 nm, 300/600 nm), 130 nm depth and surface of 200 μm x 200 μm for each arrays (Figure 4.5). The soft mold utilized is the bi-layer h-PDMS/PDMS stamp previously described in chapter 2.

Soft UV-NIL was performed in an Amonil/Ge/PMMA tri-layer. A 300 nm thick PMMA layer was spin coated on the glass and prebaked at 180 °C for 10 min. A 10 nm thin Ge layer was then deposited by electron beam evaporation (Plassys MEB550SL) on top of the PMMA layer. A 180 nm thick Amonil resist (AMO, MM4) layer was finally spin coated on the top to fabricate the tri-layer. After applying an optimal pressure 10 psi (which

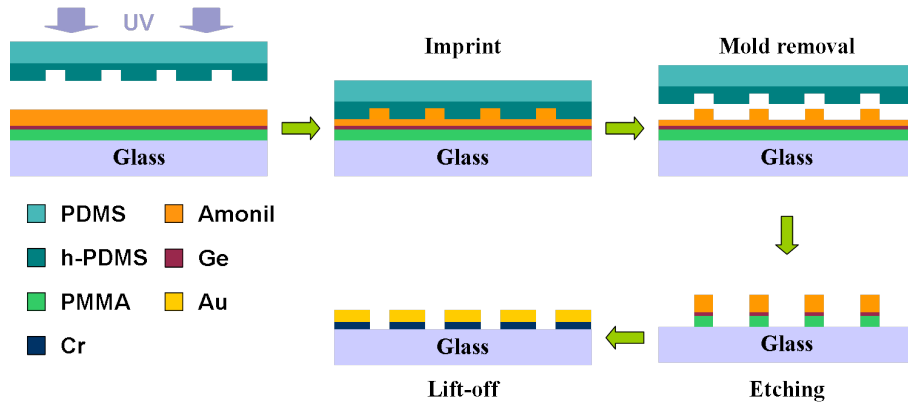


Figure 4.4: Description of the nanohole fabrication process based on soft UV nanoimprint.

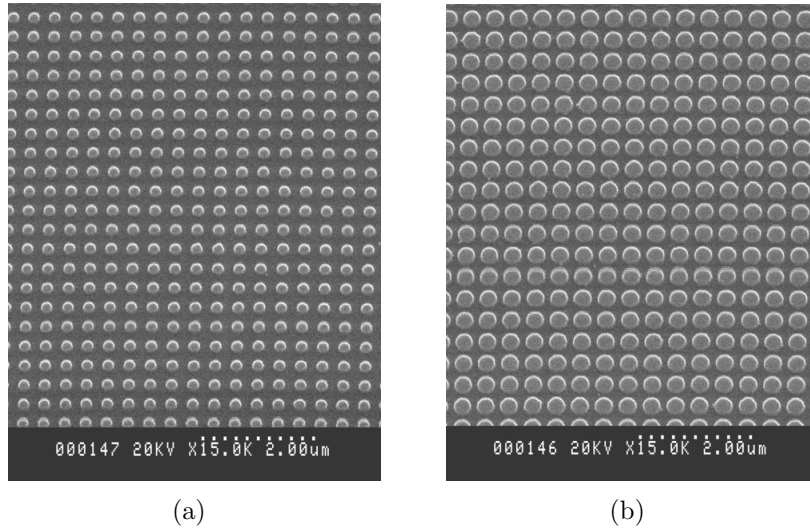


Figure 4.5: Scanning electron micrography (SEM) recorded on the Si master for nanodot gratings, with different diameter d and period p : (a) $d = 200$ nm, $p = 400$ nm; (b) $d = 300$ nm, $p = 600$ nm. The height of the pattern is about 130 nm.

has been previously discussed in chapter 3), Amonil resist was exposed to UV light for 10 min at room temperature. Finally, the soft stamp was separated from the substrate.

After UV-NIL, three consecutive steps of RIE were performed including: (1) the Amonil residual layer was etched by O_2 (2 sccm)/ CHF_3 (20 sccm) gas mixture under a pressure of 7 mtorr and RF power 25 W during about 4 min 35 s, (2) the Ge interlayer was etched using SF_6 in 15 s and (3) finally the PMMA underlayer was etched in 2 min 30 s under pure O_2

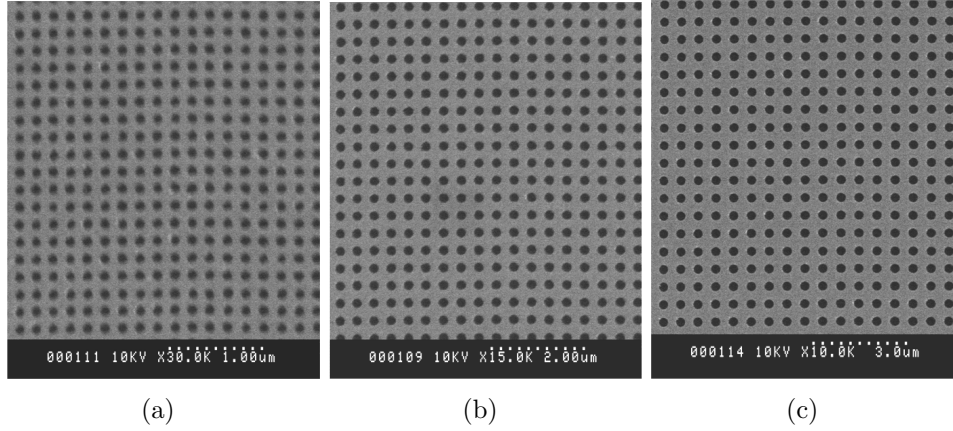


Figure 4.6: SEM images of arrays with sub-wavelength holes of different diameters d and periodicities p (a) $d = 100$ nm, $p = 200$ nm; (b) $d = 200$ nm, $p = 400$ nm; (c) $d = 250$ nm, $p = 500$ nm after Cr/Au lift-off.

plasma. After RIE, a Cr (5 nm)/Au (50 nm) layer was deposited in the tri-layer patterns and lifted off. The 5 nm chromium layer was used to improve adhesion of gold on the glass substrate. Fig. 4.6 shows SEM images of nanohole arrays with different diameters and periods after lift-off. A good homogeneity and uniformity can be observed for each pattern.

Pattern size on the master (nm)	$d = 100$	$d = 200$	$d = 250$
Pattern size on the sample (nm)	$d = 99 \pm 2$	$d = 199 \pm 2$	$d = 248 \pm 3$

Table 4.1: Comparison of feature size of the Si master mold and the sample fabricated by soft UV-NIL after lift-off process.

Here we adopted the same method as described in Chapter 2 — “Image J” software — to analysis the pattern outline in each SEM images shown in Fig. 4.6, thus contributing to calculate the feature size distribution. Table 4.1 summaries the feature size values recorded on Si master and the fabricated samples after lift-off process. Only a small size difference (≤ 3 nm) of the gold nanohole is generally observed compared to the master, which is related to the optimized tri-layer pattern transfer processes. These results turns out that all of these patterns can be replicated with a well controlled process.

4.3 Experimental setup

4.3.1 Simple fluidic device fabrication

The simple fluidic device was constituted of 2 parts: (1) a glass substrate that supports the nanoholes arrays, (2) a block of PDMS containing a reservoir for approximately 500 μl solution. This device was fabricated in two steps.

First, the PDMS is prepared by pouring it on a virgin Si wafer with a thickness of about 4 mm. After degassing during 10 min, it was cured at 80 °C for 2 h. It was then peeled off from the Si wafer and the macrochamber was manually cut with a scalpel.

The PDMS was then sealed to the flat surface of the glass substrate in a reversible way because the substrate contains the gold nanohole array. To guarantee the reversibility of the sealing, we do not perform any plasma treatment to the PDMS surface and a thin layer of PMMA was partially spin coated around the gold pattern area, i.e. in the region where the PDMS layer will contact the surface. This layered configuration enables filling of the desired chemical/biological solution, as well as a perfect cleaning of the nanohole arrays after each measurement. Figure 4.7(a) and (b) shows the geometry and one typical view of this simple fluidic device with embedded nanohole arrays.

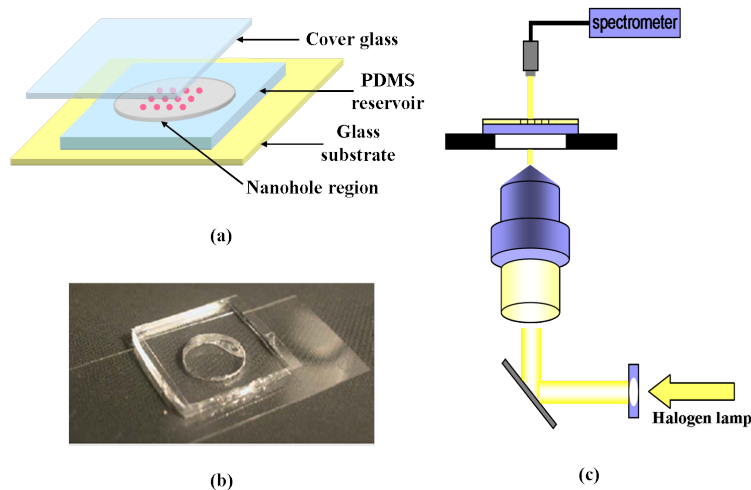


Figure 4.7: Application of nanohole array sensing elements: (a) Schematic and (b) image illustrating the architecture of the simple microfluidic device with embedded nanohole arrays; (c) Schematic of the optical configuration for transmission measurements through the periodic arrays nanoholes.

4.3.2 Chemicals

Solutions of known and controllable refractive index were required to establish the sensitivity of the nanohole array sensors and to demonstrate local chemical detection (or biological detection). To chemically modify the surface of the gold nanohole arrays:

1. Self-assembled monolayers (SAMs) of alkane thiol molecules is firstly used. Thiols are very small molecules of a few nm in length, which contain a thiol group (SH), also called “mercapto” group, at one end. Their general chemical structure is R-SH or $R(\text{CH}_2)_{nc}\text{SH}$ if they contain an alkyl chain. The molecule used in this test is hexadecanethiol (Sigma Aldrich). These alkane thiol molecules have the ability to bind spontaneously to some metals (gold, silver, platinum) and form close-packed monolayers. The binding energy of thiol group to gold of approximately 120 kJ/mol is relatively strong and the layer is very stable and free of holes. In our case, we have prepared a 10 mM hexadecanethiol (Sigma Aldrich) solution in pure ethanol. Since the kinetic of the reaction between thiols and gold is very fast, the sample was incubated only for 1 min in this solution, before being washed briefly in ethanol and then dried by nitrogen.

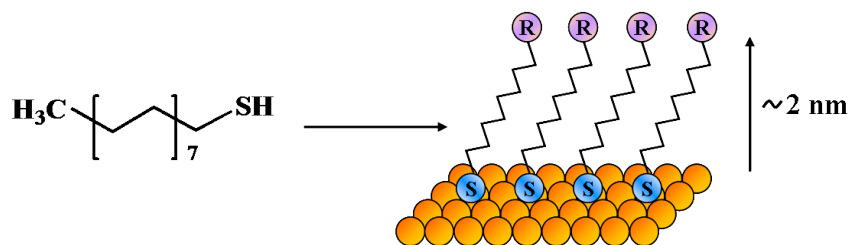


Figure 4.8: Schematic of thiol containing alkyl chains on the surface of gold.

2. Aqueous sucrose solutions with different concentration (20%, 40% and 60%) were then used. Sucrose is an organic compound with the chemical fomulation $\text{C}_{12}\text{H}_{22}\text{O}_{11}$ (Fig. 4.9). Each sucrose solution was prepared by dissolving 99% pure sucrose crystals (Sigma Aldrich) in de-ionized water. The refractive index of these sucrose solutions was varied from 1.33 (for pure water) to 1.44 (for 60% concentrated solution). A droplet of a few hundred u-litres of these solutions was placed on the surface of the sample. On each grating the measurements were first started with the less concentrated solution, and be-

fore each solution change the sample was rinsed in de-ionized water.

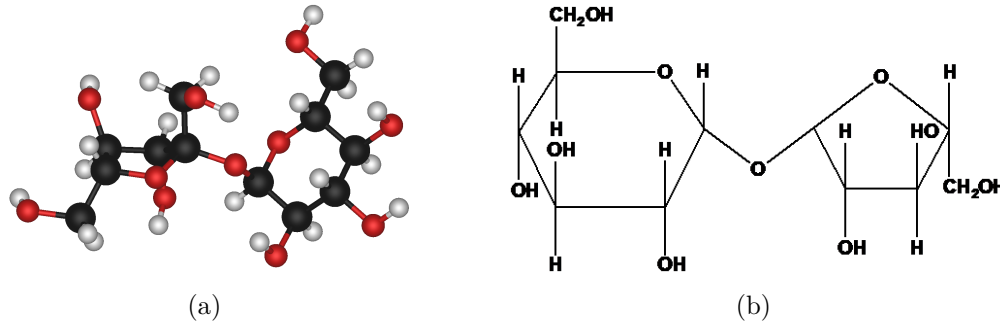


Figure 4.9: Chemical structural formula of sucrose molecular.

4.3.3 Optical measurements

Figure 4.7(c) shows a schematic of the setup for the optical measurement. A broadband unpolarized white light source from a 100 W halogen lamp was provided to the nanohole arrays at normal incidence through a 100x microscope objective (NA = 1.3). This objective ensured that only one array (200 μm x 200 μm) received the incident light. The optical transmission spectra through nanohole arrays were recorded using a Carl Zeiss Axiovert 200 inverted microscope (German) coupled with fiber to a UV/visible spectrometer (USB 2000 Ocean optics).

4.4 Optical characterization

4.4.1 SPR of nanohole arrays with different period

As a preliminary test, transmission spectra were first measured in air with no solution in top of the nanohole arrays in air. The transmission spectra obtained for nanohole arrays with different diameters and periods are presented in Fig. 4.10. As observed, increasing the nanohole diameter and the array period leads to a shift towards longer wavelengths. The transmission peak arises at $\lambda_{sp} = 542.90, 582.87$ and 625.90 nm on the Au-glass interface, respectively for $p = 300, 400$ and 500 nm (Fig. 4.10), and the measured wavelength of peak transmission were similar to the limit of detector resolution. The peak located between 530 nm and 630 nm is

designated as the (1,0) peak, which is so defined from the result of resonant excitation of the surface plasmons with the periodic structure. As it can be seen in Figure 4.10, an increase in hole diameter and period also causes spectral broadening, which reflects a shortening of the life time of the hole resonance [22].

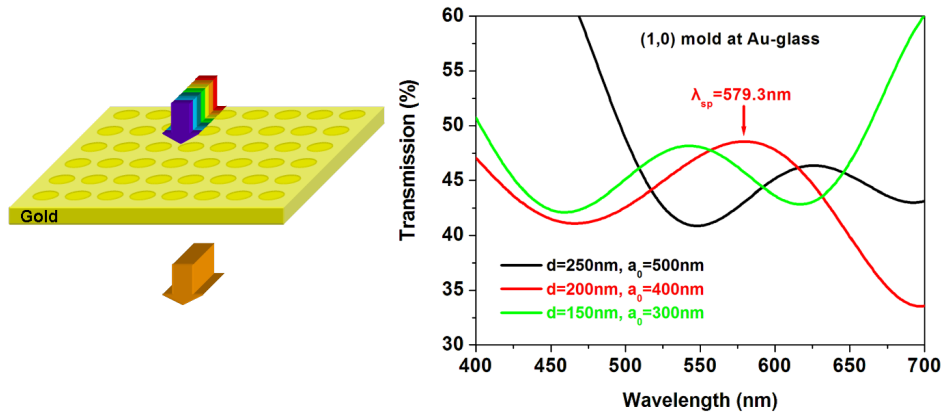


Figure 4.10: Transmission spectra obtained through three nanohole arrays with different diameters d and periodicities p (green) $d = 150$ nm, $p = 300$ nm; (red) $d = 200$ nm, $p = 400$ nm; (black) $d = 250$ nm, $p = 500$ nm.

The minima appearing before resonance in the spectrum of the nanohole array with $p = 500$ nm can be attributed to Wood's anomaly. This effect scatters incident light resonantly with wavelength in the dielectric, thus decreasing the enhanced transmission.

4.4.2 SPR after chemical modification of Au nanohole surface

We have studied the problem of how k_{sp} in the SPR spectra can be affected by surface chemical grafting. Here, the variation in the dielectric constant of the surrounding medium has a similar prominent effect on the position of the SP resonances, as illustrated in Fig. 4.11 and Fig. 4.12. All spectra were obtained for the same array with $d = 200$ nm and $p = 400$ nm.

Fig. 4.11 compares the spectrum after covalent thiol grafting and the original one. A shift of $\Delta\lambda_{sp} = 2.73$ nm coupled to a tiny transmission enhancement is observed. Since this shift of the transmission peak is too much smaller, it's difficult to conclude that this wavelength shift is really related to the binding of thiol molecular on the surface. Therefore,

solutions with different refractive index are proceeded to measure the sensitivity of the biosensor.

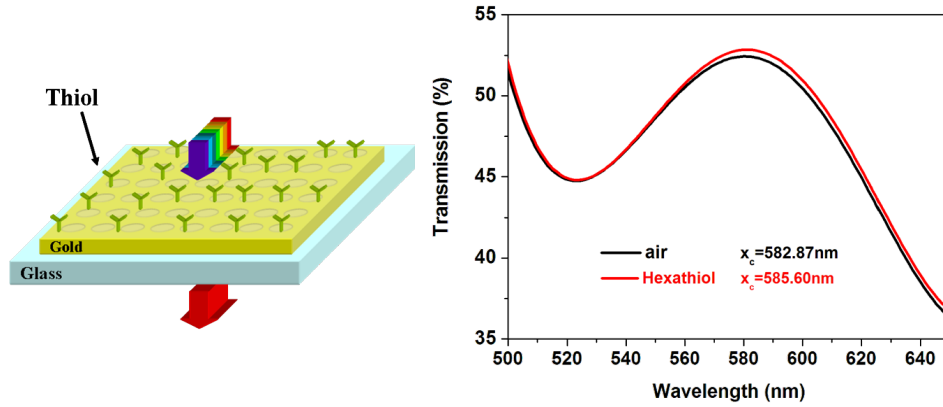


Figure 4.11: Transmission spectra obtained through the 400 nm periodicity arrays with self-assembled monolayer (SAM) hexadecanethiol.

Fig. 4.12(b) shows the transmission spectra collected for the pure water case, three different sucrose solutions spanning the range. It is observed that the spectrum is red-shift in response to the increased refractive index of pure water, sucrose solution with 20%, 40% and 60% concentration, respectively. In order to find the value of each transmission peak accurately, the curve fitting procedures were used for spectrum analysis in this study. The function used is:

$$y = y_0 + 2\frac{A}{\pi} \frac{w}{4(x - x_c)^2 + w^2} \quad (4.4)$$

in which A is the area, w is the width, x_c is the center and y_0 is the Y-values offset.

Fig. 4.12(c) presents one example of the curve fitting for 60% sucrose solution spectrum. The hollow circular curve is the original spectrum and the red solid curve is the fitted spectrum. It's obvious that this procedure gives a good fitting, as shown by the excellent overlap from visual observation. The resulted wavelengths of peak transmission (x_c) for the pure water case and all sucrose solutions (20%, 40%, 60%) obtained by using lorentz fit is 623.6 nm, 633.2 nm, 640.2 nm and 646.9 nm as listed in Fig 4.12(b).

The measurements of the transmission peak position as a function of the refractive index of liquid is displayed in Fig. 4.12(b). As the index of refraction of the liquid is increased, a approximate linear shift of the

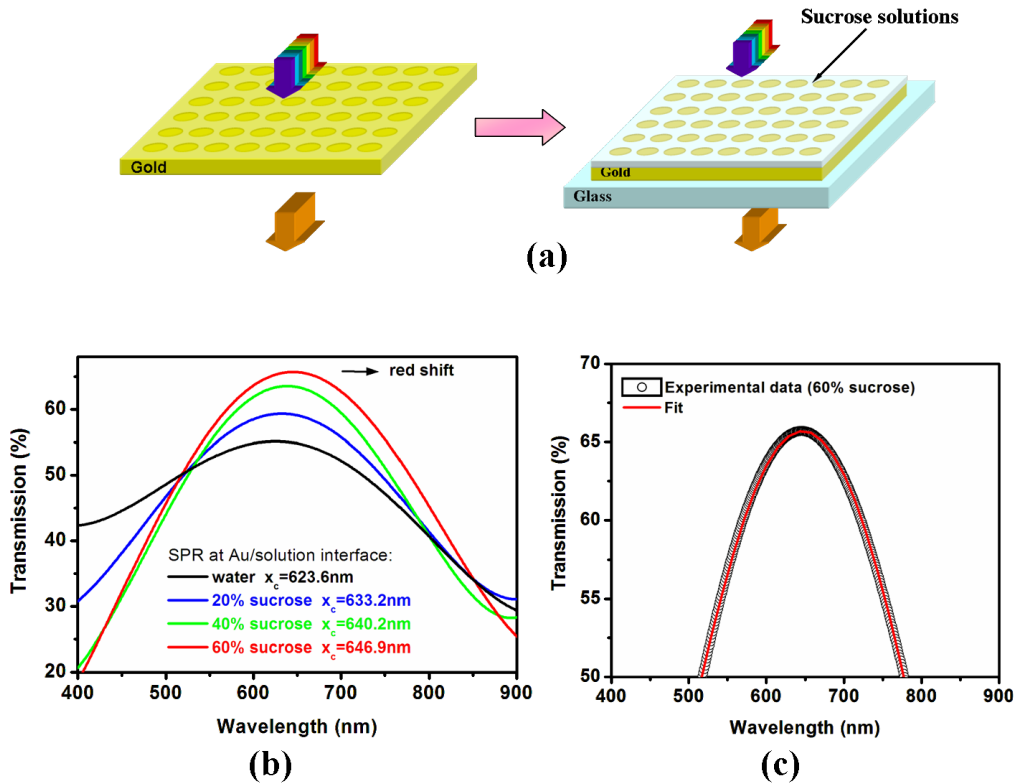


Figure 4.12: Results of sensitivity test with sucrose solutions of known refractive index. Transmission spectra were obtained through the 400 nm periodicity arrays for pure water, after sucrose solutions with increasing refractive index. (a) Schematic of sucrose flow on the gold surface. (b) Sample transmission spectra plotted together. (c) The measured value and the Lorentz fit curve for a sample with 60% sucrose solution.

resonance position to longer wavelengths is detected. The sensitivity S of our SPR biosensor can then be deduced from $S = \Delta\lambda/\Delta n_{eff}$ [23]. A shift of 26.3 nm is recorded for a change in the index of refraction of the liquid of $\Delta n = 0.11$. This results in a sensitivity of 208 nm/RIU.

Due to the unusual optical properties of the array of sub-wavelength metallic holes, an enhancement in transmission has been measured after two types of chemical change of the environment of the nanoholes. We have shown that the λ_{sp} value is very sensitive to the local dielectric environment and the observed red shift varies linearly with increasing solvent refractive index.

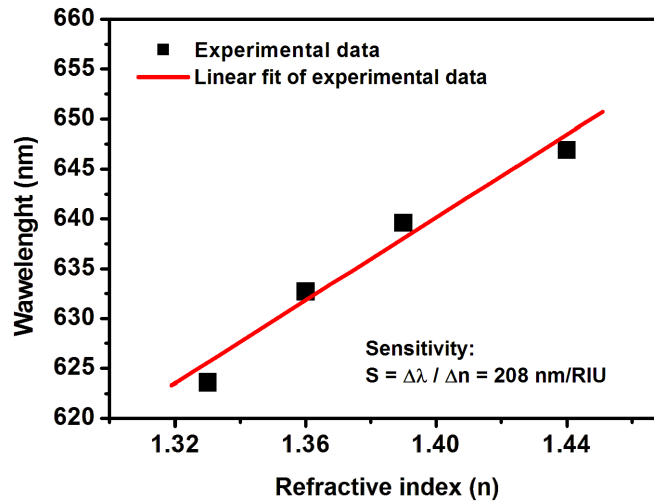


Figure 4.13: The relative redshift in peak wavelength for four peaks exhibited by the array as a function of refractive index.

4.5 Conclusion

In summary, we have presented a replication technique of metallic nanohole arrays based on soft UV nanoimprint and lift-off. The plasmonic transmission response of these nanohole arrays is related to their diameter and period. To check their sensitivity to any refractive index change in the vicinity of the nanostructure surface, different chemical solutions have been tested. For sucrose solutions, an enhancement in transmission has been observed, which is larger for high sucrose content in agreement with the dielectric index change. The sensitivity to thiol grafting has also been studied down to 2 nm thickness, which confirms the high sensitivity of nanohole arrays for real-time chemical/bio-sensing with SPR.

In the context of on chip chemical and biological analysis, such nanohole arrays can provide several unique advantages: (1) transmission mode operation at normal incidence simplifies alignment, facilitates the use of high numerical aperture optics, and permits eventual device miniaturization; (2) the footprint of a nanohole array is relative small ($\approx 10 \times 10 \mu m^2$) which enables a high packing density for multiplex array sensing; and (3) in contrast to other SPR based on colloidal nanoparticles, or roughened surfaces, nanohole arrays can be fabricated with high reproducibility. Anyway, nanotechnology methods for biochemical applications, with challenging requirements regarding dependability, cost, measurement precision, speed, and sample throughput and likewise experiencing rapid development. By

introducing advanced materials and devices, the nanotechnology-based platforms have the potential to achieve these requirements and will enable better biomolecules research.

Bibliography

- [1] T. W. Ebbesen, H. J. Lezec, H. F. Ghaemi, T. Thio and P. A. Wolff: Extraordinary optical transmission through sub-wavelength hole arrays, *Nature* **391**, 667 (1998)
- [2] H. J. Lezec, A. Degiron, E. Devaux, R. A. Linke, L. Martin-Moreno, F. J. Garcia-Vidal and T. W. Ebbesen: Beaming light from a sub-wavelength aperture, *Science* **297**, 820 (2002)
- [3] W. L. Barnes, A. Dereux and T. W. Ebbesen: Surface plasmon sub-wavelength optics, *Nature* **424**, 824 (2003)
- [4] S. Lal, S. Link and N. J. Halas: Nano-optics from sensing to waveguiding, *Nat. Photon* **1**, 641 (2007)
- [5] J. Pérez-Juste, I. Pastoriza-Stantos, L. M. Liz-Marzán and P. Mulvaney: Gold nanorods: synthesis, characterization and applications, *Coord. Chem. Rev.* **249**, 1870 (2005)
- [6] Y. Xia, P. D. Yang, Y. Sun, Y. Wu, B. Gates, Y. Yin, F. Kim and H. Yan: One-dimensional nanostructures: synthesis, characterization, and applications, *Adv. Mater.* **15**, 353 (2003)
- [7] S. H. Im, T. T. Lee, B. Wiley and Y. Xia: Large-scale synthesis of silver nanocubes: the role of HCl in promoting cube perfection and monodispersity, *Angew. Chem., Int. Ed* **44**, 2154 (2005)
- [8] S. Kim, J. -M. Jung, D. -G. Choi, H. -T. Jung and S. -M. Yang: Patterned arrays of Au rings for localized surface plasmon resonance, *Langmuir* **22**, 7109 (2006)
- [9] Y. G. Sun and Y. Xia: Increased sensitivity of surface plasmon resonance of gold nanoshells compared to that of gold solid colloids in response to environmental changes, *Anal. Chem.* **74**, 5297 (2002)

-
- [10] J. E. Millstone, S. Park, K. L. Shuford, L. Qin, G. C. Schatz and C. A. Mirkin: Observation of a quadrupole plasmon mode for a colloidal solution of gold nanoprisms, *J. Am. Chem. Soc.* **127**, 5312 (2005)
- [11] I. Pastoriza-Santos and L. M. Liz-Marzán: Synthesis of silver nanoprisms in DMF, *Nano Lett.* **2**, 903 (2002)
- [12] C. L. Nehl, H. Liao and J. H. Hanfner: Optical properties of star-shaped gold nanoparticles, *Nano Lett.* **6**, 683 (2006)
- [13] C. Genet and T. W. Ebbesen: Light in tiny holes, *Nature* **445**, 39 (2007)
- [14] D. Sinton, R. Gordon and A. G. Brolo: Nanohole arrays in metal films as optofluidic elements: progress and potential, *Microfluid Nanofluid* **4**, 107 (2008)
- [15] A. G. Brolo, S. C. Kwok, M. D. Cooper, M. G. Moffitt, C. W. Wang, R. Gordon, J. Riordon and K. L. Kavanagh: Surface plasmon-quantum dot coupling from arrays of nanoholes, *J. Phys. Chem. B* **110**, 8307 (2006)
- [16] R. Gordon, M. Hughes, B. Leathem, K. L. Kavanagh and A. G. Brolo: Basis and lattice polarization mechanisms for light transmission through nanohole arrays in a metal film, *Nano Lett.* **5**, 1243 (2005)
- [17] K. A. Tetz, L. Pang and Y. Fainman: High-resolution surface plasmon resonance sensor based on linewidth-optimized nanohole array transmittance, *Opt. Lett.* **31**, 1528 (2006)
- [18] J. Dintinger, S. Klein and T. W. Ebbesen: Molecule-surface plasmon interactions in hole arrays: Enhanced absorption, refractive index changes, and all-optical switching, *Adv. Mater.* **18**, 1267 (2006)
- [19] K. J. Klein Koerkamp, S. Enoch, F. B. Segerink, N. F. van Hulst and L. Kuipers: Strong influence of hole shape on extraordinary transmission through periodic arrays of subwavelength holes, *Phys. Rev. Lett.* **92**, 183901 (2004)
- [20] J. C. Hulst and R. P. Van Duyne: Nanosphere lithography: A materials general fabrication process for periodic particle array surfaces, *J. Vac. Sci. Technol. A* **13**, 1553 (1995)

-
- [21] J. Prikulis, P. Hanarp, L. Olofsson, D. Sutherland and M. Käll: Optical spectroscopy of nanometric holes in thin gold films, *Nano Lett.* **4**, 1003 (2004)
- [22] T. Rindzevicius, Y. Alaverdyan, B. Sepulveda, T. Pakizeh and M. Käll: Nanohole plasmons in optically thin gold films, *J. Phys. Chem. C* **111**, 1207 (2007)
- [23] A. Lesuffleur, H. Im, N. C. Lindquist and S. -H. Oh: Periodic nanohole arrays with shape-enhanced plasmon resonance as real-time biosensors, *Appl. Phys. Lett.* **90**, 243110 (2007)

Chapter 5

Plasmonic nano-grating metamaterials for biosensing

In this chapter, we demonstrate experimentally an improvement in biosensing technology that can be achieved using a plasmonic metamaterial that is capable of supporting a guided mode in a nano-grating layer. We begin by introducing the general principle of localized surface plasmon resonance (LSPR) sensor. Then, we propose the design and fundamental properties of a hybrid plasmonic nanostructure: the grating-shaped nanosandwich which is composed of a pair of metal layers separated by a dielectric to provide resonant interactions. Afterwards, we describe the fabrication method of such nano-grating structures on glass substrate by UV imprint technique. The reflection were measured experimentally with the fabricated structure, and are in good agreement with a simulation results. Finally, we demonstrate that our metamaterial design may serve as a highly efficient LSPR sensor in the near infrared region.

5.1 Introduction

Surface plasmons have played a significant role in a variety of areas of fundamental and applied research, from surface dynamics to surface-plasmon microscopy, surface-plasmon resonance technology, and a wide range of photonic applications. Currently surface plasmon based biosensor exhibit a variety of advantages, whom particularly includes: (1) Generic SPR sensor platforms can be tailored for detecting of any analyte which doesn't have to exhibit any special properties, such as fluorescence or characteristic absorption and scattering bands; (2) Unlike other interaction measurement techniques, SPR doesn't require chemical modification with, for example,

the radioisotopes or fluorescent molecules to observe the binding between the biomolecular recognition and analyte; (3) The binding event can be observed in real-time with relatively high speed; (4) SPR sensors can perform continuous monitoring as well as one-shot analyses.

Beyond the distinctive advantages described above, there are also two inherent limitations of SPR biosensor: one is in the specificity of detection, which is only based on the ability of biomolecular recognition elements to recognize and capture target analytes and preventing the non-target molecules from absorbing on the sensor surface, which will produce a false refractive index change, thus resulting in false sensing response; the other one is sensitivity to interfering effects, SPR biosensing measurements can be compromised by this effects which produce refractive index variations [1].

Today, SPR sensors have to compete with existing technologies on the basis of factors such as low cost, ease of use, robustness, sensitivity and stability. It's envisaged that this will drive research and development of SPR sensing devices in the following directions [2]:

- Improvement of detection limits which is ultimately constrained by the noise-based precision of the SPR instrument itself. Since the precision depends on both the noise caused by individual component of SPR sensor and the algorithms for data processing method, therefore, it's important to study of noise and develop of optimized algorithm for data processing for SPR sensing system.
- Development of laboratory SPR sensor platforms with a large number of sensing channels, which is required for direct detection in high-throughput screening applications.
- Development of mobile SPR sensor platforms with referencing capabilities enabling applications of SPR sensors in out-of-laboratory environments and for analysis of complex samples. Besides this, continuous efforts is also focused on to develop miniature SPR platforms based on miniaturized prism couplers and optical fibers [3].
- Development of advanced recognition elements for applications of SPR sensors in complex realistic samples.

In recent years, Localized Surface Plasmon Resonance (LSPR) based biosensor have drawn tremendous interest due to some indispensable advantages compared to the SPR based biosensor, and with the development

of new lithography technique for the patterning of large surface are, it has been argued that they may constitute a promising alternative to the propagating plasmon utilized in classical SPR sensors [4, 5, 6, 7], since it has been empirically shown that applying nanoparticles may significantly enhance its sensitivity by 1-2 orders of magnitude [8]. LSPR is nonpropagating plasmon excitations that can be resonantly excited on metal nanoparticles and around nanoholes or nanowells in thin metal films (Fig. 5.1(a)). Therefore, the instrument size and cost of LSPR can potentially be much smaller than those of conventional SPR sensors, which relies on the propagation of surface plasmon polaritons along the metal surface (Fig. 5.1(b)).

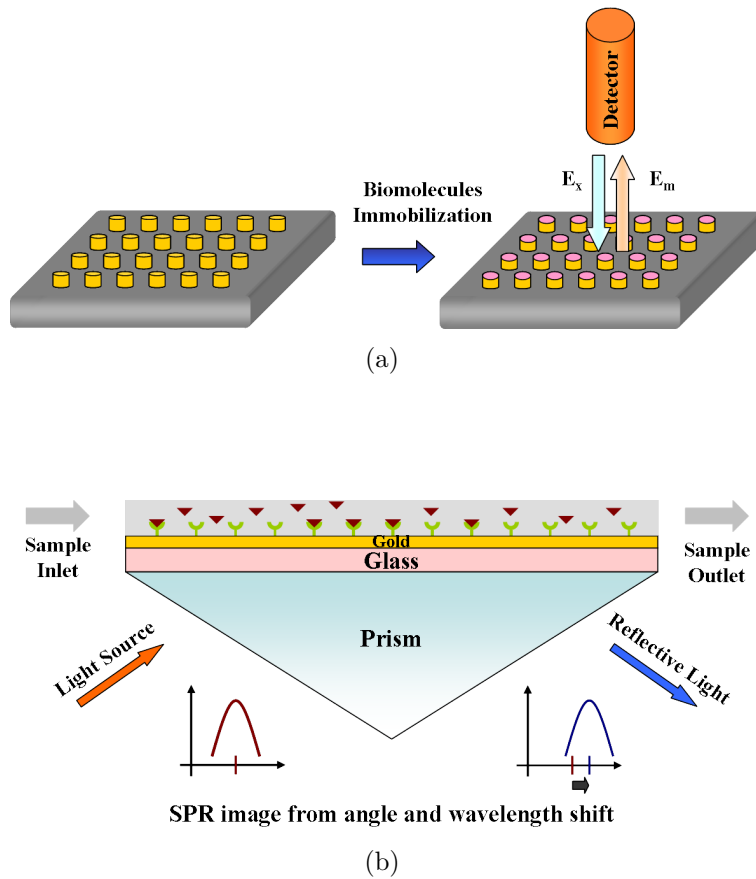


Figure 5.1: Schematic diagrams illustrating (a) a localized surface plasmon) and (b) a surface plasmon polariton or propagating plasmon.

LSPR sensing operate by transducing changes in local refractive index to wavelength shifts of the LSPR extinction band maximum. The wave-

length of LSPR corresponding to the extinction maximum λ_{max} is highly dependent on the material, size, shape and interparticle spacing of the nanoparticles as well as the dielectric properties of their local environment (i.e., substrate, solvent, and surface-confined molecules) [8, 9].

Enormous progress has been made in recent years in developing instrumentation and analysis method for high-throughput LSPR detection. In 2002, Nath et. al presents a new label-free optical method which relies on the change in the absorbance spectrum of a self assembled monolayer of colloidal gold on glass to study biomolecular interactions in real time [10]. In 2004, Enoch and coworkers studied the performance of bi-periodic gold nano-particles arrays for molecular sensing applications. By the Fourier Modal Method (FMM), the thickness of a covering dielectric layer is detected [11]. Kim et al. developed an interesting LSPR biosensor based on the “gold capped oxide nanostructure” named by them, which comprising of oxide posts with gold caps. Because of its interferometric behavior, the relative reflected intensity at surface of the chip resulted in an optical pattern that was highly sensitive to the changes in the thickness of the biomolecular layer [12]. Lately, the gold nanodimers with precisely controlled particles gaps have been demonstrated the possibility to scale the sensing volume down to the single-protein scale [16].

5.2 Localized surface plasmon resonance

5.2.1 Principle of LSPR sensing

The coupling of light to collective oscillation of electrons on the metal surface allows the creation of surface plasmon-polariton (SPPs) and localized surface plasmon-polariton (LSPs). The SPPs propagate ten to hundreds of microns in the x- and y- direction along the metal-dielectric interface and decay evanescently in the z-direction. Since the SPP dispersion curve lies to the right of the light line of the dielectric (given by $\omega = ck$) (Figure 5.2), excitation by three-dimensional light beams is impossible unless special techniques for phase-matching such as prism, grating coupling as well as excitation using highly focused beams.

Localized surface plasmons on the other hand are non-propagating excitations of the conduction electrons of metallic nanostructures coupled to the electromagnetic field. These modes arise naturally from the scattering problem of a small, sub-wavelength conductive nanoparticle in an oscillating electromagnetic field. The principle is illustrated in Figure 5.3, where

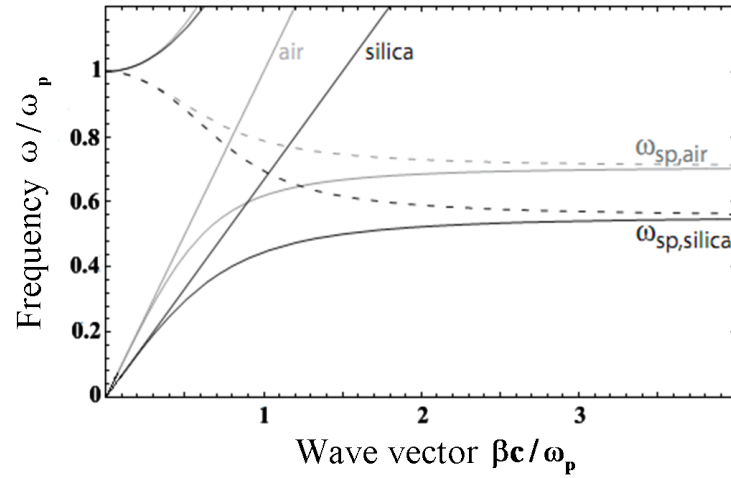


Figure 5.2: Dispersion relation of SPPs at the interface between a Drude metal with negligible collision frequency and air (gray curves) and silica (black curves) [13].

the electron cloud of a metallic NPs oscillates in phase with the incident electromagnetic field. In this case the plasmon resonances can be excited by direct light illumination, in contrast to propagating SPPs where the phase-matching have to be employed.

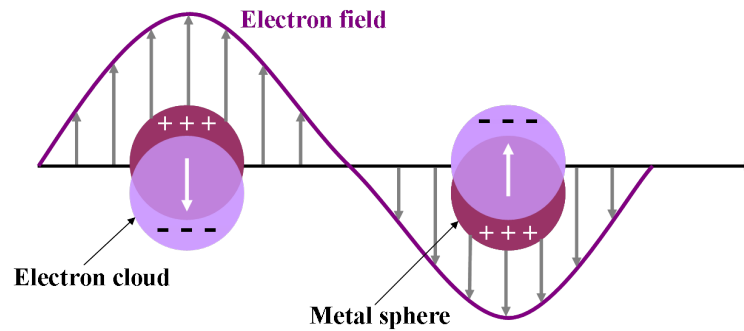


Figure 5.3: Schematic illustration of the oscillation of conduction band electrons of a metal nanoparticle with an electromagnetic field, resulting in a localized surface plasmon.

Excitation of LSPs by an electric field at an incident wavelength where resonance occurs results in strong light scattering, the appearance of intense surface plasmon absorption bands, and a significant local electromagnetic field enhancement at small metallic particles due to the small volume of the LSP mode. This field enhancement can reach up to 10^6 [14]. In order to demonstrate such local field enhancement induced by

resonant plasmons within a metallic nanostructures, Fig. 5.4 presents the calculated optical electric-field distribution on a 2 x 2 array of Au@SiO₂ core-shell NPs being placed on a single-crystal surface of gold. A diameter of the Au NPs is about 55 nm and the silica shell thickness is 4 nm. The excitation line was 632.8 nm from a He-Ne laser. When the Au NPs are brought very close to an atomically flat surface with the controllable spacing, localized surface plasmons can be excited in the nanogap, which results a large electromagnetic field enhancement. As shown in Figure 5.4, the highest enhancement of electric field appears at the junction between the particle and the substrate.

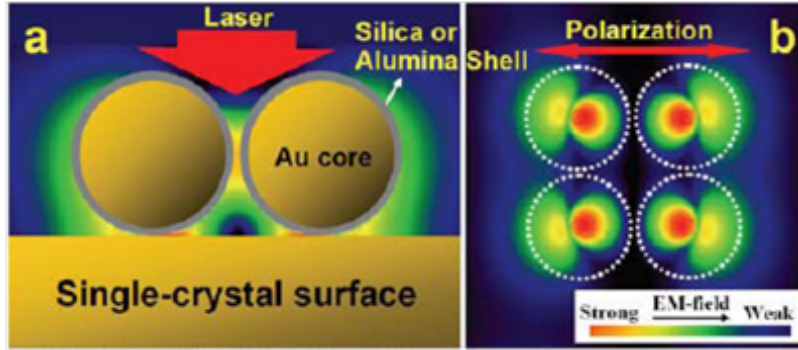


Figure 5.4: The 3D-FDTD simulation of the optical electric field distribution of a 2 x 2 array of Au@SiO₂ on a single-crystal gold surface: (a) Side-view and (b) Top view of the optical electric field distribution at the gap between the particle and the surface [15].

Typically, gold and silver NPs are chosen for most LSPR applications, other metals such as aluminum and copper can also support plasmons too. These noble metal nanoparticles exhibit LSPR resulting in strong photon absorption in ultraviolet-visible bands. Based on Mie theory which models the extinction of a single sphere of arbitrary materials, the simplest theoretical model for the extinction, $E(\lambda)$, of a spherical nanoparticles can be estimated by the following equation:

$$E(\lambda) = \frac{24\pi^2 N a^3 \epsilon_m^{3/2}}{\lambda n(10)} \left[\frac{\epsilon_i}{(\epsilon_r + 2\epsilon_m)^2 + \epsilon_i^2} \right] \quad (5.1)$$

where $E(\lambda)$ is the extinction which is equal to the sum of absorption and Rayleigh scattering, N is Avagadro's number, a is the radius of the the metallic nano-sphere, ϵ_m is the dielectric constant of the medium surrounding the metallic nanosphere, λ is the wavelength of the absorbing

radiation, and ϵ_r and ϵ_i are the real and imaginary portions of the metallic nanosphere's dielectric function, respectively. For a metal NP with $|\epsilon_r| \gg \epsilon_i$, equation 5.1 has a maximum when $\epsilon_r = -2\epsilon_m$ and LSPR condition is met. Meanwhile it can also be seen from this estimation that the extinction of a single metallic nanosphere depends on its size (a), material (ϵ_r, ϵ_i) and the surrounding environment (ϵ_m). Moreover, when the nanoparticles are not spherical, the extinction spectrum will depend on the nanoparticles's geometry. Thus, the resonance term from the denominator of Eq. 5.1 can be replaced with:

$$[\epsilon_r + \chi\epsilon_m]^2 \quad (5.2)$$

where χ increases directly with the nanoparticle's aspect ratio [6].

Based on the assumption that the metallic nanoparticles are ideal metal that have electrons move freely, the real components of dielectric functions of metallic nanosphere can be described by the Drude model as:

$$\epsilon_r = 1 - \frac{\omega_p^2}{\omega^2 + \gamma^2} \quad (5.3)$$

In this equation, ω_p is the plasma frequency, ω is the angular frequency of incident electric field and γ is a damping factor. Here, the plasma frequency ω_p is described by:

$$\omega_p^2 = \frac{Ne^2}{m\epsilon_0} \quad (5.4)$$

where m is the electron mass, e is the electron charge. If $\omega \gg \gamma$ which is common for metals at room temperature in UV-vis bands, then equation (5.4) are simplified as:

$$\epsilon_r = 1 - \frac{\omega_p^2}{\omega^2} \quad (5.5)$$

When the resonance condition $\epsilon_r = -2\epsilon_m$ is met, the frequency of the incident electric field, ω can be expressed from the derivation of equation (5.5):

$$\omega = \frac{\omega_p}{\sqrt{1 + 2\epsilon_m}} \quad (5.6)$$

Using the same inference, the resonant wavelength can be expressed as:

$$\begin{aligned} \lambda &= \lambda_p \sqrt{1 + 2\epsilon_m} \\ &\cong \sqrt{2}\lambda_p n_m \end{aligned} \quad (5.7)$$

where $\lambda_p = 2\pi c/\omega_p$, c is the speed of light in vacuum, n_m is the refractive index of the medium surrounding the metallic nanosphere. As can be seen from equation 5.7, the resonant wavelength change approximately linearly with the refractive index of the medium surrounding when the variation range of n_m is sufficient small. That is, the position of this resonance red shifts with an increase in magnitude of the dielectric constant of the medium surrounding of the NPs. Like traditional SPR sensor, LSPR also convert small changes in the local refractive index into spectral shifts in the intense nanoparticle extinction and scattering spectra and can be utilized as sensors to detect the surrounding medium.

5.2.2 Comparison with SPR sensing

The LSPR sensor retains many of the desirable features of conventional surface plasmon resonance instrument, such as the ability to monitor the kinetics of biomolecular interactions in real time without a label. Compared with SPR sensors, LSPR sensors also exhibit some differences:

- LSPR-based nanosensor have a much smaller refractive index sensitivity. However, the smaller decay lengths provide LSPR with enhanced sensitivities to make up. Moreover, the resolution gets much improved owing to the small LSPR decay length.
- The smallest footprint of LSPR sensors is smaller than that of SPR sensor. In LSPR sensing, the spot size can be minimized even down to a single nanoparticle by using single nanoparticle measurement techniques [23].
- The prototype and portable LSPR system costs less than \$5000, whereas the commercialized SPR instruments costs vary between \$150000-\$300000, which is more expensive.

Both the similarities and difference between LSPR and SPR sensors is detailed listed in table 5.1.

A clear advantage of LSPR is: less interference from refractive index, implying that the temperature stabilization is less important; simple measurement technology which is based on either straightforward transmission or reflection thus requiring simpler instrumentation — only an near-infrared/visible spectrophotometer or flatbed scanner. Importantly, the sensor can be easily multiplexed to enable high-throughput screening of biomolecular interactions in an array-based format. All these advantages can be well utilized in simple and cheap sensing equipment for

Feature/characteristic	SPR	LSPR
Label-free detection	Yes[17, 18]	Yes[8]
Distance dependence	~ 1000 nm[19]	~ 30 nm (size tunable)[20]
Refractive index sensitivity	2×10^6 nm/RIU[19, 21]	2×10^2 nm/RIU[20]
Modes	angle shift[22]	extinction[8]
	wavelength shift	scattering[23, 24]
	imaging	imaging[23, 24]
Require temperature control	Yes	No
Chemical identification	SPR-Raman	LSPR-SERS
Field portability	No	Yes
Spatial resolution	$\sim 10 \times 10$ μm [22]	nanoparticle[24]
Nonspecific binding	minimal (determined by surface chemistry and rinsing)[22]	minimal (determined by surface chemistry and rinsing)[8]
Real-time detection	time scale= 10^{-1} - 10^3 s, planar diffusion[21]	time scale= 10^{-1} - 10^3 s, radial diffusion[23]
Multiplexed capabilities	Yes[25]	Yes-possible
Small molecule sensitivity	Good[21]	Better[20]
Microfluidics compatibility	Yes	Possible

Table 5.1: Comparison between SPR and LSPR sensors [26].

bio/chemosensing. On the other hand LSPR are more complex and expensive to fabricate on large surface with conventional lithographic technique like electron beam lithography.

5.3 LSPR sensing with nano-grating metamaterials

Optical sensors based on localized surface plasmon resonances of metal nanoparticles are promising candidates for pushing the limits of the label free detection down to the ultimate limit of real time single molecule sensitivity. Moreover, LSPR offers similar merits as the conventional propagating SPR but with some prominent advantages, such as spectral tunability, strong enhancement of the local electric field and much better adaptability to modern nanobiotechnology architectures. However, nanoparticles

arranged in an aperiodic array or randomly interacting ensembles have been shown to exhibit relatively smaller resonance shift induced by surrounding medium as compared to conventional SPR sensor. In addition, with full width at half-maximum (FWHM) which is used to define the extinction curve widths broadening, the nanosensing capabilities of such disordered arrays decreased significantly. Unlike disordered configuration, one or two-dimensional periodic arrangements of metallic nanoparticles are capable of generating a deeper and narrower resonance spectrum which allows for efficient detection of the resonance shift and precise analysis of biosensing events, leading to the sensitivity of LSPR sensors has been greatly improved [27]. This is due to excitation of both SPPs and LSPs modes simultaneously within such 1D and 2D arrays. The strong coupling between LSPs and SPPs modes can give rise to a dramatic enhancement of the electromagnetic field as compared to the field intensity of LSPs and SPPs alone. Various interactions between LSPs, SPPs, and binding biomaterial in the presence of nanostructures can also lead to some different resonance properties with an additional shift of resonance angle, as well as changes in the reflectance amplitude and resonance width, resulting in significantly enhanced sensitivity of a SPR biosensor.

Based on the importance of SPPs-LSPs interactions in the sensitivity enhancement of a SPR biosensor, incorporation a dielectric into plasmonic materials has led to the construction of a new class of artificial matter—metal-dielectric metamaterials where hybrid resonances may result in negative refraction and other unique optical properties [29]. The Plasmonic metamaterials may also offer the advantages of nano-architectures, large effective area with possibility of guiding and imaging capabilities beyond the diffraction limit, nanomanipulation and nanotrapping [30, 31] and find numerous applications in such diverse areas as optical communications, chem- and bio-sensing, high-density data storage and many others. Most recently, several different groups have studied this metamaterials systems composed of a metallic layer, such as subwavelength rods, gratings and hole arrays [32, 33, 34], closely coupled to a planar metal film. The major advantage of such multilayer system is that it allows the direct observation of controlled excitation/coupling of different resonances within the structure.

5.3.1 Plasmonic nano-grating metamaterials designs

The basic element of the optical antenna array is represented in Fig. 5.5 and is composed by a pair of metal layers separated by a dielectric spacer

forming the gap of the antenna. On the bottom layer is a semi-infinite metal film which supports the LSP mode and the top layer an arrays of lines or dots nanoparticles. The dielectric layer acts as a load between the two metallic antenna components. One of the advantage of this geometry is that varying the dielectric spacer allows one to easily change the resonance wavelength. The excitation of the fundamental mode of metal-insulator-metal resonator leads to nearly perfect absorption for any incident angle this condition. This mode results by the interaction of the SPR in the semi-infinite metal film and LSPR in the nanoparticle array and the perfect optical absorption is achieved when particular matching condition are fulfilled.

The whole structure of the biosensor is is represented in Fig. 5.5 on the right panel and consists of a glass substrate with a gold film with a thickness d_1 , dielectric layer with a thickness d_2 and a two-dimensional periodic gold nano-grating with period $P = 400$ nm, linewidth $L = 200$ nm. A thin Cr layer was used to increase adherence of gold to both glass substrate and SiO_2 dielectric layer.

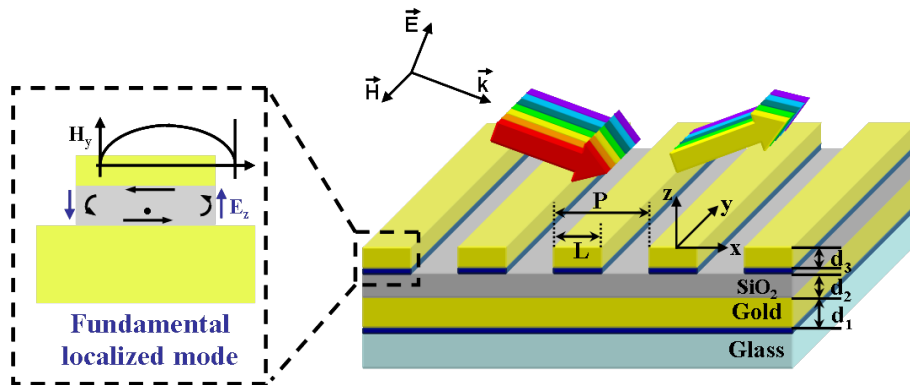


Figure 5.5: Left panel: The basic element of the optical antenna array with the fundamental localized resonance is essentially confined in the dielectric layer. Right panel: scheme of the designed metamaterial structure studied in this section consisting of SiO_2 dielectric layer between two Au films with a nanogratings on top Au layer.

All the measurements have been performed in reflection with TM polarized incident light. The excitation of the fundamental mode of metal-insulator-metal resonator leads to nearly perfect absorption for any incident angle. The nature of the resonance is clearly identified by the electric field distribution shown in Figure 5.6(a). The gray scale corresponds to the amplitude of the electric field (Fig. 5.6(a)), whereas the green (red) arrows show the real (imaginary) part of the polarization vector (Fig. 5.6(b)).

Figure 5.6(a) shows that even though the electromagnetic energy is concentrated mainly inside the dielectric spacer when incident electric field is along the nanograting vector, a considerable part is confined at the air-gold interface of the nanoparticles available for the biosensing. Meanwhile, the polarization of the electric field is strongly modified in the vicinity of the nanograting as shown in Fig. 5.6(b). Above the metal-air interface, the polarization is elliptical indicating that the light scattered by the resonant metamaterial is coupled back to the SPP mode on the gold-vacuum interface of the film.

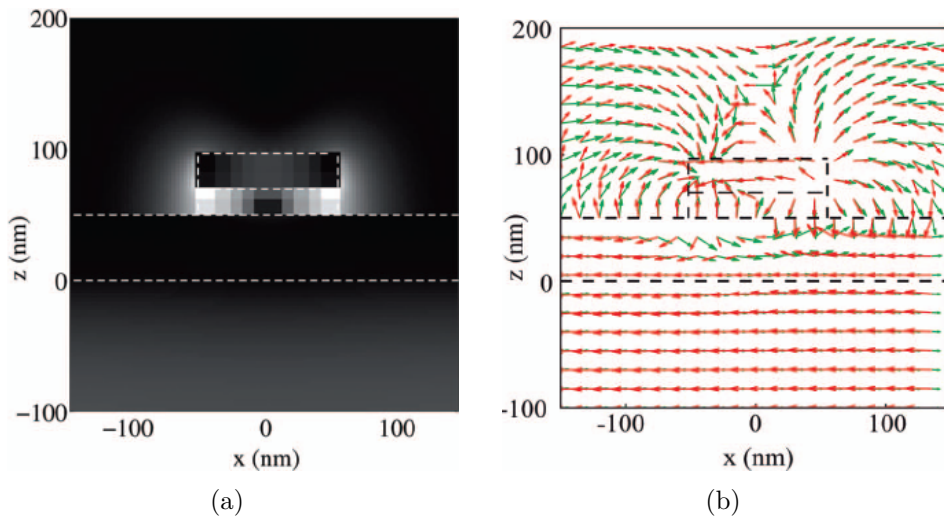


Figure 5.6: Calculated distribution of the (a) electric field amplitude and (b) polarization whereas the green (red) arrows show the real (imaginary) part of the polarization vector for a plasmonic subwavelength rectangular nanoparticle deposited on a metal slab [28].

The second high order mode located at lower frequency is sharper than the fundamental order mode and in contrast with this one presents a dependence on the angle of incidence of the light. It can be shown that the rate equipartition condition required for the nearly perfect absorption of metal-insulator-metal resonator it is fulfilled for every angles in the case of the fundamental mode and in a narrow range of angles for the second order mode.

5.3.2 Simulation results

To analyze the spectral response of the nanograting metamaterial structure and the mechanisms behind the low reflection properties of the structure,

three series of simulations have been carried out in this section, including: the thickness of the gold grating d_3 ; the thickness of the SiO_2 dielectric spacer d_2 and the thickness of the planar bottom layer of gold d_1 . These electromagnetic simulations are based on an exact modal method [35]. We consider a plane wave impinging the grating in TM polarization (the incident magnetic field is parallel to the direction y of the grating, see Fig 5.5).

a. Effects of the Au grating and SiO_2 spacer thickness

All the simulations have been performed by considering a grating of 200 nm lines with a pitch of 200 nm. We assume an infinite number of periods (x-direction, see Fig. 5.5), and a uniform structure in the grating direction (y-direction, see Fig. 5.5). The Cr adhesion layer used in the experiments is neglected. Figure 5.7 shows the simulation of the reflectivity calculated under TM polarized light at an incident angle of 50° to the normal at the surface.

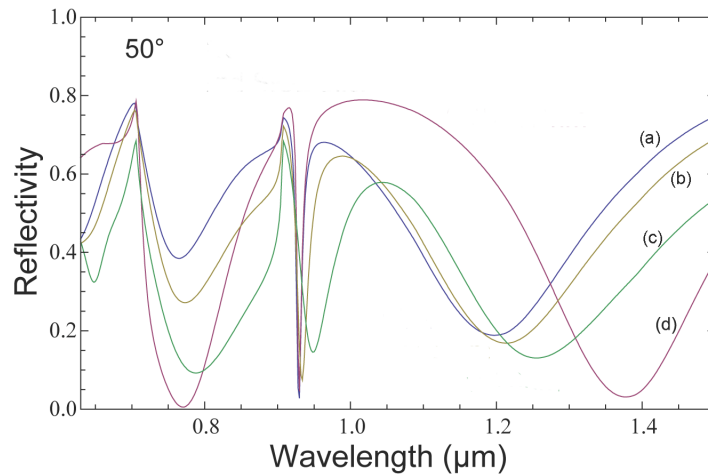


Figure 5.7: Calculated Reflectivity at 50° for a structure with gold bottom layer of 40 nm, SiO_2 layer 40 nm, gold grating of 200 nm lines, pitch 200 nm and a thickness of (a) 40 nm (b) 30 nm and (c) 20 nm. Curve (d) has been calculated considering a SiO_2 layer of 20 nm and gold grating thickness of 40 nm.

The nominal SiO_2 thickness for the curves (a), (b) and (c) is fixed at 40 nm while the thickness of the grating lines is respectively 40, 30 and 20 nm. As the thickness of the grating is reduced we observed a significant shift and a more efficient adsorption of the fundamental peak in the infrared region around $\lambda = 1.2\mu\text{m}$ and in particular for the second

order resonance in the near infrared region around $\lambda = 770$ nm. With a grating thickness of 40 nm, the same trend is observed when the thickness of the SiO_2 is reduced from 40 nm to 20 nm (curve (d) of Figure 5.7). Through changing the physical separation between the nano-gratings in the sandwich configuration, the dipole coupling can be varied, and this can be used to explore the SPPs-LSPs hybridization tuning and to improve the absorption of light at the resonances. In particular, once fixed at 20 nm the thickness of the gold grating it is possible improve further the adsorption of the fundamental resonance by decreasing the SiO_2 thickness from 40 nm to 20 nm as shown in the calculated reflection spectra of Figure 5.8) which shows a perfect absorption in the infrared region for the fundamental resonance. In this simulations the thickness of the gold bottom layer has been set to 100 nm, while in the previous simulations was 40 nm: we will see that this does not affect the the perfect adsorption of infrared perfect absorption of the fundamental resonance.

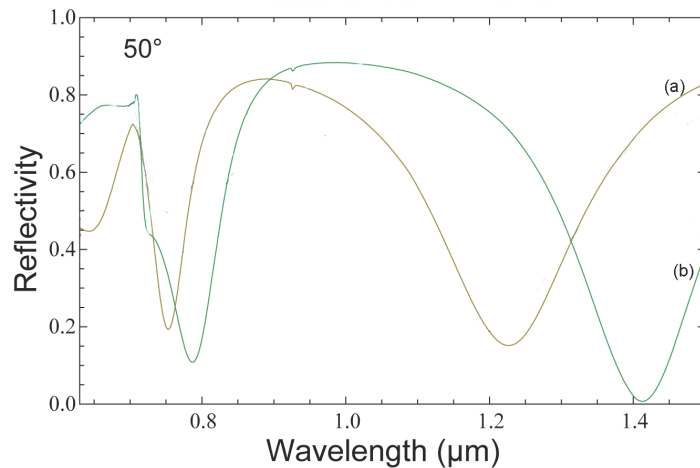


Figure 5.8: Calculated Reflectivity at 50° for a structure with gold bottom layer of 100 nm, SiO_2 layer of (a) 40 nm and (b) 20 nm, gold grating of 200 nm lines, pitch 200 nm and a thickness of 20 nm.

b. Effects of the gold bottom layer thickness

The variable in the third series of simulations is the thickness of the bottom layer of gold. Figure 5.9 shows the reflection spectra of the multilayer structures under TM polarized light, in which the thickness of gold thickness d_1 is changed from 40 nm (Fig. 5.9(a)) to 200 nm (Fig. 5.9(b)), while the grating of lines and the SiO_2 layer are fixed at 20 nm. For each

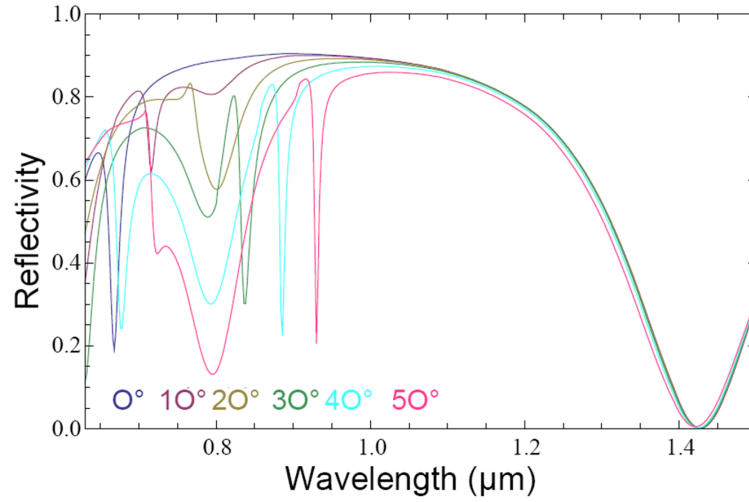
geometry, the simulations have been performed at five different angle of incidence between 0° and 50° . The most remarkable issue is related to the infrared perfect absorption of the fundamental resonance which has been achieved regardless of angle of incidence, for both the thickness of the bottom layer of gold. Moreover, we do not observe any dispersion of the fundamental resonance which is fixed at the same length wave. On the contrary, the second order resonance has a dispersion as a function of the angle of incidence and presents different absorptions intensity due to the fact that the rate equipartition condition required for the nearly perfect absorption it is fulfilled for a particular angle of incidence.

In fact, the fundamental resonance is localized in the SiO_2 spacer with a distribution of the field already shown in Figure 5.5: by using a TM polarization, the direction of the magnetic field of the incident light remains unchanged regardless of the angle of incidence and it can efficiently drive the circulating electric field inside the SiO_2 spacer at very angle of the incident light. The results indicate that the existence of planar thick metallic film results in a sharp resonance reflection peak, and its thickness can be used to optimize the depth and full width at half maximum (FWHM) of the resonance peak.

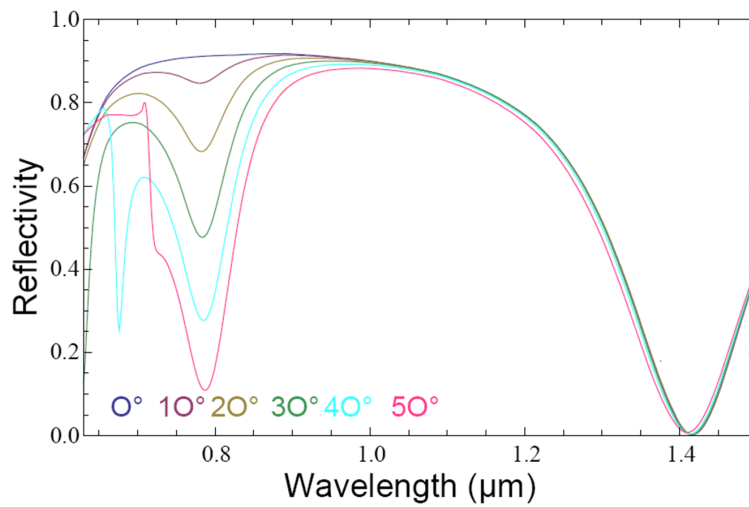
5.3.3 Fabrication techniques of plasmonic metamaterials

To create a metamaterial for optical frequencies poses a big challenge for nanofabrication since one should deal with fabrication of small periodicities on the order of 300 nm or less and tiny feature sizes nanostructures with high-precision, high-reproducibility, high-throughput and low-cost to ensure effective-medium-like medium. For radiation in the near infrared or in the visible range of the spectrum this requires sub-100 nm spatial resolution which can be smaller than the resolution of state-of-the-art photolithography, thus requiring nanofabrication processes with 100- or sub-100 nm resolution.

Due to the high-resolution requirement, electron-beam lithography is still the first choice for fabricating small-area metamaterials ($\sim 100 \text{ um} \times 100 \text{ um}$) [29]. Writing larger areas requires long e-beam writing times and hence, boosts the operation cost. Thus, this approach is only suitable for some specific designs and proof-of-principle experiments. Similar to EBL, other serial processes, like focused ion beam milling technique [36] are also not feasible for the large-scale metamaterial fabrication required by some



(a)



(b)

Figure 5.9: Reflectivity spectra calculated at different angles of incidence for a structure with gold grating of 200 nm lines, pitch 200 nm and a thickness of 20 nm, a SiO_2 layer of 20 nm and a gold bottom layer of (a) 40 nm and (b) 200 nm.

applications.

One approach to manufacturing high-quality metamaterials on a large scale ($\sim \text{cm}^2$) is provided by interference lithography (IL) [37]. This fabrication technique is based on the superposition of two or more coherent optical beams forming a standing wave pattern. Being a parallel process, IL provides a low-cost, large-area mass-production capability. Moreover, this technique could also be applied to the fabrication of future 3D metamaterials.

Another promising approach to create large-scale, high-quality metamaterials is nanoimprint lithography. Since NIL requires a stamp made by other nanofabrication techniques, it's ideal for parallel production of already optimized metamaterials, when the preliminary test structures were patterned via EBL. Thus, NIL can be seen as large-scale, low-cost process of making EBL-written pattern which offers solutions to the intrinsic EBL draw-backs.

5.4 Experimental procedure

5.4.1 Sample fabrication

Metamaterials structures that are ideally suited for fabrication via nanoimprint lithography have recently been discussed in Ref. [38, 39]. In this work, we used the soft UV nanoimprint lithography to fabricate the nano-grating metamaterials. The fabrication of metamaterials by soft UV-NIL involved two major steps: the soft UV-NIL mold fabrication and the device fabrication. A silicon master mold of 200 nm line-and-spacing grating structure was obtained by electron beam lithography and RIE, resulting a grating of 130 nm depth and 1 cm^2 area (figure 5.10).

In order to fabricate nano-grating metamaterials structures on substrates for optical characterization, several processes are needed, including: vacuum deposition of thin films, grating pattern definition by soft UV-NIL, grating pattern metalization through reactive ion etching and lift-off. The schematic of the main steps involved are shown in Fig. 5.11; the details for each step are described as follows.

- **Step 1: Deposit Au/Cr bilayer film and SiO_2 layer.**

The samples are prepared on glass substrates. After carefully solvent cleaning (the detailed procedure is described in chapter 3), Au/Cr is firstly

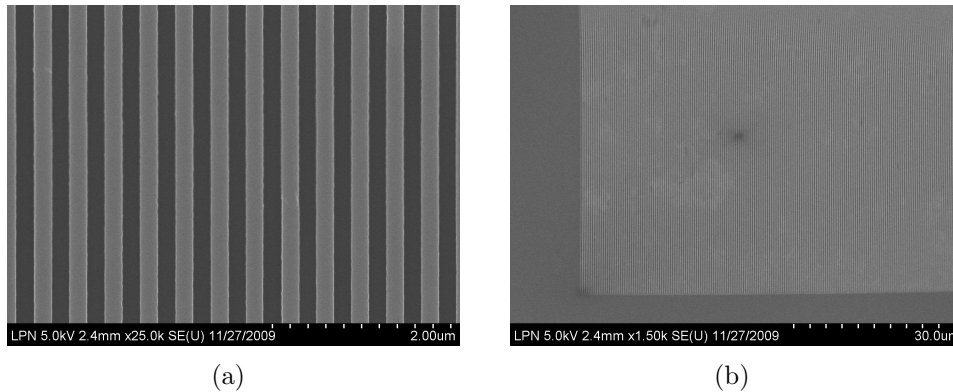


Figure 5.10: Scanning electron micrograph (SEM) images of the Si master mold with 200 nm nanoline patterns fabricated by E-beam lithography.

deposited onto the substrate using E-beam evaporation, followed by a layer of SiO_2 , is deposited on the gold layer by RF-PECVD (Unaxis-Nextral D200). The process parameters are listed in Table 5.2. The thickness of the deposited Au/Cr bi-layer systems were 200 nm/5 nm and 40 nm/2 nm respectively depending on the structure design and the thickness of the SiO_2 layer is fixed at 20 nm.

RF power (W)	50
Bias voltage (V)	42
Working pressure (mTorr)	642
N_2 flow (sccm)	198
Temperature	275 °C

Table 5.2: Process parameters for RF-PECVD deposition of SiO_2 .

- **Step 2 to step 4: Grating pattern definition by soft UV-NIL and pattern transfer by RIE.**

A tri-layer system which is prepared for nano-grating fabrication by soft UV-NIL, is deposited on top of the SiO_2 . This involves: deposition of PMMA layer first with a thickness about 300 nm. After pre-bake at 180 °C for 10 mins, 10 nm Ge was deposited by E-beam evaporator. Then, Amonil MMS10 resist with a thickness of 85 nm was deposited on top by spin coating. Soft UV-NIL was performed at the optimal condition as described in chapter 3. After separation soft stamp from the substrate, the structures were transferred into the bottom gold layer surface by three

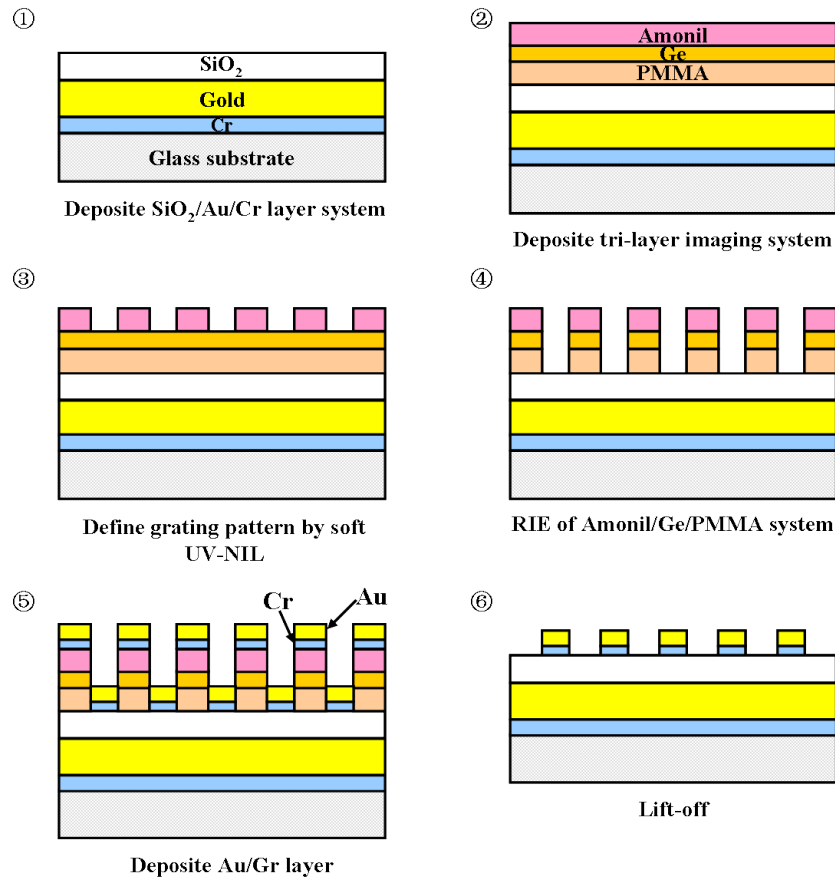


Figure 5.11: Schematic of the main steps in the sample fabrication process.

successive etching steps: the residual resist of top Amonil MSS10 is etched with $\text{CHF}_3/\text{SF}_6/\text{O}_2$ with 12/8/2 sccm gas mixture under a pressure of 7 mTorr and RF power 10 W in about 15 s, then patterns are transferred to the bottom layer with SF_6 gas in 10 s and finally the bottom PMMA layer with oxygen plasma in 2 min 30 s.

- **Step 5 & Step 6: Deposit Au/Cr bilayer film and lift-off.**

Definition of the Au nano-grating involves two steps: firstly, a Au (20 nm)/Cr (2 nm) stack is deposited onto the substrate by E-beam evaporation; secondly, the resist and all metal not adhering directly to the SiO_2 spacer is removed in acetone via lift-off process. Figure 5.12 shows the SEM image of the fabricated nanograting arrays (1 cm^2) after lift-off.

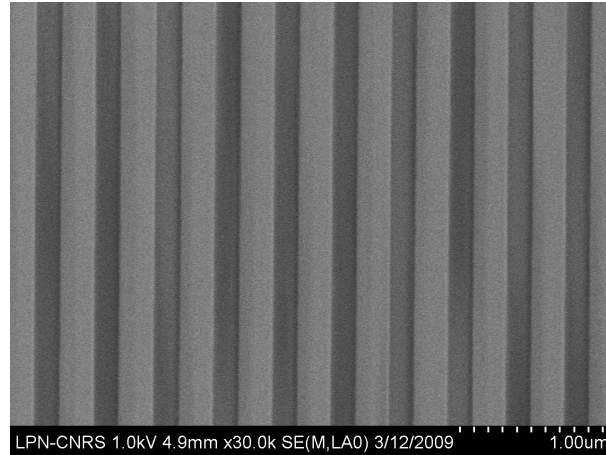


Figure 5.12: SEM image of a 400 nm period grating metamaterials after Au(20 nm)/Cr(2 nm) lift-off.

5.4.2 Optical arrangement

The primary instrument used for angle-resolved transmission and reflection measurements have been developed in our lab. The schematic diagram of the system set-up is shown in Fig. 5.13.

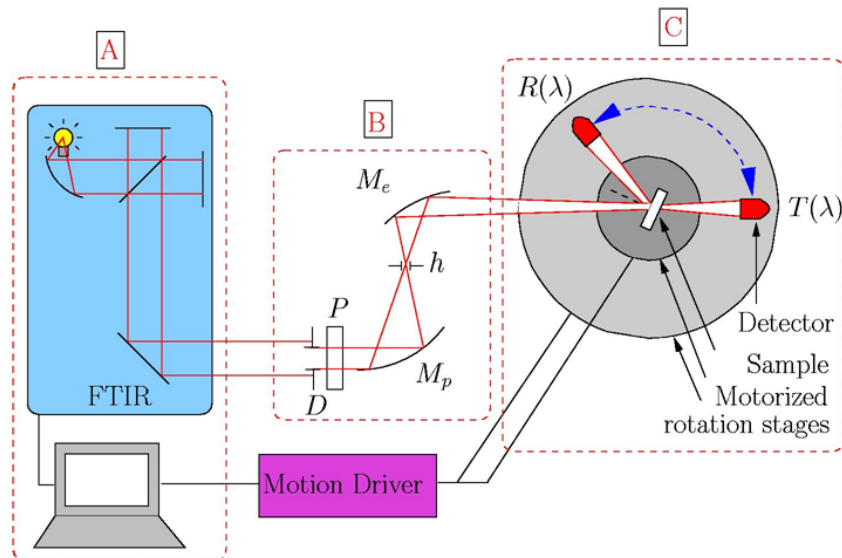


Figure 5.13: Schematic diagram of the setup for angle-resolved transmission and reflection optical measurements: A. FTIR spectrometer; B. achromatic optical focusing system; C. sample and detector rotation stages. The displacement sensor (symbolized by the double blue arrow) shows how to measure in transmission or reflection mode.

The characterization of this optical test platform can be divided into three main parts:

- A. Light source: It uses a commercial Fourier Transform Spectrometer (FTIR) (Bruker Equinox 55), which allows a measurement over a wide spectral range (from 0.7 to 16 μm for our setup) and also a spectral resolution down to 0.2 cm^{-1} .
- B. Optical focusing system: It adapts the incident beam coming from FTIR spectrometer (broad and unpolarized light) to a diameter controlled and linearly polarized beam.
- C. Detection system: Two plates driven by two rotation stages motorized co-axial and independently which allows change of both incident angle on the sample and the measured signal angle.

The sample and the InSb detector with the spectral resolution down to 40 cm^{-1} are mounted on two co-axial motorized rotation stages. The light is focused on the sample through an achromatic optical system (B. optical focusing system in Fig. 5.13): a pinhole h (diameter $250\text{ }\mu\text{m}$) is placed between a parabolic mirror M_p (focal length 69 mm) and an elliptic mirror M_e (focal lengths 40 and 50 mm). An additional diaphragm D is placed at the output of the spectrometer which allows the angular resolution $\Delta\theta$ to be tuned between $\pm 0.3^\circ$ and $\pm 1^\circ$. The light polarization is controlled by the use of several infrared linear polarizers (p). The advantage of this set-up lies in the broad accessible spectral range and in the possibility to characterize extremely small samples, thus providing a powerful tool for an extended optical characterization of 2D plasmonic crystals.

5.4.3 Biological modification of gold surface

Antibodies are used most frequently for SPR biosensing because of their high affinity, versatility, and commercial availability. The main procedure of immobilization of antibodies on the gold nanostructures surface are as follows:

Reagents and materials

N-hydroxysulfosuccinimide (Sulfo-NHS), N-(3-Dimethylaminopropyl)-N'-ethylcarbodiimide hydrochloride (EDC), 6-mercaptohexadecanoic acid, ethanol and anti-mouse IgG (F9137) were obtained from Sigma-Aldrich corporation. Figure 5.14 shows the molecular structures of NHS, EDC and

6-mercaptohexadecanoic acid. EDC is a water-soluble derivative of carbodiimide. Carbodiimide catalyzes the formation of amide bonds between carboxylic acids or phosphates and amines by activating carboxyl or phosphate to form an O-urea derivative. S-NHS is often used with the presence of EDC to assist the carbodiimide coupling. The O-urea derivative reacts with the S-NHS to form an intermediate active ester that can further react with the amine group of biomolecules to finally generate an amide bond. In these chemical procedures, the carbodiimide coupling reaction is provided by EDC and promoted by NHS.

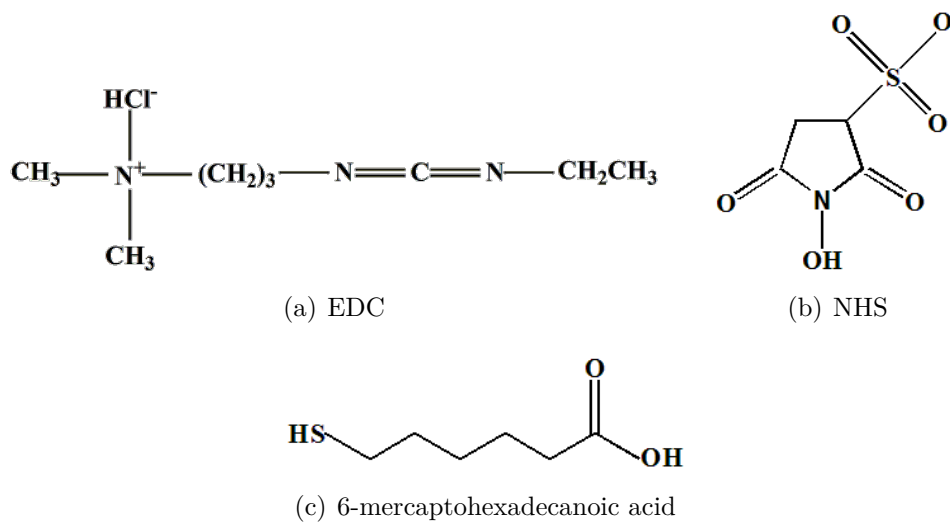


Figure 5.14: The structural formulas for EDC, S-NHS and 6-mercaptohexadecanoic acid molecules.

Antibody solution reconstitution

The original anti-mouse IgG solution-FITC antibody produced in rabbit consists of: 0.01 M phosphate buffered saline, 15 mM sodium azide with PH 7.4. The original antibody solution was used with a 1:100 dilution in fresh potassium phosphate-buffered saline (PBS) buffer to reconstitute the concentration of the antibody solution at 100 ug/ml at room temperature for 60 min.

Formation of self-assembled monolayers

Self-assembled monolayers were formed by immersing gold samples in a mixture of 300ul 6-Mercaptohexanoic acid (90%) in 50ml pure ethanol

for 2 hours at room temperature. Upon removing the gold sample from solution, the sample was washed sequentially with pure ethanol to remove the surplus of ungrafted thiol onto the surface and dried with nitrogen gun.

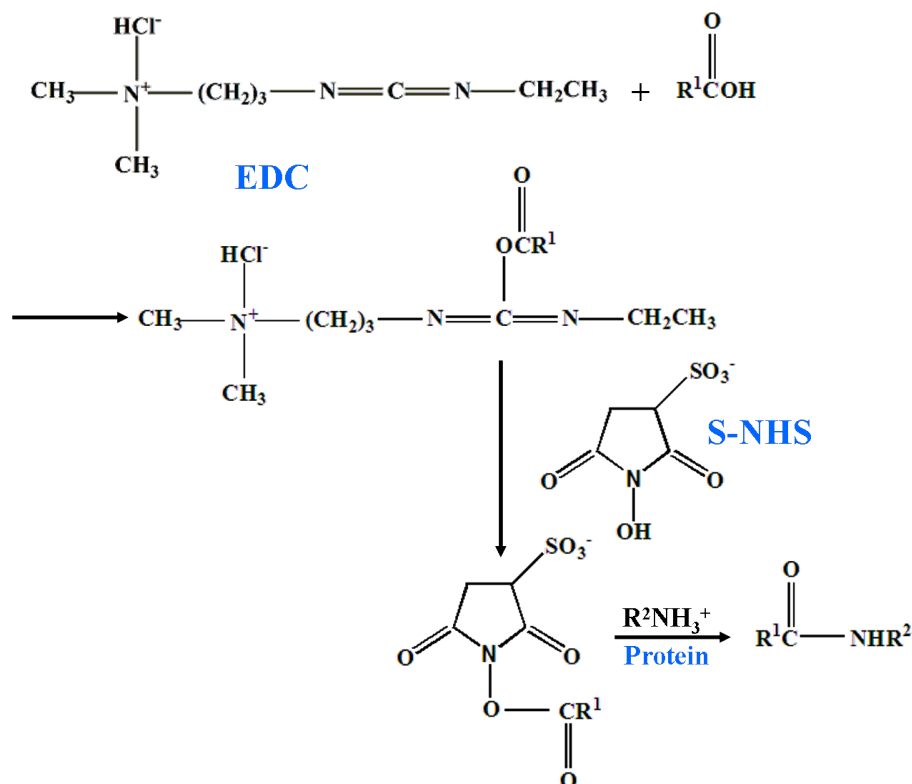


Figure 5.15: Chemical reaction of procedure adopted for immobilizing antibody on carboxylic acid end groups on SAMs.

Immobilization of anti-mouse IgG on sensor

After the antibody solution was reconstituted, it was applied to an EDC-NHS activated surface. Both EDC and NHS were diluted and mixed with fresh PBS to concentrations of 15 mg/ml as a coupling reagent. The carboxyl groups of the SAMs on the glass substrate were activated with EDC and S-NHS for 12 h at 4 °C to ensure that the carboxyl group of the SAM reacted fully with the EDC/NHS. Subsequently, the samples were incubated in 100 ug/ml anti-mouse IgG solution for 2 h at room temperature. After removed from the solutions, the samples were rinsed with PBS and dried under a steam of nitrogen. A chemical reaction illustrating in Fig.

5.15 the typical binding of the antibody to the carboxylic acid end groups on SAMs.

5.5 Results and discussion

5.5.1 Optical measurement results

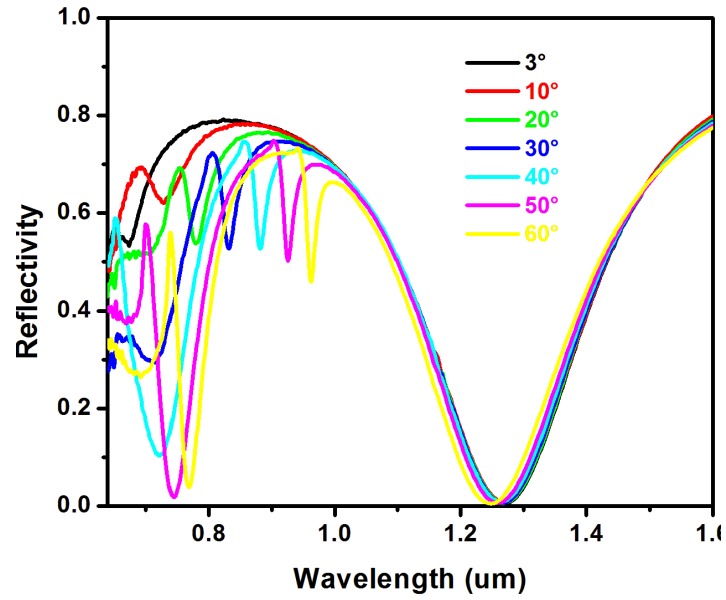
Fig. 5.16(a) and 5.16(b) show the reflection spectrum of two samples with different Au/Cr film thicknesses at various angles of incidence for TM configurations, respectively. The measured spectrum with Au/Cr 40/2 nm thick (Fig. 5.16(a)) shows three peaks, which agrees with the simulation results. In contrast, the measured spectrum with Au/Cr in 200/5 nm thickness exhibits two peaks (the comparison between two reflection spectra were also carried out at the incident angle of 50° in this part, corresponding to the simulation results). The trends seen in experimental extinction spectra show a good agreement with the numerical simulations.

The spectral positions of these peaks (wavelengths at which reflection minima occur) obtained from measurements (simulations) for the sample are shown in Table 5.3. Here we observe an good agreement between the measurement and the simulation results in the spectral positions of peak 2 for sample 1, although there is small discrepancies in the positions of peak 1 and peak 3 for both sample 1 and sample 2—with a blueshift of the features in the experimental spectrum with respect to the simulation spectrum. This could be due to fabrication imperfections and/or differences in the dielectric constants of gold and SiO_2 between simulation and experiment.

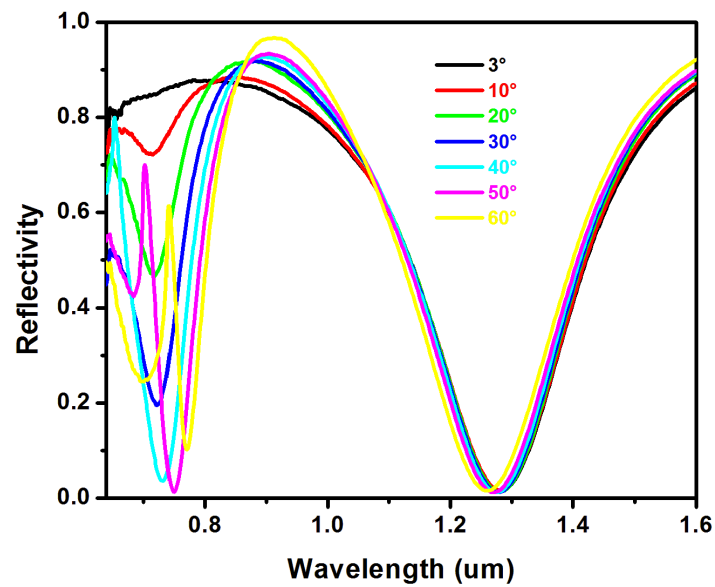
Au/Cr layer	Peak 1	Peak 2	Peak 3
40/2 nm (Sample 1)	745 nm (787 nm)	926 nm (930 nm)	1261 nm (1411 nm)
200/5 nm (Sample 2)	749 nm (795 nm)		1268 nm (1423 nm)

Table 5.3: The spectral positions of three peaks obtained from measurements (simulations) for 2 fabricated samples with different Au/Cr planar layer of metamaterial gratings when incident at 50° .

The discrepancies between the experimental and the simulation results in the amplitudes of the peak 2 in Fig. 5.16(a) is very likely to be caused by the surface roughness of the planar Au film, as well as the surface and line-edge roughness of the Au/Cr gratings. These roughness produce



(a)



(b)

Figure 5.16: Reflection spectra of the nano-grating array in the air ($n=1$) with different thickness of bottom Au/Cr layer: (a) Au/Cr=40/2 nm; (b) Au/Cr=200/5 nm.

additional scattering losses in the structure, which have been excluded in the calculation, as the perfectly flat metal/dielectric films and the ideal rectangular grating are used in the simulations.

5.5.2 Optical characterization of binding events

Finally, in order to demonstrate the feasibility of our metamaterial design may serve as a highly efficient LSPR sensor in the near-infrared, all surfaces of the Au/Cr gratings as well as the surface of the SiO₂ dielectric layer between gratings are covered by the sample materials.

In this study, the proof-of-principle experiment was performed with sample 2—with thick 200/5 nm Au/Cr bottom layer, which is sufficient to prevent coupling between the SPs on the top and bottom surfaces of the gold film. Just because of the presence of this gold mirror, the transmittance of the structure can be totally eliminated across the entire near-infrared frequency regime. The optical characteristics of the LSPR-based sensors using noble metal nanostructures were commonly detected with the help of a shift in the absorbance peak wavelength. Fig. 5.17 shows the corresponding absorption spectra of sample 2 in air obtained via $A = 1 - T - R$, where A, T and R are the absorbance, transmittance and reflectance respectively.

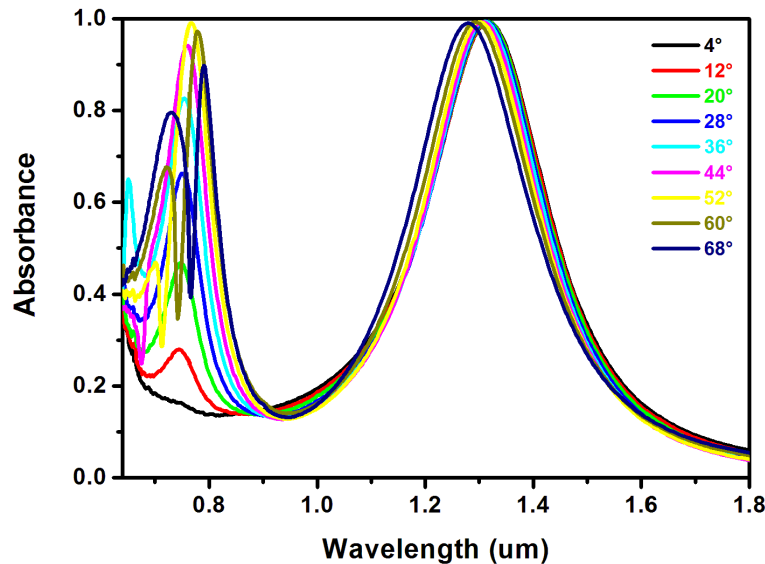


Figure 5.17: Experimental absorbance spectra of nanograting spectra in an air ($n=1$) obtained via $A = 1 - T - R$.

We carried out our tests by well-ordered orientation of immobilized antibody on the surface of nanograting metamaterial. Fig. 5.18(a) illustrates the sensing scheme that immobilize biomolecules (protein) on the sensing surface via the covalent binding. The sensing principle relies on the fact that zero reflectance occurs only for a certain refractive index of the surrounding medium. The variation of the refractive index of the surrounding medium gives rise to nonzero reflectance and therefore allows for the extremely sensitive detection of the intensity change in reflectance at a fixed frequency.

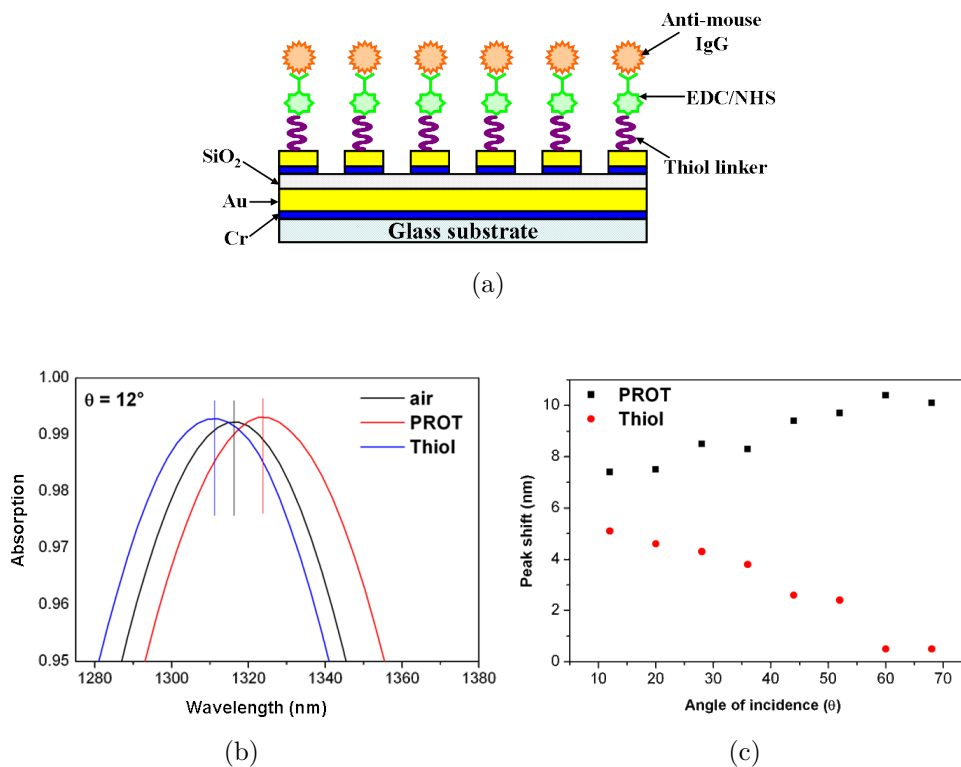


Figure 5.18: (a) Immobilization of anti-mouse IgG on the Au pattern surface using the SAM of 6-Mercaptohexanoic as an intermediate coupling layer. EDC/NHS was used to bind the anti-mouse IgG. Experimental tuning of the absorbance spectra by changing the dielectric environment which adjacent to the gold grating: (b) when incident at 12° and (c) plot of the the wavelength-associated maximum absorbance versus the incident angle.

Figure 5.18(b) shows the results of a proof-of-principle experiment performed when light incident at 12° , as characterized by the red curve in Figure 5.17, the experimental absorbance reaches a maximum of 99% at 1317 nm in air, which corresponds to an experimental reflectance reaches

a minimum of 1%. When thiol is applied onto the sample surface, a clear shift (5.33 nm) of the absorbance peak to shorter wavelength is visible. After activating sequentially by using EDC/NHS to bind with the anti-mouse IgG, it was observed that the absorbance peak shifted to higher value (5.38 nm red shift) as the anti-mouse IgG absorbed on the surface of the modified film. The experimental wavelength associated with maximum peak as a function of the incident angle for the reaction of anti-mouse IgG binding is presented in Figure 5.18(c). It can be found that the peak shift increase with the increasing of the incident angle for both thiol and protein bound. For the incident angle larger than 20° , as the incident angle increase, the peak shift nearly constant, until the incident angle increased to 60° , the peak shift increase again for the case of protein binding. This indicate that our sensor scheme suggests potential refractive index sensor platforms in which LSPR sensing is based on straightforward reflectance measurements with the exact incidence angle does not matter as much.

5.6 Conclusion

In conclusion, we have developed a fabrication method of high quality plasmonic nanograting metamaterials substrates by combining soft UV nanoimprint lithography and dielectric film deposition techniques. The nanograting arrays fabricated by soft UV nanoimprint lithography have a good homogeneity over large area (1 cm^2). The optical reflection properties of this nanograting metamaterials have been investigated. The results show that the reflection properties of the device have strong dependence on thickness of the metallic film on the glass substrate, the dielectric spacer and the metallic grating. And also, we have experimentally demonstrated our nanograting metamaterials is a perfect plasmonic absorber in the near-infrared. This absorber plasmonic nanograting sensor is very flexible and can be designed for achieving perfect absorbance in specific surrounding materials. The combination of basic sensing principles and particular physical phenomena opens up a new way for plasmonic sensing and it will facilitate a new class of nanoscopic biosensor. Finally, as the metamaterial fabrication procedure is simple and compatible with microchips and microfluidic technologies, the metamaterial-based biosensor can be integrated into complex systems such as micro total-analysis units.

Bibliography

- [1] R. Narayanaswamy and O. S. Wolfbeis. Optical sensors. Berlin Heidelberg: Springer-Verlag, 155, (2004).
- [2] J. Homola, S. S. Yee and G. Gauglitz. Surface plasmon resonance sensors: review. *Sens. Actuators B*, **54**:3, (1999).
- [3] I. Stemmler, A. Brecht and G. Gauglitz. Compact surface plasmon resonance-transducers with spectral readout for biosensing applications. *Sens. Actuators B*, **54**:98, (1999).
- [4] A. J. Haes, L. Chang, W. L. Klein and R. P. Van Duyne. Detection of a biomarker for alzheimer's disease from synthetic and clinical samples using a nanoscale optical biosensor. *J. Am. Chem. Soc* **127**:2264, (2005).
- [5] A. J. Haes, D. A. Stuart, S. M. Nie and R. P. Van Duyne. Using solution-phase nanoparticles, surface-confined nanoparticle arrays and single nanoparticles as biological sensing platforms. *J. Fluoresc* **14**:355, (2004).
- [6] C. R. Yonzon, D. A. Stuart, X. Zhang, A. D. Mcfarland, C. L. Haynes and R. P. Van Duyne. Towards advanced chemical and biological nanosensors: an overview. *Talanta*, **67**:438, (2005).
- [7] X. Y. Zhang, M. A. Young, O. Lyandres and R. P. Van Duyne. Rapid detection of an anthrax biomarker by surface-enhanced raman spectroscopy. *J. Am. Chem. Soc*, **127**:4484, (2005).
- [8] A. J. Haes and R. P. Van Duyne. A nanoscale optical biosensor: sensitivity and selectivity of an approach based on the localized surface plasmon resonance spectroscopy of triangular silver nanoparticles. *J. Am. Chem. Soc.*, **124**:10596, (2002).

- [9] T. R. Jensen, M. D. Malinsky, C. L. Haynes and R. P. Van Duyne. Nanosphere lithography: tunable localized surface plasmon resonance spectra of silver nanoparticles. *J. Phys. Chem. B*, **104**:10549, (2000).
- [10] N. Nath and A. Chilkoti. A colorimetric gold nanoparticle sensor to interrogate biomolecular integrations in real time on a surface. *Anal. Chem.*, **74**:504, (2002).
- [11] S. Enoch, R. Quidant and G. Badenes. Optical sensing based on plasmon coupling in nanoparticle arrays. *Opt. Express*, **12**:3422, (2004).
- [12] D. -K. Kim, K. Kerman, M. Saito, R. R. Sathuluri, T. Endo, S. Yamamura, Y. -S. Kwon and E. Tamiye. Label-free DNA biosensor based on localized surface plasmon resonance coupled with interferometry. *Anal. Chem.*, **79**:1855, (2007).
- [13] S. A. Maier. Plasmonics: Fundamentals and applications. Springer, (2007).
- [14] P. Galletto, P. F. Brevet, H. H. Girault, R. Antoine and M. Broyer. Enhancement of the second harmonic response by adsorbates on gold colloids: the effect of aggregation. *J. Phys. Chem. B*, **103**:8706, (1999).
- [15] J. F. Li, Y. F. Huang, Y. Ding, Z. L. Yang, S. B. Li, X. S. Zhou, F. R. Fan, W. Zhang, Z. Y. Zhou, D. Y. Wu, B. Ren, Z. L. Wang and Z. Q. Tian. Shell-isolated nanoparticle-enhanced raman spectroscopy. *Nature*, **464**:392, (2010).
- [16] S. S. Aćimović, M. P. Kreuzer, M. U. González and R. Quidant. Plasmon near-field coupling in metal dimers as a step toward single-molecule sensing. *ACS Nano*, **3**:1231, (2009).
- [17] L. S. Jung and C. T. Campbell. Sticking probabilities in adsorption from liquid solutions: alkylthiols on gold. *Phys. Rev. Lett.*, **84**:5164, (2000).
- [18] V. H. Pérez-Luna, M. J. O'Brien, K. A. Opperman, P. D. Hampton, G. P. López, L. A. Klumb and P. S. Stayton. Molecular recognition between genetically engineered streptavidin and surface-bound biotin. *J. Am. Chem. Soc.*, **121**:6469, (1999).
- [19] L. S. Jung, C. T. Campbell, T. M. Chinowsky, M. N. Mar and S. S. Yee. Quantitative interpretation of the response of surface plasmon resonance sensors to adsorbed films. *Langmuir*, **14**:5636, (1998).

- [20] A. J. Haes, S. L. Zou, G. C. Schatz and R. P. Van Duyne. Nanoscale Optical Biosensor: Short Range Distance Dependence of the Localized Surface Plasmon Resonance of Noble Metal Nanoparticles. *J. Am. Chem. Soc.*, **108**:6961, (2004).
- [21] L. S. Jung and C. T. Campbell. Sticking probabilities in adsorption of alkanethiols from liquid ethanol solution onto gold. *J. Phys. Chem. B*, **104**:11168, (2000).
- [22] J. M. Brockman, B. P. Nelson and R. M. Corn. Surface plasmon resonance imaging measurements of ultrathin organic films. *Annu. Rev. Phys. Chem.*, **51**:41, (2000).
- [23] A. D. McFarland and R. P. Van Duyne. Single silver nanoparticles as real-time optical sensors with zeptomole sensitivity. *Nano Lett.*, **3**:1057, (2003).
- [24] R. P. Van Duyne and A. J. Haes. Nanoparticle optics: sensing with nanoparticle arrays and single nanoparticles. *Proc. SPIE-Int. Soc. Opt. Eng.*, **5223**:197, (2003).
- [25] E. A. Smith, W. D. Thomas, L. L. Kiessling and R. M. Corn. Surface plasmon resonance imaging studies of protein-carbohydrate interactions. *J. Am. Chem. Soc.*, **6140**:125, (2003).
- [26] D. A. Stuart, A. J. Haes, C. R. Yonzon, E. M. Hicks and R. P. Van Duyne. Biological applications of localized surface plasmonic phenomena. *IEE Proc.-Nanobiotechnol.*, **152**:13, (2005).
- [27] S. L. Zou and G. C. Schatz. Narrow plasmonic/photonic extinction and scattering line shapes for one and two dimensional silver nanoparticle arrays. *J. Chem. phys.*, **121**:12606, (2004).
- [28] G. L ev eque and O. J. F. Martin. Tunable composite nanoparticle for plasmonics. *Opt. Lett.*, **31**:2750, (2006).
- [29] V. M. Shalaev, W. S. Cai, U. K. Chettiar, H. -K. Yuan, A. K. Sarychev, V. P. Drachev and A. V. Kildishev. Negative index of refraction in optical metamaterials. *Opt. Lett.*, **30**:3356, (2005).
- [30] S. Lal, S. Link and N. J. Halas. Nano-optics from sensing to waveguiding. *Nature Photon.*, **1**:641, (2007).

- [31] A. N. Grigorenko, N. W. Roberts, M. R. Dickinson and Y. Zhang. Nanometric optical tweezers based on nanostructured substrates. *Nat. Photon.*, **2**:365, (2008).
- [32] A. V. Kabashin, P. Evans, S. Pastkovsky, W. Hendren, G. A. Wurtz, R. Atkinson, R. Pollard, V. A. Podolskiy and A. V. Zayats. Plasmonic nanorod metamaterials for biosensing. *Nat. Mater.*, **8**:867, (2009).
- [33] I. I. Smolyaninov. Two-dimensional plasmonic metamaterials. *Appl. Phys. A*, **87**:227, (2007).
- [34] F. J. Garcia-Vidal, L. Martín-Moreno and J. B. Pendry. Surfaces with holes in them: new plasmonic metamaterials. *J. Opt. A: Pure Appl. Opt.*, **7**:897, (2005).
- [35] S. Collin, F. Pardo, R. Teissier and J. -L. Pelouard. Strong discontinuities in the complex photonic band structure of transmission metallic gratings. *Phys. Rev. B*, **63**:033107, (2001).
- [36] C. Enkrich, F. Perez-Williard, D. Gerthsen, J. Zhou, T. Koschny, C. M. Soukoulis, M. Wegener and S. Linden. Focused-ion-beam nanofabrication of near-infrared magnetic metamaterials. *Adv. Mater.*, **17**:2547, (2005).
- [37] N. Feth, C. Enkrich, M. Wegener and S. Linden. Large-area magnetic metamaterials via compact interference lithography. *Opt. Express*, **15**:501, (2006).
- [38] W. Wu, E. Kim, E. Ponizovskaya, Z. Liu, Z. Yu, N. Fang, Y. R. Shen, A. M. Bratkovsky, W. Tong, C. Sun, X. Zhang, S. -Y. Wang and R. S. Williams. Optical metamaterials at near and mid-IR range fabricated by nanoimprint lithography. *Appl. Phys. A*, **87**:147, (2007).
- [39] W. Wu, E. Kim, E. Ponizovskaya, Z. Yu, A. M. Bratkovsky, P. Chaturvedi, N. X. Fang, R. Shen, X. Zhang. Optical metamaterials fabricated by nanoimprint lithography. *Proc. SPIE*, 6462, (2007).

Conclusion

The research conducted in this thesis is concentrated on the development of soft UV nanoimprint lithography and the exploration of its application for surface plasmon resonance biosensors. We have studied different aspects of soft UV nanoimprinting processes. This technique has allowed us to study surface plasmons phenomena in a series of metallic nanostructures with different surface morphologies and geometries. Evaluating the results from our proof-of-principle experiments, we can conclude that soft UV-NIL is an optimal flexible nanofabrication technique with high-throughput that allows patterning on large areas with high resolution.

Soft UV-NIL requires the development of various technologies such as fabrication of master and replica mold, deposition of an anti-sticking layer, imprinting process, and imprinting systems. We have first investigated the fabrication of master mold. Three different resists for EBL were chosen and the processes were experimentally optimized. For the replicated soft stamp three different configurations have been studied: PDMS stamp, h-PDMS/PDMS stamp and PFPE/PDMS stamp. It turned out that the process using both h-PDMS/PDMS and PFPE/PDMS stamps were suitable for patterning sub-100 nm features. Although the master patterned by EBL worked successfully, its fabrication process is still not suitable for mass production because of their long writing time and expensive equipments. In this context, we have specifically developed a reliable NIL process for replicating and inverting expensive EBL master molds with good shape homogeneity and size uniformity.

With the NX-2500 imprint machine from Nanonex company, imprints were then performed on different substrates with widely varying surface morphology. All features on the stamp were faithfully imprinted under the optimized working parameters (imprint pressure 10 psi, imprint temperature 20 °C, pumping time 1 min 30 s, processing time 2-4 min and

UV time 10 min for Amonil resist). For subsequent successfully pattern transfer into the undercoating polymer resist layer, we have shown that it is first essential to minimize the thickness of the UV resist residual layer. Our analysis showed that the minimum residual layer thickness achieved for the resist Amonil MSS10 was around 28 nm. Secondly this minimized residual layer has to be anisotropically etched in order to obtain a good dimension control on the substrate. Satisfactory results in both sidewall profile and surface roughness have been achieved with our optimized RIE processes (NXR7, NXR22, NXR27, NXR28 and NXR29). Finally, several pattern transfer methods including lift-off (bi-layer and tri-layer system), reactive ion etching and ion beam etching have been tested. We found that a tri-layer system is the best way to enhance process latitude. For feature size down to 100 nm, we proposed to use IBE for pattern transfer.

The developed soft UV-NIL processes have been applied to two types of surface plasmon resonance sensing investigations. Firstly, high quality and large area gold nanohole arrays were integrated into simple fluidic device for transmission enhanced SPR biochemical studies. The fabricated nanoholes arrays showed a good homogeneity and controllable feature size with the precision of several nanometers. The results obtained by measuring the transmission spectra of the samples with different diameter and period showed that the plasmonic transmission response of these nanohole arrays is related to their diameter and period. Furthermore, to check their sensitivity to any refractive index change in the vicinity of the nanostructure surface, different chemical solution have been tested, which confirms the high sensitivity of nanohole arrays for real-time chemical/bio-sensing with SPR.

Secondly, we developed a fabrication method of high quality plasmonic nanograting metamaterials substrates by combining soft UV nanoimprint lithography and dielectric film deposition techniques. The optical reflection properties of this nanograting metamaterials have been investigated both by simulation and experiment. The reflection properties of our device exhibit a strong dependence on thickness of the metallic film, the dielectric spacer and the metallic grating. We have experimentally demonstrated that our nanograting metamaterials is a perfect plasmonic absorber in the near infrared which can be designed as a new class of nanoscopic biosensor.

To conclude this thesis work, soft UV nanoimprint lithography offers simple, high resolution, wafer-scale fabrication of plasmonic structures and opens up great opportunities for a wide variety of real-life plasmonic applications, ranging from subwavelength optical interconnects to biosensors. Moreover, a soft UV-NIL based technology platform allows the integration

of plasmonic components into more complex device geometries, such as microfluidic channels for applications in chemical, bio-sensing and lab-on-a-chip devices.